Nuclear Fusion Project
Annual Report of the
Association Forschungszentrum
Karlsruhe/EURATOM
October 1994 – September 1995

Projekt Kernfusion

Januar 1996

Forschungszentrum Karlsruhe

Technik und Umwelt

Wissenschaftliche Berichte

FZKA 5688

EUR 16749 EN

Nuclear Fusion Project
Annual Report of the
Association Forschungszentrum
Karlsruhe/EURATOM

October 1994 - September 1995

compiled by G. Kast

Projekt Kernfusion

Januar 1996

Preface

The Fusion Project of the Karlsruhe Research Center (FZK) was founded in 1982 under an association agreement with the Commission of the European Communities to support the European Fusion Technology Programme.

Various nuclear fission programmes and earlier component development for particle accelerators were the basis for a broad input of FZK in almost all areas of the newly founded Next Step and Long Term Fusion Technology Programmes.

Major test facilities were built or upgraded during the past decade. To name only the most important ones: TOSKA, a test facility for large (up to 5 m size) superconducting magnets, the tritium laboratory TLK with more than 1000 m² of experimental area and 20 g of tritium inventory, EDITH, a demonstration environment for full scale remote maintenance equipment, and the dual beam facility to simulate irradiation effects under fusion conditions.

Having been developed for the requirements of the Next European Torus Programme initially, most of the installations are equally well suited for the International Tokamak Experimental Reactor ITER (TOSKA, TLK and smaller set-ups for the test of vacuum pumping systems, plasma facing materials and microwave components). Today about fifty percent of FZK's fusion programme is contracted to ITER via the contribution of the European home team.

Medium term, cooperation on the recently approved Wendelstein 7X Stellarator will form an increasing constituent of our programme concentrating on the areas of gyrotron development and qualification of superconducting coils.

The FZK fusion project has permanently put emphasis on supporting the development of breeding blankets and related materials research.

With the recent selection of blanket concepts in the European frame, a concentration process has been initiated which will result in some restructuring of our blanket programme. We are confident that the results documented in this report will be relevant to the future work of the European Blanket Development Group.

Closely related to blanket development is the long term materials programme. FZK has concentrated on reduced activation ferritic-martensitic steels. Important project resources for irradiations and hot cell work are devoted over long periods of time to characterize and improve the performance of suitable structural materials. A major fraction of underlying technology support (support for not strongly task oriented effort) is applied to this work area.

The yearly report of the FZK-EURATOM association is structured according to the organizational scheme of the European Technology Programme. ITER references are given in the nomenclature valid during the reporting period.

The annexes provide the reader with some information on participating departments and on the project management structure.

The achievements documented in this report were made possible due to the support of the partners of FZK, the Federal Republic of Germany, the State of Baden-Württemberg and by additional funds of the Commission of the European Community. The involvement of industry and the cooperation with many research institutes sharing with us the interest in the development of nuclear fusion is particularly acknowledged.

J.E. Vetter

Contents   Page

Plasma Facing Components and Plasma Engineering

Introduction:

Work on a limited choice of ITER tasks for the qualification of plasma-facing materials and components has been continued.

Within PPM 6 tritium retention behaviour and the effect of neutron damage has been studied for beryllium and carbon-based wall protection materials and an increase in tritium retention with fluence has clearly been determined irrespective of fundamental difficulties to quantify damage annealing and to distinguish between the amount of tritium generated in the material and what would be taken up from the plasma. Work is being continued under tasks T 221 and T 227.

Major experimental work on thermal fatigue behaviour of water-cooled First Wall mock-ups has been carried out under task T 9, the former PDT 1. A comparative long-term test was made for specimens with and without artificial cracks, accompanied by calculations on temperature and stress distribution. An inspection of the samples after every 10 000 cycles allowed for a follow-up of crack initiation and propagation. In addition to this ITER-related work the test facility was used to validate the design concept for the thermal contact between CFC-tiles and the water-cooled steel plate of the new divertor for ASDEX-UG.

Within ITER-related task T 226b, previously PPM 3, the improvement and validation of calculation codes for modelling disruptive erosion reduction at the divertor plates due to vapour shield formation was continued. The existing code was extended to properly describe the MHD motion of the plasma shield in the inclined magnetic field and to account for heat radiation and reabsorption in a self-consistent way. After validation of the model against disruption simulation experiments divertor plate erosion was calculated for the candidate divertor materials in an ITER geometry.

Under ITER-task T 26/T 246 (previously PPM 4) the capability of the cryogenically cooled sapphire window for the transmission of electron-cyclotron heating power and its limitations under radiation are studied. The intrinsic losses to be expected and the positive feedback of high power load have been quantified and proved to be consistent not only with European but only US and Japanese window developments. The tolerable neutron fluence derived from an ambient temperature irradiation was verified by a more sophisticated low temperature irradiation program. Investigations for alternative window concepts (based on Si or CVD diamond grades) with much less stringent cooling conditions are ongoing.

H.D. Röhrig

G 17 TT 25 EU (T 226 b)
Plasma Disruption Simulation

Improvement and validation of the one dimensional (1D) code FOREV-1 for modelling of plasma shield formation and calculation of disruption erosion was the main activitiy in the period to be reported. Fig. 1 schematically shows the divertor
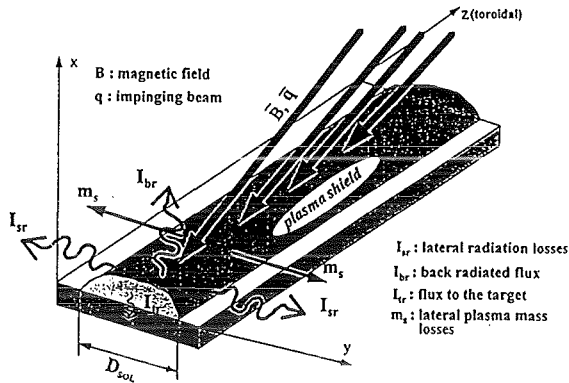
Fig. 1: Divertor with inclined magnetic field

situation with the plasma shield and the finite width (D_{SOL}) of the incoming disruptive plasma stream. A 1½D magnetohydrodynamics (MHD) model was developed and is used in the FOREV-1 to describe the MHD motion of the plasma shield in the inclined magnetic field.

For the radiation transport the forward reverse method with 6 directions per hemisphere is used. As radiation transport mainly determines the erosion three radiation transport approaches are available in the code: radiative heat conduction, multigroup opacity, and self consistent modes. In the multigroup opacity approach the opacities are produced with an optimized frequency mesh which allows to resolve the profiles of important lines. The optical data are calculated with the CRE model taking into account reabsorption of radiation in optically not thin plasma. Another important feature of the 1½D MHD code is spatial mesh optimization which allows to use a dense mesh in regions of large plasma temperature and density gradients and permanently several cells for describing the energy and momentum deposition of the incoming ion beam. Losses of plasma mass and radiative energy through the side surfaces (lateral losses) are taken into account using simplified models. The real tokamak situation requires a 2D description. Therefore development of the 2D FOREV-2 with 2½D MHD model was started with beginning of 1995.

Validation of the physical models used in both FOREV codes against disruption simulation experiments was done and plasma shield formation and divertor plate erosion was calculated for the divertor candidate materials Be, C and W [1 - 3]. Fig. 2 shows as example a 2D distribution of the density in the plasma shield produced in the ITER divertor slot as obtained with FOREV-2 for a beryllium target hit by a plasma stream of maximum power density of 100 GW/m² at y = 8 cm and a half width of the plasma stream of D_{SOL} = 5 cm. The target is at x = 0 cm. The vacuum magnetic field is 5 T in
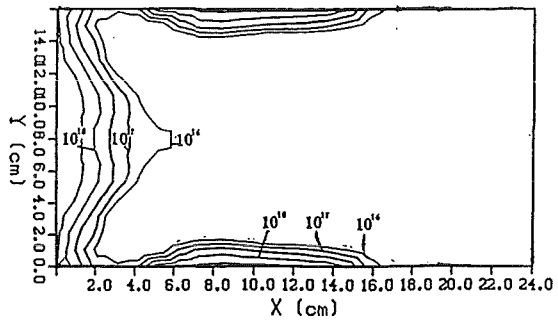
Fig. 2: Ion density contour for beryllium target with plasma stream power density of 10 MW/cm² after 22 μs

z- and 0.5 T in x-direction. Erosion of the walls caused by lateral radiation is clearly seen. 7 % of the incoming power causes heating and erosion of the divertor plate, about 28 % is radiated to the side walls with a radiation intensity of 0.4 MW/cm² at distances up to 20 cm from the target. Movement of vaporized mass parallel to the target and increase of the width of target erosion due to lateral radiation are clearly seen.

Widening of the erosion zone at the target and erosion at side walls results in formation of a 2D plasma shield with rather complex structure. Detailed 2½D MHD modelling of the dynamics of the plasma shield in the ITER divertor slot will be performed in a next step.

Literature:

[1] B. Bazylev et al., IEEE ICPS 1995, 5 - 8 June 1995, Madison, Wisconsin, 95CH35796, p. 93.

[2] B. Bazylev et al., 22 EPS Conf. on Controlled Fusion and Plasma Physics, Bournemouth 3rd - 7th July 1995, Vol. 19c, part II, p. 277.

[3] H. Würz et al., Seventh International Conference on Fusion Reactor Materials (ICFRM-7) Obninsk, September 25 - 29, 1995.

Staff:

B. Bazylev[2]
F. Kappler
I. Landman[1]
S. Pestchany[1]
G. Piazza
H. Würz

[1] Troitsk Institute for Innovation and Fusion Research, Troitsk, Russia

[2] Luikov Institute, Minsk, Belarus

G 52 TT 246 EU (T 26/T 246)
Ceramics for Heating and Current Drive and Diagnostic Systems

Following the given frame of the ITER tasks, the effects of radiation on candidate insulator materials, especially on window materials for electron cyclotron (EC) systems, are studied under application relevant conditions. The targets are to establish the limitations of the presently available "cryo-window" concept based on sapphire and to pursue promising alternative concepts based on special silicon grades and on CVD diamond.

The aspects of the dielectric properties were mainly investigated at the application frequency of 145 GHz. For the "cryo-window" concept, the earlier studies had established a solid data base for various grades of Sapphire and had supplied a description of the expected intrinsic losses ("2-phonon-model") and of their dependence on temperature and frequency. The results obtained by low power measurements now proved to be consistent with high power studies using the evolution of window temperature profiles during gyrotron operation (Fig. 1).
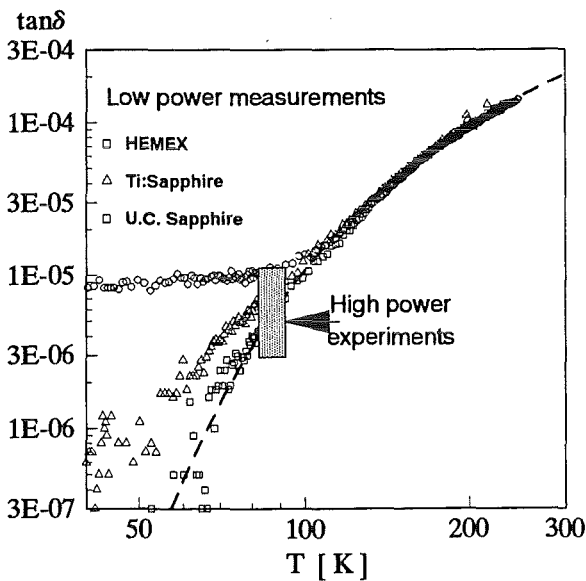
Fig. 1: The dielectric loss in sapphire at 145 GHz according to the 2-phonon-model (broken curve) compared to results from low and high power measurements.

The relevance of this data base gave positive input to the window characterization of ITER gyrotron developments, mainly to European activities at the FZK and at Cadarache, but also for the US and Japanese sapphire-based window concepts. Thus, it could be found that the Japanese sapphire grades did not show unusually high dielectric absorption as it was suspected in first high power studies but followed more or less the minimum curve for intrinsic losses. The temperature rise in a sapphire window developed at MIT was consistent with a description using the 2-phonon model.

The present recommendation for an acceptable neutron fluence at the "cryo-window" near the torus was set to 10^{21} n/m^2 (E > 0.1 MeV) following the post-irradiation experiments after a neutron irradiation at $T_{irr} \approx 320$ K ("ambient T"). In this summer, the irradiation project at 77 K could be performed for this fluence at Petten ("cryogenic T"). After irradiation, the specimens were taken at well defined intervals to 200 K (during transport) or to 300 K (before measurement), which reflects in a way the thermal history of an actual window during and after operation of EC wave systems. Preliminary data for one special sapphire grade (HEMEX) gave no evidence for significant differences to the previous post irradiation dielectric data. In this case, critical enhancement of radiation defects does not appear even at the much lower irradiation temperature. In addition, the test stand for measuring neutron-irradiated specimens under X-ray irradiation was realized and calibrated. Up to the presently obtained X-ray dose rates of 0.5 Gy/s, no additional radiation-enhanced dielectric loss was found at 35 GHz even for specimens neutron-irradiated up to 10^{23} n/m^2, which had significant neutron-induced increases in loss.

The investigations for the alternative window concepts which promise operation temperatures much closer to ambient conditions concentrated on demonstrating the availability of window relevant sizes of suitable silicon and CVD diamond grades and on bringing together a suitable specimen set for the neutron-irradiations scheduled for next year. Indeed, the procedure of gold doping in high purity silicon grades, which was followed in cooperation with the Institute of Applied Physics/Nizhny Novgorod (RF), proved to be adequate also for discs with larger diameters (4") and thickness (3.5 mm). A model window disc was formed and its dielectric characterization showed extremely low loss levels (Fig. 2) allowing an operation at 210 K.

The same doping procedure is now being applied to the test set prepared for the neutron irradiation. The complimentary test set for CVD diamond was procured by a development at DeBeers (UK) by which specimens with losses around $5 \cdot 10^{-5}$ were realized. Similary good properties were found for the largest diamond disc test so far (40 mm dia x 1.1 mm).

Literature:

[1] J. Molla, A. Ibarra, R. Heidinger, E.R. Hodgson; Electron-irradiated silicon: An optimized material for gyrotron windows, J. Nucl. Mater. 218 (1995), 108-112.

[2] V.V. Parshin, R. Heidinger, B.A. Andreev, A.V. Gusev, V.B. Shmagin; Silicon as an advanced window material for high power gyrotrons, Int. J. of Infrared and MM Waves, 16 (5) (1995), 863-877

[3] V.V. Parshin, R. Heidinger, B.A. Andreev, A.V. Gusev, V.B. Shmagin; Silicon with extra low losses for Megawatt output gyrotron windows; Digest of the 20th Int. Conf. on Infrared and MM Waves, Orlando (USA), 11.-15.12.1995
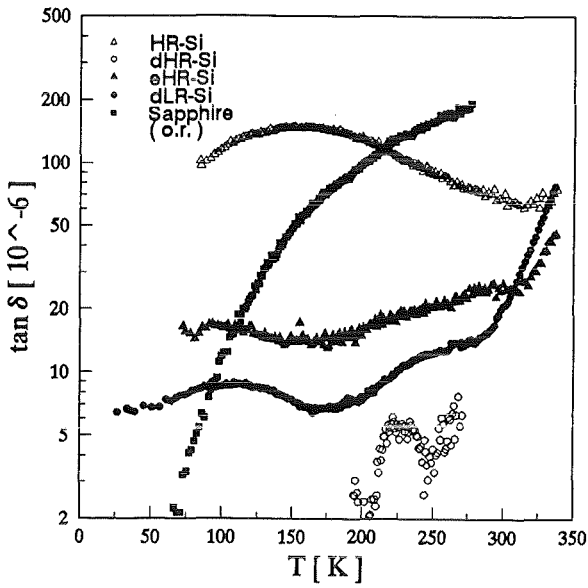
Fig. 2:   The dielectric loss at 145 GHz in various silicon
           grades compared to loss in sapphire. The open
           circles represent data measured for a grade from a
           model window disc.

[4]   G. Garin, G. Bon-Mardion, M. Pain, R. Heidinger, M.
       Thumm, A. Dubrovin, E. Giguet, C. Tran; Cryogenically
       Cooled Window: a New Step toward Gyrotron CW
       Operation; Digest of the 20th Int. Conf. on Infrared
       and MM Waves, Orlando (USA), 11.-15.12.1995

[5]   R. Heidinger, G. Link; The MM-Wave Absorption in
       Sapphire and its Description by the 2-Phonon Model;
       Digest of the 20th Int. Conf. on Infrared and MM
       Waves, Orlando (USA), 11.-15.12.1995

Staff:

M. Blumhofer
R. Heidinger
P. Severloh
L. Steinbock
H. Zimmermann

Thermophysical Properties

The thermal conductivity of BeO.

With a laserflash technique the thermal diffusivity a of BeO
was measured on three samples of different thicknesses. The
mean value of the thermal diffusivity up to 1500°C as function
of temperature is given in Fig. 3.

Because of the high transparency to the laser wavelength
(1.064 µm), the measurements were difficult and resulted in a
standard deviation of about 8 % at room temperature and

Thermal Diffusivity a of BeO
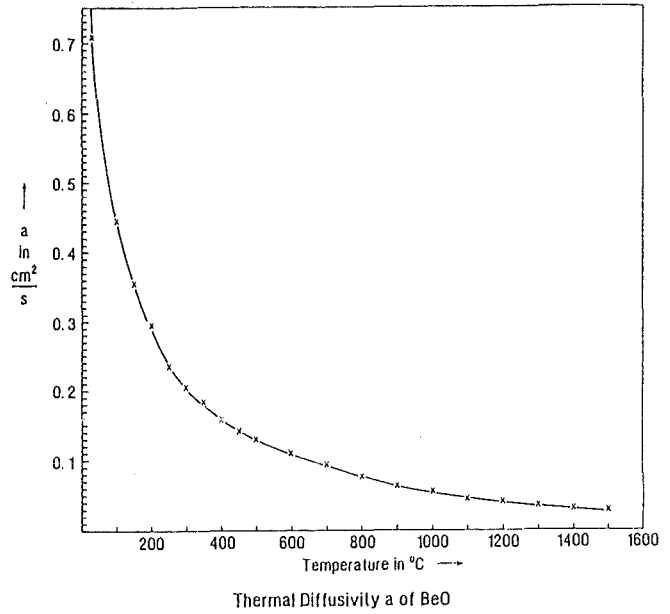
Fig. 3:   Mean values of thermal diffusivity of BeO vs.
           temperature

5 % for T > RT. Using known specific heat data c_p and the
measured density ρ of the samples, the thermal conductivity,
was determined, according to

$$\lambda = a \cdot c_p \cdot \rho$$

The temperature function of the thermal conductivity is
presented in Fig. 4.

Thermal Conductivity λ of BeO
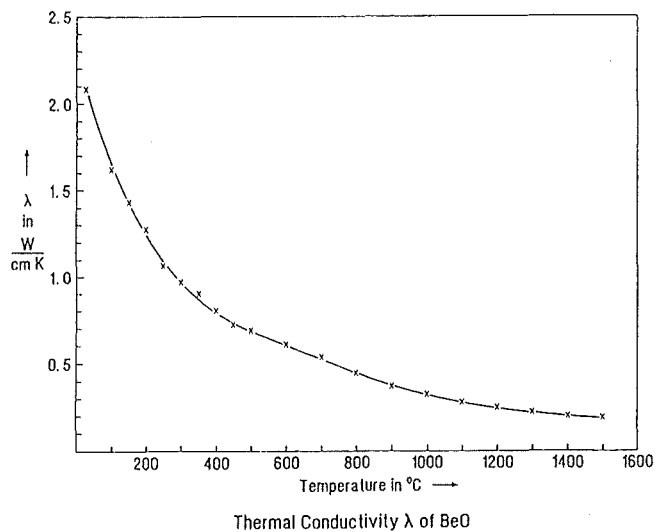
Fig. 4:   Thermal conductivity of BeO vs. temperature

up to 600°C the thermal conductivity follows a linear
relationship given by

$$\lambda = (0.16 + 0.83 \cdot 10^{-3} \, T)^{-1} \qquad [\lambda] = W/cm\,K$$
$$[T] = °C$$

The characterization of this material is not yet finished. By RFA-element analysis the following impurities were found Si, Mg, S, Mn, Cu. The subseqent preparation of BeO for microstructrual analysis, showed (Fig. 5) the ceramic to consist of two phases in a composition of ~ 90 vol. % BeO + 10 vol. % of a second oxide.

This fact makes difficult the interpretation of mechanisms and the correction of the thermal conductivity for porosity as well. The characterisation of this ceramic is still going on.

Due to safety reasons all investigations on BeO-ceramics were performed under hot cell conditions, except the RFA -analysis.

The determination of the thermal diffusivity of irradiated AlN and SiC is finished. It was performed in the laserflash equipment in the hot cells. Fig. 6 shows an example on highly irradiated SiC (19dpa) and its recovery behaviour.

In preparation of the laserflash equipment for very fast samples like CVD-Diamond and pure Si a new evaluation software was installed and experimentely tested. Summarising the results: we are able to measure the thermal diffusivity down to half rise times < 1/4 of laser pulse width.

The low temperature laserflash equipment was tested down to a sample temperature of 10 K. The testing is still going on.

Literature:

[1] B. Schulz, H. Ziegler; Determination of the thermal diffusivity (conductivity) on High Radioactive Materials: Brochure Forschungszentrum Karlsruhe

[2] L. Dusza, M. Hoffmann, B. Schulz; The application of the Laserflash method to very thin samples. 4th Int. Workshop on Subsecond Thermophysics, DLR Köln, 26 - 29 June 1995

Staff:

G. Haase
P. Mangai
B. Schulz
H. Ziegler

Fig. 5:   Micrograph of "BeO", non etched
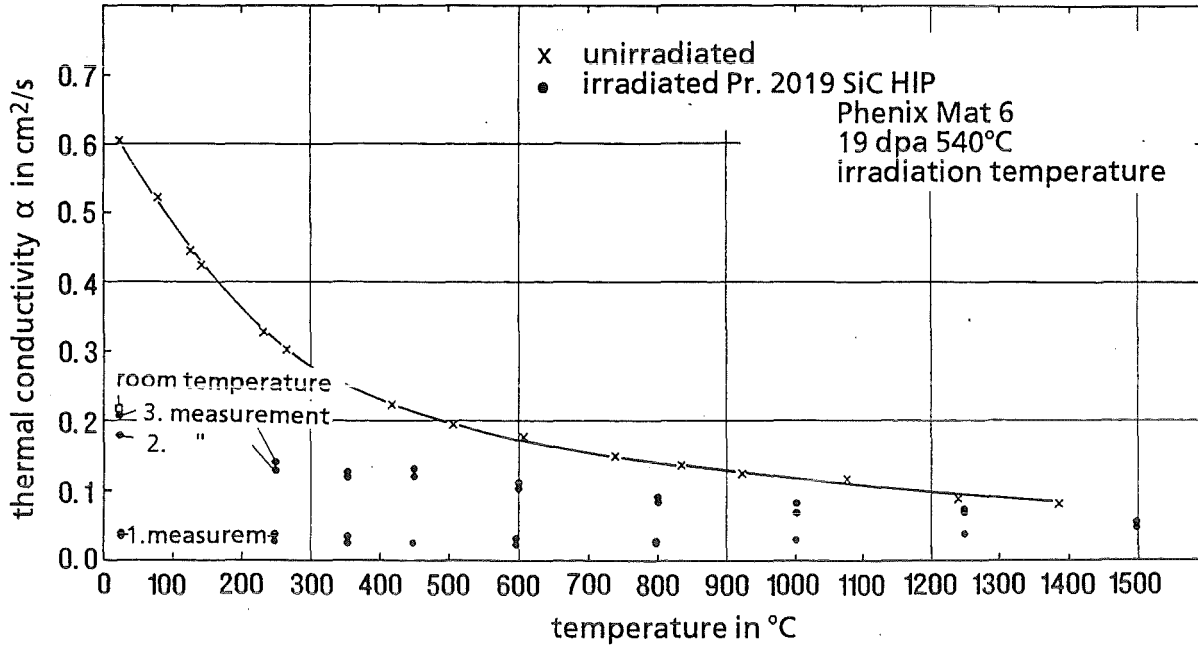
Fig. 6: Thermal diffusivity of highly irradiated SiC and its recovery behaviour.

G 17 TT 25 EU (T 227)
Tritium Permeation and Inventory

Subtask 2:   H/T Retention Studies in Neutron Irradiated
Graphites, CFCs and Doped C Composites

Staff:

E. Damm
T. Eberle
H. Jakisch
J. Lebkücher
K.H. Simon
A. Weisenburger
H. Werle
H. Ziegler

Carbon-based materials and beryllium are considered as protective layers for plasma-facing components of fusion reactors. Previous studies for graphite indicated an increase of tritium retention with neutron damage leading to tritium inventories which present a severe safety problem.

A common NET/ECN/FZK program has therefore been initiated to investigate the effect of neutron damage on tritium retention in carbon-based materials and in beryllium. Tritium retention is studied by loading unirradiated and irradiated samples in a H_2/T_2 atmosphere and determining the loaded inventory by annealing.

For graphite and CFCs, which were mainly investigated at ECN, in agreement with previous studies, an increase of tritium retention with damage was observed below 0.1 dpa. But whereas in the previous work an increase of more than a factor ten was found, in this study, only a factor of about five was observed.

For beryllium, which was studied at FZK, the determination of tritium retention is difficult because of the huge amount of neutron-produced tritium in irradiated beryllium. At least a large fraction of the neutron-produced tritium must be released before loading studies can be performed. This requires so high temperatures (> 850 °C) that probably any neutron-induced traps are annealed. The samples were loaded at various pressures in a HT+HTO atmosphere (HZ) or in a pure HT atmosphere (IRCH). Independent of the type of loading a gradual increase of tritium retention with fluence is observed in the range $\leq 4 \cdot 10^{22}/cm^2$ (≤ 40 dpa), resulting in a retention, which is at $4 \cdot 10^{22}/cm^2$ about a factor ten higher than that of unirradiated material (Fig. 1). This increase is assumed to be due to irreversible changes in the microstructure of the samples caused by helium bubbles transport.

Literature:

[1]   H. Werle, "Retention of Tritium in Irradiated Beryllium", FZK, Internal Report, Sept. 1994.

[2]   J. Lebkücher, A. Weisenburger, H. Werle, "Release of Loaded Tritium from Irradiated Beryllium and Graphite", FZK, Internal Report, August 1995.

[3]   H. Kwast, H. Werle, C.H. Wu, "Tritium Retention in Neutron-Irradiated Carbon-Based Materials and Beryllium", 7th Int. Workshop on Carbon Materials, Stockholm, Sept. 21 - 22, 1995.
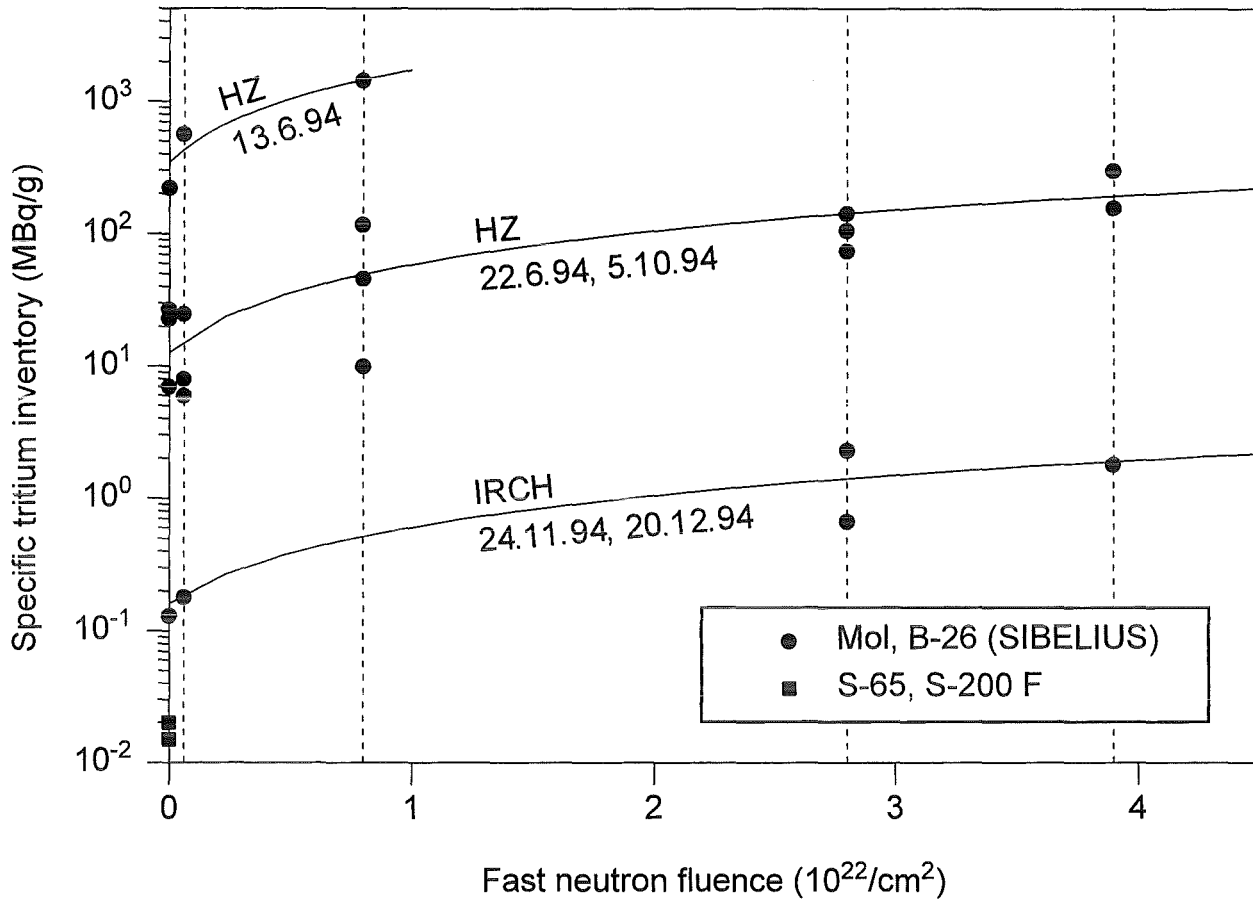
Fig. 1: Tritium retention as a function of fast neutron fluence for beryllium ($10^{21}/cm^2$ corresponds to 1 dpa).

G 16 TT 16 EC (T 9)
Fabrication and Testing of Water Cooled, Small Size FW Mock-ups

Subtask 4: Thermal fatigue testing of small mock-ups with and without artificial

Task T 9 includes a continuation of the earlier NET task PDT 1.4. One of its goals would be to generate experimental data that could be utilized for verifying and for improving computer codes that are able to predict the failure by thermal fatigue of first wall structures.

The test facility FIWATKA is used to perform such thermal fatigue tests with geometrically relatively simple small size mock-ups made from stainless steel AISI 316 LN; the specimens are 260 · 52 · 28 mm in size and are continuously water-cooled through two 12 mm i.d. cooling channels. Three of these specimens are being tested in parallel. Two specimens were weakened in zones of high stresses by artificial defects electro-eroded to a depth of up to 1 mm, one specimen at the heated surface between the channels and the other specimen at the inner surface of a cooling channel; the third specimen was left without defects for comparison. The position and the orientation of the artificial cracks have been chosen on the basis of finite element calculations: Exploiting the symmetry of the specimen, a two dimensional model based on the hypothesis of generalized plane strain was constructed. This kinematical hypothesis is especially appropriate for analyzing thermal stresses in plate like structures. First, the temperature distribution was calculated. In a second step, the resulting temperature distribution was the input for the calculation of stresses and strains for a linear thermoelastic material. The steepest temperature gradient is found right between the heated surface and the cooling channel. Because of this, the largest stress amplitudes are found in this region close to the surface of the cooling channel and in the opposing portion of the heated surface.

The long-term thermal fatigue test consists of subjecting the specimens to a surface heat flux of 75 W/cm² for 80 seconds and of repeating this load every 180 seconds. These data were chosen on the basis of an analysis of the transient heat transfer problem of the specimen. For the calculation of the transient temperature distributions, the graphite heaters of FIWATKA were included in the finite element model, in order to represent the thermal dynamics of the system as realistically as possible. In order to avoid creep damage in the specimen, the maximum heat flux loading had to be defined such, that the temperatures at the heated surface between the cooling channels did not exceed 450 °C. A single heating cycle consists of a ramp of linearly increasing heat flux, a phase of constant heating, a ramp of linearly decreasing heat flux, and a closing phase with almost zero load. The phases of constant loading had to last for enough time, in order to reach stationary conditions. In this way the minimum duration of the heating cycle was found, which ensured realistic conditions in view of the loading conditions in a fusion reactor. After every 10 000 cycles the specimens are inspected with an eddy current method in order to identify any growth of the artificial defects. During a total of 40 000 cycles the test which is still continuing, revealed crack initiation and a heavy propagation at the defects inside the cooling channel; the velocity of crack growth increased and the maximum crack depth reached 4 mm out of the 5 mm thick wall.

An end of the test will be reached when either complete penetration or crack arrest will have been detected. On a repetition of the test, that would last for another couple of month, will be decided when the results of model calculation and experiment can be compared.

Cooperation with IPP Garching: Tests on the Thermal Transmittance of Compliant Layers at Divertor II of ASDEX-UG

ASDEX-UG is to receive a new divertor which consists of CFC tiles that are pressed to a water-cooled stainless steel plate; a compliant layer between the tile and the plate is to improve the thermal contact between the two; the contact should be good enough so that the energy that is stored in the tile during the shot is transferred to the plate during the dwell time of 10 minutes before the next shot starts.

The FIWATKA facility was used as a heat source to determine the heat transmittance characteristics of several types of compliant layers ranging from no layer to layers covering the contact surfaces partly or fully. In general compliant layers made from laminated (flexible) graphite (Sigraflex) resulted in heat transmittances adequate for the problem. The tests confirmed the earlier observation [1] that the heat transmittance may be improved by increasing the area of close contact even if this is paid for with additional layer thickness; thick layers may promote the contact since they offer the flexibility necessary for good overall contact even at low contact pressures. Good results were also gained, when the contact area was covered with the compliant layer only partly limited to zones of the most intense cooling of the plate; here ineffective zones were omitted and the contact pressure was increased by, at constant contact force, reducing the contact area.

Literature:

[1]   G. Hofmann et al.; Heat Flux Testing of Protection Tiles in front of a First Wall Mock-up; Proc. of the 18th SOFT, Aug. 1994 in Karlsruhe, p. 379.

Staff:

E. Diegele
E. Eggert
G. Hofmann
M. Kamlah
G. Rizzi

Superconducting Magnets

Introduction:

The confinement of plasma in ITER relies on a super-conducting magnet system consisting of 20 D-shaped toroidal field coils, a central solenoid to drive the plasma current and a set of poloidal field coils for plasma stabilization. FZK is together with the EC Home Team and other associated European laboratories involved in the development of these magnet systems. Components of ITER conductors, subsize conductor assemblies are examined for their performances. Materials to be used in coil construction are qualified for their application under cycling load. Cryogenic loops and components are developed to establish stable forced flow conditions to cool the magnets. An important task is now the upgrading of the magnet test facility TOSKA for the testing of the ITER TF model coil manufactured by industrial methods, which will be applied for the construction of the ITER plant.

The safety of superconducting magnets is analyzed by computer code still under development and by experimental studies of effects, potentially initiating a sequence of events leading to an accident.

H. Knuth

MCOI 1/2 ITER TF-Model Coil Development

Subtask 1: Monitoring Manufacture of the Toroidal Field (TF) Model Coil

The aim of the subtask is the support of the NET Team in design and the fabrication of the ITER TF model coil.

The change of the ITER Director and the following ITER design review led to a stop in the TF model coil work by the new ITER Director. A new concept for the ITER TF coil was selected by the JCT at the February 1995 Magnet Workshop in Naka.

The EU Home Team was requested to elaborate an adapted model coil concept till mid April 1995. In joint collaboration the NET-Team and the superconducting magnet laboratories (CEA, Cadarache, ENEA Frascati, FZK Karlsruhe) elaborated the new model concept and the test configuration (TF model adjacent to the EU LCT coil), which presented in the April 1995 magnet work shop and in May 1995 TAC Review Informal Meeting. The importance having the model coil tested at the end of the EDA forced that the TF model coil order have to be placed end 1995. The TF model coil specification were completed in mid June 1995 and a call of tender was released to the European industry. FZK staff participated in about 10 meetings and contributed to the test configuration design as well as to test facility related items (cooling flow sheet, instrumentation, interfaces, see also MTOS-1).

PKF-PL organized more manpower that the structural analyses of the model coil configuration can be performed at FZK site (see NET contracts).

The evaluation of the TF model coil offers will start in second half of September 1995.

FZK was requested by industry to contribute directly to the model coil fabrication by making available the all basic components (axial- and radial insulation breaks, cold and warm instrumentation feedthroughs) developed for the Polo model coil.

Subtask 3: Basic Development for High Voltage Technique for Components used in Model Coil and Test Facility (Feedthroughs, Insulation , Breaks, Current Leads etc.)

The aim of the subtasks is the transfer of the know-how in the development of high voltage components gained in the Polo project to the ITER model coils.

3.1 The cryogenic Partial Discharge device ("cryo PD device")

Extended partial discharge (PD) measurements were performed and evaluated on the Polo coil during testing (see MTOS-1). Besides this a facility was taken in operation in order to clarify the basic behaviour of partial discharges at low temperatures. Investigations at test samples with predefined voids were done [1]. First PD measurements on quartz glass samples with a natural void (bubble) showed very high inception voltages due to low gas densities and a very smooth surface inside the void. This inception voltage was too high in comparison to the withstand voltage of the whole test device. Therefore samples of epoxy resign were used for further measurements. The voids inside the samples were filled with air at different pressures or with He gas.

Cooling down the sample the inception voltage U_i is nearly remaining constant down to a temperature of 80 K for air filled voids. Below this value U_i is changing due to the decreasing of the gas density by condensation. Below a temperature of 45 K no PD was detected at all. For He filled voids U_i remained nearly constant down to a temperature of about 20 K, which was the lowest obtainable temperature of the test device so far.

Up to now the very high amplitudes which were measured at the Polo model coil at 4.2 K could not be reproduced at the He filled samples with their constant void size over the whole temperature range. This indicates a geometrical alteration in the insulation system of the Polo model coil, e.g. an increasing of the number of delaminations where PD can be found or a changing of the gaps size by cooling down.

The present activities concentrate on the design of samples with electrode bounded voids to study the impact of the electrode surface on the initial conditions for PD in delaminations. Furthermore a new high voltage croystat feedthrough will be applied to the test device which allows to operate the cryo PD device inside a bath cooled cryostat for investigations at temperatures down to 4.2 K.

3.2 Cold feedthroughs for instrumentation cables

Facing the demands of the ITER model coil it is necessary to improve the insulation design of the Polo cold instrumentation feedthroughs. For the ITER coil the vacuum of the cryostat tank has to be separated from the guard vacuum of the cold instrumentation feedthroughs. A model of a cold feedthrough with such a separated guard vacuum was designed and constructed and is now under test. The first cooling down shows the mechanical strength and He tightness of the insulations part (glass filled epoxy, filament winding). The electrical strength of 20 kV DC was demonstrated under vacuum (p < 1 Pa) and for He gas inside the guard vacuum area at p > 104 Pa. AC partial discharge measurements are going on to restrict the favourable He pressures for the separated guard vacuum area.

Literature:

[1] M. Irmisch, B. Stegmaier, A. Ulbricht: Partial discharge behaviour at cryogenic temperatures, submitted to 9th Int. Symp. on High Voltage Engineering, Graz, Austria, Aug. 28 - Sept. 1, 1995.

Staff:

S. Fink (since 1.6. 1995)
M. Irmisch (Subtask 3)
P. Komarek
Ch. Sihler
A. Ulbricht (Subtask 1)
G. Wieczorek (since 1.10.94)
G. Zahn

N 11 TT 19 94-02-95 FE 02 (MTOS 1)
Preparation of ITER TF-Model Coil Test Facility

Subtask 1: Preparation of TOSKA Facility for the Test of the ITER TF Model Coil

The aim of the task is the upgrading of the TOSKA facility for testing the ITER TF model coil. An intermediate step is the testing of the LCT coil at 1.8 K up to 11 T field level in the task MBAC. Useful basic components and testing methods were the outcome of the Polo project (previous tasks M4, M8 and MTOR). The developments are applicable for the ITER model coils.

The TF model coil activity was resumed with the decision for the new ITER TF coil concept. Industrial offers for the TF model coil are available in second half of September 1995 (see subtask MCOI-1).

The Polo project was concluded at March 31, 1995 with a test of the 80 kA power supply used lateron in the TF model coil test. The Polo coil achieved unique results withstanding typical tokamak field transients as expected from the design.

The preparations for the 1.8 K test of the LCT coil and the upgrading of the facility are in progress.

1. The TOSKA Facility for Testing the ITER TF Model Coil (MC)

1.1 The test configuration according to the new TF coil concept

The new TF model coil and its configuration is shown in Fig. 1 and 2. The TF model coil has according to the full-size TF coil a circular thin jacketed conductor embeded in the grooves of five radial shear disks (Fig. 3, pancake design). The stacked pancakes are enclosed in a thick steel case. The TF model coil is mounted in a frame simulating the structural supporting system of the full-size coils. The frame is part of the intercoil supporting structure between the TF model coil and the LCT coil. The present status of TFMC programme is described in subtask MCOI-1.

1.2 Upgrading of the facility

After finishing of the Polo coil test programme the activity for proceeding with upgrading of the facility has been started.

Vacuum vessel modifications:
The installation of an additional flange ($\varnothing$ 500 mm) and a bore in the LN$_2$-shield were necessary to have two flanges available for the model coil current leads. The work is completed. A complete exchange of the in vessel piping is running.

Cryogenic supply system:
The installation of the 2. section of He transfer lines between

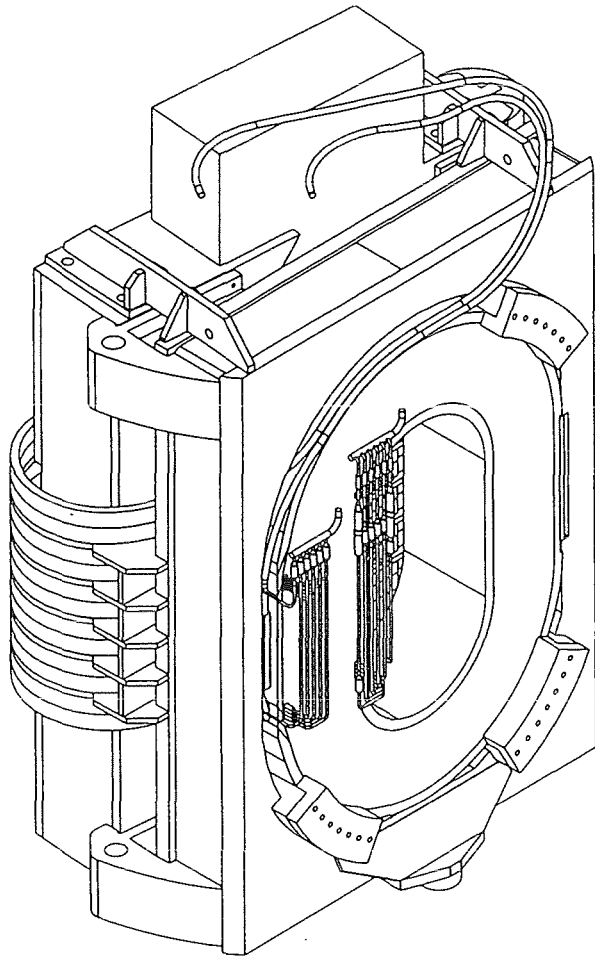Fig. 1: The TF model clamped in a steel frame by 3 wedges. The steel frame is part of the supporting structure between the LCT coil and the TFMC.
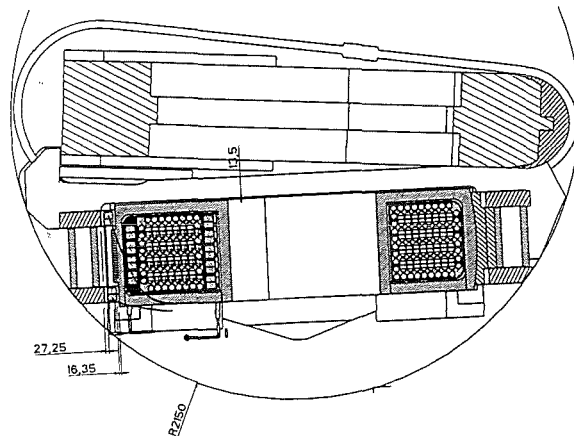

Fig. 2: Cross-section in the midplane of the configuration LCT-TFMC.

the 2 kW refrigerator and the valve box, the control cryostat and the vacuum vessel is running.

Instrumentation, control and date acquisition:
The 15 year old instrumentation and cabling of the control
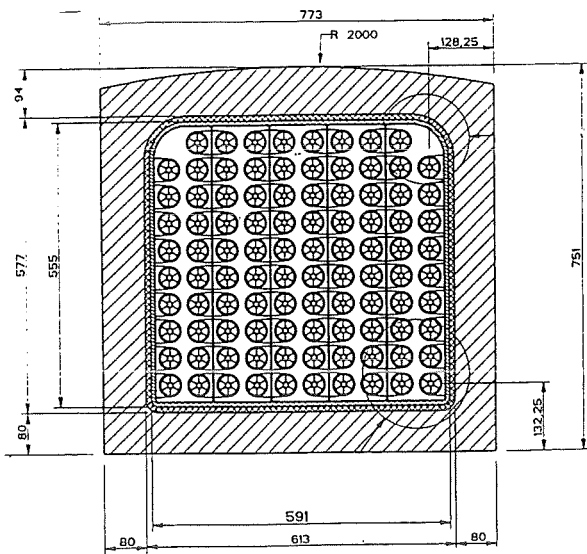
Fig. 3:   The TFMS cross-section according to the design
           principle of the fullsize TF coils.

room was completely removed. The new pretested control
racks are ready for installation. A patching assigment for all
sensors was prepared. The connection of the acquisition
processors (programmable logic controllers, rt-VAX,
Hottinger scanner, analogic controllers) to the visualisation
system VXL was realized and successfully tested in single
mode operation.

Software work proceeded with:
Work of configuration of the ORACLE Data Base like user
interfaces for extraction of parameters and administration of
control data continues.
Integration of 21 controllers out of 40 for the operation of
the LCT coil for the 1.8 K test.
Establishing of alphanumerical life graphical display for
remote observation of the sensor values during testing.

Electrical supply system:
The installation of the high current components of dump
circuit of the LCT coil was completed. The installation of the
control circuit is running. The parallel operation of the 30 kA
and 50 kA power supply was tested with the Polo coil as
inductive superconducting load. The results are described in
section 2.

1.3   Special Calculations

a)   Eddy current forces in the nitrogen shield
      The modified Polo switching circuit will be used for
      testing of the high voltage loading of the ITER TF
      model coil by a fast discharge. The magnetic field and
      the vincinity of the nitrogen shield generate eddy
      currents in and forces between coil and nitrogen shield
      during fast discharge. The relatively thin wall thickness
      of the nitrogen shield and supports optimized for low
      heat input required calculation effort to make a

reliable estimation of the forces to avoid movement or
damage. A numerical analytical method was used
which was checked by earlier performed finite
element calculations with the LCT coil. The results
agree within sufficient accuracy [1]. The maximum
eddy current and radial force density in the nitrogen
field are shown in Fig. 4 and Fig. 5.
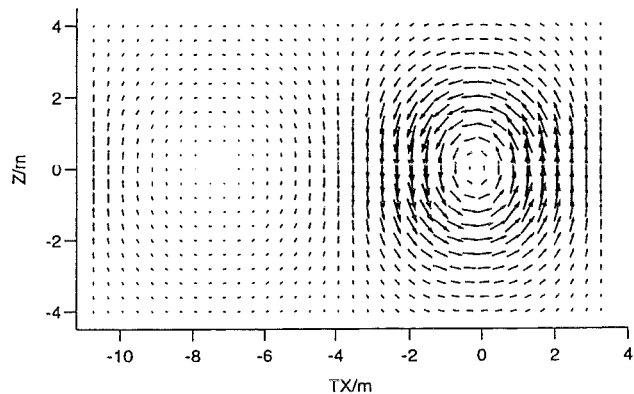
Fig. 4:   Distribution of the eddy current density in the LN$_2$
           shield at the time of maximum current density.
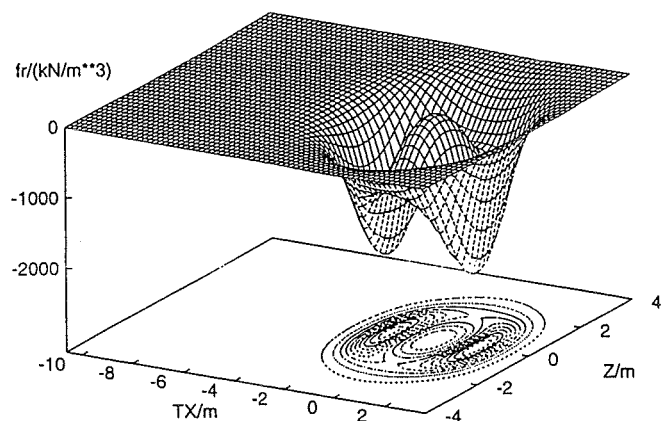
Fig. 5:   Distribution of the radial force density in the LN$_2$
           shield at the time of maximum load.

According to the results of the eddy current force
calculations the buckling behaviour of the nitrogen
shield was investigated by a finite element analysis.
The inclusion of an existing stiffening ring in the
nitrogen shield middle in the FEM model led now to a
sufficient large safety factor ($\sim$ 4, static calculation)
against buckling.

b)   Transient behaviour of the TF model coil
      During pulse voltage testing of the Polo model coil it
      was found that 150 % transient overvoltages
      oscillations occured. Calculations by a detailed Polo coil
      network model were in good agreement with the
      measurement [2]. Stimulated by this results a ITER TF
      model coil (design [3]) network was elaborated and
      investigated with typical transients occuring during the
      switching process of the Polo counter acting current

switch used for such fast discharges of TF model coil. The transient behaviour was investigated for three cases [4]: Shear plates grounded, shear plates connected to the conductor joint potential between two layers and shear plates floating. The best transient behaviour was obtained in the second case. The results indicate that the transient behaviour of shear plate type winding in a layer or pancake design has to be carefully analysed for designing the insulation system and for optimizing grounding conditions.

2. Test results of the Polo model coil [5]

Two test phases were performed in the last quarter of 1994. The experiment was successfully terminated in the first quarter 1995 by testing the parallel operation of the 30 kA and 80 kA power supply in conjunction with a super-conducting coil.

2.1 Magnet properties gained during the whole test

The coil quenched independently from the ramp rate (100 A/s - 1.5 kA/s) at currents between 24 kA to 25 kA which corresponds to about 70% of the short sample critical current (Fig. 6). A comparable degradation was observed also for a cable short sample used in former stability experiments and also in an about 3 m conductor piece which was used as superconducting busbar in the current lead test. For this last sample training steps were observed up to the 50 kA current limit of the power supply. This effect, stability considerations and quenching during half coil discharge, confirm that this is a real critical current degradation which has no simple explanation.
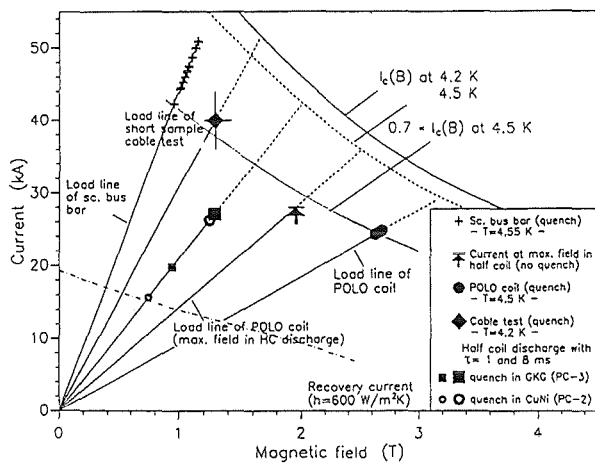
Fig. 6: Load lines for the Polo conductor short examples; Polo half coil and Polo coil I_c tests in comparison with extrapolated strand Ic (mixed matrix Cu-CuNi).

A network scheme for two double pancakes and the joint between them represents one half of the Polo coil (Fig. 7). One half of the coil has a conductor with CuNi tape wrapped

subcables the other one prepreg {Glass/Kapton/Glass=GKG} wrapped subcables. Each conductor end of both coil halfes ends in a terminal (two conductor ends end via the center joint in the center terminal, one end in the plus-, the other one in the minus terminal). In case of quenching of one pancake the compensated voltage taps on the subcables at the joint showed a current redistribution of the subcable currents for the GKG cable across the terminals. The voltage increase at the adjacent not quenched pancake is explained by the cable internal inductance, which was qualitatively confirmed by a network simulation (Fig. 8). It was assumed in the network simulation that the subcables quenched one after each other with maximum time delay $\Delta t = 30$ ms. A quench in one of the pancakes with CuNi tape wrapped subcables, such voltage traces at the joints were not observed. The current redistributes itself already via the transverse resistance in the cable.
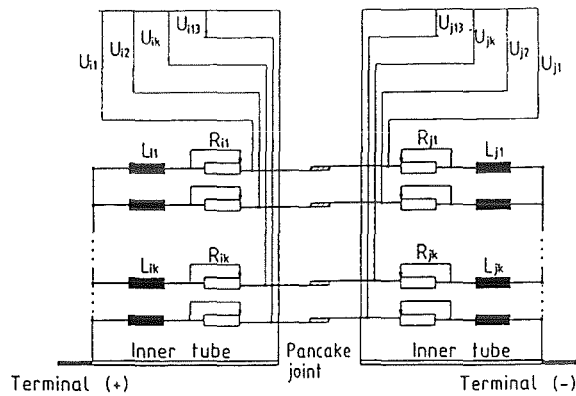
Fig. 7: Equivalent circuit of a Polo coil half (two double pancakes, one joint in between, e.g. terminal (+) ≡ terminal winding center, terminal (−) ≡ terminal (−).
L_{ik}, L_{jk}: Subcable inductance, k = 1...13 subcable index, i and j pancake index, i, j = 1...4 / i≠j.
The complete inductance matrix is used in the network model not indicated in circuit diagram.
R_{ik}, R_{jk}: Resistive region representation.
U_{ik}, U_{jk}: Compensated voltages.

This model was also used to perform ramping calculations [6]. It was found that small changes in the mutal inductance between adjacent subcables lead to a current distribution in them which is not symmetric. This was identified as the only reason in getting a not symmetric current distribution in the cable during ramping. This can cause a premature quench.

2.2 Behaviour under tokamak typical field transients

A special switching circuit was used to generate fast field transients in the Polo coil winding (Fig. 9). One half of the coil was fast discharged while the other half was shorted /half coil discharge).
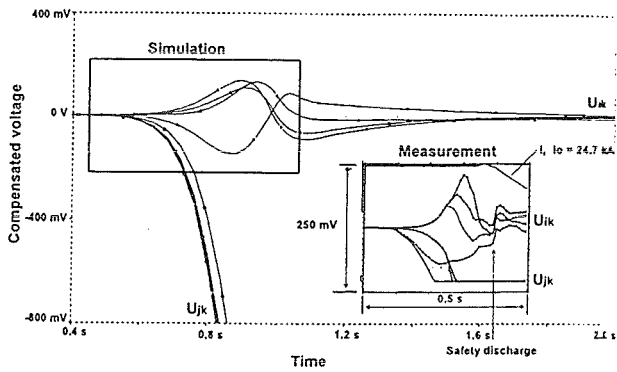
Fig. 8: The traces of the compensated subcable voltages in pancake 3 and 4 in case of a quench in pancake 4. The results from the network simulation are in good qualitative agreement with the measurements assuming that the subcables went normal one after each other.
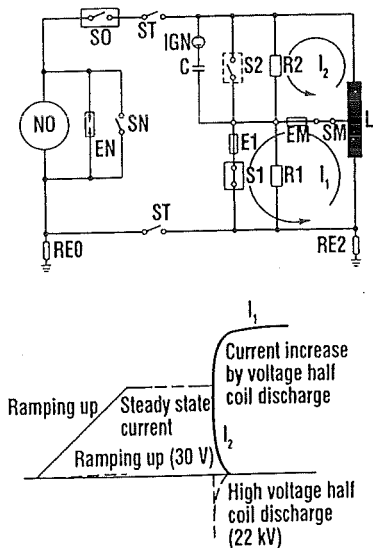
Fig. 9: The Polo current source, switching circuit and schematic current and voltage traces.
High voltage and safety discharge: SM open
Half coil discharge: SM closed.

The procedure was as follows: The current was increased in steps. At each step half coil discharges were performed until a quench occured.

The current decay in the short circuited half coil was ~ 7 s without quench. The time constant of 7 s was chosen according to current loading of the switch SM. A quench during half coil discharge triggered a safety discharge with a exponential decay time of about 125 ms.
The transition from a non-quenching discharge to the quenching discharge was sharp within a ΔI ~ 100 A. The

discharges were performed with different "time constants" (time until $0.63 \, I_{max}$) of 1 ms to 14 ms.

The compensation scheme of the quench detector was able to ignore the transient and unbalanced voltages with a 500 ms delay and a quench detection level of 30 mV.

The stability limits for both cable types were investigated by calculation models and were within 30% in agreement with the measurements (Fig. 10). For currents above 25 kA the quenching deviated from the stability calculation for the GKG cable. The reason was that this current was near the load line limit of the half coil as indicated also in Fig. 6.
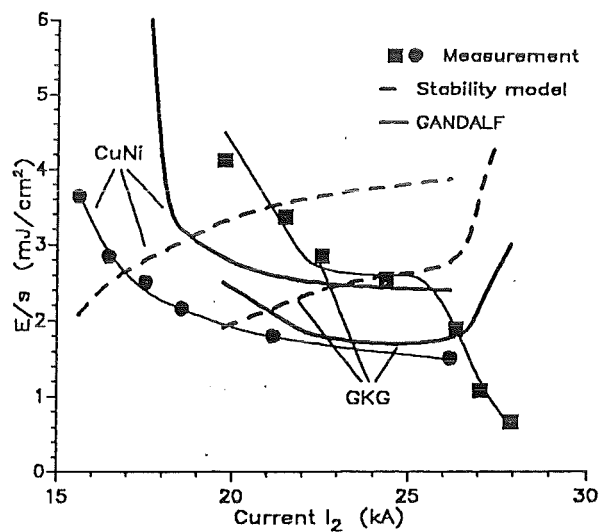
Fig. 10: E/s (energy pro surface unit) vs. maximum current during quench and stability limit calculated with GANDALF and with the stability model. The thin solid lines are only plotted to guide the eyes [7].

2.3 Mechanical measurements

The test of the Polo coil offered also the possibility of performing mechanical measurements which were compared to results of a finite element model with orthotropic material properties. In detail the following load cases were investigated:

- Extension of coil diameter during exitation;

- Twisting of the winding cross-section during half coil discharge;

- Bending of the coil by attraction forces by fast discharge in a stainless steel short circuit ring beneath the coil (Fig. 11, Fig. 12).

All experimental results are in excellent agreement with the calculations [8].
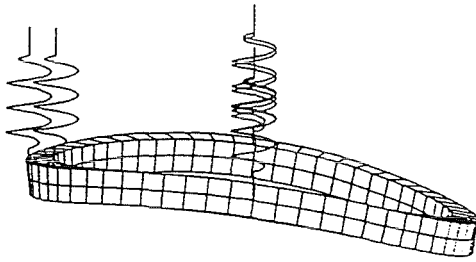
Fig. 11: Calculated displacement of the winding dis-
charging the coil into the short circuit ring beneath
it. Initial coil current I_0 = 15 kA, discharge
resistance 110 mΩ, max. current in short circuit
ring 28 kA, displacement magnification factor 35.
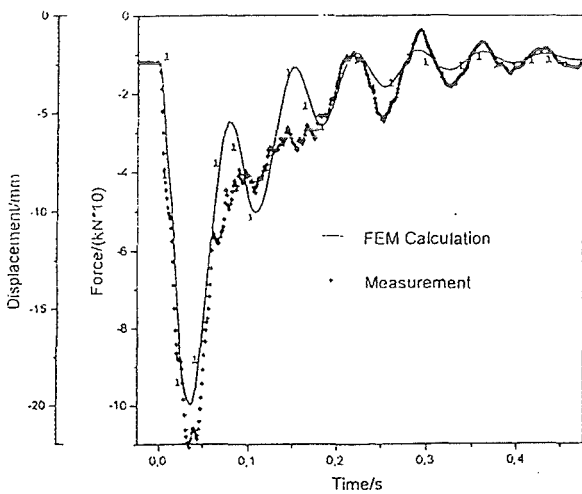
Fig. 12: Calculated and measured dynamic reaction of the
coil (winding displacement and reaction force in
northern and shouthern suspension, I_0 = 15 kA,
R_{dis} = 110 mΩ).

2.4 High voltage tests

Beside the usual determination of the magnetic properties
also the high voltage insulation properties were investigated
during the testing (DC test, AC partial discharge measure-
ments, pulse voltage tests). The insulation properties of the
coil were measured at room temperature and at 4 - 6 K before
and after every test phase. Pulse voltage tests were only
performed in the beginning. They showed that the coil had to
be described in an equivalent network. The pulse spectrum
excited the network to oscillations which led to internal
transient overvoltages of 150% [2] between double pancakes.
The application of AC Phase Resolved Partial Discharge (PRPD)
measurements for assessment of insulation properties of
superconducting magnets were applied the first time at
cryogenic temperatures. The apparent charge was measured
at the three coil terminals as well as at the joint boxes [9]. The
measured apparent charge was at low temperature
reproducibly 5 times larger than at room temperature, except
the minus terminal. The level increased again with the time in
which the coils were at operation temperature (about a
factor 4 for operation > 1 month). The PRPD measurements
during a time period of 1 min (3000 periods) made obvious
differences between the conductor terminals at room and
low temperature. The method demonstrates its potential for
insulation diagnostic but needs basic investigation for better
understanding and interpretation of the results [10].

2.5 Test of the 80 kA power supply

The parallel operation of the 30 kA and 50 kA power supply
getting 80 kA current for the model coil available was tested
up to 22 kA with the Polo coil as inductive load. A big effort
was spent to adjust the control circuit of both power supplies
so that all fault conditions in the different operation modes
of the power supplies lead to a controlled safety discharge. It
was found that the converter mode operation shifted the
current from 50 kA to 30 kA power supply what means that
the 30 kA power supplies has to carry the sumed current. This
is 80 kA at nominal current and is from the present view not
permitted. Investigations for solving the problem are
running.

2.6 Conclusions

The finished experimental program of the Polo project at
FZK/ITP demonstrated:

The high voltage technique for superconducting fusion
magnets up to 20 kV range was developed and mastered.
Suitable high voltage and transient testing methods were
applied at 4 K. High voltage power pulses and extreme fast
ramp rates (∼ 200 T/s) were obtained by a specially developed
switching circuit.

The conductor fulfills the expected stability margins for
transient fields. The ramp rate was only limited by the
expected stability margin or by the magnet critical current.
The two stage cabling of the conductor and the consequently
followed rotation symmetry in the conductor, joints and
terminals can be the explanation for having seen no ramp
rate limitations.

The mechanical behaviour of the coil is in excellent
agreement with the finite element calculation which means
that the determination of the orthotropic material properties
and boundary conditions were mastered.

All experimental results with respect to the development of
superconducting fusion magnets (e.g. ITER), have been a
contribution to master the achievement of challenging
specifications.

Literature:

[1] A.M. Miri, F. Schunn, C. Sihler et. al.: Berechnung der
Wirbelstromdichten und -Kräfte in der Umgebung
großer supraleitender Spulen für den magnetischen

Einschluß bei der Kernfusion. Electr. Eng. 78 (1985), p. 223-228, Springer Verlag 1995.

[2] C. Sihler, A.M. Miri, M. Irmisch, A. Ulbricht, F. Wüchner: Transient Voltage Oscillations in a Large Superconductive Coil. 9th Int. Symp. on High Voltage Engineering, Graz, Austria, Aug. 28 - Sept. 2, 1995.

[3] Technical Specification for a Toroidal Field Model Coil for the ITER Tokamak. ANSALDO Document N. 700 RM 06073, 07.06.1994.

[4] A.M. Miri, C. Sihler, M. Droll, A. Ulbricht: Modelling the transient behaviour of a large superconducting magnet subjected to high voltage pulses, Proc. IPST '95 Int. Conf. on Power Syst. Transients, Lisbon, Portugal, Sept. 3-7, 1995.

[5] M. Darweschsad, R. Heller, G. Friesinger, M. Irmisch et al.: The Polo Coil, a Prototype Tokamak Poloidal Field Coil, Design, Features and Test Results, Proc. MT-14, 10-16 June 1995, Tampere, Finland.

[6] C. Sihler, R. Heller, W. Maurer, C. Schmidt, A. Ulbricht, F. Wüchner: Analysis of the Electrodynamics of Subcable Current Distribution in the Superconducting POLO Coil Cable, FZKA 5653 Forschungszentrum Karlsruhe, September 1995.

[7] R. Heller, C. Schmidt, A. Ulbricht: Stability of a Poloidal Field Coil in Rapidly Changing Magnetic Fields, ibidem.

[8] C. Sihler, G. Friesinger, H. Kathol, A. Ulbricht, F. Wüchner: Structural Analysis and Measurements of the Mechanical Behaviour of the Polo Coil under Static and Dynamic Load, ibidem.

[9] M. Irmisch: Hochspannungsisolationsdiagnostik an supraleitenden Großmagneten, FZKA 5615, Forschungszentrum Karlsruhe, 1995.

[10] M. Irmisch, B. Stegmaier, A. Ulbricht: Partial discharge behaviour at cryogenic temperatures, submitted to 9th Int. Symp. on High Voltage Engineering, Graz, Austria, Aug. 28 - Sept. 1, 1995.

Staff:

H. Barthel
H. Bayer (till 31.12.94)
F. Becker
S. Darweschsad
G. Dittrich (since 1.7.94)
P. Duelli
S. Fink (since 1.6.1995)
G. Friesinger
A. Götz
P. Gruber
A. Grünhagen
W. Heep
R. Heller
W. Herz
H. Irmisch
H. Kathol
R. Kaufmann
K.-H. Kleiber
P. Klingenstein
L. Lang (since 1.10.94)
O. Langhans (from 1.7.94 to 31.12.94)
W. Lehmann
W. Maurer
I. Meyer (since 15.5.95)
G. Nöther
A. Nyilas
U. Padligur
K. Rietzschel
C. Schmidt
G. Schleinkofer
K. Schweikert
Ch. Sihler
E. Specht
H.-J. Spiegel
H. Stiefel (since 1.7.94)
M. Süßer
A. Ulbricht (for 2.)
D. Weigert
G. Wieczorek (since 1.10.94)
F. Wüchner
G. Würz
G. Zahn (for 1.)
H.P. Zinecker
V. Zwecker

MBAC   High Field Operation of NbTi at 1.8 K

Subtask 1:   He II Forced Flow Cooling: 1.8 K Test of EC LCT
          Coil plus Development of Circulation Pumps

The 1.8 K cooling technique is indispensible, if technically
applicable superconducting materials shall obtain their
highest field levels. Therefore the task was started with a
programme part for the development of components
included in such a cooling circuit and is continued with the
operation of a large forced flow cooled fusion magnet, the
Euratom LCT coil. The last experiment is an intermediate step
in the sequence for upgrading the TOSKA facility for the ITER
TF model coil test (Task MTOS).

The 1.8 K Test of the Euratom LCT Coil

The LCT coil is ready for installation in the vacuum vessel. The
other activities for preparing the facility for the 1.8 K test of
the LCT coil are described in the Task MTOS section 1.2. The
test is scheduled for the first half of 1996. This test will take
the TOSKA facility again in operation with a new control
system and an extended cryogenic supply by the 2 kW
refrigerator.

Staff:

H. Barthel
H. Bayer (till 31.12.94)
M.S. Darweschsad
G. Friesinger
A. Götz
A. Grünhagen
R. Heller
W. Herz
I. Meyer (since 15.5.95)
G. Nöther
K. Rietzschel
E. Specht
J. Spiegel
C. Sihler
F. Süß
M. Süßer
A. Ulbricht
D. Uhlich (till 31.12.94)
D. Weigert
F. Wüchner
G. Zahn
V. Zwecker

Vacuum and Fuel Cycle

Introduction:

In the pumping area FZK has been awarded the ITER task T 228 which has the objective to solve crucial issues of a cryopumping system for ITER with minimized tritium inventory and maximized helium pumping speed. Both issues ask for a decrease in cooling times and heating up times for regeneration to the order of a few minutes or even less. Whereas fast cooling was demonstrated in the HELITEX-facility using supercritical helium in conjunction with an ITER-suited low thermal inertia cryopanel, several methods are being tried out for fast heating in the modified TITAN facility. Thermal calculations have shown a very satisfactory agreement with the experimental results, so far.

Work in the area of Tritium Technology has gone through an exciting phase. The catalytic fuel clean-up process as developed by FZK and selected by the ITER-JCT at the beginning of 1995 as the reference method has been technologically proven in the CAPRICE facility with increasing amounts of tritium up to a fusion-typical DT mixture, and the ITER specifications asking for a decontamination factor of more than 10^6 have been fully met. Results of this work are described in more detail under Subtask 2 of T 299. Supporting activities concerning the determination of the optimum operation range and the tolerability of chemically active impurity gases for permeators which are essential components for tritium recovery from the exhaust gas, are carried out under Subtask 1 of T 299.

Task TEP 3 deals with tritium storage. In addition to ZrCo the intermetallic compound $Zr_{0.8}Ti_{0.2}Co$ has extensively been studied.

The tritium inventory in the Tritium Laboratory Karlsruhe has been increased to nearly 10 g in order to cope with the demands of the experiments. For accountancy purposes calorimetry has become an important tool. In addition to the very accurate calorimeter developed by FZK, an industrial type allowing for a faster tritium assay will shortly by available. Interesting calorimetric results are reported under TRIT-1.

H.D. Röhrig

G 18 TT 22 EU (T 228)
Cryopump Development

1. Cryopanel Fast Cooling Experiments at the HELITEX Test Facility

1.1 Introduction

One of the objectives of the ITER task T228 is to develop methods for fast regeneration of cryopanels of ITER primary torus cryopumps. The main reasons for demanding fast regeneration are:

- Reduction of the tritium inventory of the pumping system,

- increase of the pumping efficiency of the pumping system.

By shortening the pumping and regeneration time cycle it is possible to reduce the total releasable tritium inventory of the primary pumps to values < 180 g as specified in ITER-DDD.

The aim is to shorten the individual regeneration time of a single cryopump to less than e.g. 4 minutes. Rapid heating and cooling methods for cryopanels have to be developed in order to fulfill this requirement.

The first two series of preliminary cryopanel fast cooling experiments have been performed at the HELITEX test facility using supercritical helium (4.5 K, >3 bar).

1.2 Description of the Test Facility

The main parts of the HELITEX test facility are the test cryostat where the actual experiment takes place, the control cryostat where the supercritical helium flow is controlled and the auxiliary systems. These systems are: gas supply, gas exhaust, vacuum pumping, data acquisition, process control, gas analytics etc.

The coolant for the HELITEX test facility is supplied directly by the LINDE 300 helium liquifier plant via a cold line. An overview of coolant flow is given in Fig. 1. There are two alternatives for the coolant flow: either return of supercritical helium back to the control cryostat after passing the cryopanel or exhaust of supercritical helium into a gasometer after heating up to ambient temperature in a water bath. The flow of supercritical helium is limited to 30 g/s due to the capacity of the LINDE 300 liquifier.

The test chamber is a cryostat with a total internal volume of ~11.4 m³ cooled by LN_2. The total operating gas pressure inside the cryostat is < 10^{-4} mbar.

The test cryopanel is installed inside the LN_2 shielding (Fig.2).

The test cryopanel (Fig. 3) is made of a stainless steel tube (12 x 1 mm) onto which two sheet fins (1 x 100 x 1000 mm) have been laser beam welded. After welding the panel was gal-

vanically plated with copper (0.5 mm) to equalise the temperature profile across the panel.

The temperature instrumentation of the panel includes 6 resistor gauges (carbon glass resistors CGL 1500) inserted into copper blocks which are soldered to the panel surface. Two resistor gauges are installed inside the coolant channel at the inlet and outlet of the panel.

The total mass of the cryopanel is 3.4 kg (2.1 kg SS and 1.3 kg Cu).

1.3 Performance of the Tests

Before starting a test, the cryostat is pumped out by a turbomolecular pump and cooled down by LN_2. After reaching the LN_2 temperature level the coolant supply piping system of the cryopanel is cooled down to the operating temperature level of ~5 K by supercritical helium.

The panel is heated by supercritical helium (SCHe) to the start temperature level of ~100 K and thereafter the actual fast cooling test starts by opening a valve for a predetermined throughput of SCHe through the panel. The SCHe is being exhausted through a water bath heater into a gasometer.

The coolant pressure inside the panel is controlled by a release valve downstream of the heater. The pressure inside the panel is kept above 3 bar during the cooling period to make sure that the supercritical flow conditions are fulfilled.

Seven experiments have been performed under parametric variation of SCHe throughput (5, 10, 15, 20 g/s) keeping the SCHe inlet temperature and pressure constant (4.5 K, >3 bar).

1.4 Test Results

In spite of the incomplete data acquisition system it was possible to demonstrate the technical feasibility of cryopanel fast cooling by SCHe.

As expected the duration of the cooling down phase is depends on the SCHe throughput. For the smallest throughput of 5 g/s SCHe a cooling down time of 126 s was measured. For the largest throughput of 20 g/s SCHe a cooling down time of 44 s only was measured. The values given here refer to the temperature gauge TIR 409 which is located 28 mm horizontally from the central coolant tube and 23 mm vertically from the upper fin edge.

During cooling down the temperature profile across the panel was not uniform. Time differences of 10 - 40 s were measured for the different locations at the panel to reach the same temperature level.

In the diagram (Fig. 4) some temperature curves are shown of the cool-down experiment with the throughput of SCHe of 15 g/s. The SCHe temperature at the panel exit cools down rap-
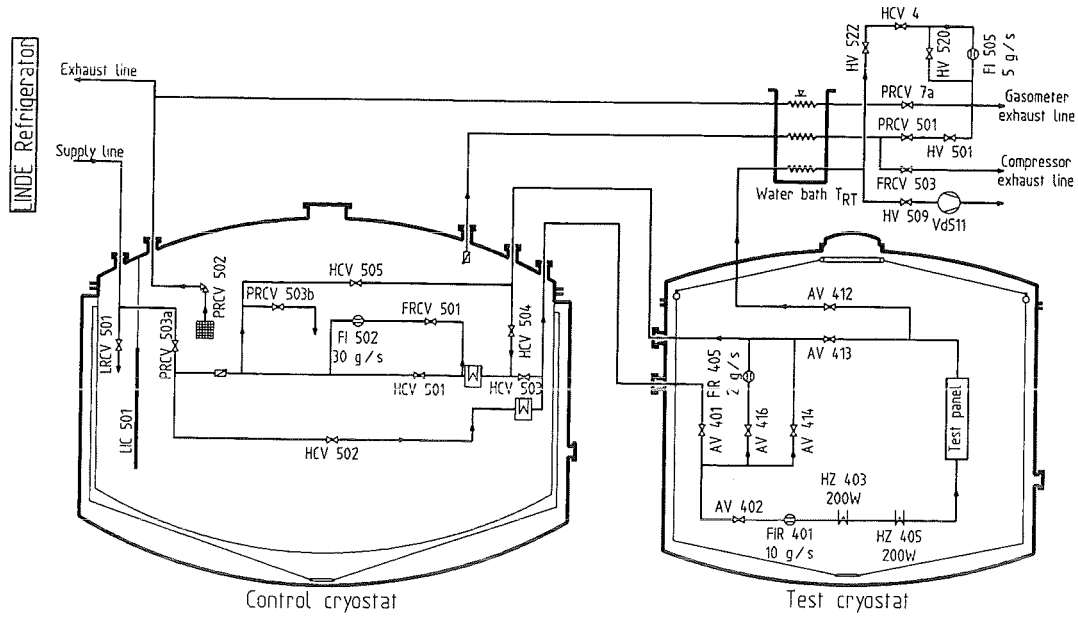
Fig. 1: Simplified flow sheet of the HELITEX test facility
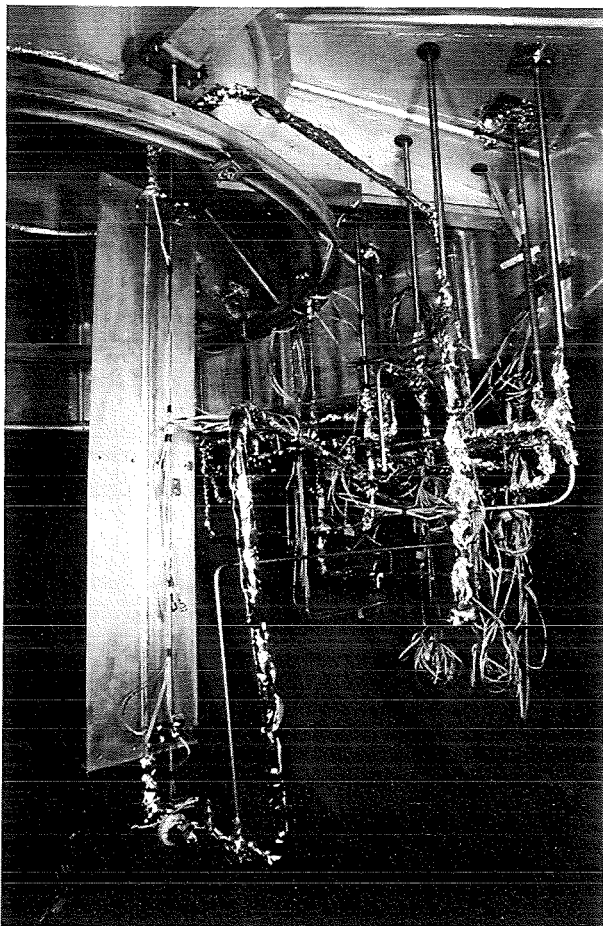
Fig. 2: View of the cryopanel inside the HELITEX test cryostat

idly in 2 - 3 s, the panel temperature gauges show different cooling behaviours depending on the location at the panel.

1.5 Calculated Results

Calculations were carried out in order to check the feasibility and to estimate the temperature/time behaviour of the test cryopanel during the fast cooling process.

To get detailed information about the temperature distribution across the panel surface and its change with time, an unsteady state calculation was based on the following assumptions:

-   Symmetrical panel geometry: the calculation can be limited to one sheet fin, treated as a finite slab that starts at the weld of the tube wall and extends horizontally to the total length of $s = L = 0.1$ m (see Fig. 3);

-   the initial temperature distribution is taken uniformly constant;

-   first boundary condition: linear heat flux (with constant heat transfer coefficient referring to the turbulent flow in the central tube) at the SCHe-cooled side of the slab;

-   second boundary condition: adiabatic surface (neglection of thermal radiation from the LN_2 surroundings) at the other side;

-   constant thermal properties (of copper);

-   constant temperature of the coolant.
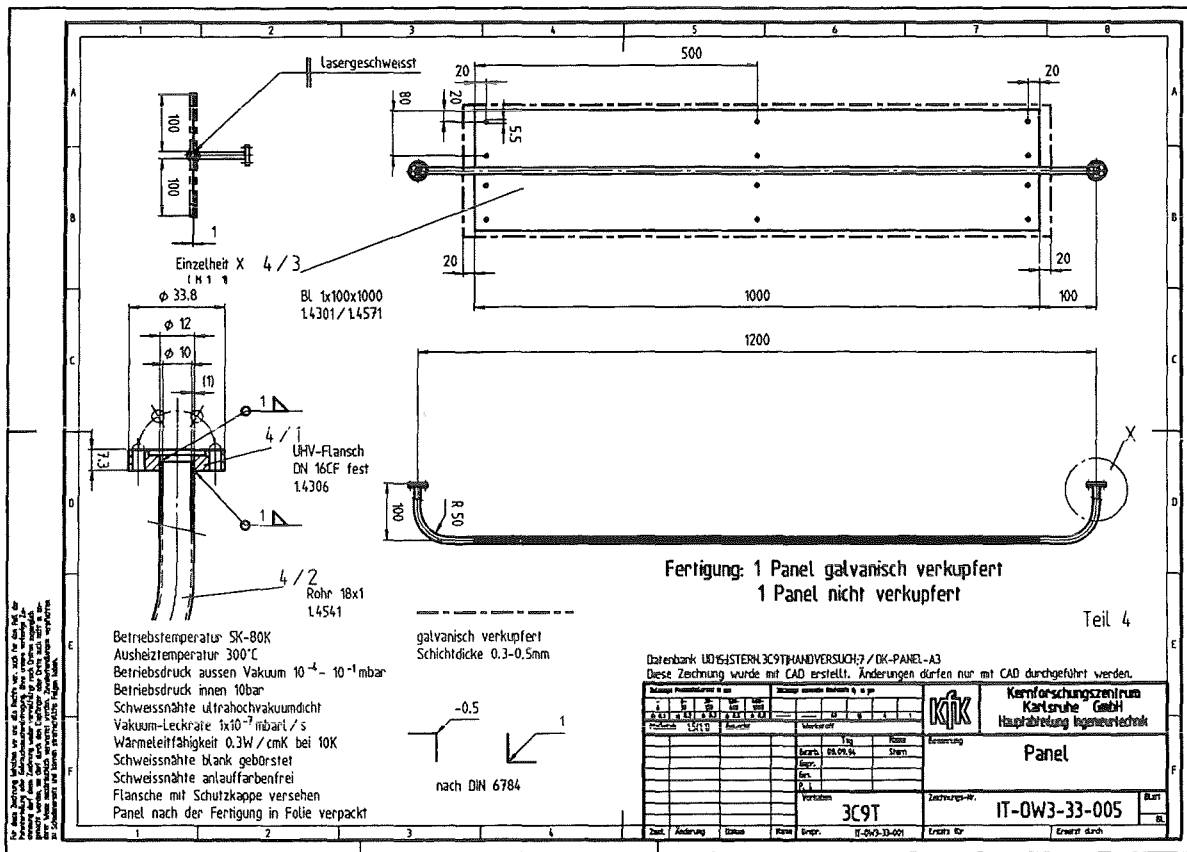
Fig. 3: The cryopanel
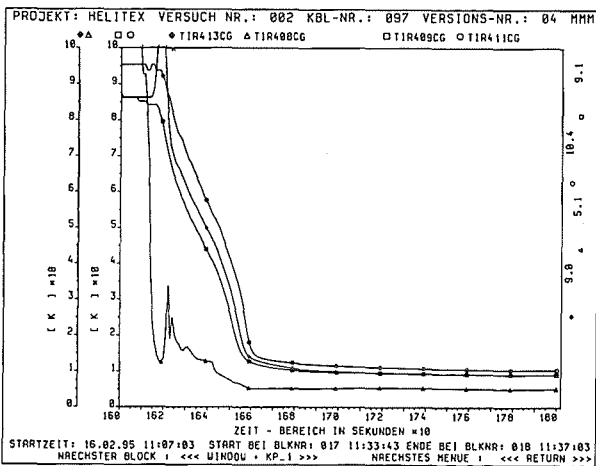
Fig. 4: HELITEX test facility, cryopanel fast cooling experiment with the supercritical helium flow of 15 g/s, cryopanel and supercritical helium temperatures versus time

Because of the adiabatic surface, the resulting temperature distribution across the slab of total length L is equivalent to the one across one half of a slab of length 2L, subjected to prescribed linear heat flux symmetrically at both sides [1, 2]. Consequently the analytical solutions, given in standard textbooks [3, 4] can be used.

The results for minimum and maximum investigated SCHe throughput are presented in Tab.1. The duration of the cooling process from 100 K to 6 resp. 7 K is given for the two distances, where the temperature sensors were attached. Furthermore, a characteristic time constant τ is specified that is per definition taken at the intersection of the tangent line on the cool-down curve at 70 K and the tangent line at 7 K.

Tab. 1: Duration of the cooling phase for minimum and maximum coolant flow and for two positions on the panel.

	$\dot{m} = 5$ g/s		$\dot{m} = 20$ g/s	
s [mm]	28	87.5	28	87.5
t [s] (7 K)	375	380	140	145
t [s] (6 K)	428	433	160	165
τ [s]	128	129	46	50

Obviously the temperature differences across the panel surface at the end of the cool-down performance are rather small.

The equalisation of the temperature during cooling is exemplified in Fig. 5; it does still apply in the case of maximum coolant flow, which means greatest influence on temperature uniformity. The homogeneity of the cooling process can be
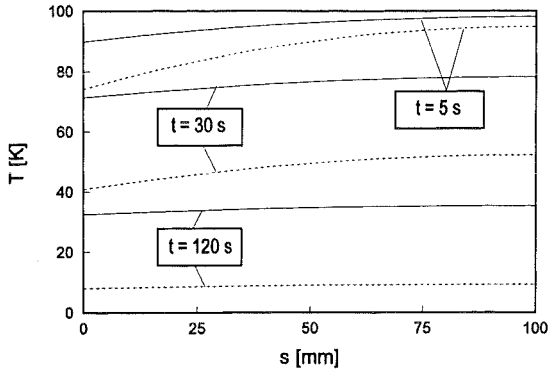
Fig. 5: Calculated temperature distribution across the test cryopanel for three fixed times at SCHe flows of 5 g/s (solid lines) and 20 g/s (dotted lines).

described with the calculated time differences to reach the same temperature level at two different positions. A comparison between the measurement position s = 28 mm and the end of the fin at s = L = 100 mm yielded maximum time lags of about 10 s. These time differences turned out to be rather insensitive to a variation of the SCHe mass flow. The measured time differences have been somewhat larger due to the delaying influence of the SS material, that has been neglected in the present model.

Finally in Fig. 6 a direct comparison is made between the mea-
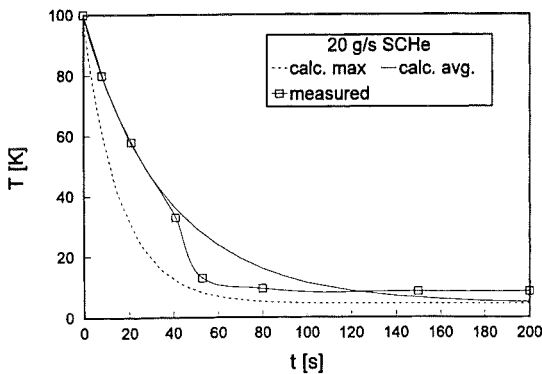
Fig. 6: Comparison of calculated (averaged and maximum thermal conductivity) and measured cool-down curves of the test cryopanel at a SCHe flow of 20 g/s.

sured and the calculated cooling performance at a SCHe flow of 20 g/s. As pointed out above, our calculations were made using integral temperature-averaged values for thermal properties of copper. The typical change in curvature at lower temperatures (see Fig. 4) can be attributed to the very strong temperature dependence of copper thermal conductivity in this temperature range (local maximum at 20-40 K, depending on purity). To exemplify that influence, Fig. 6 also shows a cooling curve, calculated with thermal properties representing the region of maximum thermal conductivity. Obviously the beginning of the cooling can be very well described with averaged properties, whereas at lower temperatures the strong temperature dependence of the thermal properties

has to be considered. If this is taken into account, the agreement between calculation and measurement is reasonable.

A matter that still has to be settled is that there remains a constant temperature difference of approximately 3.5 K between measurement and expected value for long cooling times. These differences may be due to measurement errors.

1.6 Further Panel Testing

At the HELITEX test facility further extensive fast cooling cryopanel tests are being prepared. A cryopanel in quilted design has been procured. The panel is made by hydrostatic forming of prewelded stainless steel sheets. The dimensions of the panel are 150 x 1000 mm. It is horizontally oriented in the cryostat test vessel surrounded by a LN_2 cooled shielding (Fig. 7). The cryopanel is cooled by supercritical helium flow of max. 30 g/s. The tests are scheduled to start at the end of 1995.

The first preliminary cryopanel fast cooling experiments with supercritical helium demonstrate the feasibility of fast cooling for large panels in a time of less than one minute. A test programme with a cryopanel in quilted design is being prepared.

2. Cryopanel fast heating tests at the TITAN test facility

2.1 Introduction

At FZK the applicability of various heating methods for cryopanels has been investigated. For the co-pumping cryopanels the needed temperature rise is from ~5 K to ~80 K. The following heating methods have been studied:

- forced gas flow,
- attached coaxial heaters,
- infrared radiation,
- microwave heating,
- glow discharge heating.

The microwave and plasma heating methods have been investigated together with an industrial company by order of FZK. No sufficient heating could be achieved by a 2.45 GHz microwave field. In contrast to this, rapid heating of metal is possible by the glow discharge heating. The disadvantage of the glow discharge method is the possible disturbance of ions by the tokamak magnetic field and the necessity to use ionised gas at relatively high pressure.

Experiments on heating up the panels by infrared heat radiators and alternatively by the forced gas flow heating method have been prepared and partly carried out at the TITAN test facility.

For additional tests a cryopanel with directly attached coaxial heaters is being prepared. A special copper coating is used to equalise the temperature profile across the panel. The calculations show the feasibility to reach heating times of less than 30 seconds.

2.2 Test Facility

The TITAN (Tieftemperaturadsorption) facility which has previously been used for pumping tests of adsorption cryopanels has been modified for the needs of the heating tests. Figs. 8 and 9 show a vertical and horizontal cross-section of the test rig. The test arrangement is mounted in a vertical cylindrical vacuum vessel with a diameter of 700 mm and a height of ~2200 mm. Its total volume is ~700 l and the maximum operating overpressure amounts to 10 bar.

To simulate the 80 K walls inside the ITER cryopump, the test panel is shielded by a cylindrical annular LN_2 pool with a maximum LN_2 volume of 40 l. At the bottom, the shield is protected from direct radiation by a chevron baffle which is held at 80 K.

The panel with a length of 500 mm and width of 350 mm is positioned in the 80 K volume (s. Fig. 10). It is manufactured in quilted design. Two stainless steel plates, each 0.5 mm thick, are fixed together by welding. The channels are generated by hydrostatic forming of stainless steel plates using pressurized

water between the plates. To enable pumping of ITER relevant gas mixtures the panel has been coated with activated charcoal type $SC\,II$. The inorganic cement Thermoguss 2000 has been used as the bonding. Sorbent and bonding are applied by a manual spraying technique with a thickness <3 mm.

The panel is cooled by LHe. The flow rate is controlled by a throttle valve in the exhaust line.

For the IR-heating tests a heater rod has been positioned in front of each panel side together with reflectors in order to focus the radiation to the panel area. Every heater has an electrical input power of 500 W.

The maximum intensity of radiation depends on the temperature. The wavelength for 300 °C is 5 μm, for 650 °C 3.1 μm, for 800 °C 2.7 μm. The emission coefficient of the outer Incoloy 800 tube amounts to 0.7 - 0.8.

6 Fe/Rh temperature sensors are positioned on one side of the panel (Fig. 11) to monitor the temperature profile. A further CERNOX thin-film sensor with a response time of 15 ms is fixed to the exhaust flange for giving the control signal to the throttle valve. Three of the Fe/Rh sensors are covered with three layers of Al foil to investigate the measuring difference caused by the 80 K environmental radiation, because it is not
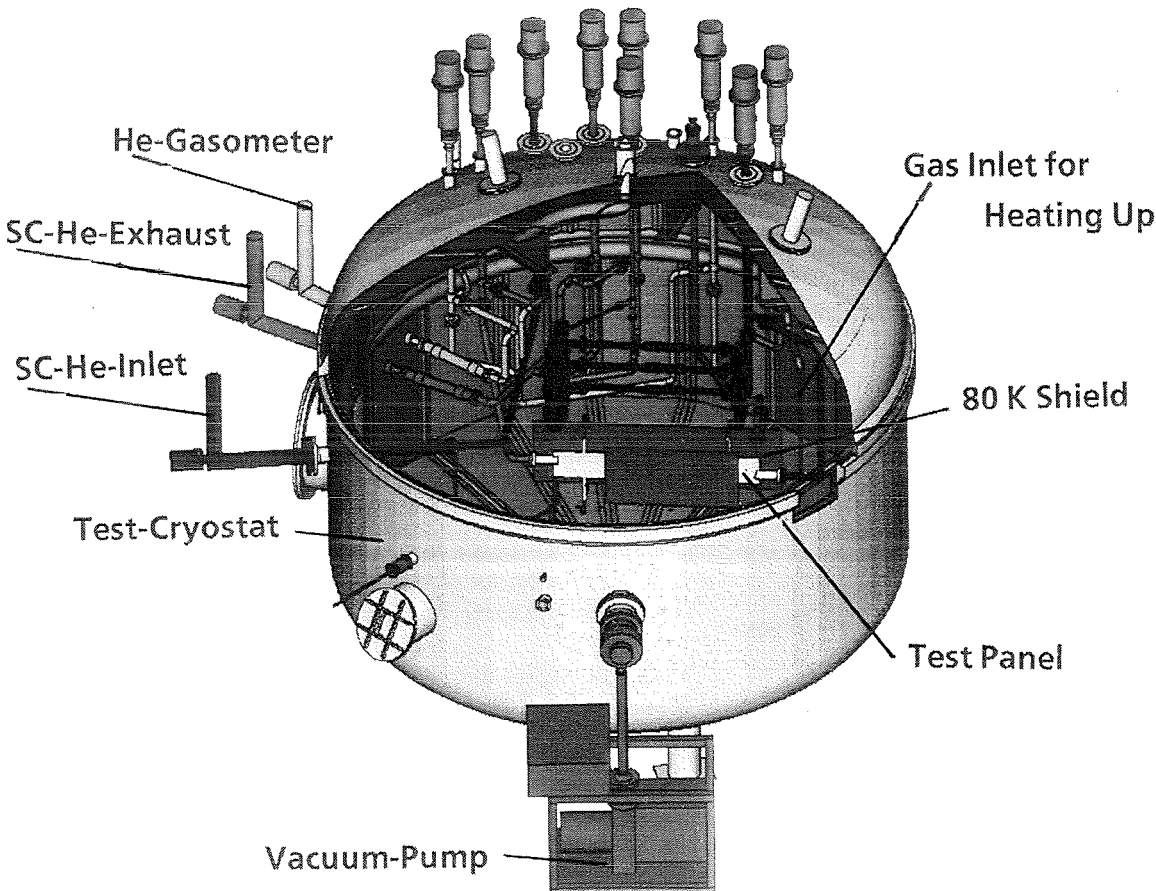
Fig. 7: View of the cryopanel installed inside the HELITEX test facility
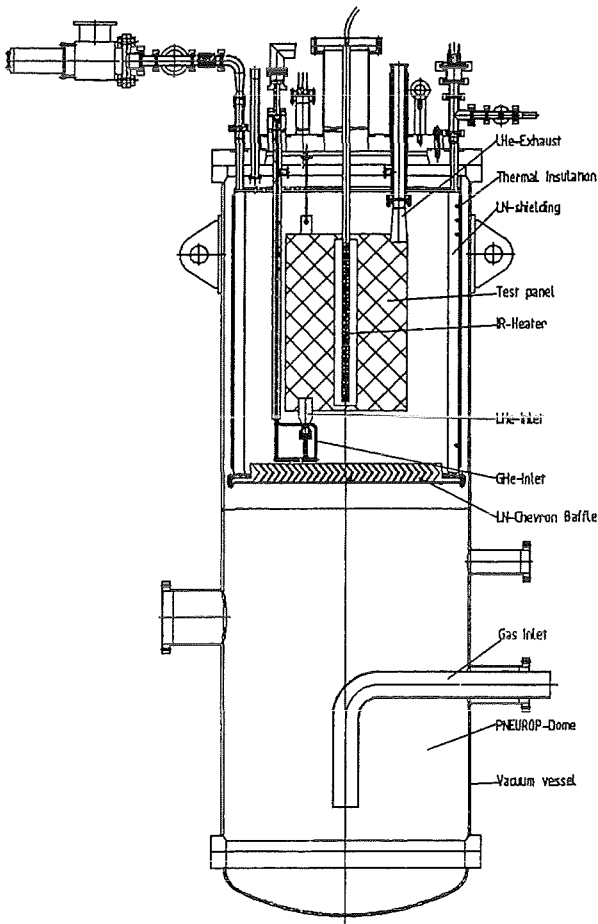
Fig. 8: Vertical cross-section of TITAN facility
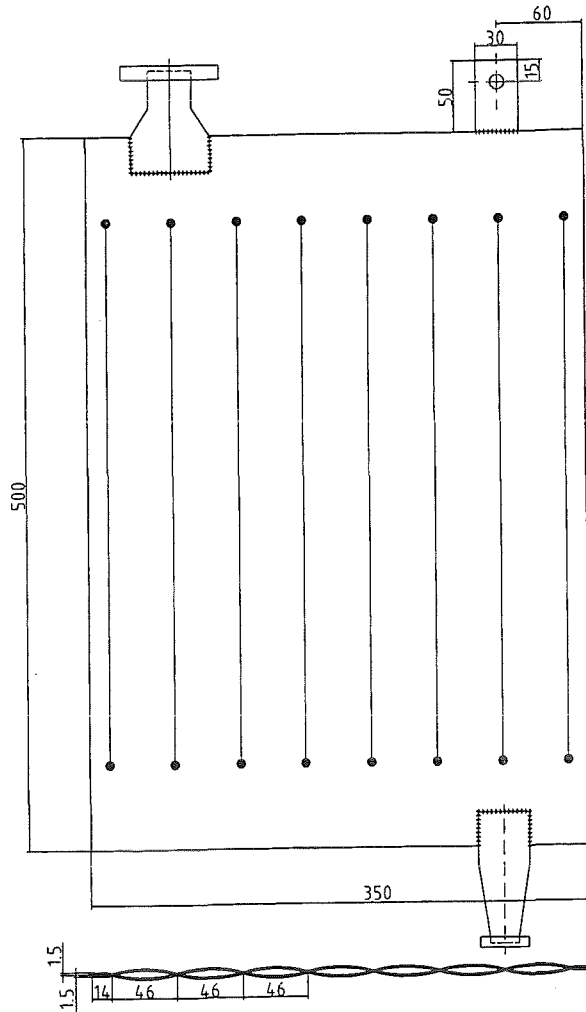
Fig. 10: Test panel in quilted design
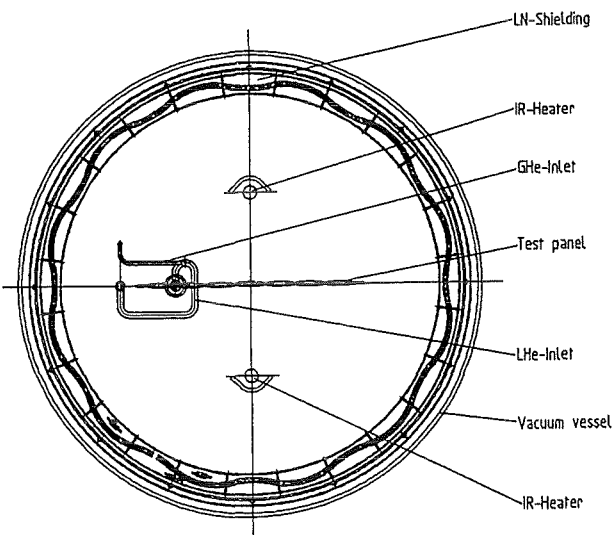
Fig. 9: Horizontal cross-section of TITAN facility

possible to measure directly the temperature of the activated charcoal particles.

The test rig allows alternatively heating up by He gas with ambient temperature. The He gas is fed into the panel by a

tube 6 x 1 mm which is connected to the LHe supply line. When the LHe flow is stopped the warm He gas flows from a pressure bottle into the panel. The mass flow rate can be varied between 1 g/s and 4 g/s. The operation pressure is kept at about 10 bar.

The gas mixture to be pumped is metered into the lower part of the vessel which is designed as a PNEUROP dome. The TITAN facility is being supplied by liquid nitrogen from a stationary LN_2 storage tank via a vacuum insulated transfer line.

Liquid helium is being supplied from a dewar transport vessel with a volume of 450 l. At the TITAN facility all cryogen reservoirs are opened to the atmosphere by relief valves.

During the tests the panels are loaded with ITER relevant gas mixtures. After the pump period the panel is heated up and the released gases are pumped down by the auxiliary mechanical pumping system for the evacuation of the TITAN facility. Metering and compositional analysis of the released gas as a function of time and/or temperature is foreseen and is expected to yield crucial information on fast regeneration behaviour of the cryosorption panel.
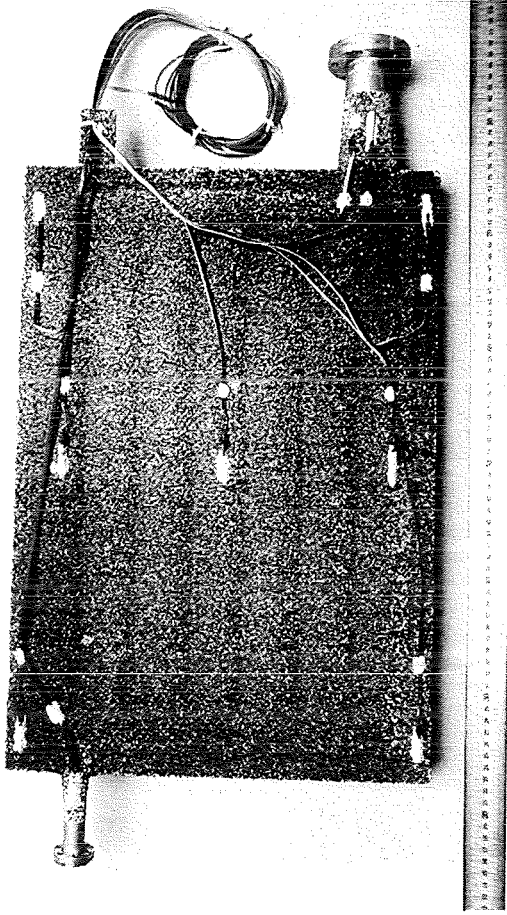
Fig. 11: Test panel coated with activated charcoal and temperature sensors attached

The results of the various heating tests at the TITAN facility will be reported in the next annual report.

2.3 Cryopanel Heat-up Calculations

Calculations were made to estimate the times necessary for fast heating of the adsorption cryopanels that are planned for investigation in TITAN. For the forced gas flow heating method an easy-to-use calculation routine was developed based upon the simplified energy conservation equations and the Fourier approach for heat transfer. The model uses a uniform temperature for the whole panel (the average caloric temperature); it gives the panel temperature T_p as a function of time and the helium temperature T_{He} as a function of the axial position and time. An error propagation calculation shows that the influence of thermal radiation from the LN_2 shielding onto the panel surface is negligible. In this case the temperature of the panel (specific heat capacity at constant pressure c, length L = 0.5 m, mass m_P = 5 kg) can be calculated from the following equation:

$$T_p(t) = \left(T_p(t=0) - T_{He,in} \right) \cdot e^{\omega t} + T_{He,in}$$

with the eigenvalue ω:

$$\omega = - \frac{\dot{m}_{He} \cdot c_{He}}{m_p \cdot c_p} \cdot \left[1 - \exp \left(\frac{h \cdot d \cdot n \cdot L}{\dot{m}_{He} \cdot c_{He}} \right) \right]$$

The heating time t_h is then given by the expression

$$t_h = \frac{1}{\omega} \cdot \ln \frac{T_p(t) - T_{He,in}}{T_p(t=0) - T_{He,in}}$$

The overall heat transfer coefficient h is calculated with standard equations for laminar resp. turbulent flow in tubes with hydraulic diameter d [3]. The heating time depends on the helium entrance temperature $T_{He,in}$ and the mass flow $\dot{m}_{He}$. It is planned to do experiments with He under pressure of 10 bar. Taking the velocity of 50 m/s in the He supply pipe of diameter 6x1 this results in a total mass flow of 1.008 g/s, which is distributed in 7 channels with lancet-like geometry (see Fig.10, hydraulic diameter d is 6.6 mm).

Calculations were also made for a higher total mass flow of 16.1 g/s, referring to a velocity of 50 m/s at the entrance tube section of the panel. The results for two different entrance temperatures that may be understood as best and worst case are shown in Tab. 2.

Tab. 2: Calculated heating times for forced GHe flow method and temperature rise from 5 to 75 K

$T_{He,in}$ [K]	300	300	80	80
$\dot{m}_{He}$ [g/s]	1.008	16.1	1.008	16.1
$T_{He,out}$ [K]	153	149	77	77
w_{chan} [m/s]	2.024	31.0	0.695	11.1
flow	lam.	turb.	lam.	turb.
h [W/m²/K]	95	1288	54	1096
t_h [s]	29	2	384	21

The heating times can be controlled by adjusting the appropriate GHe mass flow. An increase in mass flow by a factor of 16 leads to 16 to 20 times greater heat transfer coefficients and shorter heating times.

The duration of the heating phase with attached electrical co-axial heating elements can easily be estimated from the heat capacity of the panel that gives a heat consumption of 24.7 kJ for heating up to 75 K resp. 50 kJ for heating up to 100 K. As it is planned to install a total of 3 kW electrical power, heating times of less than 20 s can be expected.

The results show the feasibility of fast heating with both the GHe forced flow method and the electrical heating method.

Literature:

[1]   Mikhailov, M.D.; M.N. Özisik : Heat Transfer Solver.
       Prentice-Hall, New Jersey 1991

[2]   Tautz, H. : Wärmeleitung und Temperaturausgleich.
       Verlag Chemie, Weinheim 1971

[3]   VDI-Wärmeatlas, 4. Auflage, VDI-Verlag, Düsseldorf
       1984

[4]   Carslaw, H.S.; J.C. Jaeger : Conduction of heat in solids,
       2nd ed. Oxford University Press 1959

Staff:

C. Day
A. Edinger
H. Haas
J. Hanauer
M. Hespeler
T. Höhn
W. Höhn
S. Horn
B. Kammerer
U. Kirchhof
H. Knauß
J. Laier
A. Mack
J. Özdemir
D. Perinić
W. Reeb
R. Rinderspacher
R. Simon
D. Stern
U. Tamm
J. Weinhold
D. Zimmerlin

N 32 TT 08 EU (T 299)
Development of Plasma Exhaust Processing Technology

1. Permeation and Catalytic Cracking

Subtask: PETRA Experiment

The front-end permeator of the Tokamak exhaust processing system separates elemental hydrogen isotopes from the remainder of the exhaust gas to produce a product stream suitable for direct recycle to the Torus Fueler. Hydrogen isotopes are separated from impurities by permeation through palladium/silver alloy membranes, which are uniquely permeable to hydrogen. Tritium compatible Metal Bellows pumps are proposed to provide the pure hydrogen pressures required to achieve hydrogen recoveries of > 95 %.

With the aim of selecting adequate an permeator/pump combination and of determining achievable decontamination factors series of runs were conducted in the experimental facilities PETRA and FREND. Decontamination factors were determined for protium noble gas mixtures (97 % H_2 + 3% He or Ar). The results indicate that at a given pure gas flow rate approx. three times higher decontamination factors can be achieved with helium than with an impurity such as argon.

Fig. 1 shows some break-through curves of pure hydrogen
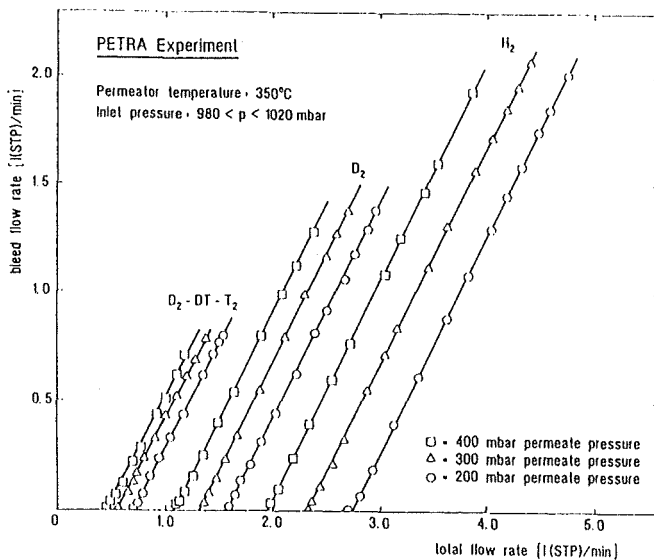
Fig. 1: PETRA Experiment: permeation data

isotopes as function of the feed flow obtained with the permeator installed in the facility PETRA of the Tritium Laboratory Karlsruhe. The permeator of PETRA has a permeation area of 0.12 m² and is operated at 350 °C. In these runs the feed gas pressure was kept constant within the range 980 < p < 1020 mbar and the pure gas pressure was kept constant at values of 200, 300 and 400 mbar. As onewould expect, initially all hydrogen isotopes fed into the permeator permeate and no bleed stream is observed. While

the pressure in the bleed region is of the order of one bar there is no driving force for the gas to flow. Once the maximum permeation rate through the permeator for a given hydrogen isotope is attained a break through into the bleed exit of the permeator takes place and gas begins to flow. As shown in the Figure the permeation rate increases from protium to deuterium to the equimolar deuterium/tritium mixture (0.25 T_2 + 0.5 DT + 0.25 D_2). Correspondingly, deuterium/tritium breaks through much earlier than protium. From the data it is evident that the investigated isotope effect is quite pronounced. The effect of permeate pressure on the break-through corresponds to that expected from the well known $p^{1/2}$ relationship.

Considerable effort has been invested into the systematic experimental investigation of the effect of increasing partial pressures of the inert diluent helium on the ionization current measured with a small volume ionization chamber at various initial pressures of an equimolar deuterium/tritium mixture. Gas analysis of the investigated mixtures was performed by radio gas chromatography. The results revealed a considerable isotope effect during the thermal release of gas from isotopically substituted ZrCo hydrides. At a given temperature, the dissociation pressure of the ZrCo hydrides was found to decrease substantially in the order protonide, deuteride, and tritide. The ionization chamber tested with the PETRA facility was developed at the Forschungszentrum Karlsruhe and is now commercially available.

In addition, a detailed model was developed to calculate the ionization current of the ionization chamber as function of DT pressure mentioned. An excellent agreement between the experimental results and the theoretical calculations was obtained when an ion recombination factor of 6 x 10⁻⁶ [cm³ ions/s] was used in the computation (see Fig. 2).

After completion of 9 months of operations with the PETRA facility testing all components with an equimolar DT mixture (permeation experiments, numerous loading/deloading operations with a ZrCo storage bed, characterization of scroll pumps and metal Bellows pumps, grab sampling, frequent pumping off of decay helium, etc.) all the tritium gettered on the ZrCo bed of the PETRA facility was recovered on a transportable uranium bed (Amersham storage bed). From a comparison between the amount of tritium originally introduced into the experiment in February 1995 and that recovered after 9 months it was concluded that less than 3 % remained unaccounted for in the primary system (remained dissolved in the structural materials, in the palladium/silver of the permeator, gettered in ZrCo) or was discharged into waste either directly or via sampling bottles.

Staff:

U. Bernd	E. Kirste
L. Doerr	H. Munakata (guest scientist)
S. Grünhagen	R.-D. Penzhorn
K. Günther	J. Wendel
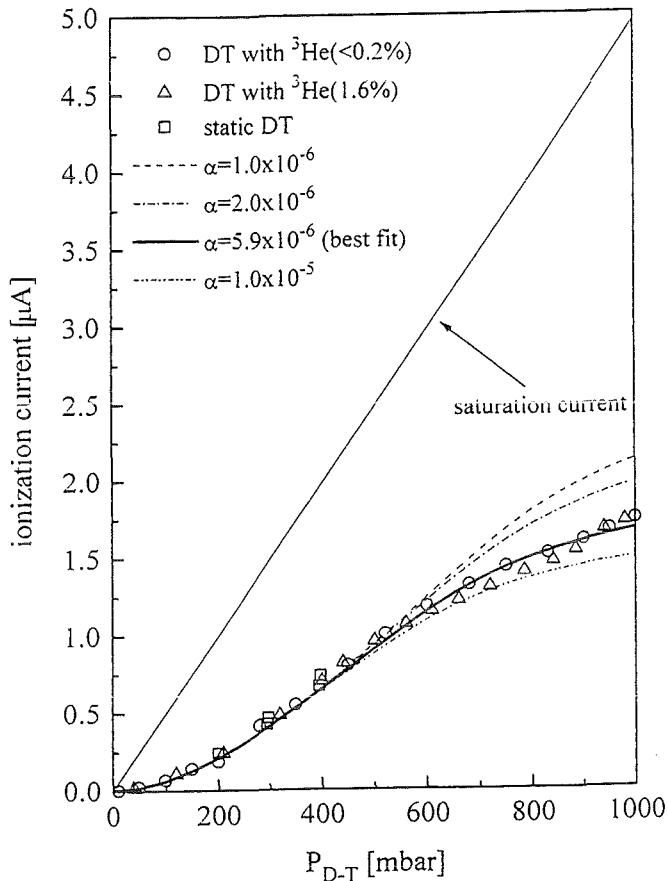
Fig. 2: Modelling of a small volume ionization chamber

possible to investigate other fuel clean-up concepts, such as the HITEX process, without major modifications of the facility.

A nickel catalyst is used in the Caprice facility for hydrocarbon cracking. In previous laboratory experiments it was shown that this catalyst actively promotes the water gas shift reaction. Loop runs with the Caprice facility indicated, that with the water gas shift catalyst the conversion rate was higher and the final humidity level lower than with the nickel catalyst. This is apparent from the data shown in Figure 3. Indeed, the exponential decrease observed for the dew point
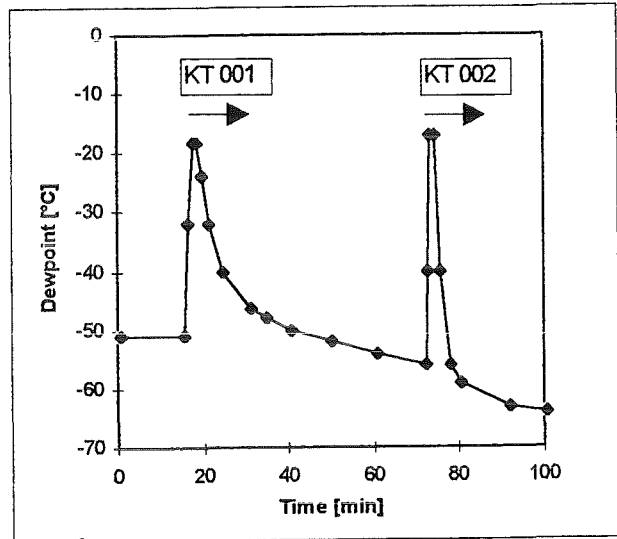
Fig. 3: Water gas shift reaction on the two different catalyst beds

Subtask 2:   Catalytic Cracking Process

To demonstrate the tritium operation of an integral fuel clean-up system based on the catalytic cracking / permeation process, the technical facility Caprice (Catalytic Purification Experiment) was designed, manufactured and commissioned at the Tritium Laboratory Karlsruhe (TLK). Important design guidelines were the minimization of i.) the amount of non-recoverable tritium and ii.) the tritium inventories in the various components.

Caprice is a highly versatile experimental facility to test and demonstrate the separation of impurities from hydrogen isotopes by a palladium/silver permeator. The impurities are processed by a combination of catalytic cracking and water gas shift (WGS) reactions with permeation of hydrogen isotopes through palladium/silver. The design throughput of the facility is 9.6 mol/h DT and 1.7 mol/h tritiated and non-tritiated impurities. The gases can be routed in a number of distinct ways and the components are designed to be valved in or out to examine different process sequences. It is also

with the nickel catalyst (KT001) operated at 450 °C is less steep than is the case with the water gas shift catalyst (KT002) operated at 200 °C. From a thermodynamical point of view, the lower temperature of the latter favours a higher degree of conversion. While the nickel catalyst will support the water conversion via the WGS reaction, it is not suitable as main catalyst for this purpose because it operates at a high temperature, which favours the kinetics but not the decomposition equilibrium.

For the cracking of hydrocarbons, temperatures of 450 - 480°C are needed, mainly to decompose methane. At this temperature, the Boudouard equilibrium between carbon and carbon oxides is promoted on the nickel catalyst, which leads to the formation of carbon monoxide required to support the water gas shift reaction. Because of this 'in situ chemistry' the catalytic process is not at all sensitive to the feed gas composition.

Figure 4 shows impurity separation and processing by a once-through mode, not originally foreseen with the Caprice facility (dotted line). A steady-state flow rate of about 0.4 mol/h was fed into the impurity processing loop giving rise to a waste gas stream such as given in Table 1.

The cycling flow rate within the impurity loop was about 40 mol/h. Notably, no carbon oxides were introduced with the

Table 1: Flow rates during a once-through mode
experiment

	Feed [mol/h]	Waste[mol/h]	DF
total	4.941	0.305	
D_2	4.6	below GC - detect. limit	
He	0.29	0.301	
CO	-	0.0021	
CO_2	-	0.0016	
D_2O	0.0054	0.0002	
CD_4	0.071	0.0003	200
ΣD_2	4.75	0.0008	6000

feed gas. In spite of this, water was converted into molecular hydrogen due to the already discussed in situ production of carbon monoxide (gasification of carbon deposit) and the occurance of the water gas shift reaction. Under the prevailing conditions the carbon deposition rate on the Ni-catalyst was calculated to be 0.8 g/h.

The decontamination factor (DF) determined for methane was about 200, the integral DF about 6000.

The results of a typical experiment at low tritium concentrations (T/D ≈ 0.005) are depicted in Figure 5. In this run the impurity processing loop was operated including the WGS reactor (KT002) and the nickel catalyst reactor (KT001) as well as the permeator (PP002). The processed gas consisted initially of helium with carbon oxides, tritiated water and tritiated methane. When the experiment was initiated, the nickel catalyst KT001 was bypassed and the permeator was valved in. As soon as the WGS catalyst was taken on line a sharp drop in dew point down to levels of - 60 °C was observed. The tritium activity droped with approximately the same rate law, but not to background levels. This is explained by the fact that under the prevailing conditions methane remains unaltered.

When the valves to KT001 were opened a transient rise in dew point was observed. The registered dew point is at first higher than that of the original gas mixture. This is caused by the well-known water gas shift equilibrium between carbon oxides, water and hydrogen attained at the nickel catalyst at temperatures of 450 °C. After a period of a few minutes the dew point decreased to back ground levels on account of the WGS reaction, which now takes place on both catalysts.

Because the ionization chamber can not distinguish between tritiated hydrogen, methane and water the activity remains practically constant when KT 002 is integrated into the loop. As soon as the process gas passes through KT001 methane is cracked and the hydrogen liberated is continuously removed from the impurity processing loop via the permeator. This
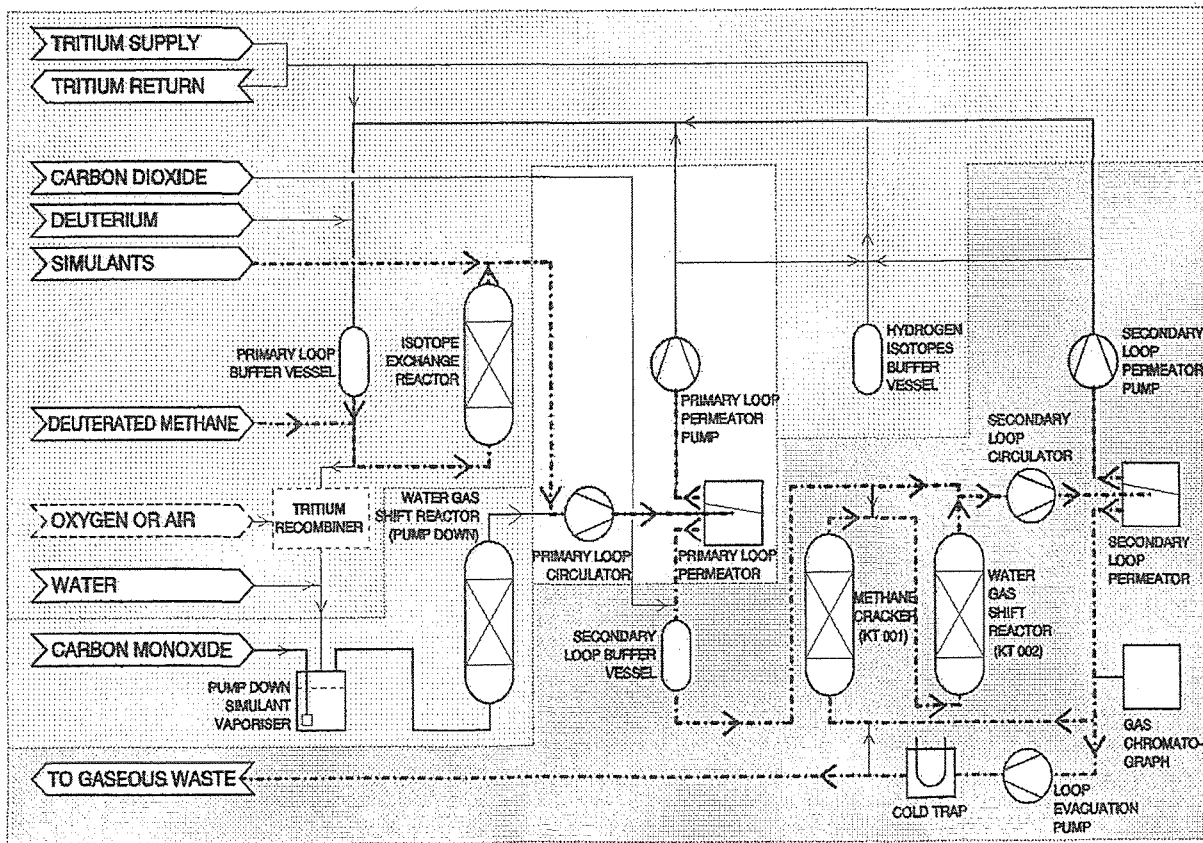
Fig. 4:   Once-through operation of the Caprice facility

10000

KT002 KT001 + KT002

KT001: Methane Cracker
KT002: WGS-Reactor

Activity
Dew Point

Activity [Ci/m³]

Dew Point [°C]
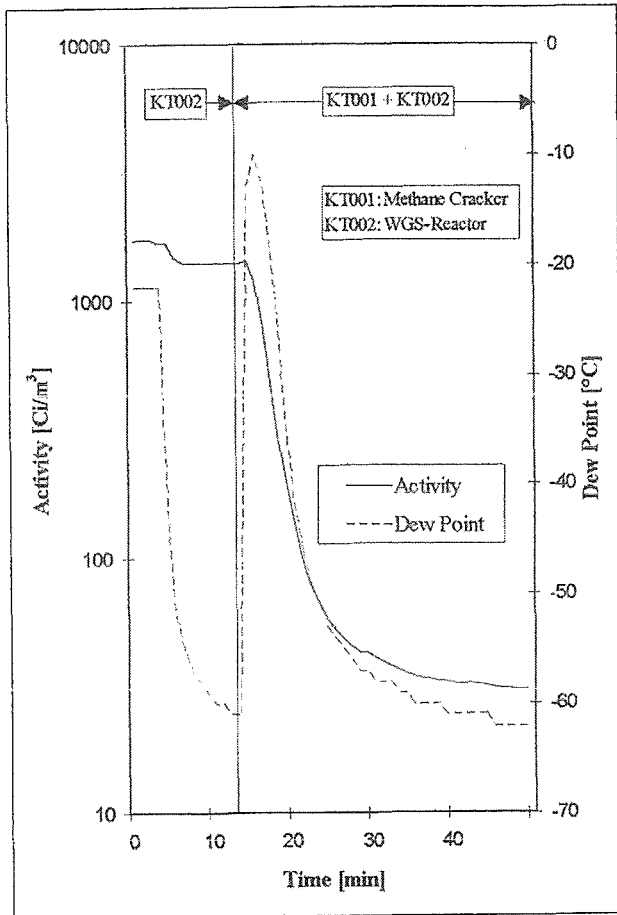
Fig. 5:   WGS reaction and WGS reaction combined with
hydrocarbon cracking during a typical tritium run

leads to the observed decrease in activity down to the steady-state contamination level of the ionization chamber.

The experiments performed so far with the Caprice facility have shown that the original design specifications were fully met.

The Caprice facility and its peripheral systems have now been sufficiently tested to permit an increase of the tritium concentrations from now tracer levels successively up to 50 % tritium in deuterium.

Laboratory investigations of the permeator / catalyst combination (Permcat) for isotopic swamping has sufficiently progressed to allow the design, construction and manufacture of a component suitable for the Caprice facility. A semi-technical component is already being manufactured and is expected to be ready for installation into Caprice by the end of this year.

It was shown that after only minor modifications of the Caprice facility, experiments to test the Hitex - process can be performed.

Staff:

M. Glugla
K. Günther
T.L. Le
W. Leifeld
R.-D. Penzhorn
K.H. Simon

2. TRIT-1 Tritium Supply and Management: Calorimetric Measurements at the TLK

The Tritium Laboratory Karlsruhe (TLK) employes calorimetry as a non-destructive assay (NDA) technique for the determination of tritium together with PVT-c (pressure/volume/temperature-concentration) measurements. The latter, used to verify the amount of tritium received or delivered to a system, are performed both in the facilities of the infrastructure as well as in those of the experiments. For the calorimetric assay of tritium small portable uranium getter beds are employed.

Since the commissioning of the experiments PETRA and CAPRICE and the beginning of their routine operation during spring 1995 numerous calorimetric measurements have been carried at the TLK. The tritium inventories determined so far have covered a range of 1.5×10^{12} to 8.9×10^{14} Bq.

The calorimeter used for the measurements described above is one developed several years ago at the Forschungszentrum Karlsruhe; it is of isothermal shield design. In October 1995 a second calorimeter manufactured by ANTECH will be delivered to the TLK. This calorimeter is of isothermal measurement chamber design with a constant temperature profile towards its periphery. Partly because of their different measurement principles, both calorimeters are considered to be complementary. The FZK calorimeter, shown to have a detection limit of less than 10^{12} Bq, generally requires a measurement period of the order of 70 h. The ANTECH instrument, on the other hand, is anticipated to have a detection limit about a factor of two to three higher; the time required for a measurement, however, will probably be much shorter. For these reasons it is planned to use the ANTECH calorimeter predominantely to support the routine operation and that developed at FZK for the more specialized as well as for the comparative tritium assays.

Considerable improvement of the shipper/receiver results were accomplished in the past months after the shipper incorporated several improvements into the previously employed PVT-c measurement equipment. The beneficial effect of the improvements became apparent with two recent tritium shipments in uranium beds containing volumetrically specified amounts of tritium equivalent to 1.295×10^{15} and 5.940×10^{14} Bq, respectively. Calorimetric analysis of the getter beds received by the TLK showed that whereas in older measurements shipper/receiver differences of up to 5 % were detected, the more recent measurements delivered results that agreed to 99.93 (1.295×10^{15} Bq sample) and 99.61 % (5.940×10^{14} Bq sample), respectively with the shipper. Because of the importance of tritium safeguards, efforts to further improve these assays are continuing.

Earlier runs with uranium getter beds having tritium inventories of the order of 1.1×10^{12} Bq indicated that standard deviations < 1% were achievable at these inventory levels. Therefore, interlab comparative calorimetric measurements with one and the same uranium bed were initiated in cooperation with JET. Within the frame of this programme a uranium bed specified by JET to contain 7.4×10^{11} Bq tritium as determined with a calorimeter developed in that laboratory was sent to Karlsruhe for verification of its tritium content. From measurements still in progress it is apparent that the agreement between both measurements is satisfactory and that consequentially heat power levels of less than 1 mW are still detectable with the FZK calorimeter.

Staff:

L.Dörr
H. Kapulla
R. Kraemer
R.-D. Penzhorn

TEP 3   Tritium Storage

In a series of runs an originally equimolar DT mixture gettered in ZrCo was released at progressively increasing temperatures. When the release was restricted to low pressures, i.e. 3.2 mbar, a gas analysis performed by radio gas chromatography revealed the presence of protium as an impurity. As seen from the data in Table 1, at this low partial pressure the contribution of protium to the concentration in the gas phase is quite significant. As the pressure over the getter is increased the percentage of protium decreases to very low values and the composition above the getter approaches that of an equimolar deuterium-tritium mixture. These results clearly show, that the hydrogen isotope effect in the $ZrCo/Q_2$ (Q = H, D, T) system is fairly large. It is due on one hand to the increasing dissociation pressure when going from protium to tritium and, on the other, to the faster diffusion rate of the lighter hydrogen isotopes through the ZrCo bulk. As a result it is necessary to wait much longer to attain equilibrium pressure when a DT mixture is released from ZrCo tritide instead of protium.

The intermetallic compound $Zr_{0.8}Ti_{0.2}Co$ has been identified as a candidate storage material for tritium because of its low pyrophoricity, its high resistance towards thermally induced phase changes and the low dissociation pressures of the hydrides at room temperature. To learn more about the properties of this material, several pressure-composition measurements were performed at 50, 100 and 150 °C, respectively. Typical data obtained at 150 °C are shown in Fig. 1. The isotherms indicate that even at this relatively high temperature the dissociation pressures are comparatively low. At 100 °C the pressures are lower by a factor of 3-5 at a
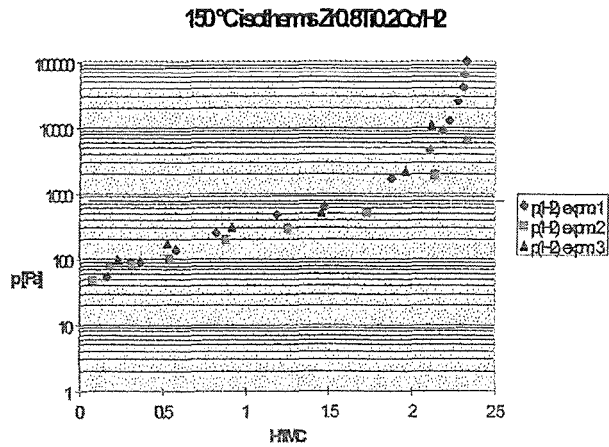
Fig. 1:   Pressure/composition isotherms of the $Zr_{0.8}Ti_{0.2}Co/H_2$ system

given concentration of hydrogen in the intermetallic compound. The only drawback of $Zr_{0.8}Ti_{0.2}Co$ as a getter material for tritium storage appears to be the poor reproducibility of the p - c results. Presently, the effect of the previous history (including activation) of the various samples under investigation is being examined more carefully.

Staff:

R.-D. Penzhorn
M. Sirch
M. E.Willin

Table 1:   Analysis of isotopc hydrogen (in %)

D-T [mbar]	Method	H_2	HD	D_2	HT	DT	T_2
3.2	TCD	---	---	---	---	---	---
	calc. from ICS	23.07	22.26	7.84	22.98	14.97	8.88
6.4	TCD	---	---	---	---	---	---
	calc. from ICS	22.90	24.49	8.04	21.40	15.42	7.74
25.2	TCD	bdl	14.07	20.11	11.56	36.77	17.48
	calc. from ICS	2.88	13.57	19.61	11.20	35.63	16.93
150.3	TCD	bdl	7.52	23.17	6.15	42.76	20.39
	calc. from ICS	0.71	7.34	23.27	6.09	42.38	20.22
902.5	TCD	bdl	6.55	23.04	5.61	43.25	21.28
	calc. from ICS	0.57	7.34	23.18	5.63	43.36	21.23

TCD   = thermal conductivity detector
bdl   = below detection limit
ICS   = calc. from ionization chamber signals after Schott and Genty

Vessel In-Vessel

G 16 TD 17 EU (D 202)
Shielding Blanket Development and Design

3-D Neutronics and Shielding Analysis for the ITER Machine

Shielding analysis is a necessary step in the design of ITER which provides quantitative performance and safety parameters. The objective of this task is to perform transport shielding calculations for the ITER machine by using three-dimensional Monte Carlo methods. Neutronics analyses in support of specific shielding blanket and vacuum vessel design optimisations are provided. The work complements and is closely co-ordinated with tasks on other aspects of the problem performed by the other ITER partners.

FZK Sub-task: Updating of ITER torus sector model for MCNP-calculations and 3d-shielding calculations

A global sector model of the ITER torus had been developed jointly by the University of Wisconsin and Kernforschungszentrum Karlsruhe in 1994 in the framework of design task D4. An updating of this model has been performed in 1995 to integrate both a new divertor and a new shielding blanket design. The divertor modelling was again performed at the University of Wisconsin, while the shielding blanket modelling was performed at FZK.

The updated model is based on the 24-coil design of ITER. A torus sector of 7.5° was used for the modelling. The TF-coils and the vacuum vessel were not changed, while the shielding blanket segments have been completely replaced with respect to the previous model. This holds for both the radial build of the blanket segments and their poloidal arrangement around the vacuum chamber, see Fig. 1 for a vertical cross-section of the MCNP-model.

At the inboard side a detailed description of the radial build has been used for the shielding blanket: first wall (0.5 cm Be, 0.5 cm Cu, 1.0 cm Cu/water, 1.0 cm SS-316), 10 heterogeneous layers of steel and water, respectively, 4 homogenised steel/water layers with a total thickness of 8.5 cm, 9.7 cm manifold and 7 cm back steel plate. The total thickness of the shielding blanket at the inboard side is 50.5 cm. The vacuum vessel is composed of a 5 cm front steel plate, a 30.5 cm homogeneous steel/water mixture, a 5 cm thick steel plate and a 5 cm Pb/B_4C shield.

Shielding calculations have been performed with the MCNP-code for obtaining the radial neutron flux distribution at the inboard side of the ITER torus (first wall/shielding blanket/vacuum vessel/TF-coil) and the radiation loads to the inboard TF-coil. Appropriate importance sampling techniques (geometry/particle splitting with Russian Roulette and iteratively optimised particle weights) have been applied to direct the particle tracks through the blanket/shielding system and arrive at statistically reliable scorings for the nuclear responses at the front of the TF-coil. 320,000 source
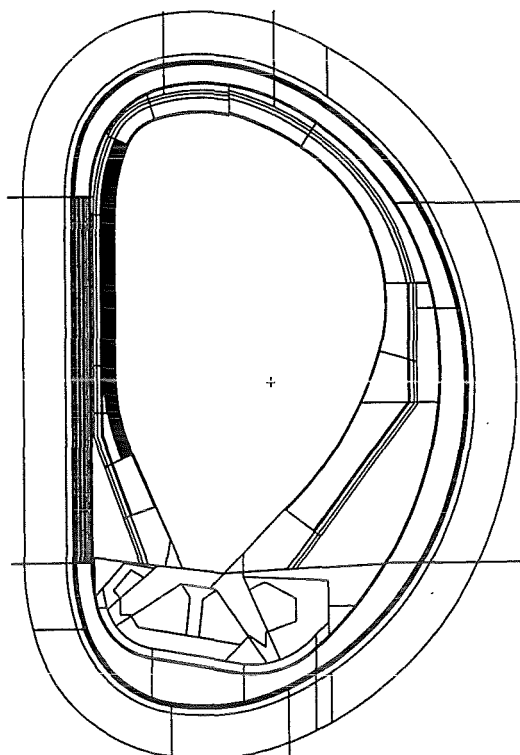
Fig. 1: Vertical cross-section of the updated MCNP torus sector model with shielding blanket modules

neutron histories were followed in the shielding calculation consuming about 10h CPU time on the IBM 9021 mainframe.

Various nuclear responses were calculated for the vacuum vessel (peak nuclear heating, peak dpa-rate, peak helium production, etc.) and the TF-coil. The main results for the radiation loads to the superconducting TF-coil (i. e. fast neutron fluence, peak heating rate, radiation dose to the copper insulator, epoxy radiation dose, etc.) are displayed in Table 1. Note that the required radiation limits can be safely met for the present shielding blanket assuming an integral operation time of 3 years.

Staff:

U. Fischer

Table 1: Radiation loads to the inboard TF-coil at a
poloidal height of 120 to 200 cm above torus
mid-plane, results of three-dimensional Monte
Carlo shielding calculations (1500 MW fusion
power, 3 full power years operation)

	Radiation load limits	ITER shielding blanket
Peak dose to electrical insulator (Epoxy) [rad]	$5 \cdot 10^9$	$5.85 \cdot 10^8$
Peak displacement damage to copper stabiliser [dpa]	$6 \cdot 10^{-3}$	$4.15 \cdot 10^{-4}$
Peak fast neutron fluence (E > 0.1 MeV) to the Nb_3Sn superconductor [cm^{-2}]	$1 \cdot 10^{19}$	$6.52 \cdot 10^{17}$
Peak nuclear heating in winding pack [mWcm^{-3}]	5.0	0.134

G 16 TD 21 EU (D 203)
Breeding Blanket Development and Design

A breeding blanket concept is under development to provide the tritium fuel necessary to achieve the technical objectives of the Enhanced Performance Phase of ITER operation. It is based on a modular design similar to that of the shielding blanket modules of the Basic Performance Phase. Both the module segmentation and the dimensions are the same to allow a simple replacement of the shielding by the breeding blanket modules. A water-cooled ceramic breeder blanket concept with beryllium multiplier is being investigated. A layered structure is used for the breeder/multiplier/coolant configuration to allow a compact blanket design needed to meet both the required shielding performance and tritium breeding potential.

FZK Sub-task: Three-dimensional neutronic analysis of the ITER breeding blanket

The objective of this sub-task is to determine the nuclear performance of the breeding blanket by means of three-dimensional Monte Carlo calculations with the MCNP-code. This includes the calculation of the global tritium breeding ratio, the heat generation and the shielding efficiency. This sub-task is conducted jointly by ENEA Frascati and FZK Karlsruhe.

Based on the 24-coil design of ITER, an appropriate 3d torus sector model has been developed for the shielding blanket in the framework of task D202. Using this model, the shielding blanket modules were replaced by breeding blanket modules. Inside the blanket modules the heterogeneous array of beryllium blocks, breeder and cooling layers has been integrated (see Fig. 1 for a horizontal cross-section). Li_2ZrO_3 is

Fig. 1: Horizontal cross-section of an inboard breeding blanket module (MCNP model)

used as breeding material in the form of a pebble bed with a packing factor of 70%. The ^6Li-enrichment is assumed at 50%.

The total blanket thickness amounts to 25.3 and 31.9 cm, inboard and outboard modules, respectively. There are not more than two breeder layers contained in the inboard and three ones in the outboard modules, each one having a radial thickness of 1 cm. A global tritium breeding ratio of T=0.89 was obtained for the applied torus sector model when using FENDL-1 nuclear data in the Monte Carlo calculation.

The torus sector model, equipped with the breeding blanket, was submitted as MCNP input deck to ENEA Frascati for further neutronic calculations.
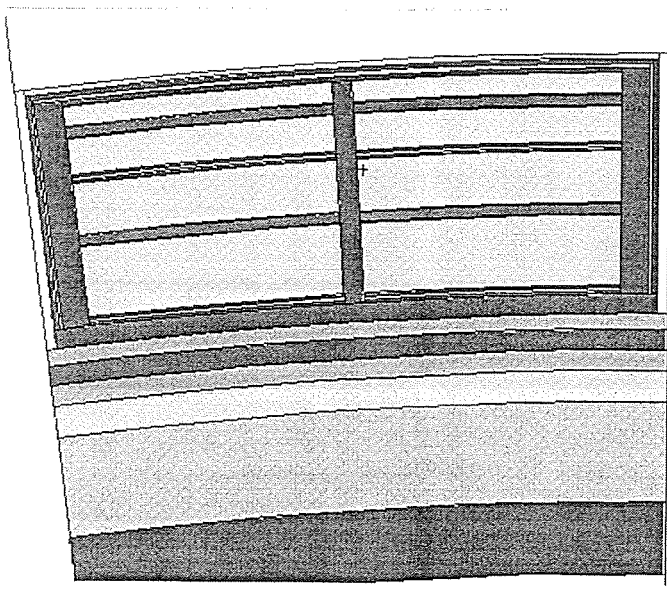
Staff:

U. Fischer

G 16 TT 82 EU (T 218)
Shielding Neutronic Experiments, Heat Deposition and Afterheat Measurements, Tritium Neutronic Experiments

Shielding Neutronics Experiments

One of the main functions of the shielding blanket (SB) in ITER is to protect the vacuum vessel (VV) and the toroidal field coils (TFC) from the penetrating neutron and gamma-radiation. The computational methods and nuclear data used in the shielding calculations, therefore, need to be properly validated. For that purpose, an integral bulk shield experiment is being performed at the Frascati 14-MeV Neutron Generator (FNG). The main objective of this experiment is to validate the nuclear performance of the ITER shielding blanket and vacuum vessel. The experimental set-up closely replicates the layout of the ITER inboard shielding blanket, vacuum vessel and toroidal field coil, both with regard to the material composition and its radial arrangement. The SB/VV/TFC mock-up consists of a 96 cm thick shielding block made of alternate plates of SS-316 (5 cm thickness) and perspex (2 cm thickness, for simulating water layers). The SS-316/perspex configuration is backed by a 30 cm thick block of alternate SS-316 and copper layers for simulating the TF-coil. The lateral dimensions amount to 100 cm x 100 cm for the shield block and 47 cm x 47 cm for the TF-coil.

The FNG bulk shield experiment is conducted in a collaboration between ENEA Frascati, CEA Cadarache, TU Dresden, FZK Karlsruhe, KIAE Moscow, and MEPhI Moscow. It is planned to measure neutron and photon spectra, the nuclear heating, reaction rate distributions as well as the induced activation inside the SB/VV mock-up. In order to meet the requested objective, the analysis of the experiment will be performed with the same computational tools and data that are in use for ITER design and shielding calculations: the MCNP Monte Carlo transport code and the FENDL/MC-1.0 nuclear data library. As a result, the experiment and its analyses will provide the data base for the evaluation of design safety factors.

FZK Sub-task: Three-dimensional pre-analysis of the ITER bulk shield experiment at FNG

A major problem in this experiment concerns the measurement of the nuclear responses at the back side of the 96 cm thick SB/VV mock-up. Without additional back shield, the neutron radiation would be dominated by the background radiation due to backscattering events from the walls of the experimental hall ("room-return effect"). To cope with this, it was proposed to use an additional polyethylene back shield around the back part of the SB/VV/TFC mock-up.

Three-dimensional neutron transport calculations were required to properly quantify the room-return effect, check the need for an additional back shield and proof that the background radiation can be sufficiently reduced by the proposed polyethylene shield. This was accomplished by

means of three-dimensional Monte Carlo calculations with the MCNP-code. The basic 3d-model of FNG with experimental bunker and walls was provided by ENEA Frascati.

At FZK the ITER shield mock-up configuration was integrated to that model. In addition, further refined models were developed to allow the application of different importance sampling techniques needed to perform the different types of Monte Carlo calculations for assessing

- the direct neutron penetration through the mock-up with no room-return effect

- the room-return radiation with no background shield

- the neutron radiation in the mock-up with additional polyethylene back shield taking into account the background radiation

- the room-return radiation through the polyethylene back shield.

Fig. 1 shows a typical vertical cross-section of the mock-up
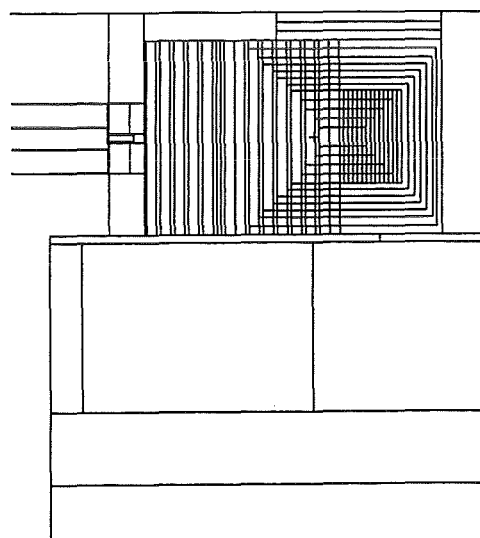
Fig. 1: Vertical cross-section of FNG with ITER SB/VV/TFC mock-up configuration (MCNP model)

model with a fine spatial segmentation scheme applied for the importance sampling. The particle/geometry splitting technique with Russian Roulette was applied for that purpose. For each type of calculation a specific map of optimised particle weights was used. Reliable statistical results were obtained by tracking about 200,000 source neutron histories in the direct penetration case, and 2 to 3 million histories in the calculations of the background radiation. In any case the consumed CPU-time was not more than 8 hours on the IBM-9021 mainframe.

Fig. 2 compares the neutron flux distributions obtained in the back part of the SB/VV/TFC mock-up for the four analysed

FW/SB/VV/TFC mock-up: Total neutron flux profile
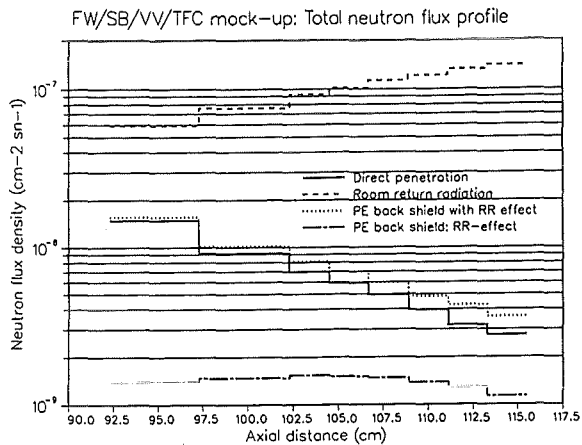
Fig. 2: Neutron flux distribution in the back part of the SB/VV and the front part of the TFC-mock-up (Results of 3d Monte Carlo calculations, normalized to one source neutron)

cases. Obviously, the direct neutron penetration radiation is dominated by the background radiation both at the back of the SB/VV mock-up (up to 102.5 cm) and the TFC-mock-up: the total neutron flux decreases from $3.7 \cdot 10^{-3}$ cm^{-2} (source neutron) -1 at the front surface to $9.2 \cdot 10^{-9}$ cm^{-2} (source neutron) -1 at the back plate of the SB/VV mock-up in case of the direct penetration, whereas it is amounts to $7.6 \cdot 10^{-8}$ cm^{-2} (source neutron)$^{-1}$ at that location when taking into account the room-return effect. Therefore, it would not be possible to detect the direct neutron radiation by measurement at the back of the SB/VV mock-up without additional back shield.

When applying a polyethylene back shield around the TFC and the back of the SB/VV mock-up, the background radiation is reduced by almost two orders of magnitude. In this case, the background contributes 10 - 15 % to the total neutron flux density at the back of the SB/VV as well as at the front of the TFC mock-up. Consequently, the polyethylene back shield is sufficient to allow the measurement of direct penetrating radiation at these deep locations.

Literature:

[1] U. Fischer, 3-D Pre-analysis of the ITER Bulk Shield Mock-up Experiment at FNG, ITER Review Meeting on Task T218 „Shielding Neutronics Experiment", Frascati, Italy, March 1-3, 1995.

Staff:

U. Fischer

The contribution of TU Dresden to Task T 218 consists in spectral neutron and gamma flux measurements and in preparation of two techniques for nuclear heating measurements.

1. Measurement of spectral neutron and gamma fluxes

The mock-up is outlined in Fig. 3. It consists of slabs made from Perspex (2 cm thickness each) and SS316 (5 cm thickness each) and has a front area of 100 x 100 cm². The total thickness of the assembly is 97 cm including an 1 cm thick Cu layer in front. Behind this assembly a block of Cu and SS316 plates is arranged imitating the coils for the toroidal magnetic field (dimensions: depth 30 cm, area 47 x 47 cm²). The rear part of the assembly is surrounded with a polythene shield covering also the last 30 cm of the Perspex / SS316 block to reduce room-return background.

For neutron and gamma spectra measurements two positions have been agreed upon in the preceding planning of the experiment [2]:

Position A: Measurement inside the first SS316 slab behind the 6 cm thick Perspex layer (total depth 42.5 cm from the front of the assembly). This position characterizes the boundary of the shield blanket.

Position B: Measurement in the next to last SS316 layer (total depth 89.5 cm from the front). This position is close to the boundary of the vacuum vessel with the coils.

Estimations for measuring times and desired neutron generator parameters were derived from calculated spectral fluxes of neutrons and photons in positions A and B, respectively, taking into account the detector responses. The spectra were calculated with the Monte-Carlo code MCNP [3] and the data library FENDL-1 [4] for the material assembly of Fig. 3. They are presented in Figs. 4 and 5.

A NE213 scintillator with diameter of 3.8 cm and length of 3.8 cm will be employed for simultaneously measuring the spectral neutron flux in the range E > 1 MeV and the spectral photon flux in the range E = 0.2 MeV. Additionally a stilbene scintillation spectrometer will be used in the energy range above 700 keV. The low-energy range of the neutron spectrum will be measured by a proton recoil proportional counter spectrometer. The hydrogen or methane filled proportional counters allow to measure neutron spectra in the range from about 10 keV to about 1.2 MeV, so that a sufficient overlap with the scintillation counter spectra is realized.

2. Techniques for nuclear heating measurements

Suitable methods for nuclear heating measurements in a blanket mock-up based on thermoluminescence detectors and ionization chambers were successfully developed at CEA Cadarache and ENEA Frascati. The TUD group is investigating

a scintillating fiber and a Si-sensor with the aim to obtain additional information on nuclear heating, especially in mock-up cells where high sensitivity is needed [5-7].

A calculation with the Monte-Carlo code MCNP [3] and the data library FENDL-1 [4] was performed to estimate the nuclear heating in several cells of the inboard-blanket mock-up at FNG. In addition to the cell positions A and B positions C (central part of the last Perspex plate) and D (first copper plate of the assembly simulating the TF-coils) were considered. The results are outlined in Table 1.

In SS316 and Cu the photon heating is one order of magnitude stronger than the neutron heating whereas in Perspex neutron heating is more important than photon heating. The organic scintillator behaves very similar to Perspex. Therefore it is suitable for measuring the sizable neutron component of heating in Perspex. The Si-sensor
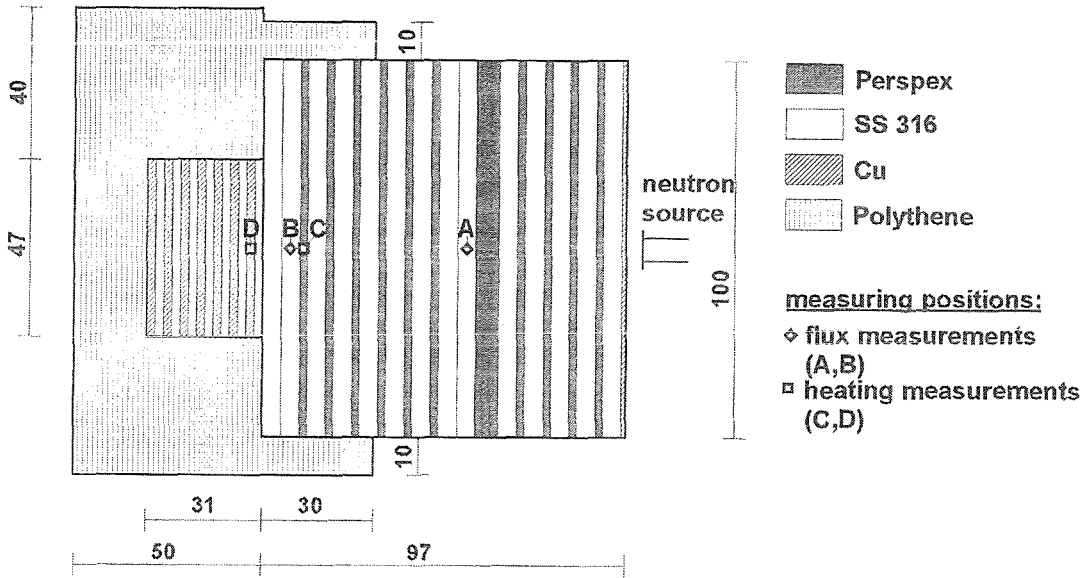
Fig. 3:   Bulk shield assembly
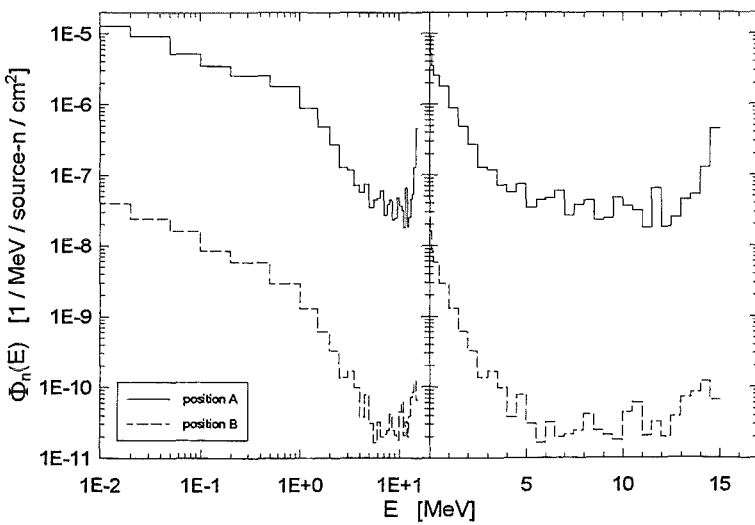
Fig. 4:   Calculated spectral neutron fluences in positions A and B for one source neutron (logarithmic and linear energy axes)
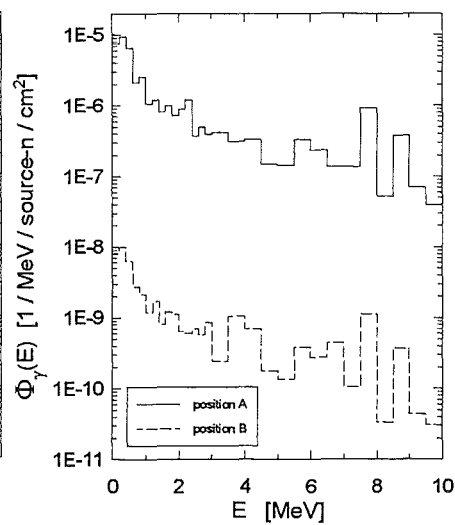
Fig. 5:   Calculated spectral photon fluences in positions A and B for one source neutron

records specific photon heating which is the dominant component in SS316 and Cu.

To determine the detector response of the used scintillating fiber (BICRON, type BCF-12) Monte-Carlo calculations with a modified NRESP-7 code from PTB Braunschweig [8] were performed, which allowed to calculate the energy deposition in the fiber by different reactions on H and C.

The response of the Si-sensor was calculated with MCNP-FENDL. Both methods were checked in neutron-gamma fields generated by 14 MeV neutrons [6].

Literature:

[2]   H. Freiesleben, W. Hansen, D. Richter, K. Seidel, S. Unholzer, Report on Detailed Design of Neutron and Gamma Spectra Measurements, Report TUD-IKTP/95-02, Dresden, April 1995 and EFF-DOC-390, July 1995

[3]   J. F. Briesmeister (ed.), MCNP - A General Monte Carlo N-Particle Transport Code, Version 4A, LA-12625-M, Los Alamos N. L., 1993

[4]   S. Ganesan and P. K. Mc Laughlin, FENDL/E - Evaluated Nuclear Data Library of Neutron Interaction Cross-Sections, Photon Production Cross-Sections and Photon-Atom Interaction Cross-Sections for Fusion Applications, Version 1.0, IAEA-NDS-129, Vienna, 1994

[5]   H. Freiesleben, K. Merla, D. Richter, K. Seidel, Tests of a New Technique for Nuclear Heating Measurements Using Scintillating Fibers, EFF-DOC-302, June 1994

[6]   K. Merla, D. Richter, K. Seidel, S. Unholzer, H. Freiesleben, Investigation on Nuclear Heating Measurements with Scintillating Fiber and Si-Sensor at the FNG Mock-up, EFF-DOC-389, July 1995

[7]   H. Freiesleben, K. Merla, D. Richter, K. Seidel, S. Unholzer, Nuclear Fusion Project, Annual Report of the Association Forschungszentrum Karlsruhe/EURATOM, Oct. 1993 - Sept. 1994, FZKA 5515, EUR 16100 EN, p. 43-45, Jan. 1995

[8]   G. Dietze and H. Klein, NRESP4 and NEFF4 Monte Carlo Codes for the Calculation of Neutron Response Functions and Detection Efficiencies for NE213 Scintillation Detectors, Report ND-22, Braunschweig, October 1982

Staff:

H. Freiesleben
W. Hansen
K. Merla
D. Richter
K. Seidel
S. Unholzer

Table 1:   Calculated specific nuclear heating in cells of the mock-up (Fig. 3) for mock-up materials and for sensor materials

Cell	Material/sensor	Specific heating by neutrons (MeV/g)	Specific heating by photons (MeV/g)
A	SS316	1.52E-8	4.28E-7
	Si	7.59E-8	4.26E-7
B	SS316	1.41E-11	4.36E-10
	org. scint. (NE213)	7.21E-10	4.68E-10
C	Perspex	9.27E-10	7.09E-10
	org. scint. (fiber)	9.12E-10	6.12E-10
D	Cu	3.01E-12	4.29E-11
	Si	1.68E-11	4.31E-11

NDB 1   Neutronics Data Base Development

FZK contributes to the development and qualification of the European Fusion File (EFF) and the international Fusion Evaluated Nuclear Data Library (FENDL). Improved nuclear cross-section data evaluations for structural materials and data testing against integral experiments are the main activities in this area.

EFF-1 Development: Cross-section evaluation for structural materials

The 1993 evaluation of resonance parameters for ^{56}Fe + n below 0.86 MeV has been revised. This was necessary because new information about systematic versus statistical errors indicated that one set of resonance analysis results had been given too much weight in the first version [1]. For the unresolved region above 0.86 MeV a newly developed cumulant expansion [2] has been used to assess the impact of cross-section fluctuations on the efficiency of thick iron shields. The conclusion was that self-shielding factors are quite important up to 2 to 3 MeV but practically negligible above 4 to 5 MeV. This theoretical assessment was confirmed by recent benchmark calculations with and without fluctuating cross-sections performed at Petten.

FENDL-1 nuclear data library: Co-ordinated international benchmark validation task

The Fusion Evaluated Nuclear Data Library FENDL is a compilation of fusion-oriented data files selected from the nuclear data libraries ENDF/B-VI (USA), BROND (Russian Federation), JENDL (Japan) and EFF (European Union) in an international effort initiated and co-ordinated by the IAEA Nuclear Data Section. The FENDL-1 data file is the recommended reference library for design calculations in the Engineering and Development Activity (EDA) phase of the ITER project. For use in Monte Carlo (MCNP-code) and discrete ordinates (e. g. ONEDANT/TWODANT, ANISN/DOT) transport calculations, FENDL-1 working libraries have been processed by R .E. MacFarlane, Los Alamos National Laboratory, using the NJOY code system.

Prior to their use in design calculations there is a need to validate the FENDL-1 working libraries through integral data tests. An international FENDL benchmark validation task was launched for that purpose with the main objective to perform data tests on a short term time scale for attesting the quality and completeness of the FENDL-1 working libraries for fusion applications. In addition to that, the results of the data testing were assumed to contribute to the further improvement of FENDL data and thereby give guidance to the development of the FENDL-2 data file.

Several laboratories and institutions from the European Union, Japan, the Russian Federation and the United States have contributed to the benchmark task, organised by FZK. A large variety of existing integral 14 MeV benchmark experiments was analysed with the FENDL-1 working libraries, i. e. the FENDL/MC-1.0 (Monte Carlo) and the FENDL/MG-1.0 (multigroup) data library covering the majority of the fusion-relevant materials (see Table 1).

Results of the benchmark analyses have been collected over one year mainly through the computer network. In an IAEA consultants' meeting, the contributed benchmark results have been extensively discussed and evaluated [3]. The benchmark experiments, analyses, as well as detailed results and recommendations are documented in a comprehensive final report on the FENDL benchmark task [4]. The major findings and conclusions of the benchmark task are summarised as follows.

(1) Neutron multiplication and breeding materials

The neutron multiplication power can be well predicted for both neutron multiplier candidates, beryllium and lead. In addition, the neutron spectra in lead assemblies can be calculated very satisfactorily. This does not hold for beryllium: there is a need for a revision of the secondary energy-angle distributions and, possibly, the (n,2n) cross-section.

The data quality of the breeding material lithium look rather satisfactory. The measured angular neutron spectra for Li$_2$O. e. g. can be well reproduced.

For the breeding material constituents aluminium, silicon and zirconium there is a clear need for an improvement of the neutron emission cross-section data: the measured leakage spectra cannot be reproduced satisfactorily with FENDL-1 data. In addition, obvious deficiencies are detected in the secondary energy distributions of the (n,xn)-reactions. Thus there is a strong need for an updating of the Al, Si and Zr evaluations.

(2) Structural and/or shielding materials

For the most important structural material iron there is an underestimation of the measured neutron spectra below $\approx$ 1.5 MeV which especially affects the calculations of the shielding efficiency. This discrepancy may be resolved with the inclusion of the fine resonance structure in the total and partial iron cross-section data above 0.8 MeV, as it is accounted for e. g. in the current EFF-3 iron evaluation.

No evidence for urgent data improvements can be deduced from the available benchmark results for chromium and manganese, whereas the results for copper suggest a revision of the emission cross-section data both in the high energy (5-10 MeV) and low energy (E < 0.1 MeV) range. For nickel there is a need for better experimental integral data.

The results from the available benchmark experiments for the shielding material tungsten indicate the need for a data revision, although the discrepancies found in the calculated neutron spectra are not too serious.In the analysis of the SS-316 bulk shield experiments, an increasing trend of underestimating the high energy tail (E > 10 MeV) of the neutron spectrum was observed at deep locations inside the

steel blocks. This may lead to serious underestimations in calculating radiation damages to the superconducting coils in fusion devices like ITER. In addition, there are indications that low energy spectra (E<0.1 MeV) are underestimated in the SS-316 experiments.

(3) Other materials

For most of these materials the results from the available benchmark experiments indicate the need for further improvements of their cross-section data. Especially this holds for titanium, cobalt, fluorine, oxygen, nitrogen, and graphite.

For niobium and molybdenum the deviations between measured and calculated neutron spectra are less serious.

(4) Gamma-ray spectra and heating rates

There is an overall good agreement between experiments and the FENDL-1 calculations for the materials LiF, CF_2, Al, Si, Ti, Cu, Mo, W, and Pb for the gamma heating rates. The agreement for Cr, Mn, Co and Nb is not satisfactory. This holds likewise for the gamma-ray spectra. In addition, a serious underestimation of the high energy gamma spectrum (E>5 MeV) is observed for lead.

Table 1: Integral experiments and analyses contributed to the FENDL-1 benchmark validation task

Type of Integral Experiment	Material Configuration	Material	Experiment	Benchmark analysis
TOF-measurements of angular leakage spectra	Cylindrical slabs	Li_2O, Be, C, O, N, Fe, Pb	FNS/JAERI	FNS/JAERI
In-system measurements of neutron spectra & reaction rates	Cylindrical slabs	Li_2O, Be, C, Fe, Cu, W	FNS/JAERI	FNS/JAERI, Hitachi Ltd., KIAE Moscow
TOF-measurements of neutron leakage spectra	Spherical shells	Be, Be-Li, Li, Li_2O, LiF, C, CF_2, Al, Si, Ti, Cr, Mn, Co, Ni, Cu, Zr, Nb, Mo, W	Universities of Osaka & Kyoto	Universities of Osaka & Kyoto, FZK Karlsruhe, IPPE Obninsk, KIAE Moscow
TOF-measurements of gamma ray leakage spectra	Spherical shells	LiF, CF_2, Al, Si, Ti, Cr, Mn, Co, Cu, Nb, Mo, W, Pb	Universities of Osaka & Kyoto	FNS/JAERI
Bulk shield experiment	Cylindrical block	SS-316	FNS/JAERI	FNS/JAERI, UCLA
Bulk shield and streaming experiment	Rectangular block, with and without duct	SS-316	ORNL	RSIC/ORNL
Bulk shield and nuclear heating experiment	Rectangular block	SS-316, SS-316 and perspex	ENEA Frascati	ENEA Frascati
TOF-measurements of neutron leakage spectra	Spherical shells	Be, Al, Fe, Pb-17Li	IPPE Obninsk	IPPE Obninsk, KIAE Moscow, FZK Karlsruhe
TOF-measurements of neutron leakage spectra	Spherical shells	Be	FZK Karlsruhe	FZK Karlsruhe, Hitachi Ltd.
TOF-measurements of neutron and photon leakage spectra	Rectangular slab, with and without straight gap	Fe	TUD Dresden	TUD Dresden, FZK Karlsruhe
Multiplication experiment	Spherical shells	Be	KIAE Moscow	KIAE Moscow
Mock-up shield experiment	Rectangular slab, with and without straight gap	Fe	MePhI-KIAE Moscow	KIAE Moscow

The measured gamma heating rates for iron, copper and SS-316 can be reproduced satisfactorily, although there is a trend for underestimating them in the analysed benchmark experiments.

With regard to the data quality, it can be summarised that fusion nuclear data have reached a high confidence level with the available FENDL-1 data library. With few exceptions this holds for the materials of highest importance for fusion reactor applications. As a result of the performed benchmark analyses, some existing deficiencies and discrepancies have been identified that have to be removed in the forthcoming FENDL-2 data file.

In addition to that, the performed benchmark analyses allow a direct comparison of the quality of the two different computational approaches and working data libraries used: the Monte Carlo technique with FENDL/MC-1.0 data (MCNP-code) and the discrete ordinates procedure with FENDL/MG-1.0 multigroup data (e. g. ONEDANT/TWODANT -code). In general, the two approaches give the same results, as has been shown both for analyses of spherical shell and slab experiments. There are, however, two exceptions to this rule encountered in the course of the benchmark analyses: (i) transport problems involving neutron thermalisation cannot be properly accounted for in discrete ordinates calculations with multigroup data in the VITAMIN-J group structure and (ii) deep penetration problems can be better described by Monte Carlo calculations with continuously represented cross-section data than by discrete ordinates calculations with multigroup data.

It is to be summarised, that the Monte Carlo technique with continuously represented cross-section data allows to handle the encountered fusion neutronics problems with confidence while discrete ordinates calculations do not. Consequently, care has to be taken in applying the FENDL/MG-1.0 library to fusion neutronics problems where it may not be appropriate.

Staff:

U. Fischer
F. H. Fröhner
H. Tsige-Tamirat
E. Wiegner

Literature:

[1] F. H. Fröhner, Proc. Internat. Conf. Nucl. Data for Science and Technology, Gatlinburg 1994, Vol. 2, p. 597.

[2] F. H. Fröhner, Progress Report NEA/NSC/DOC(95)10, 1995, p. 7.

[3] IAEA Consultants' Meeting on ‚Benchmark Validation of FENDL-1", Forschungszentrum Karlsruhe, Germany, October 17-19, 1995.

[4] U. Fischer (Ed.), Integral Data Tests of the FENDL-1 Nuclear Data Library for Fusion Applications, Summary Report of the International Working Group on ‚Experimental and Calculational Benchmarks on Fusion Neutronics for FENDL Validation", Draft, October 1995, to appear as IAEA/NDS-report.

NDB 2-2   Neutronics Data Base -
Shield Penetration Experiments

1.   Benchmarks of SS-316 Nuclear Data

Nuclear shield parameters of fusion reactors such as ITER are determined by the neutron and photon fluxes within and behind the shield. In the development of shield blankets the test of the calculational tools of the neutronics, i.e. nuclear data and codes, has been identified as an important issue [1,2]. The structural material of the shield blanket is stainless steel SS-316 with iron as the main element.

In the previous phase A of benchmark experiments the spectral fluxes of neutrons and photons from an iron slab irradiated with 14 MeV neutrons were investigated [3].

Now, in Phase B angular fluxes from a SS-316 slab were studied. Three different directions of the slab were chosen with respect to high sensitivity to secondary particle angular distributions. Because ducts and gaps in the blanket enhance the radiation load on the parts behind, the same assemblies but with a gap were investigated, too.

The geometry of Phase B is shown in Fig. 1. The collimator was constructed such that only those neutrons and photons could be observed by the detector which leak from the central part (diameter 12 cm) of the SS-316 assembly. Additionally, the neutron source was positioned in such a way that no directly transmitted but only scattered neutrons move in detector

direction. The slab itself had the same dimensions as in Phase A (100 x 100 x 30 cm³). A vertical 5 cm wide gap was arranged in the centre of the slab.

With a NE213 scintillator the spectral neutron flux in the range E > 1 MeV, the spectral photon flux in the range E = 0.4 MeV, and the neutron time-of-arrival spectrum were measured simultaneously. For the low-energy range of the neutron spectrum (70 keV < En < 2.5 MeV) a second spectrometer system with a stilbene scintillation detector and hydrogen-filled proportional counters was employed.

Calculations were performed with the 3-dimensional Monte-Carlo-code MCNP [4], version 3B, taking into account all details of the experimental arrangement. The data base is EFF-1, the European Fusion File version 1 [5].

The presentation of all spectral distributions would exceed the frame of this report. As an selected but typical example results are shown in Figs. 2 and 3 for geometry B20. All neutron spectra show a surplus of measured neutrons as compared to the calculation for energies of about 3 MeV ... 13 MeV, and (in resemblant manner) in the independently determined Фn(t) for t > 80 ns up to about t = 200 ns. The results confirm similar discrepancies already stated in phase A [6]. Reasons can be found in conjunction with the neutron emission cross section Onm , the angular distribution of which is assumed to be isotropic in EFF-1 (with the exception of elastically scattered neutrons) [7]. But, precompound processes result in forward peaked inelastically scattered

B11: α = +24,3°, gap width 5 cm

B10: α = +24,3°, without gap

B21: α = 0°, gap width 5 cm

B20: α = 0°, without gap

B31: α = -24,3°, gap width 5 cm

B30: α = -24,3°, without gap

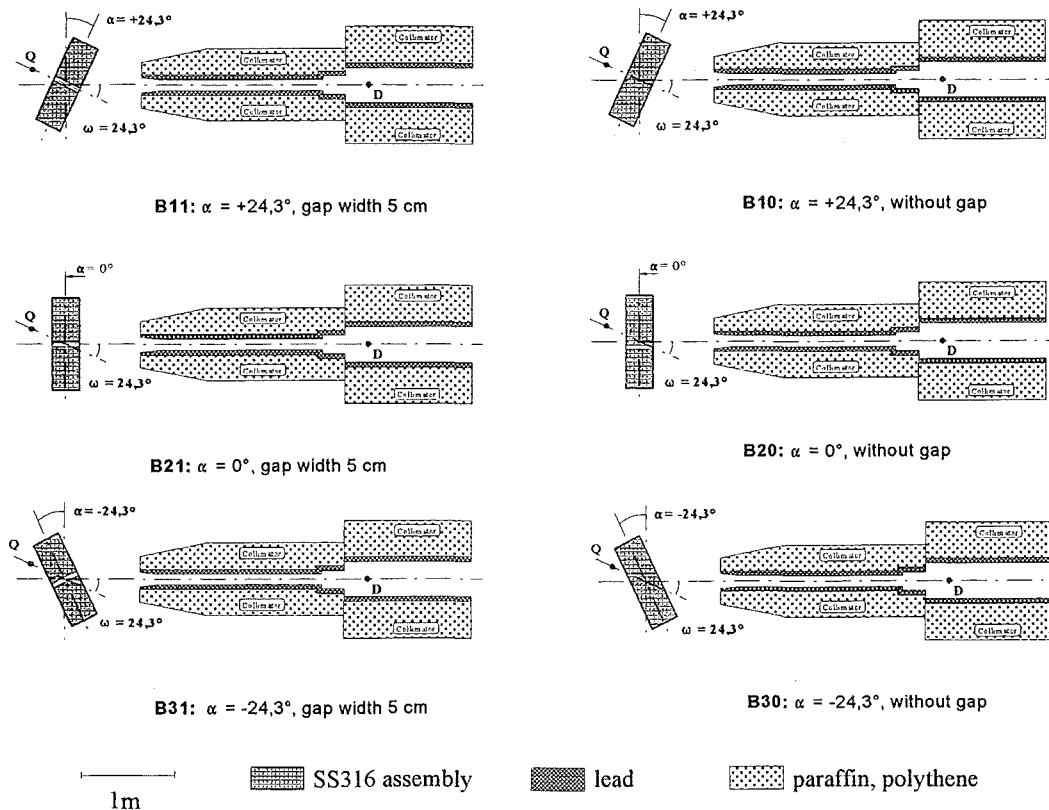1m   ▦ SS316 assembly   ▨ lead   ▒ paraffin, polythene

Fig. 1:   Geometries of the SS-316 experiment (Q: 14 MeV neutron source, D: detector)
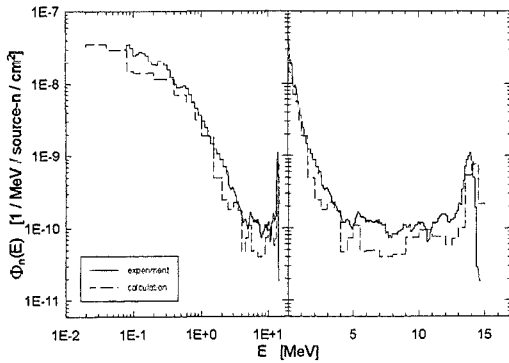
Fig. 2: Spectral neutron fluence for geometry B20 (logarithmic and linear energy axes)
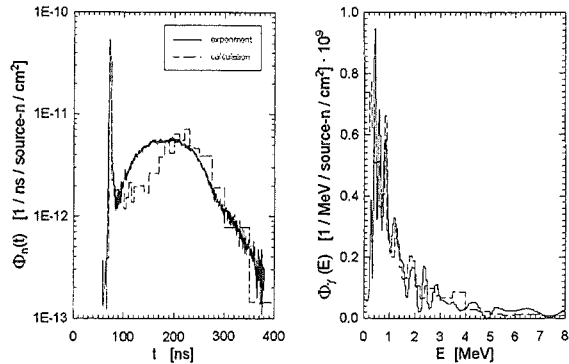
Fig. 4: Influence of the gap on the experimental spectral neutron fluences, goemetries B10 and B11 (logarithmic and linear energy axes)
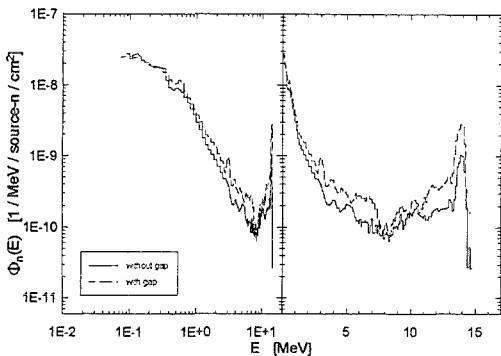
Fig. 3: Neutron time-of-arrival fluence and spectral photon fluence for geometry B20
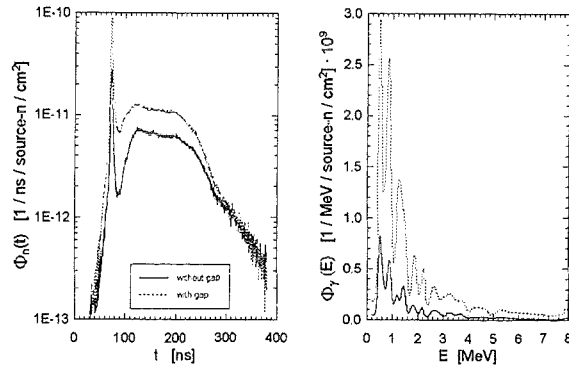
Fig. 5: Influence of the gap on the neutron time-of-arrival fluences and spectral photon fluences (experiments), geometries B10 and B11

neutrons for E from about 5 MeV up to the incidence energy. Also the total photon fluence is underestimated because of this discrepancy in the neutron transport.

A remarkable neutron excess was measured in the energy range E < 0.2 MeV, too.

A gap has considerable influence on both, the neutron and the photon fluence penetrating and leaking the slab assembly (see Figs. 4 and 5 for the measured spectral fluences selected for geometries B10 and B11 as a typical example). Whereas the low-energy part of the neutron spectra is only weakly influenced by the gap, at energies with forward-peaked neutron emissions a remarkable streaming is observed.

2. EFF-2 and FENDL-1 calculations

The second version of the European Fusion File EFF-2 [8] contains files with double differential cross sections (energy and angle), and most of the discrepancies observed with EFF-1 data are expected to be eliminated. With the availability of EFF-2 files processed for Monte Carlo calculations [9] and with the code version MCNP-4A [10] the calculations were repeated. Also the data library for the ITER design FENDL-1

[11] describes the inelastic scattering angular dependent and was used in MCNP-4A calculations, too.

For four of the assemblies, experimentally investigated in the frame of subtask NDB2-2, calculations with EFF-2 and with FENDL-1 data were carried out [12]. Fig. 6 and Table 1 show the results for the solid Fe slab.

Significant improvements are achieved compared to EFF-1 data in the spectral neutron flux between E = 3 MeV and 14 MeV, as well as in the corresponding time-of-arrival intervall t = 80 ns to 200 ns. As expected, also the total photon flux is sensitive to the neutron angular distributions, and its description is improved with EFF-2 and with FENDL-1 data.

Remaining differences almost disappear in a wide range for the Fe slab benchmark with the new evaluation EFF-3 as demonstrated by Hogenbirk et al. [13].

--47--

Literature:

[1] W. Daenner, ITER Expert Meeting on Shielding Experiments and Analysis, Garching (FRG), Febr. 12-14, 1990, ITER-IL-5-0-5, 1990

[2] A. Santamarina and T. Parish, Sensitivity and Uncertainty Analysis of the NET Magnet Neutronic Design Parameters to Uncertainties in Cross Section Data, CEA 917/333, 1991

[3] H. Freiesleben, W. Hansen, D. Richter, K. Seidel, S. Unholzer, Nuclear Fusion Project, Annual Report of the Association Forschungszentrum Karlsruhe/EURATOM,

Oct. 93 - Sept. 94, FZKA 5515, EUR 16100 EN, p. 40, Jan. 1995

[4] J. F. Briesmeister, MCNP - A General Monte Carlo Code for Neutron and Photon Transport, LA-7396, Los Alamos N. L., 1986

[5] H. Gruppelaar, Processing of the EFF-1 and EFF-2 Data Files, EFF-DOC-46

[6] W. Hansen, D. Richter, K. Seidel, S. Unholzer, Test of Neutron and Photon Data in an Iron Benchmark Experiment with 14 MeV Neutrons, Proc. Int. Conf. on Nucl. Data for Science and Technol., Vol. 2, p. 913, Gatlinburg (USA), 1994
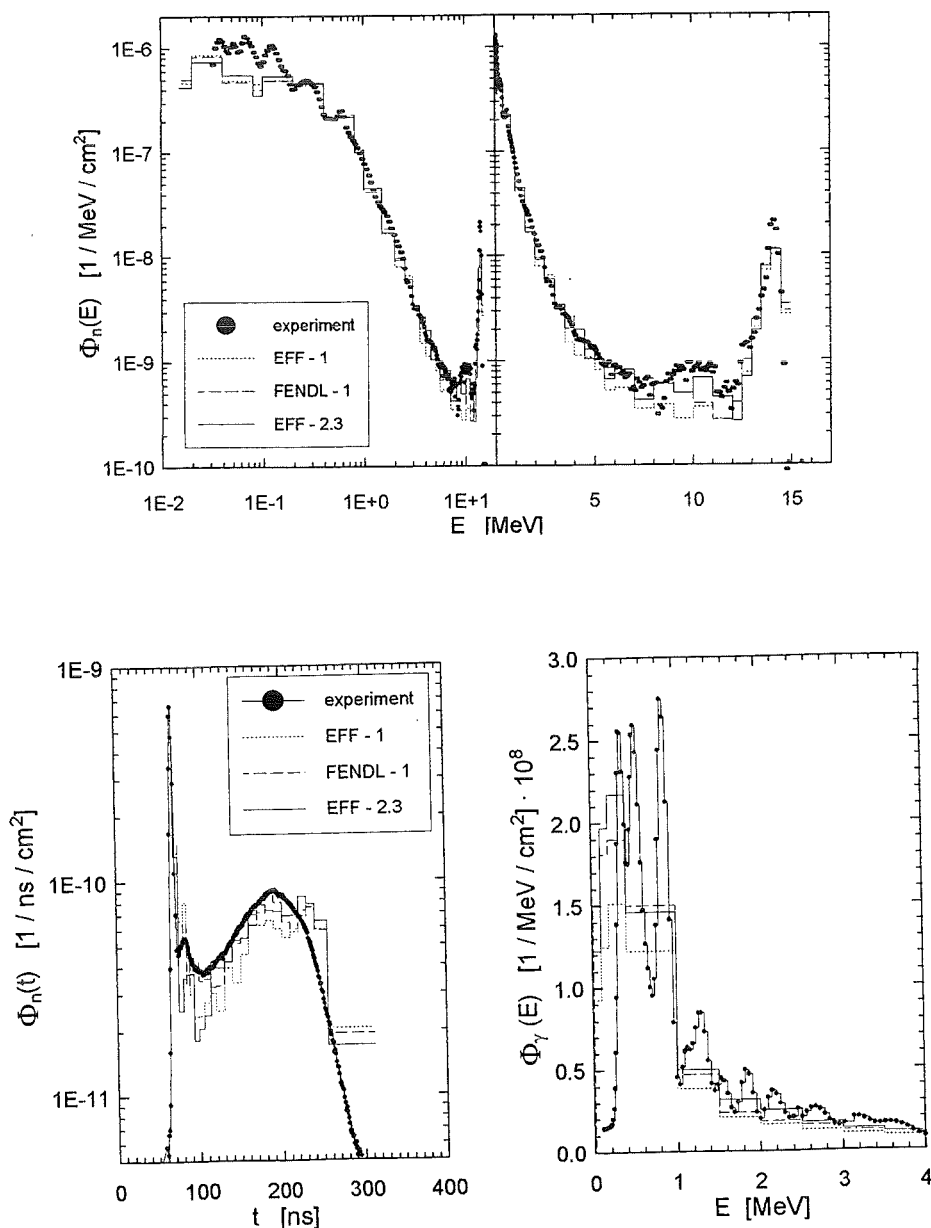
Fig. 6: Spectral neutron and photon fluences per one source neutron measured from the solid Fe slab and compared to calculations with library data from EFF-1, FENDL-1 and EFF-2

Table 1: Comparison of calculated to experimental neutron and photon fluences per one source neutron in energy and time-of-arrival intervalls, respectively, from the solid Fe slab

| Range | | Calculation / Experiment | | |
E / MeV and t / ns, respectively		EFF-1	EFF-2	FENDL-1
E_n	0.04 - 1.0	0.86 ± 0.10	0.89 ± 0.10	0.88 ± 0.10
	1.0 - 5.0	0.90 ± 0.04	0.95 ± 0.04	0.94 ± 0.03
	5.0 - 10.0	0.65 ± 0.04	0.92 ± 0.08	1.00 ± 0.07
	10.0 - 15.0	0.77 ± 0.03	0.87 ± 0.03	0.87 ± 0.04
t_n	0 - 80.6	0.82 ± 0.03	0.83 ± 0.03	0.84 ± 0.03
	80.6 - 200.	0.75 ± 0.06	0.85 ± 0.07	0.90 ± 0.07
E_γ	0.2 - 8.0	0.62 ± 0.02	0.82 ± 0.02	0.76 ± 0.02

[7]   H. Freiesleben, W. Hansen, D. Richter, K. Seidel, S. Unholzer, Shield Penetration Experiments, Final Report to Subtask NDB2-2 of the European Fusion Technology Programme, TUD-IKTP/95-1, Dresden, 1995

[8]   J. Kopecky, H. Gruppelaar, Status of the European Fusion File (Revision EFF-2.3), EFF-DOC-203, 1993

[9]   L. Petrizzi, Processing EFF-2.3 with ACER and NJOY to Produce an MCNP Working Library, EFF-DOC-369, 1995

[10]   J.-F. Briesmeister (ed.), MCNP - A General Monte Carlo N-Particle Transport Code, Version 4A, LA-12625-M, Los Alamos N. L., 1993

[11]   S. Ganesan, P. K. McLaughlin, FENDL/E - Evaluated Nuclear Data Library of Neutron Interaction Cross-Sections, Photon Production Cross-Sections and Photon-Atom Interaction Cross-Sections for Fusion Applications, Version 1.0, IAEA-NDS-129, Vienna, 1994

[12]   H. Freiesleben, W. Hansen, D. Richter, K. Seidel, S. Unholzer, TUD Fe-Slab and SS316-Slab Experiment Compared with EFF-2 Calculations, EFF-DOC-388, 1995

[13]   A. Hogenbirk, A. J. Koning, H. Gruppelaar, Validation of the EFF-3.0 Evaluation of 56Fe, EFF-DOC-382, 1995

Staff:

H. Freiesleben
W. Hansen
D. Richter
K. Seidel
S. Unholzer

Remote Handling / Maintenance

Introduction:

Due to the activation of most components of a fusion reactor, all operations of inspection, maintenance, connection and disconnection, assembly and disassembly will have to be carried out remotely from the very start of the machine. Hands-on or semi-remote maintenance will be possible only in limited areas and for some peripheral components.

The maintenance of the in-vessel components has been identified as a key problem. The equipment for in-vessel maintenance will have to operate under extreme conditions of radiation and temperature. The large variety of operations to be carried out requires versatile and replaceable tools attached to different work units with large lifting capabilities. The high availability targeted for the next machine will require that in-vessel operations have to be carried out with relatively high speed.

In the last years most of the FZK work concentrated on the development and qualification of an in-vessel handling unit (IVHU) with an articulated boom transporter (ABT) and different work units (task RHT 1). This system is primarily needed for the maintenance or replacement of in-vessel components during short term interventions.

The Experimental Device for In-Torus Handling EDITH is the prototype of this system. It was required to demonstrate that the maintenance of plasma facing components can be carried out with the anticipated reliability and time.
EDITH is a full scale ABT, supplemented by a full scale mock-up simulating the upper half of a torus sector. The hardening of sensitive IVHU components like motors and resolvers for ITER typical temperature and radiation levels has been performed in close cooperation with SCK/CEN Mol within EC Task T35.

Task RHT 1 includes also the further development of a remote handling workstation (RHWS) which can be applied to different remote handling tasks for fusion plant maintenance (former task RHB 1).

Task RHT 1 will be finished by the end of 1995.

Task T 43 (Remote Pipe Cutting and Welding) concentrated on the development of cutting, welding and weld inspection tools for concentric cryogenic lines.

This task has been finished.

A. Fiege

RHT 1   Articulated Boom Transporter

Subtask 2: EDITH Prototype Articulated Boom

The objective of this subtask is the development and qualification of the articulated boom system prototype EDITH, in particular:

- Development and basic investigations of the boom concerning static and dynamic behaviour, manoeuvrability and controllability, position accuracy, and repeatability of motion.

- Demonstration of reliable remote handling procedure execution by means of a flexible guidance and control system

- Demonstration of the suitability to carry out delicate tasks (e.g. armour tiles replacement or Be-spray)

- Demonstration of the capability to handle loads up to 1 t (e.g. divertor plates, bumper limiters)

Mechanics of the ABS

The articulated boom system (ABS, Fig. 1) consists of the articulated boom transporter (ABT) including the end-effector positioning unit (EEPU), the manipulator handling unit (MHU) for performance of delicate tasks like armour tile replacement, tools for tile replacement, and a divertor plate mock-up fork for carrying the load. The working environment includes the torus sector mock-up with an array of tiles and a divertor plate mock-up. The ABT consists of four links which are attached via a cantilever arm to the support structure. At the front link the end-effector positioning unit (EEPU) is mounted which again can be equipped with different end-effectors like the manipulator handling unit (MHU) as a multi-purpose unit or a divertor handling unit. For the tile replacement the MHU is applied. As an interim end-effector it combines two different electric master/slave manipulators which were available at FZK. The manipulators are connected by means of an adaptation unit which compensates their different geometry and provides an additional roll joint. Between the EEPU and the adaptation unit the manipulator positioning unit is installed which has an additional yaw joint; thus allowing to work with the manipulators radially to the torus. Two overview cameras equipped with pan-and-tilt heads, two operation cameras mounted at camera arms are part of the viewing system, and four lamps. Instead of a divertor handling unit which could not be developed during the task a simple divertor fork is available as an ad-hoc solution for performance of heavy load transporting and positioning. A magazine rack provides a divertor deposit. The spatial arrangement of the EDITH test field is shown schematically in Fig. 2 and in the photos in Fig. 3 and Fig. 4 [1,2,3].

Guidance and Control System

To support the operator in remote task performance a guidance and control system was developed and installed in the EDITH control room providing two working places, one for co-ordination and assistance tasks and the other for manual work with servo-manipulators. The overall architecture is shown in Fig. 5, the main components are a remote handling workstation providing operational support and the hierarchically organized control system.
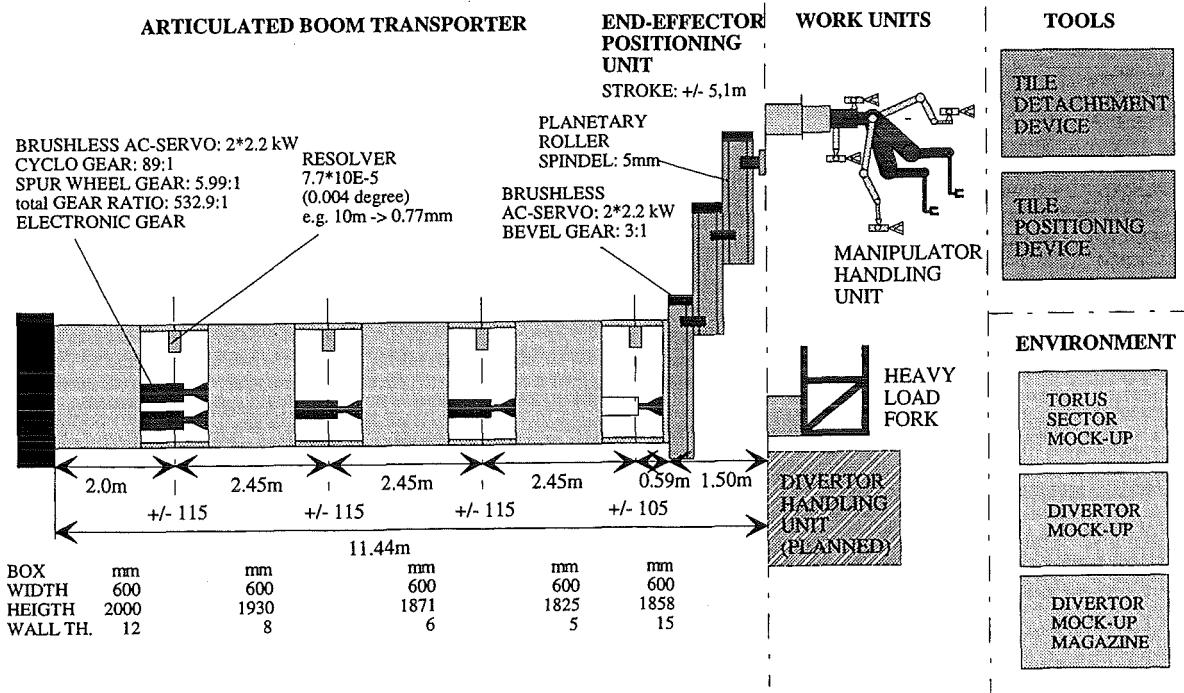

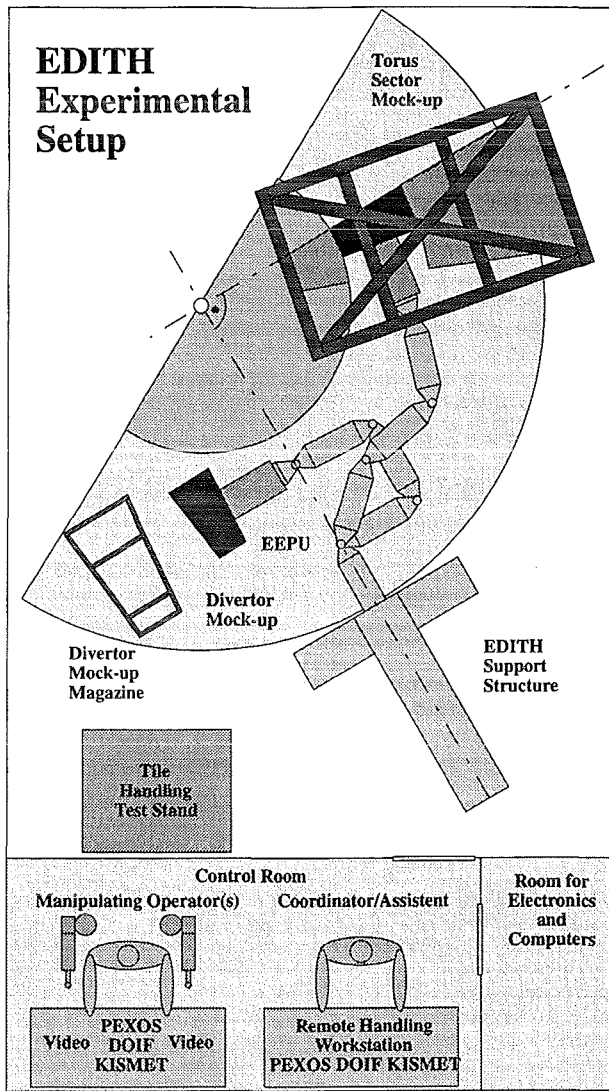Fig. 1: EDITH articulated boom system

EDITH
Experimental
Setup

Torus
Sector
Mock-up

EEPU

Divertor
Mock-up

Divertor
Mock-up
Magazine

EDITH
Support
Structure

Tile
Handling
Test Stand

Control Room

Manipulating Operator(s)   Coordinator/Assistent

Room for
Electronics
and
Computers

PEXOS
Video DOIF Video
KISMET

Remote Handling
Workstation
PEXOS DOIF KISMET

Fig. 2:   EDITH test field

Fig. 3:   EDITH ABT with divertor, torus mock-up, magazine

The guidance system is represented by a **remote handling workstation** (RHWS) [4,5,6], standard TV monitors, and the master systems of two master-slave manipulators. The RHWS provides the non-conventional man-machine interface and operational support during planning, training, and execution of procedures. The analysis of maintenance procedures showed that three types of maintenance task abstractions are sufficient and convenient for a comprehensive operational support: the representation and simulation of the procedures (handbook information), the representation of the working space geometry including motion paths, and the representation of the device functions. Therefore, the RHWS consists of three subsystems according to those three aspects: PEXOS (Procedure Editing, Simulation, Execution, and Monitoring System), KISMET (Kinematic Simulator, Monitor, and Programming Environment for Telemanipulation), and DOIF (Device Operating Interface). The RHWS was developed in the former task RHB1. According to experiences in the tile exchange experiment some additional developments were done: (1) the PHbutton module provides access to the PEXOS documentation via mouse-sensitive photos and drawings, (2) the DOIF-MSM intergrates the control of the FZK universal master-slave control system MONSUN [7] into the workstation, (3) the pedal system PEDSY provides DOIF

control by foot, allowing the operator to control, for example, a camera while using a master-slave manipulator, and (4) integration of the re-designed DOIF subsystem.

In the context of remote handling procedure development at JET a FZK delegate applied KISMET to the experiments. For the new ‚Short Boom" the models were developed and the communication link to the control system thus providing a virtual device for control system testing. Calibration curves of the boom resolver system based on theodolite measurements were applied to the KISMET system resulting in a drastic enhancement of modelling accuracy of the KISMET monitoring. The camera control DOIF VIEW and the camera control network have been enhanced.

The **control system** is hierarchically organised and consists of a management system (program and parameter management, teach/repeat functions, safety functions), the path control for EDITH, and the camera system control. Main research topic in this area was the fast, precise, and safe motion of the transport arm.

Previous measurements showed, that the EDITH manipulator system operates with an repetition accuracy below 5 mm. Taking account of single joint *positioning accuracy*, theoretical considerations showed, that there might be a repetition accuracy of 8 mm possible in the worst case. To evaluate the absolute positioning accuracy of the complete EDITH system several measurements have been performed.
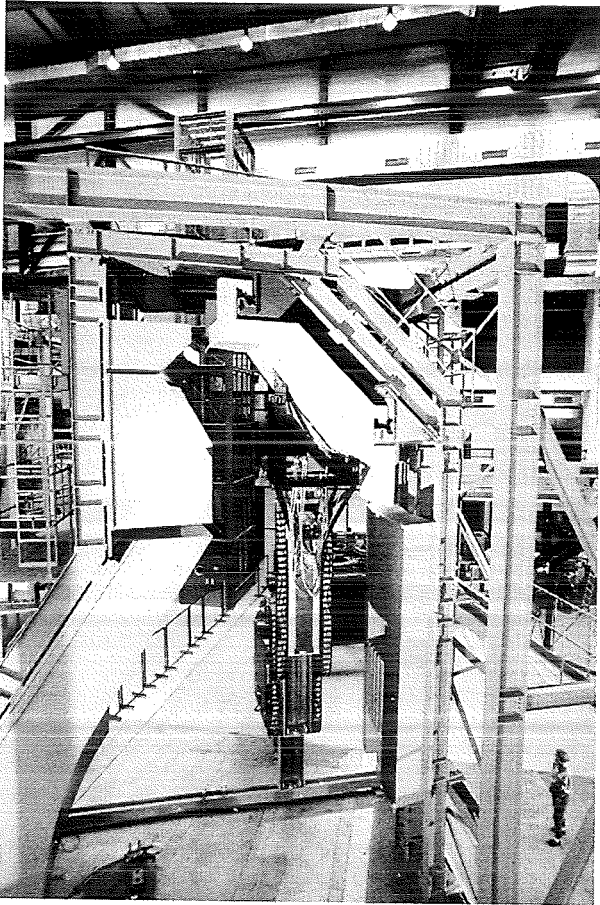
Fig. 4:   EDITH EEPU, fork, divertor, torus, mock-up

Fig. 5:   Guidance and control system architecture

The joint positions were measured and simultaneously the

Fig. 6:   Remote Handling Workstation

resolver values of the joint resolvers were registrated. Figure 7 shows the resulting calibration curve. The difference

Fig. 7:   Differences between external measured angles and resolver values

amounts up to 0.008 rad. This amounts to values, which are much higher than the accuracy of the resolver itself. According to the resolver manual the absolute accuracy of the resolver system should amount to 0.003 rad without the gear. If the resolvers gear is taken into consideration, this value will be reduced by a factor of 20 to 0.00015 rad. In addition to the joint resolvers there have been measurements to identify the the *absolute positioning accuracy* of the tool center point TCP. Tab. 1 shows the cartesian deviation of the TCP position separated to the three cartesian cordinates (dx, dy, dz). The 5th column (dpos) shows the absolute distance to the target point. The first three points TCP1 to TCP3 are measured with a theodolite system, also registrating the joint positions. That is the reason why the deflections dx,dy,dz are more precise. The other values were measured relative to known points. The accuracy of that measurement is estimated to be 5 mm. As a final conclusion there can be fixed, that the absolute positioning accuracy amounts to 75 mm (requested goal: 100 mm).

While the absolute positioning accuracy is valid in steady state, the *dynamic accuracy* was tested in other experiments. The ABT was commanded to move a rectangular path. This move has been executed several times in 2 ways: (1) the ABT

Table 1:   Absolut positioning accuracy

Point	dx	dy	dz	dpos
TCP1	-42.0	16.0	31.5	54.88
TCP2	16.5	13.1	31.5	28.57
TCP3	1.9	-3.6	22.6	22.96
124s	45.0	-50.0	30.0	73.65
123s	-40.0	-10.0	60.0	72.8
57s	20.0	-10.0	20.0	30.0
56s	-25.0	15.0	5.0	29.58
21s	50.0	40.0	0.0	64.03
4	0.0	70.0	0.0	70.0

moved around the rectangle with a stop at each corner, (2) the ABT moved around the rectangle without a stop at any corner. The cartesian velocity had been chosen to be 20 mm/s. There was no payload mounted at the flange.

In both cases the difference between ideal path and the real path was less 20 mm. The repetition accuracy of such a path has been shown to be within 1 mm. That was a surprise, because the repetition accuracy was shown to be nearly 5 mm.

For *demonstrating handling of heavy loads* the joint velocities had been reduced to a third of the maximum value (0.05 rad/s instead of 0.15 rad/s). Bigger movements (transport operations) had been executed as joint position moves. Cartesian moves, however, were used in situations, when there was the need of pre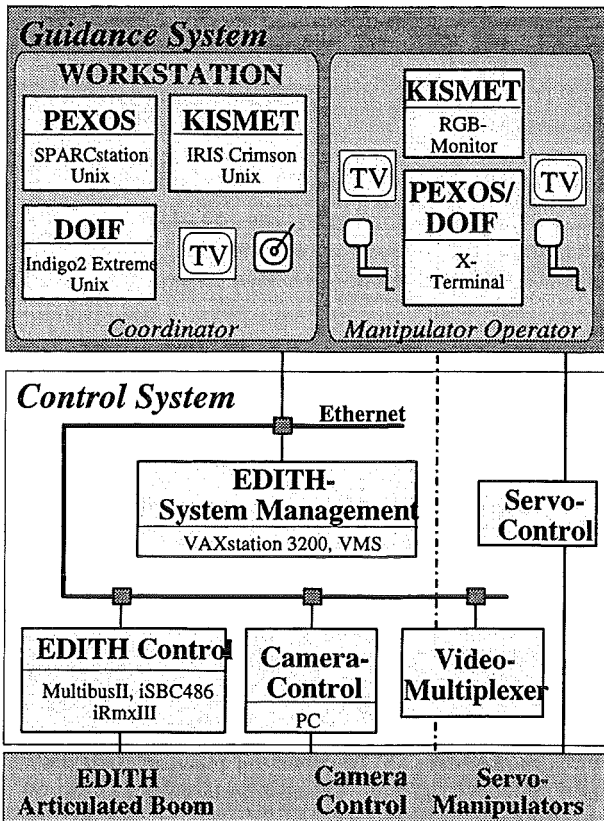cise movements. This was necessary in the upper part of the mockup, when the load was attached or detached. In this area, the distance to the walls was about 20 mm. Those linear moves were performed at a velocity of 20 mm/s (translation) 0.02 rad/s (rotation) and accelerations (decelerations) of 1 mm/s2, 0.005 rad/s2. As a result there can be fixed: The EDITH system is able to transport heavy loads quite well down to a commanded motion step of 5 mm, which is a very good result for controlling a boom type transporter of these dimensions.

Three different *control structures* have been investigated. The first one was designed to damp the first Eigen frequency. The second one was a state space controller with a rise time of about 2 seconds. The third one was a controller, which was based on a reference model with nonlinear decoupling of the axis with a inverse dynamic model. Especially the second one showed a big dependancy on axis configuration and system

parameters like inertia and friction. The other two controllers were quite robust. While the first controller type is slightly dependent on axis configuration, the model based controller promises a good, well defined system behaviour, which is independent of axis configuration and not sensitive in case of changing parameters. Reality however showed, that it is not easy to bring such a controller to a sufficient operation. The first controller, however, works in nearly every situation sufficiently.

The **validation of the dynamic model** that is used in the simulation has to be performed by comparing simulation results with the data measured during the dynamic qualification tests. For comparing simulation results with measured data, the simulation model needs to represent the actual experimental configuration as close as possible. Therefore, the dynamic model has been re-arranged to the combined model of ABT and EEPU; the proper validation task is underway.

Subtask 3:   Divertor Plate and Armour Tile Handling

Objective of this subtask is the design, manufacture and commissioning of armour tiles and divertor plates handling equipment. The equipment has to be tested, followed by the demonstration of the tile replacement in the mock-up. Divertor plate exchange was reduced to demonstration of transporting and positioning heavy loads

Armour tile handling

For completion of last year's work [8] minor enhancements concerning armour tile intermediate storage were done.

Divertor plate handling

Topic of the last year was the heavy load transportation and positioning experiment. This experiment replaced the planned divertor handling experiment because the DHU was not available. Therefore, the boom was equipped with a simple load fork for getting over the divertor dummy. Because the fork, in contrast to the DHU, has no extra DoF, the transporter had to be used also for fine positioning and fine motion control near the divertor position: This was not a design goal, but a test for the abilities of the motion control.

The preparation of the heavy load handling experiment required the following modifications and changes: (1) replacement of the MHU by the load fork, (2) equipment of the torus mock-up with a divertor mock-up, (3) provision of a divertor magazine.

During the planning and preparation phase of the heavy load handling task the whole procedure was planned and modelled by PEXOS and KISMET. Furthermore the EDITH transportation pathes were taught-in. Video sequences, textual descriptions, photos, and drawings of all relevant working steps were produced and integrated. At the end of these preparation not only a complete multimedia documentation was available but also an executable high-

level program integrating all agents of the task including the operators. Fig. 8 shows schematically the test arrangement

Fig. 8: Divertor exchange procedure with intermediate work procedure states

including the motion paths and intermediate transportation states. The PEXOS task vizualisation is shown in fig. 9: it features the high-level task description by actions and states and their inter-relationships.

The complete divertor mock-up exchange is controlled via the RHWS. PEXOS guides the operator in performing the task by visualization of the tasking states and providing advices enhanced by multimedial information. After each subtask the operator has to start the next step via PEXOS. For spatial monitoring (motion monitoring) KISMET is used, for supervision of forking the divertor, in addition, four fork cameras looking along the prongs are available. Supervision of the EDITH control system functions is done via the EDITH DOIF visualizing EDITH control states and **parameters.**

Results of the heavy loads experiment

The experiment demonstrated that the EDITH articulated boom transporter fulfills the given requirements, that means it can transport heavy loads up to 1 t precise and safe between requested positions in the torus.

The complete procedure was successfully planned, co-ordinated, and controlled via the remote handling workstation. The RHWS also provides a comprehensive documentation of the procedure including texts, operator remarks, drawings, photos, video sequences, graphical animations, and procedure step related device control commands for the transporter, the DOIF system, and KISMET. This documentation guarantees a repetition of the procedure with the same quality. With the developed RHWS a general purpose (generic) software tool is available for supporting

Fig. 9: PEXOS screen visualizing the work procedure by a network of actions and states and additional action/state related information

the operator to perform complex maintenance procedures of any kind.

Subtask 4: Manipulator Positioning Unit

Due to the fact that this task is suspended by NET there are no FZK activities in this field.

Subtask 5: Pre- and Post Irradiation Testing of Boom Components

The results of the experiments were documented. Radiation hard motors, resolvers, and cables were made available fulfilling the NET/ITER requirements [9,10,11,12].

Literature:

[1] Suppan, A. et al.: The NET Articulated Boom: Preliminary Investigations and Justification for a Full Scale Prototype. KfK 4809, December 1990.

[2] Suppan, A. et al.: EDITH - A Prototypical Articulated Boom System for NET/ITER. In: Ferro, Gasparotti, Knoepfel: Fusion Technology 1992, Proceedings of the 17th Symposium on Fusion Technology, Rome, 14-18 September 1992, Vol. 2, p. 1599-1603.

[3] Suppan, A. et al.: Experimental Device for In-Torus Handling - EDITH Intermediate Report. KfK 5252, October 1993.

[4] Leinemann, K.: NET Remote Workstation, KfK-Bericht 4785, KfK, Karlsruhe, Oct. 1990.

[5] Leinemann, K., Katz, F., Knüppel, H., Olbrich, W.: Synthetic Viewing: Comprehensive Work Representation Making Remote Work More Transparent to the Operator. Fusion Engineering and Design 29(1995) 317-323

[6] Leinemann, K., Katz, F., Olbrich, W.: PEXOS - Procedural Operator Support and Coordinating Component of a Remote Handling Workstation. Unpublished Internal Report, March 1995.

[7] Breitwieser, H., Weber, W.: MONSUN a Distributed Manipulator Control System Utilizing Network Technology. IFAC-Workshop on Human-Oriented Design of Advanced Robotics Systems, DARS '95, Vienna, September 19-20, 1995

[8] Fiege, A., Haferkamp, B., Knüppel, H., Leinemann, K., Suppan, A., Woll, J., Maisonnier, D.: Testbed EDITH and first practical experiences gained in the operation. FUSION TECHNOLOGY 1994, Elsevier Science B.V, 1995, p. 1379-1382

[9] Rohrbacher, H.A., Rahn, A., Suppan, A., Decreton, M., Moons, F., Maisonnier, D., Englert, K.: Radiation and Temperature Hardened Components for In-Vessel Handling Equipment. FUSION TECHNOLOGY 1994, Elsevier Science B.V, 1995, p. 1395-1398

[10] Rohrbacher, H.A.: Gamma Irradiation Effects and Environment Compatibility for Resolvers, Electronics, and Plastics with Respect to their Applicability to NET and ITER. . Unpublished Internal Report, June 1995.

[11] Englert, M.: Post-Irradiation Tests of the MOL F2-3 Experiment. Unpublished Internal Report, January 1995.

[12] Suppan, A., Englert, M.: Irradiation of Motors for In-Vessel Handling Equipment. Unpublished Internal Report, April 1995.

Staff:

G. Dillmann
B. Dolensky
H. Gutzeit
B. Haferkamp
A. Hinz
W.E. Hörl
F. Katz
H. Knüppel
U. Kühnapfel
K. Leinemann
W. Link
A. Ludwig
G. Müller
W. Müller
A. Rahn (KfK-AG Mol)
H.A. Rohrbacher
M. Salaske
U. Schygulla
A. Suppan
J. Woll

T 43   Remote Pipe Welding and Cutting

The objective of this task was to qualify cutting and welding tools for concentric cryogenic lines and to design and specify the tools for remote weld inspection.

The design, the technical description and the call for tender specification of a set of cutting welding tools as well as the draft of the specification for procurement of the inspection tools was submitted to the NET-Team. A European wide call for tender for the cutting/welding tools was performed by the NET-Team. The placement of the fabrication order with the industry was, however, stopped due to the JCT decision not to choose the concentric design version of cryogenic lines for ITER.

Therefore the task has been finalized. A final report is under preparation.

Literature:

[1]   Ferro, C., Gasparotto, M., Knoepfel, H., Fusion Technology 1992, Proceedings of the 17th Symposium of Fusion Technology, Rome, Italy, 14-18 September 1992, Volume 2, pp. 1574 - 1578.

[2]   Kast, G., Nuclear Fusion Project, Annual Report of the Association FZK/Euratom, October 1993 - September 1994, FZ;A5515, EUR 16100 EN

Staff:

L. Gumb
A. Schäf
M. Selig

Safety and Environment

Introduction:

Within the European Fusion Technology Programme 1992-94 the safety analyses for NET/ITER which are being performed in parallel to the design efforts address mainly two different areas:

Safety Assessment Studies

- Basic Safety Criteria
- Personnel Safety Assessment
- Analysis of Reference Accident Sequences
- Plant Safety Assessment

and

Plant Related Studies

- Radioactivity Inventories and Source Terms
- Environmental Impact of Tritium and
  Activation Products
- Waste Management and Decommissioning

The KfK contributions to this program concentrate on:

- Analyses of reference accident sequences in super-
  conducting magnets and

- Calculations of individual and collective doses to the
  public for routine and accidental releases of tritium
  and activation products.

The investigations on blanket safety are included in the blanket programme.

H. Knuth

SEA 3   Analysis of Reference Accident Sequences

Subtask 2: Magnet System Safety

Within the subtask 3.2 FZK investigates the thermal and mechanical behaviour of the magnet system during accidents.

During the period reported here code development and validation of MAGS have been major parts of the work. The work on structural analysis has been emphasised and is now focusing the ITER TF coil test to be performed in TOSKA.

a)   Thermal analyses for the magnet system

Extended application of the MAGS module SARUMAN in Karlsruhe and in other Labs revealed that the results show a dependence on the selected axial mesh size. Variation of this parameter influences as well the quench velocity as the peak pressure. This dependence vanishes if the length of a mesh element is in the order of 1cm to 2cm, at least in the vicinity of the quench front. For a conductor having a length of about 1km such a mesh size is prohibitive. Another problem with the SARUMAN code is that conductors with a central hole, being typical for ITER coils, cannot be modelled. These were the reasons for the development of the code GANDALF [1] at the NET-Team.

GANDALF solves a momentum equation for the hole and the bundle area, respectively, and with averaged mass fluxes a mass- and an energy balance equation. I.e. only one thermodynamic state for the Helium is assumed in a conductor cross section, while heat transfer and friction coefficients are different for the hole and the bundle. The equations are solved with 1d linear finite elements. This allows also for a simple manipulation of the mesh element density e.g. by subdivision of a mesh element in case of an arriving quench front or dropping mesh elements if the front has passed.

This code has been adapted and implemented into the MAGS code system. The varying mesh is now handled with the module MOVEMESH refining the initial coarse grid due to different criteria, e.g. arriving of a quench front, a steep pressure gradient along the coolant channel or requested by the user. The solution of the Helium balance equations is done with the module GANDALF. While the original GANDALF allows heat conduction only along the conductor in MAGS this was extended to 3d. The new modules have been applied on a sample problem considering quench in an ITER typical conductor and a Wendelstein 7X typical conductor [2].

To analyse also accidents within the cryostat the material properties package of Nitrogen has been extended below the triple point. Assuming air consisting of pure Nitrogen air ingress accidents into the cryostat can now be handled. As an example a temperature profile through a fusion plant is shown in Fig.1. Gas volumes are modelled for the Crane hall, the volume between cryostat wall and the thermal radiation shield, around the magnets and around the vacuum vessel.

These volumes are bounded by walls whose temperatures are calculated either with a 1d or a 3d model. Frost formation on the magnets is calculated.
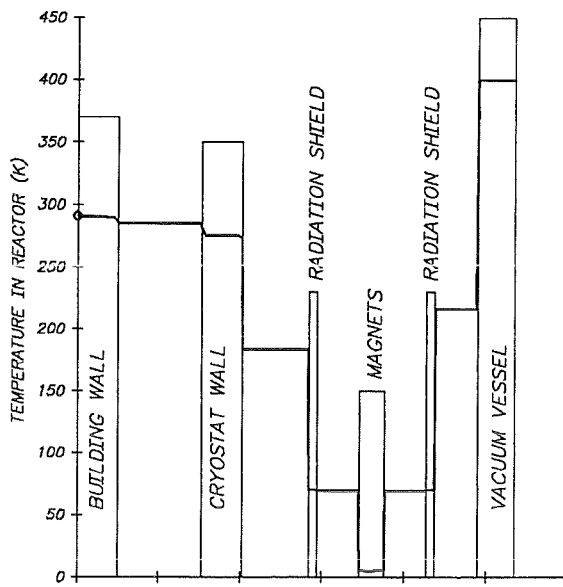

Fig. 1:   Temperature profile through a fusion plant

As reported earlier, for validation of the MAGS code the 3d Quench experiment is performed in co-operation with ITP at FZK. The focus of this experiment is to examine the axial and transversal quench propagation in a coil having forced flow Helium coolant. For the tests a one layer coil, wound with two conductors in hand, is used.

After a delay of several months the Wendelstein-7X conductor arrived at Karlsruhe in spring this year. However, it was twisted along its axis and the surfaces were not plane. For conductor to conductor heat transfer experiments such a geometry is not acceptable. Therefore, a specially developed rolling procedure was necessary for reshaping the conductor.

For a good tracing of the quench propagation the coil is heavily instrumented. Besides voltage tabs and thermocouples on the jacket the jacket was opened at some places to measure temperature and pressure of the Helium directly.

As shown in Fig. 2 the coil is wound. Presently the instrumentation is installed. After preparation of the STAR facility to accommodate the coil, the coil will be installed at the end of this year. First shake down tests will be performed then.

The coil has a length of about 0.8 m. Between the bifilar wound turns insulation blocks are fixed such that the conductors have contact only on one side. The conductors are electrically insulated. To ensure heat conductance, however, the conductors are pressed against each other with a lot of small brackets. In the middle of the coil the distance between the turns is enlarged. This is to accommodate the heater for
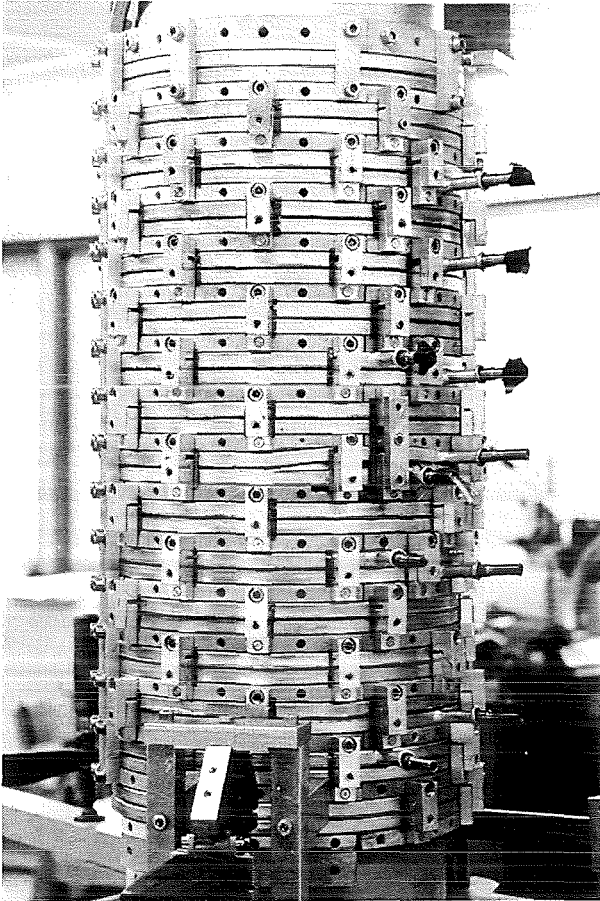
Fig. 2:   View of the test coil

MISES STRESS

Fig. 3:   Bucking structure under fault loading

quench initiation. On the right hand side tubes are visible, they are for Helium pressure measurement.

b)   Analysis of the mechanical behavior of the coil casings under accident conditions

The mechanical investigations for the bucking structure under fault conditions have been continued for the 1994 design where the relatively thick bucking cylinder was inside the solenoid.

Earlier investigations with a simple ring model had the result that a short circuit in a TF-coil during a fast dump leads to the most unfavorable loadings concerning the stability. When the solenoid is current loaded during the transient a possible instability is enhanced.

In a further step a more detailed 2D analysis has been done using the FEM-code ABAQUS [3] for the cross section in the equatorial plane. The solenoid and the bucking cylinder segments are under friction contact loaded by the above mentioned non axisymmetric worst case forces. The Fig. 3 shows that under such a loading the cylinder segments begin to slide and gaps between the solenoid and the bucking cylinder segments open up (displacement magnification factor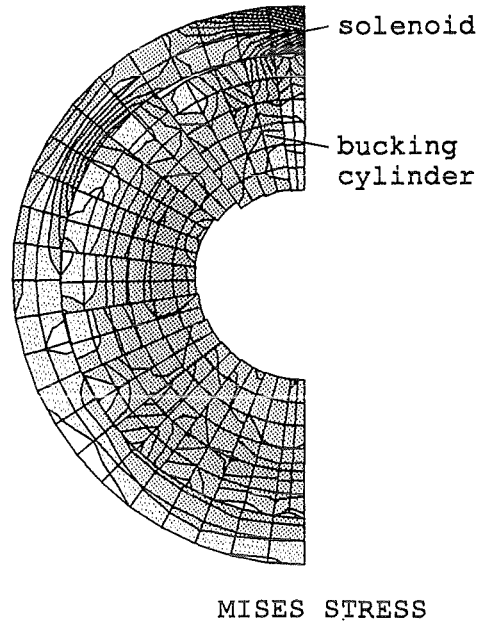 = 10). As a consequence stress concentrations in the solenoid occur due to bending. Thus, the stress is redistributed from the bucking cylinder to the solenoid.

So far, the predictions of the simple ring model seem to be confirmed. But there is still some doubt in the ability of the FEM code to model sliding under friction correctly.

Meantime the ITER design has been changed. There are now two thin torsional cylinders inside and outside the solenoid which are used for bucking and torsional support as well. To avoid current induction they are devided into insulated segments too. Investigations for the new design will be done later on.

Literature:

[1]   L.Bottura: A quench simulation model for the ITER magnets; The NET-Team c/o Max Planck IPP, Boltzmannstr.2 D-8046 Garching June (1994)

[2]   R.Meyder: Investigation on Effects of conductor concepts on 3D quench propagation in Superconducting coils using the code system MAGS; To be published in Journal of Fusion Energy

[3]   ABAQUS - Hibbit, Karlsson & Sorensen, Inc.

Staff:

G. Bönisch
B. Dolensky
W. Kuhn
R. Meyder
S. Raff

CTA-EU-D 36 (SEP 2)
Environmental Impact of Tritium and Activation Products

A first version of the new improved OBT-formation and translocation model for wheat plants has been finalised. The OBT formation is directly coupled to processes such as photosynthesis, respiration, metabolic exchange and maintenance of the plant. Comparison calculations with plant experiments carried out in the years 1993 - 1995 at FZK, Karlsruhe, show that the photosynthesis process was not considered correctly. In some cases the model overestimated the OBT formation, even if the growth rate was modelled correctly [1]. This lead to the assumption that a nonlinear reduction factor has to be introduced into the model. However, the processes involved are not yet fully understood. When completed, the model will be implemented in UFOTRI, the accident consequence assessment code for tritium releases [2].

Within the BIOMOVS II (BIOsheric MOdel Validation Study - phase II) study tritium models including UFOTRI are tested and compared with each other and with experimental data. As the present scenario gives only artificial conditions, no experimental verification of the models is possible. But the conclusion may be drawn at the present state, that the process oriented models are usefull for understanding the processes of the tritium transfer in the environment, whereas compartment approaches are more suitable for dose assessments, but they are of questionable help for describing the time dependency of the tritium concentration in the environment. Modelling of the soil and the dynamics of OBT proved to be the critical points of the models. The report of the model comparison will be ready by the end of 1995. Two new scenarios have been outlined covering the reemission process from the soil and the vegetation as well as the OBT formation during daytime and night-time conditions. Calculations have been performed with UFOTRI and the new advanced OBT model. A first comparison of the results with the experimental data took place at the end of May during the meeting of the BIOMOVS-II tritium working group at Belgirate, Italy. The model results of UFOTRI for the reemission scenario showed in principle a rather good agreement with the calculations. However, the flux out of soil and plants in the morning and evening was always overestimated. The data for the OBT- formation scenario were not opened at this meeting.

Scientists from the 'Zentrum für Strahlenschutz und Radioökologie' (ZSR) have performed a series of small-scale field studies at FZK. Two experiments on reemission after a one-hour HTO deposition were carried out, one at sunrise (7:00 a.m.) and one at sunset (9:00 p. m.). UFOTRI was used for comparison calculations with these experiments. UFOTRI runs with the default reemission data set show a poor agreement in the first hour for both cases. The agreement is improved, however, after modification of the default values. From the findings it can be concluded that at least the initial

reemission rate should be modelled independently of the H_2O evaporation rate.

Starting in the last contract period, the EXCEL program DOSEEX has been developed which can be used to scale and to easily combine precalculated dose values of unit releases of up to 290 fusion/fission relevant nuclides for 5 exposure pathways for estimating radiation doses resulting from source terms with non-unit release rates. Additionally, it is possible to adjust the run conditions via input parameters, such as building dimensions, stack height and others. The version 1.1 of DOSEEX, including a user guide has been finalised and delivered to the JCT. The final documentation and intercomparison calculations between DOSEEX and the computer codes UFOTRI and COSYMA are documented in [3].

For accidental and normal operation releases, the computer codes UFOTRI, COSYMA [4] and NORMTRI [5] have been applied for investigations within SEAFP (Safety and Environmental Aspects of Fusion Power) and the European environmental subtask SEP2.2. Within SEAFP, dose calculations have been performed for unit releases (1g) of tritium, corrosion products from water coolant loops, of first wall erosion products (V-15Ti, MANET2, La12TaLC) and of different coating materials (beryllium and tungsten). he results have been documented in [6] and [7]. In the frame of the European-environmental subtask SEP2.2, dose assessments were started for the site of Greifswald. Probabilistic calculations for accidental release conditions were performed for HT, HTO and activated steel. Two different release heights - 10 m with building wake effects and 100 m without any influence from the building were considered. Normal operation conditions were investigated for HT, HTO and activated steel, assuming a release via a stack only.

Dose conversion factors and concentration factors in food of about 70 relevant activation product nuclides are under way to be implemented in COSYMA, the program package for assessing the radiological and economic impact of nuclear accidents.

The work on developing models for the assessment of doses to individuals and the public resulting from contamination of waterbodies after an accidental release of radionuclides, has been continued. The hydrological model chain which consists of the run-off model RETRACE-2, the river model RIVTOX, the lake model LAKECO and a simple dose model has been successfully coupled [8]. The model chain is undergoing test and validation studies on the Ilja river (Ukraine), the Pripjat river (Russia) and the Rhine catchment (mainly Germany). The results for the Ilja river show a good agreement for the basic flow, however peak run-off events were partly underestimated. The data sets on radionuclides will be enhanced till the end of the year, covering then H, Co, Sr, Ru, Cs, I and Pu.

Literature:

[1] Diabaté, S., Müller, J., and Raskob, W.
Organically Bound Tritium Formation and Translocation in Crop Plants, Modelling and Experimental Results
in: Proc. of the 'Fifth Topical Meeting on Tritium Technology in Fission, Fusion and Isotopic Applications, Belgirate, Italy, 28.5.95 - 03.6.95, to be published

[2] Raskob, W.
Description of the New Version 4.0 of the Tritium Model UFOTRI Including User Guide
Report KfK-5194, Kernforschungszentrum Karlsruhe (1993)

[3] Meyer, D. and Raskob, W.
Final Report on Code development (DOSEX) and Dose calculations in the frame of ITER for the Year 1994.
Report FZKA-5511, Forschungszentrum Karlsruhe (1995)

[4] COSYMA: A New Program Package for Accident Consequence Assessment.
Joint report by Kernforschungszentrum Karlsruhe GmbH and National Radiological Protection Board
Commission of the European Communities, Report EUR-13028 EN (1991)

[5] Raskob, W.
Description of NORMTRI: a Computer Program for Assessing the Off-Site Consequences of Air-Borne Releases of Tritium during Normal Operation of Nuclear Facilities.
Report KfK-5364, Kernforschungszentrum Karlsruhe (1994)

[6] Raskob, W.
Results for SEAFP-subtask A 10:
Calculations of Individual and Collective Doses to the Public for Routine and Accidental Releases of Tritium and Activation Products.
Report FZK-5512, Forschungszentrum Karlsruhe (1995)

[7] Raskob, W.
Assessment of the Environmental Impact from Tritium Releases under Normal operating Conditions and after Accidents.
in: Proc. of the 'Fifth Topical Meeting on Tritium Technology
in Fission, Fusion and Isotopic Applications, Belgirate, Italy, 28.5.95 - 03.6.95, to be published

[8] Raskob, W., Tkalich, P., Heling, R., Popov, A.
Konzept zur modellmäßigen Beschreibung von kontaminierten Einzugssystemen in RODOS, dem Entscheidungshilfesystem nach kerntechnischen Notfällen in Europa.
in: 9. Fachgespräch "Überwachung der Umweltradioaktivität"
München-Neuherberg, 25.-27.04. 1995, to be published

Staff:

W. Raskob
I. Hasemann
D. Meyer

Studies for ITER / NET

Introduction:

By granting study contracts to FZK, ITER/NET draws upon special expertise available in the laboratory. In contrast to the technology tasks which extend over a longer period of time and consist in most cases of experimental work, study contracts are agreed on short notice and are of limited duration.

ERB 5000 CT 940027 NET (NET 94-343)
Quench Analysis for Magnet Safety Assessment

The prediction of the behaviour of the ITER coils (CS and TF) under quench conditions is required as basic part of the magnet safety analysis. When the conductor starts to quench, voltages, transient helium pressures and local temperature gradients develop such that they have the potential to initiate faults.

The analysis of quench requires

● prediction of the one-dimensional helium flow along the conductor,

● tracing of the three-dimensional propagation of quench to adjacent conductors by heat conduction.

The behaviour of the inner layers of the central solenoid CS and the inner pancakes of the outer poloidal field coil P5 during quench have been investigated. Both, CS and P5, are different with respect to magnetic field and winding type.

Parameter studies have shown that the propagation of the normal zone with time is strongly dependent on the size of the mesh used in the model. Node distances in the order of a few centimeters are necessary to get a well-converged result. Due to the large size of the ITER coils, the number of nodes as well as the number of links become very large.

Despite this fact, as a first attempt a model of two inner layers of the central solenoid (ITER-CS) as well as of the 3 inner double pancakes of the outer poloidal field coil have been created using a node distance of 2 meters. In case of the CS, the high-grade HP-2 conductor has been used, and current scenario as well as hydraulic network of the helium connection lines have been modeled. The initial normal zone (INZ) was located in the center of the first layer (high field region) over a length of 10 meters. In case of P5, the HP-1 conductor has been selected and the helium connection lines have been modeled as well. The initial normal zone was located in the center of the winding pack, i.e., in the low field region, over a length of 10 m.

In conjunction with the ITER-JCT and the EU Home Team, a set of fault conditions were selected which simulate the failure of quench detection system, power supply fault, and a short between terminals. The aim was to look for critical corners in the design and to sketch solutions for it, if possible.

The results of the analysis can be divided into three parts:

1. faults which result in marginal temperatures in the coil

2. faults which are urgent because they lead to high temperatures in the coil, but active protection is possible

3. faults which are urgent and there is no way to protect.

It turns out that the failure of the quench detection system is the less urgent one because it is possible to force a self quench of the coil, e.g., by introducing a resistance in the circuit which can be switched on if a failure occurs. It should be foreseen to have different quench detection systems in the coil for redundance.

The power supply fault is urgent because the coil could not be disconnected from the current supply. But an external resistance would help because it increases the total voltage of the circuit resulting in a reduction of the current flowing in the coil (self-dump).

A short between the coil terminals is the most urgent one because an external resistance could obviously not help and the total energy stored in the coil have to be dumped in it.

These results are generally valid for both the CS and P5 coil. But there is one important exception: If looking into the outer poloidal field coil P5, it turns out that the quench propagation velocity is very low. This is due to the low magnetic field in the winding and the large thermal resistance in transversal direction. So the resistive voltage across the coil will increase very slowly and a self-dump would not protect the coil against damage because it would be initiated too late. The only way for the P5 coil would be, in our opinion, to install quench heaters to fire long lengths of conductor. Because of the relatively marginal magnetic field, the energy to quench the conductor would be large, i.e., the amount of power for the heater would be very high.

As an example, some numbers from the results of the inner layers of the CS in case of a short between terminals are given: The maximum temperature in the conductor is about 400 K (extrapolated from the calculations), the maximum helium pressure 400 bars. After 24 s, the whole two inner layers are quenched, the maximum resistive voltage is about 2.9 kV. This leads to a so-called self dump of the coil. The maximum helium mass flow at inlet/outlet is about 800 g/s. This has to be taken into account for the design of the safety valves. For comparison, the same quantities are presented for the P5: The maximum temperature is above 450 K, the maximum helium pressure is about 50 bars, the normal conducting length after 60 s is only about 190 m, the corresponding resistive voltage is about 60 V.

Figure 1 shows the conductor temperature and the coil current as a function of time for the CS, Figure 2 shows the same quantities for the P5.

In summary it can be said that the fault like a short between terminals will lead to a destruction of the coil because it is not designed to dump its whole energy.

Staff:

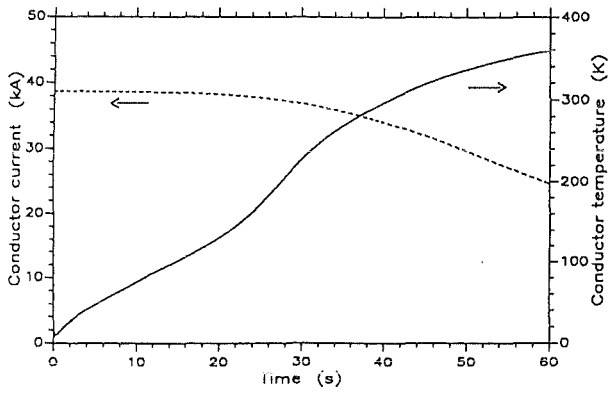R. Heller

Fig. 1:   Hot spot temperature and coil current as a
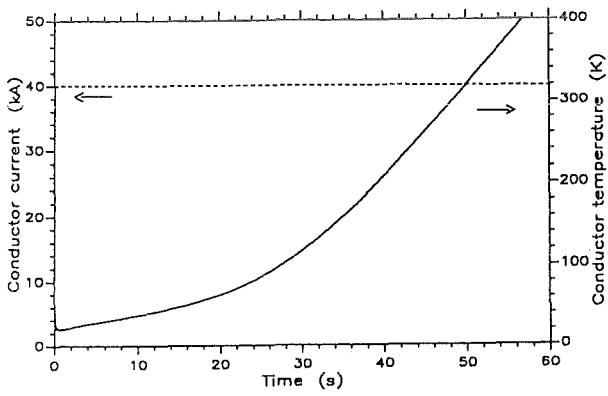   function of time for the inner layers of the CS

Fig. 2:   Hot spot temperature and coil current as a
           function of time for the inner pancakes of the P5

ERB 5000 CT 950044 NET (NET 95-379)
Nb₃Al Measurement for the Japanese Home Team

The NET-contract was performed as a collaboration between FZK/ITP and JAERI. The samples were delivered by JAERI and measured in the high field test facility at FZK/ITP Karlsruhe. The contract received ITER credit and was concluded by the submission of the final report to the NET-Team in July 1995 [1].

The superconducting parameters of Nb_3Al conductors degrade much less with respect to mechanical stress/strain in comparison to those of Nb_3Sn foreseen for the ITER magnets. Therefore, in this contract industrially fabricated Nb_3Al basic strands and subsize "Cable in Conduit" (CIC) conductors are investigated and compared with conductors based on Nb_3Sn.

The samples have been fabricated by Sumitomo Electric/ JAERI. The basic strand of $\varnothing$ 0.81 mm contains 240 filaments and was manufactured by the Jelly Roll process. The CIC samples consists of an outer Stainless Steel or Titanium conduit (O.D. = 9 mm) and a 36 strand cable, using a void fraction of 36 %. Reaction heat treatment: 13 hours/800°C. Both the basic strands and CIC's were tested in different inserts of the FBI test facility at FZK/ITP.

The critical current, I_c, versus applied axial strain, ε, of SS and Ti jacketed Nb_3Al CIC samples is illustrated in Fig. 1. Like comparable Nb_3Sn conductors I_c shows a maximum as a function of static strain. The maximum critical current, I_{cm}, is about the same for both samples while the prestrain, ε_m, is much higher for the SS jacketed conductor than for the Ti

jacketed one. This results from the higher contraction of the SS jacket during cooling from reaction to LHe temperature which puts the superconducting filaments in a higher compressive state leading to a stronger decrease of I_c. The ratio I_{co}/I_{cm} represents a measure of degradation which is about 0.7 and 1 for the SS and Ti sample, respectively.

Sample CIC-SS behaves reversible under static loaded and unloaded conditions. That means the irreversible strain, ε_{irr}, is at least as high as the highest strain value measured (1.2 %). Dynamic loading and unloading up to 1000 strain cycles (0.2 - 0.5 %) does not influence the static I_c vs ε characteristic. However, about the same application of cycling on the Ti jacketed conductor decreases I_c considerably (Fig. 1). I_c vs ε measurements on Nb_3Al strands (not shown here) exhibit almost the same characteristic as the Ti jacketed subcable without the effect of cycling.

The most important strain data of the basic strand, SS and Ti jacketed 36 strand CIC of both Nb_3Al and Nb_3Sn are compared in Tab. 1. Note that in case of the SS conductor at about the same prestrain the Nb_3Sn conductor degrates much more than the Nb_3Al type under the same test conditions.

Tab. 1: Comparison of Nb_3Al and Nb_3Sn strand, SS and Ti jacketed CIC (13 T, 4.2 K)

Conductor		I_{co}/I_{cm}	ε_m (%)
Nb_3Al	STRAND	~ 1	~ 0
	CIC-SS	0.73	0.65
	CIC-Ti	~ 1	0.1
Nb_3Sn	STRAND	0.95	0.15
	CIC-SS	0.45	0.7
	CIC-Ti	0.95	0.2

This is also illustrated in Fig. 2 where the critical current density versus magnetic field without applied strain for the same group of conductor is shown. Comparing Nb_3Al and Nb_3Sn at B = 12 T one observes about the same values of J_c for the basic strand and the Ti jacketed samples, while the CIC-SS sample housing Nb_3Al strands exhibits a clearly higher J_c than the comparable conductor with Nb_3Sn wires. That means with respect to J_c Nb_3Al CIC conductors are favored in the 12/13 T region. More detailed results are presented in [1].

Literature:

[1]   W. Specking: Final Report, July 1995, Contract ERB 5000, CT 950044 NET (NET 95-379)
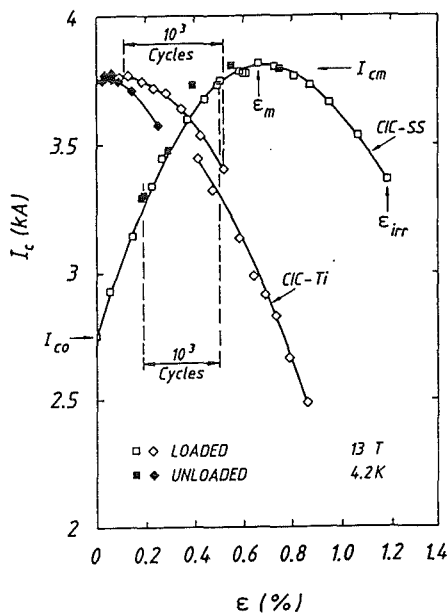
Staff:
H. Kiesel
W. Specking
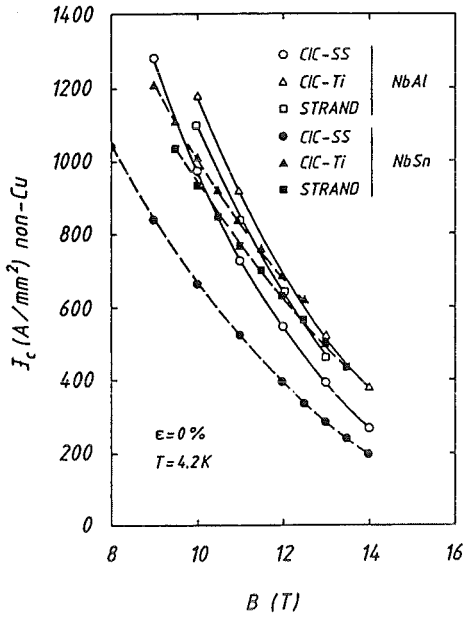

Fig. 1:   Strain dependence of critical current of Stainless Steel and Titanium jacketed "Cable in Conduit" subsize conductors. Note the Ic degradation of Ti sample after cycling.

Fig. 2: Comparison of critical current density of Nb₃Al and Nb₃Sn basic strand, SS and Ti jacketed conductors.

ERB 5000 CT 940059 NET (NET 94-358)
Assessment of the Use of High Temperature Superconductor in the ITER Current Leads

The purpose of this study was to investigate the possibility of using High Temperature Superconductors (HTSC) for a current lead design for the ITER Toroidal Field Coil system, i.e., DC operation is considered. A reference current of 50 kA has been selected for the study although the coil current of the TF coils have been changed in the mean time from 46 kA to 60 kA.

Several projects especially in Europe and in the US have started the development of high current binary current leads using bulk HTSC like Bi-2212 and tape HTSC like B-2223 sheathed with an Ag(Xat.%)Au alloy. A third solution would be zone melted YBCO(Y-123).

It turns out that the reduction in refrigeration power will be in the order of 3 - 5 compared to a conventional copper lead if using a heat sink at about 70 K. The spread covers for example the uncertainties in refrigerator efficiency and contact resistance. How to realise the heat sink at 70 K depends on the design of the refrigeration system; LN_2-cooling as well as 60 K He-cooling would be possible.

In the study, Bi-2223 tape as well as Bi-2212 bulk material have been investigated. The big advantage of Bi-2223 tapes sheated with an alloy of Ag(X at.%)Au (where X is in the range of 3 to 10) is its heigher critical current density together with an absence of generation of a hot spot in case of the creation of a normal zone. Therefore, Bi-2223 tapes are the favoured option for HTSC current leads. Because the Bi-2212 bulk HTSC is extensively studied (experimentally and numerically in DC and AC operation), this material could be an alternate option for a 50 kA current lead design. The problem of a hot spot could be overcome by using stainless steel rods as a by-pass, its thermal conductivity being low enough for this purpose. Also the smooth U(I) characteristic of this material, i.e., n-values between 2 and 10, may help to broaden the hotspot region. The lower critical current density can be treated by enlarging the cross section of the HTSC part.

For both options, the optimization for a 50 kA current lead was done using the code CURLEAD developed in our institute. Calculations were done for 50 kA as well as for zero current, 60 K He-cooling was chosen. The results were compared to a conventional design using a copper current lead of the POLO type to calculate the reduction in refrigeration power. Some intention has been given to the problem of the behaviour of the current lead in case of an interruption of the helium mass flow.

Figure 1 shows the temperature profile along the current lead length for a steady state current of 50 kA resp. zero current in case of the use of Bi-2223 tapes (left) and of i-2212 bulk (right). Figure 2 shows the temperature profile aft different times after interruption of helium mass flow for a steady state current of 50 kA in case of the use of Bi-2223 tapes (left) and of Bi-2212 bulk (right).

The comparison of Bi-2223 tapes and Bi-2212 bulk leads to the following statements: The most important difference of Bi-2223 tapes sheathed with Ag/Au alloy and Bi-2212 bulk material is the behaviour in case of a quench because the temperature increases at the 70-K level due to, e.g., loss of coolant mass flow. The absence of an electric stabilizer forces the bulk material to very high temperatures due to its low thermal conductivity and high electrical resistivity.

This leads to the following results:

● Since the critical current density is not homogeneous across the HTSC, the location of the maximum temperature in the HTSC part is not exactly known. Therefore, the voltage drop will be a better detector for a quench. Besides the step-like behaviour of the curves in case of the Bi-2212 bulk material (which is an effect of the discretization), the main difference is the higher maximum temperature for a given voltage drop. This is due to the lower thermal conductivitiy which results in a higher temperature gradient to conduct heat.

● The second result is the different time scale for reaching the critical temperature, i.e., melting point of soft solder. For Bi-2212 bulk material, the critical time is one order of magnitude smaller than for Bi-2223 tapes. Therefore, if detecting a quench, the time for discharging the coil system is smaller for Bi-2212 bulk material which makes the design more critical.

The behaviour of Bi-2212 bulk material discussed above makes the design more complicated because it requires a metallic by-pass to carry the electric current in case of a quench of the HTSC. This could be realised, e.g., by stainless steel which simultaneously acts as a mechanical reinforcement. The amount of stainless steel has to be chosen such to guarantee a safe energy discharge of the coil system.

As a conclusion, the use of Bi-2223 tapes sheathed with an AgAu alloy is the favoured option. So in the study the HTSC part including the connection regions to the coil/bus system as well as to the copper part of the lead has been designed taking into account the different thermal contractions of the materials and the fact that the HTSC material is very sensitive to forces and/or torques.

As an outlook a time schedule and a cost estimation for one 50 kA current lead was given.
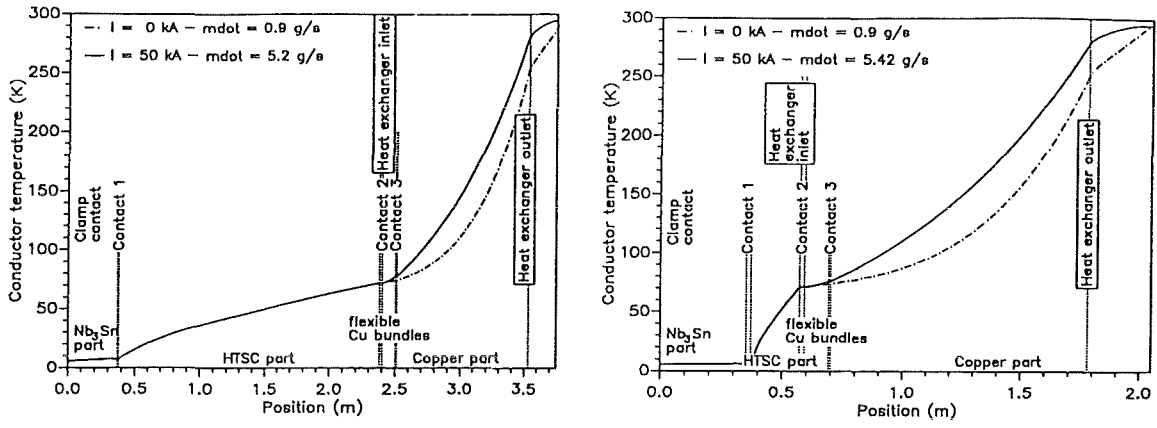
Staff:

R. Heller

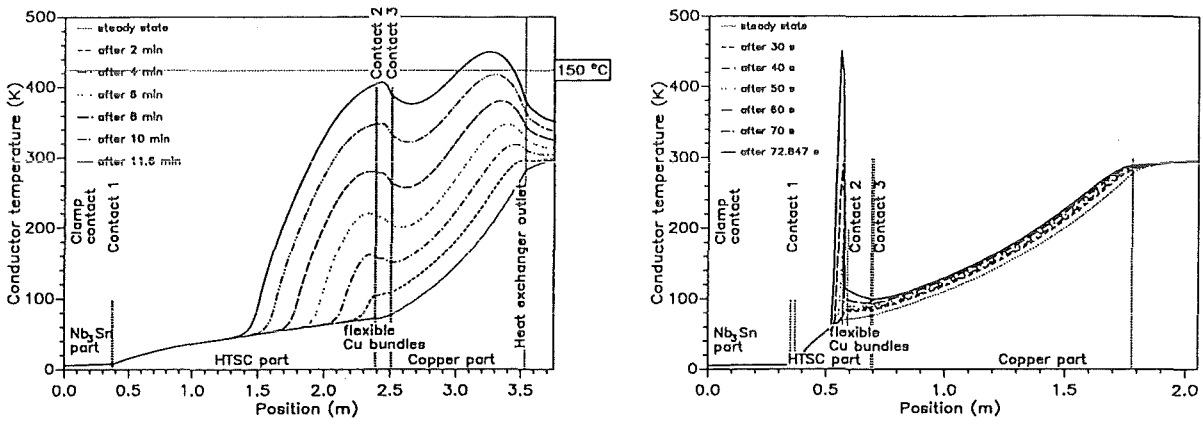Fig. 1: Temperature profiles for the Bi-2223 (left) and Bi-2212 (right) option for 50 kA and zero current

Fig. 2: Temperature profiles for the Bi-2223 (left) and Bi-2212 (right) option for 50 kA at different times after helium mass flow interruption

ERB 5000 CT 950064 NET (NET 95-384)
ITER Magnets and TFCM Stress Analysis

To get ITER relevant stress conditions for the toroidal field model coil (TFMC) tests in the magnetic field of the LCT-coil to be performed in the TOSKA cryostat are prepared.

This work had its focus on the structural analysis of the intercoil structure (ICS) between the TFMC and the LCT-coil which was under design by CEA-Cadarache. The ICS fixes the coil positions in such a way that in-plane and out-of-plane loadings due to Lorentz forces allow for the simulation of typical TF-coil stress situations e.g. the front leg pressure against the central bucking post or the out-of-plane bending of a TF-coil and its load transfer to the upper and lower crowns of the ITER design.

On the other hand the ICS has to provide a load transfer between the TFMC and the LCT-coil in such a way that deformations and stresses in the LCT-coil are limited. And finally the ICS itself should have a safe design since the loadings are rather high.

The work performed so far aimed at a safe design. The Lorentz force loading has been determined using the EFFI code [1]. Due to the chosen coil positions the TFMC has a resulting in-plane loading towards the front side whereas the LCT-coil has a resulting in-plane load towards its back leg. Due to the out-of-plane loading the coils attract one another.

A detailed structural analysis of the ICS has been performed by a solid-shell model shown in Fig. 1. It turned out that
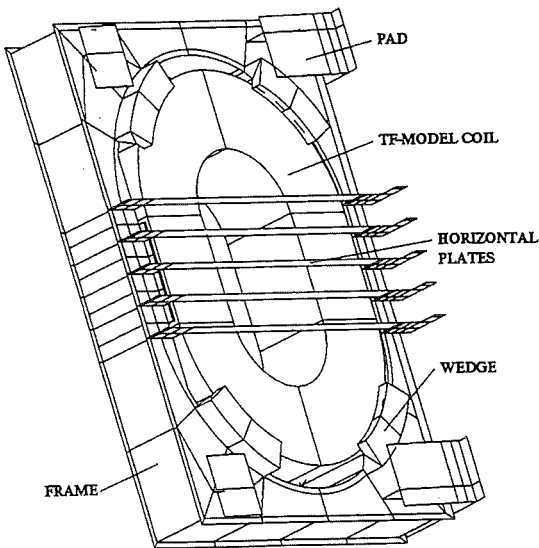

Fig. 1: Intercoil Structure and Model Coil

nearly all structural parts are rather highly loaded. Critical points are the load transfer between the TFMC and the ICS-frame at the wedges and the load transfer between the ICS-frame and the LCT-coil at the horizontal plates (Fig. 1). Due to

the tiebands of the LCT-coil in that region the design has strong restrictions.

The global behavior of the TFMC-ICS-LCT coil assembly has been studied by the simple beam-shell model shown in Fig. 2.
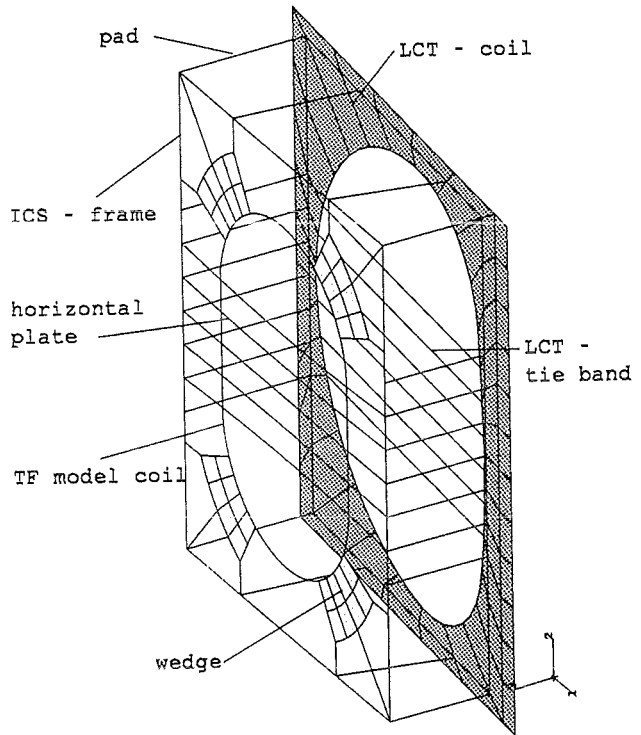

Fig. 2: Shell-Beam Model of the Coil Configuration

It allows e.g. to take into account the stiffness of the LCT-coil on the highly static indeterminate load transfer between ICS-frame and LCT-coil and to design the supporting points in order to prevent high displacements or stresses in the LCT-coil. Using the model many design variants have been tested to find an optimum and safe design.

In a further step the more detailed behavior of the coil system will be analysed by coupling the model of Fig. 1 with a solid-shell model of the LCT-coil.

Later on investigations concerning the ITER relevance will have to be performed.

Literature:

[1] S. J. Sackett, "EFFI - a Code for Calculating the Electromagnetic Field, Force, and Inductance in Coil Systems of Arbitrary Geometry", UCRL-52402 (1978)

Staff:

B. Dolensky
R. Meyer
S. Raff

Gyrotron Development
(includes ITER Task G 52 TT 03 FE)

1. Introduction

A main goal of the gyrotron development program at the Research Center Karlsruhe (FZK) is the design, construction and test of high-power gyrotron oscillators for electron cyclotron wave (ECW) applications and diagnostics of magnetically confined plasmas in controlled thermonuclear fusion research. For the next generation of fusion machines such as the stellarators LHD in Japan and W7-X in Germany and the ITER tokamak, millimeter (mm)-wave generators operating at long pulses up to CW with an RF output power in excess of 1 MW per unit at frequencies from 140 to 170 GHz are required. Since efficient plasma heating (ECH) and current drive (ECCD) need axisymmetric, narrow, pencil-like mm-wave beams with specific polarization, single mode emission of the sources is necessary in order to generate a TEM00 Gaussian beam for low loss transmission and for efficient plasma heating.

The fusion gyrotron development at FZK concentrates on five important items: improved quasi-optical (q.o.) mode converters, high efficiency by energy recovery via a single-stage depressed collector (SDC), frequency tunability, 2 MW unit power (coaxial gyrotron) and high power mm-wave windows for the gyrotrons and the plasma torus. The experimental and theoretical activities are organized within the EURATOM/ITER gyrotron and window development program (ITER Tasks T24 and T25).

2. Experimental Results of the $TE_{10,4}$ Gyrotron

The experimental results and numerical simulations of the 0.7 MW, 140 GHz, $TE_{10,4}$ gyrotron with axial RF output have been published elsewhere [1].

In the following the experimental results of a $TE_{10,4}$ mode gyrotron with advanced internal quasi-optical (q.o.) mode converter, that provides a separation of the electron beam from the rf beam, are given.

The maximum output power $P_{out} = 0.6$ MW was achieved at a beam voltage $U_b = 83$ kV and an electron beam current $I_b = 27$ A. The overall efficiency for that power is 27%. The highest efficiency of 32 % (electronic efficiency of 38%) was measured for an rf power of 0.5 MW at $U_b = 79$ kV and $I_b = 20$ A.

The operating mode was identified by the rf frequency of the output signal. The purity of the output mode is determined by a thin dielectric transmission target whose temperature distribution and thus the power distribution of the beam is monitored by an infrared camera. The beam was found to be a TEM_{00}-mode with 94.5 % purity.

Due to the limited energy absorption capability of the calorimeter the long pulse measurements were performed with a dielectric target placed into the beam. This target had been calibrated at intermediate pulse lengths by comparing the results with those obtained with the calorimeter.

The measured output power shows a strong dependence on pulse length (Fig. 1). It was not possible to operate the
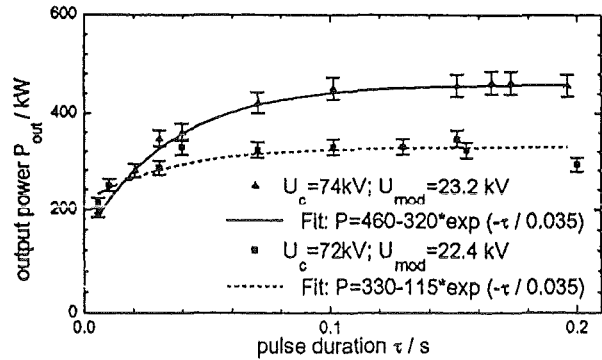

Fig. 1: Dependence of output power on pulse length for an average beam current of 18 A

gyrotron at 79 kV necessary for high power output at short pulses. At these values the gyrotron could not be excited in the desired $TE_{10,4}$-mode. This effect is caused by the voltage depression inside the resonator. For a beam current of 20 A and without neutralisation the effective voltage inside the resonator is calculated to be decreased by 5 kV compared to the cathode voltage. For short pulse operation the effective voltage in the resonator is only 74kV, instead of the applied cathode voltage of 79 kV. In long pulse operation, however, the voltage depression is compensated by neutralisation and the effective voltage approaches the applied cathode voltage of 74 kV. From the exponential fit a neutralization time constant of 35 ms was found which is in good agreement with the one of 30 ms estimated for a pressure of $2\text{-}3 \cdot 10^{-8}$ mbar.

The dependence of output power on pulse length also can be seen in Fig. 2. The output power increases strongly with
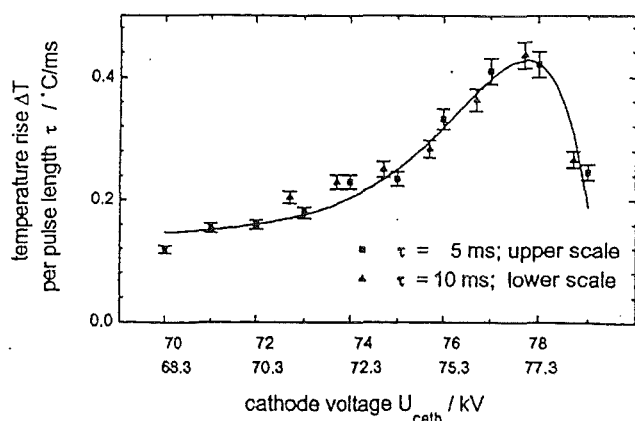

Fig. 2: Dependence of output power on cathode voltage for different pulse lengths

increasing cathode voltage and reaches a sharp maximum at cathode voltages which are dependent on the pulse length. For high voltages above a certain limit the power drops and

no oscillations can be excited. This is the reason why for cathode voltages exceeding 74 kV the achievable pulse length decreased with increasing beam voltages.

The highest output power for a pulse length of 0.2 s was measured to be 460 kW. To improve the tube efficiency a single-stage depressed collector (SDC) [2,3] biased by a variable resistor has been installed. Voltages of up to 25-30 kV could be applied without a reduction of output power. The body current, however, increased strongly with the collector voltage. This behaviour is produced by a non-adiabatic motion of the electrons in the retarding collector region.

With the SDC the efficiency could be increased from 34% to a value as high as 51 % at a collector voltage $U_{coll} = 24$ kV.

During the long pulse experiments a reversible change of frequency could be observed. With an output power of 460 kW the frequency decreased by about 400 MHz during a pulse of 0.16 s. From the frequency dependence it is possible to calculate the cooling conditions of the resonator. According to the exponential decrease of the frequency a heat transfer coefficient from copper to water of 8.5 W/cm²/K was found and a power loss density of the cavity surface of 3.7 kW/cm² were calculated.

From Table 1 one can see that during the long pulse

Table 1: Experimental results of the $TE_{10,4}$-gyrotron (the efficiencies with depressed collector are given in brackets)

fre-quency [GHz]	mode purity [%]	catho-de voltage [kV]	output power [kW]	efficien-cy [%]	pulse length [ms]
140.2	94.5	79	600 500	27 32 (48)	12 30
140.5	94.5	74	460 460	31(47) 31(51)	200 130

experiments the frequency was irreversibly shifted by about 300 MHz to higher frequencies. This was confirmed by mechanical measurements of the cavity geometry. The initially cylindrical geometry had been changed to an almost parabolic shape with the smallest diameter at the center of the cavity. This change in geometry strongly influences the Q-value and the power loss density in the cavity, which was calculated to only 3.6 kW/cm² with the new geometry, and this value agrees very well to the one of 3.7 kW/cm² found experimentally.

The irreversible frequency change to higher frequencies can be explained by a simple theoretical model assuming that the internal stresses during a pulse exceed the elastic range for heated copper.

A summary of the results of the $TE_{10,4}$ gyrotron is presented in Table 1 [4,5,6,7].

3. Experimental Results of the $TE_{22,6}$ Gyrotron

In order to generate an output power of 1 MW or even more at long pulses up to CW, modes of higher order than $TE_{10,4}$ have to be used [8]. To handle the heat problems in long pulse operation, the maximum rf wall losses have to be less than approximately 3.5 kW/ cm². A 1 MW $TE_{22,6}$ gyrotron has been tested at FZK. In a first step a non improved q.o. mode converter has been used. The diode-type magnetron injection gun (MIG) with a LaB_6 emitter was designed in collaboration with the Institute of Applied Physics (IAP) in Nizhny Novgorod and has been manufactured and successfully tested there using the retarding field method. he main parameters of the gyrotron are given in Table 2.

Table 2: Design parameters of the $TE_{22,6}$ gyrotron

P_{out}	= 1 MW	α	= 1.4
U_{cath}	= 80 kV	B_{cav}	= 5.54 T
I_{beam}	= 40 A	R_{beam}	= 7.93 mm
J_{cath}	= 3.6 A/cm²	ΔR_{beam}	= 0.23 mm
B_{cath}	= 0.187 T	R_{cav}	= 15.57 mm
R_{cath}	= 45.2 mm	L_{cav}	= 15 mm
θ_{cath}	= 21.5°	Q_{diff}	= 1000
		P_{max}	= 3.5 kW/cm² for 1.16 MW in the cavity

In short pulse operation (0.2 ms) the output power as function of the beam current has been measured. The maximum output power $P_{out} = 0.94$ MW was achieved at a beam voltage $U_b = 85$ kV and an electron beam current $I_b = 53$ A. The efficiency for that power with a collector voltage $U_{coll} = 27$ kV was 31 %. The maximum efficiency of 37 % was measured for an rf power of 0.8 MW at $U_b = 80$ kV and $I_b = 42$ A and a collector voltage $U_{coll} = 28$ kV. The results are summarized in Fig. 3.

In order to enhance the efficiency the operation with the depressed collector has been investigated. A typical experimental result is shown in Fig. 4. The measured value of Ibody does not increase within the accuracy of the measurements (± 20 mA) over the whole investigated range. For the given example P_{out} starts to decrease above $U_{coll} \approx 27$ kV. Due to the rf-interaction in the cavity the electron beam becomes strongly energy distributed such that at higher retarding collector voltages a part of the electron beam may be reflected. The indicated value of the reflected current $I_b(E)$ has been calculated for the same parameters with an incident spread $\delta\beta_{\perp rms} = 10$ %, which has been taken according to the measurements of the beam parameters. The
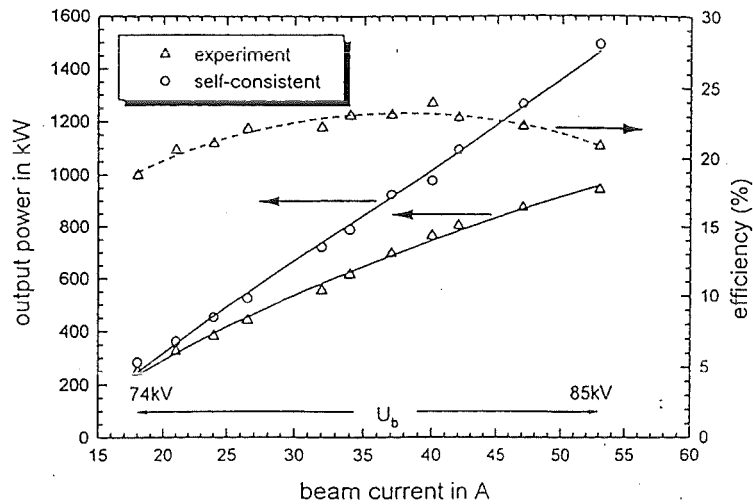
Fig. 3 : Output power and efficiency as function of the beam current . The magnetic field was kept constant. The beam voltage was optimized for maximum output power
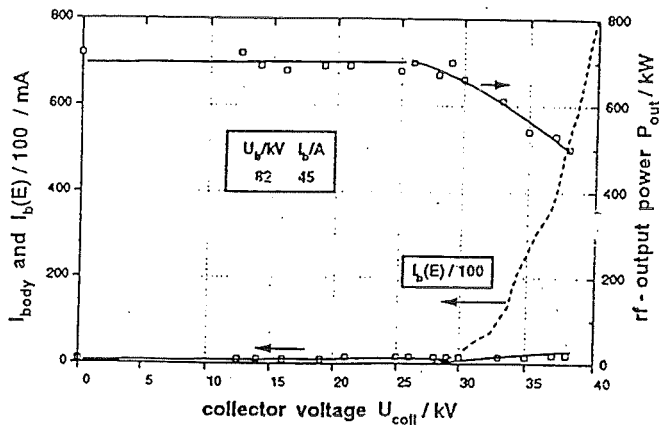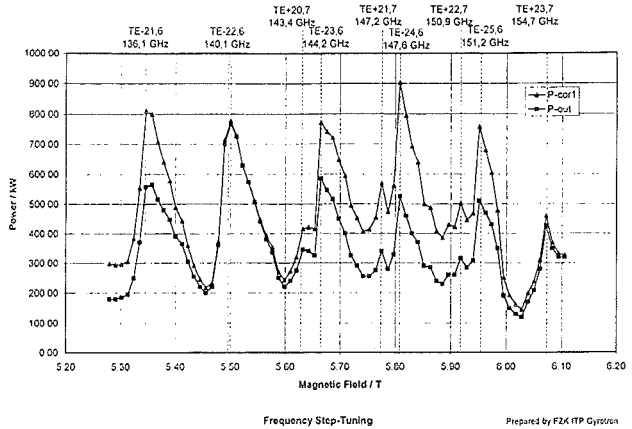

Fig. 5: Slow stepwise tuning of the $TE_{22,6}$ gyrotron at $U_{cath} = 80$ kV, $I_b = 40$ A and $R_{beam} = 8.1$ mm

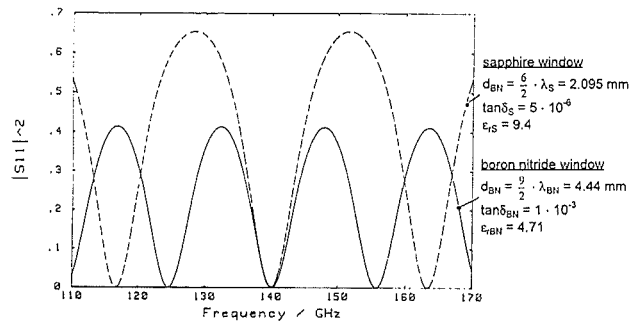140 GHz. The reflectivity increases to more than 40 % with frequency (Fig. 6).

Fig. 4: Experimental I_{body}, I_b(E) and P_{out} vs. U_{coll} for the $TE_{22,6}$ gyrotron. $U_b = 82$ kV, $I_b = 45$A, $P_{rf} \approx 1.4 \cdot P_{out}$

Fig. 6: Reflectivity of output windows

appearance of the reflected electrons coincides with the starting of degradation of P_{out}. Around $U_{coll} \approx 30$ kV the signal of the capacitive probe started to become noisy (oscillating frequency about 1 MHz).

The possibility of slow frequency step tuning by variation of the cavity magnetic field and corresponding change of the operating mode (series of $TE_{-m,6}$ modes with m = 21, ...,25) has been demonstrated experimentally. The tube was operated at $U_{cath} = 80$ kV, $I_b = 40$ A with short pulses (<1 ms). The measured output power P_{out} versus magnetic field is given in Fig. 5. In a second curve P_{cor1} the power reduction due to the reflectivity of the output window has been corrected to zero window reflections. The single disk output window of pyrolytic boron nitride with a thickness of d = 4.44 mm corresponding to 9 half wavelengths is matched to

The experiments showed that competition between the corotating $TE_{-m,n}$ and counter-rotating $T_{Em-3,n+1}$ modes can be completely eliminated by use of the diode startup method. In order to generate the counter-rotating modes $TE_{+m,7}$ (m=20,...,23 from 143.4 to 154.7 GHz) with the correct rotation to exit the tube, the cavity magnetic field had to be reversed. The measured output power level has been in the range of 0.7 to 0.8 MW (corrected for reflections).

In order to study gyrotron operation for the advanced ECW-startup scenario we also investigated modes with frequencies further apart from 140 GHz, that was the $TE_{-19,5}$ (118 GHz) and the $TE_{-25,7}$ (162 GHz) mode. Due to the different cavity magnetic fields the α-value is changed as for a fixed compression ratio B_{cav}/B_{gun} the transverse velocity $\beta_{\perp}$ scales inversely proportional to the magnetic field in the gun. For the $TE_{-19,5}$-mode the α-value increases to 1.7 or higher leading to reflection of the electrons and beam instabilities. To decrease α the magnetic field at the gun and thus the beam radius was increased. The experimental results for 80 kV/40 A operation are summarized [7,9,10] in Table 3. The power values are corrected for window reflections (Fig. 6).

Table 3: Modelling experiment for advanced ECW-startup in ITER.

Frequency/GHz	117.9	140.1	162.3
Mode	TE$_{-19,5}$	TE$_{-22,6}$	TE$_{-25,7}$
Power /MW	0.75	0.83	0.97
Efficiency / %			
with SDC	32	37	36
without SDC	23	24	26
Pulse length / ms	1	10	1
α-value	1.2	1.4	1.1

In the case of large step frequency tuning a triode MIG would be advantageous because of the possibility to adjust α.

4.   TE$_{28,16}$ Coaxial Cavity Gyrotron for 1.5 MW

Microwave sources in the 2 MW-power region are needed for economically attractive ECH on future fusion experiments such as W7-X and ITER. A coaxial 1.5 MW, 140 GHz, TE$_{28,16}$ gyrotron with an inverse magnetron injection gun is under development at FZK, in collaboration with the IAP Nizhny Novgorod and the Helsinki University of Technology. In the coaxial geometry mode competition in very large cavities (D/λ > 25) [11] can be reduced and also decreases the voltage depression of the electron beam dramatically (from 11 to 1.4 kV) which leads to higher efficiencies. A first version of the coaxial gyrotron with an axial waveguide output has been fabricated and assembled. It can be operated to a pulse length of 0.3 ms. It is limited by the heat load capability of the collector, which is part of the output waveguide. In a second step the design will be modified in order to allow long pulse operation. Especially because of the present power limit of RF output windows the mm-wave power will be split into two beams and coupled out radially through two windows.

A LaB$_6$ electron gun of the diode type having a central rod close to the ground potential surrounded by the cathode (inverse magnetron injection gun, IMIG) has been designed in collaboration of IAP and FZK and fabricated at the IAP. This construction allows fixing and cooling of the inner rod from the gun side. The main design parameters are summarized in Table 4.

First the electron gun has been tested at scaled down parameters with the method of retarding fields. In these tests it has been found [12] that the average velocity ratio α agreed well with the calculated values. An upper value for the rms-value of the relative transverse velocity spread is found to δβ$_{\perp rms}$ ≤ 9 %, sufficient for reliable operation of the gun at the nominal values. Preliminary rf-tests have been performed at IAP with a simple coaxial cavity with an uncorrugated and non-tapered inner rod (R$_{cav}$ = 29.8 mm, R$_{cav}$/R$_i$ = 4,

Table 4: Design parameters of the 1.5 MW, TE$_{28,16}$ coaxial cavity gyrotron

P$_{out}$	= 1.5 MW	a	= 1.4
U$_{cath}$	= 90 kV	B$_{cav}$	= 5.54 T
I$_{beam}$	= 50 A	R$_{beam}$	= 10.0 mm
J$_{cath}$	= 2.8 A/cm²	ΔR$_{beam}$	= 0.25 mm
B$_{cath}$	= 0.207 T	R$_{cav}$ = 29.8 mm (R$_{cav}$/R$_i$ = 3.7, 1° taper)	
R$_{cath}$	= 56 mm	L$_{cav}$	= 20 mm
θ$_{cath}$	= 9°	Q$_{diff}$	= 2030
		p$_{max}$ = 1.25 kW/cm² for 1.72 MW in the cavity	

L$_{cav}$ = 20 mm, Q = 2000) at pulse lengths of 20μsec. In these tests an rf output power of 1 MW with an efficiency of 23 % has been measured at 140 GHz (TE$_{28,16}$) and 1.3 MW with an efficiency of 29 % at 133 GHz (TE$_{27,15}$). No indications of beam instabilities between the IMIG gun and the cavity have been observed.

The axial version of the coaxial gyrotron at FZK became ready for measurements recently. First the radial position of the beam in the cavity relative to the inner rod has been measured using the possibility of radial displacement of the beam with sc dipole coils of the magnet. At this occasion it was found that in addition to a small misalignment of the beam axis relative to the inner rod the current density was unfortunately not uniform around the azimuth resulting in an approximately semicircular electron beam. This was because a part of the cathode filament was short-circuited resulting in an azimuthally non-uniform temperature distribution. Under this conditions the tube was operated for a few days up to the nominal parameters before the filament was practically entirely short-circuited such that nearly no electron current was emitted anymore. At the operation with the semicircular beam the pulse length had to be limited to about 100 μsec because of the higher power density at the collector surface. Under this conditions a maximum rf output power of 420 kW was measured at 90 kV and 35 A corresponding to an efficiency of only 13 %. It is not known if single or multi mode oscillation existed in the cavity under these conditions. The low efficiency is thought to be caused by a simultaneous oscillation of the both azimuthal directions (+,-) of the TE$_{28,16}$ mode. The frequency of the TE$_{28,16}$ mode was measured to be 139.96 GHz in good agreement with the nominal value. The gun will be repaired soon and the experiments will be continued.

A gyrotron relevant for CW-operation with a dual transverse rf-beam output and a depressed collector is under construction. For the quasi-optical rf output system two ways are under consideration. First, the cavity mode is launched

directly. This requires mirrors of a large size. Second, in order to reduce the size of the mirrors the operating $TE_{-28,16}$ mode will be converted into the degenerate $TE_{+76,2}$ mode. By that the size of the mirrors can be reduced, however, the losses in the output taper and launcher increase.

5. ECH window development

This ECH window development is being performed in collaboration with IMF I (H.E. Häfner and P. Norajitra). In a high power experiment at IPP Garching using a Russian 140 GHz, 0.5 MW, 1 s gyrotron the power absorbed in a circular, liquid nitrogen edge cooled single disk sapphire window was determined. Within the experimental uncertainties, the measured loss tangent values of $8 \pm 4 \times 10^{-6}$ in the temperature range between 87 and 95 K are in agreement with cold test measurements for HEMEX sapphire (Fig.7). Owing to a special cold nitrogen gas flushing system the
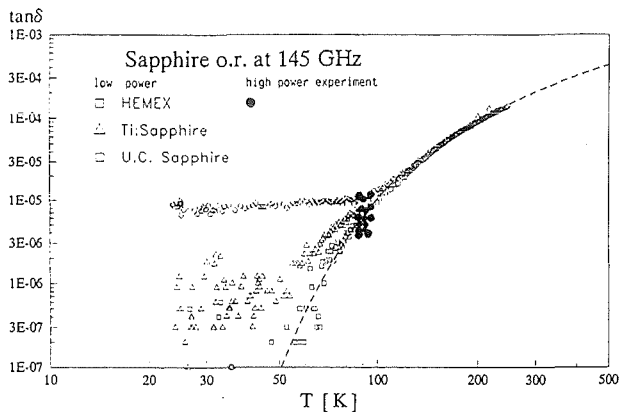

Fig. 7: Dielectric loss of various sapphire grades at cryogenic temperatures

window calorimeter could be operated with only minor freezing and no rf arcing problems during a whole working day.

An assessment has indicated that the use of an elliptical rf beam with flattened power distribution and an aspect ratio of 8:1 (252 mm x 32 mm window aperture) or of a ring-shaped elliptical beam with an aspect ratio of 3:1 (156 mm x 52 mm) allows a power transmission capability of 1 MW, CW at 170 GHz through a rectangular liquid nitrogen edge cooled single disk sapphire window with the same aspect ratio. First finite element calculations on stress distribution and 10 bar overpressure show that all stresses are well below the admissible limits.

First finite element calculations on a large aspect ratio rectangular Brewster window (680 mm x 12 mm) with water edge cooling at 293 K show that Au-doped Silicon and Diamond are possible candidates for 170 GHz, CW operation and will be considered in the further design. The window assembly consists of asymmetrical arrangement of a corrugated circular HE_{11} to corrugated square waveguide transition with a side $a = 1.848\ T$ and a quasi-optical

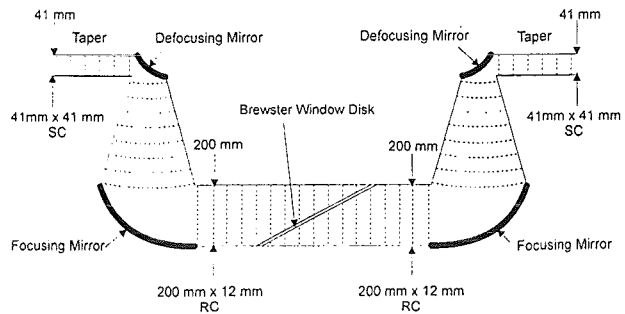corrugated rectangular waveguide taper to 200 mm x 12 mm incorporating the window (Fig. 8).

Fig. 8: Large aspect ratio rectangular Brewster angle window

Finite element calculation on a liquid neon edge cooled single disk sapphire window using pessimistic values of loss tangent and thermal conductivity show a CW power transmission capability for a Gaussian/HE_{11}-power distribution of 2.8 MW, 2.3 MW and 1.8 MW at 140 GHz, 170 GHz and 220 GHz, respectively, allowing even 2 MW, CW windows at 170 GHz. Calculations on stress distribution and 5 bar overpressure and the final principle design are in progress [13].

Literature

[1] G. Gantenbein, E. Borie, G. Dammertz, M. Kuntze, H.-U. Nickel, B. Piosczyk, M. Thumm, IEEE Trans. Plasma Science, 22, 861-868 1994.

[2] M. Thumm, E. Borie, G. Dammertz, O. Höchtl, M. Kuntze, A. Möbius, H.-U. Nickel, B. Piosczyk., C. Semmle, A. Wien, Proc. 19th Int. Conf. on Infrared and Millimeter Waves, JSAP Cat. No.: 941228, 57-58, Sendai 1994.

[3] M. Thumm, E. Borie, G. Dammertz, C. Grüber, O. Höchtl, C. Iatrou, S. Kern, M. Kuntze, A. Möbius, H.-U. Nickel, B. Piosczyk, A. Wien, 9th Joint Workshop on Electron Cyclotron Emission and Electron Cyclotron Resonance Heating, Borrego Springs, CA, January 22-26, 1995

[4] M. Thumm, FZKA 5564, Apr. 1995.

[5] M. Thumm, Fusion Engineering and Design, 30, 139-170, 1995

[6] G. Dammertz, E. Borie, O. Höchtl, C. Iatrou, S. Kern, M. Kuntze, A. Möbius, H.-U. Nickel, B. Piosczyk, A. Wien, Proc. ITG-Conf. Vakuumelectronic and Displays, Garmisch-Partenkirchen, Germany, 109-114, 1995.

[7]   M. Kuntze, O. Braz, G. Dammertz, C. Iatrou, S. Kern, A. Möbius, B. Piosczyk, G. Soudée, M. Thumm, A. Wien, Proc. SPIE Int. Microwave Pulses III, 2551, 347-355, San Diego, 1995.

[8]   G. Gantenbein, E. Borie, O. Dumbrajs, M. Thumm, Int. J. Electronics, 78, , 771-787, 1995.

[9]   H.-U. Nickel, FZKA 5513, Feb. 1995.

[10]   M. Thumm, E. Borie, G. Dammertz, C. Grüber, O. Höchtl, C. Iatrou, S. Illy, S. Kern, M. Kuntze, A. Möbius, H.-U. Nickel, B. Piosczyk, C. Semmle, A. Wien, Proc. MIOP '95, Sindelfingen, 314-320, 1995.

[11]   V.A. Flyagin, V.I. Khishnyak, V.N. Manuilov, A.B. Pavelyev, V.G. Pavelyev, B. Piosczyk, G. Dammertz, O. Höchtl, C. Iatrou, S. Kern, H.-U. Nickel, M. Thumm, A. Wien, O. Dumbrajs, Proc. 19th Int. Conf. on Infrared and Millimeter Waves, JSAP Cat. No.: 941228, 75-76, Sendai, 1994.

[12]   V.K. Lygin, V.N. Manuilov, A.N. Kuftin, A.B. Pavelyev, B. Piosczyk, Int. J. Electronics, 79, 227-235, 1995.

[13]   Norajitra, P., H.E. Häfner, M. Thumm, 20th Int. Conf. on Infrared and Millimeter Waves, Lake Buena Vista (Orlando), December 11-15, 1995.

Staff:

W. Baumgärtner
E. Borie
O. Braz (Uni Karlsruhe)
H. Budig
G. Dammertz
P. Grundel
C. Iatrou (EC-Fellowship/Guest Scientist)
S. Illy
S. Kern (Uni Karlsruhe)
M. Kuntze
G. Michel (ab 1.4.95, Uni Karlsruhe)
A. Möbius
N. Münch
B. Piosczyk
M. Pereyaslavets (Minerva Fellowship)
G. Redemann (bis 1.10.95)
M. Thumm
R. Vincon
A. Wien (bis 31.7.95, Uni Karlsruhe)

High Power Windows
(includes ITER Task G 52 TT 0 FE)

Starting from the previously examined concept [1, 2] of a liquid nitrogen edge cooled sapphire single-disk window at Forschungszentrum Karlsruhe a number of alternative concepts have been considered in additional field studies related to the coolant (LNe, 27 K; H$_2$O, 293 K), window material (diamond, silicon) and the window geometry (circular, rectangular), by which concepts the potential could be enhanced of achieving 1 MW transmission power. Furthermore, the frequency (140 GHz, 170 GHz) and the power profile (Gaussian, flat, annular) have been taken into account as sub-parameters.

1. Assessment and design calculations for sapphire windows with liquid neon cooling

The previous design calculations were performed for a circular sapphire disk of about 140 mm diameter and 1.8 mm thickness which is embedded in a 90 mm diameter waveguide and cooled by liquid nitrogen at 77 K in an annular space around the edge. Taking into account the loss tangent of Ti-doped sapphire tanδ = 3.15x10^{-12}xT$^{3.3}$ [3] and the best value of thermal conductivity [4] the calculations yield maximum transmission power at 140 GHz of 0.5, 0.7 and 1.0 MW for a Gaussian, flattened and annular profile, respectively.

Since the thermal conductivity of sapphire reaches its maximum at about 30 K (Fig. 1) and the value of the loss tangent is very small at this temperature as well an enhancement of the power transmission capability could be achieved by using liquid neon as a coolant at 27 K instead of liquid nitrogen.

Finite element calculations on a liquid neon edge cooled single disk sapphire window using pessimistic values of loss tangent tanδ = 1.48 x 10^{-11} x f (GHz) x T^2(K) [5] and of thermal conductivity [6] at this low temperature range show a CW power transmission capability for a Gaussian/HE11-power distribution of 2.8 MW and 2.3 MW at 140 GHz and 170 GHz, respectively (Fig. 2).

2. Assessment and design of a medium aspect ratio rectangular liquid nitrogen edge cooled single disk sapphire window

Design calculations have been continued for rectangular windows with medium aspect ratio using the finite element code ABAQUS supported by the CAD program BRAVO for preparation of the discretization mesh.

The use of a flattened elliptical beam with a window aspect ratio of 8:1 (aperture: 252 mm x 32 mm) or of a ring-shaped elliptical beam with a window aspect ratio of 3:1 (aperture: 156 mm x 52 mm) and a window thickness of about 1.75 mm in both cases allows a power transmission capability of at least 1 MW at 170 GHz (see Table 1).
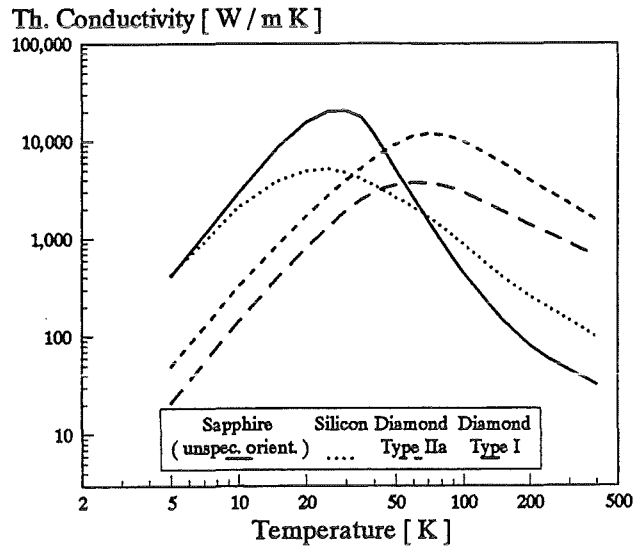
Fig. 1: Thermal Conductivity of Sapphire, Silicon and Diamond (recommended by Touloukian [4])
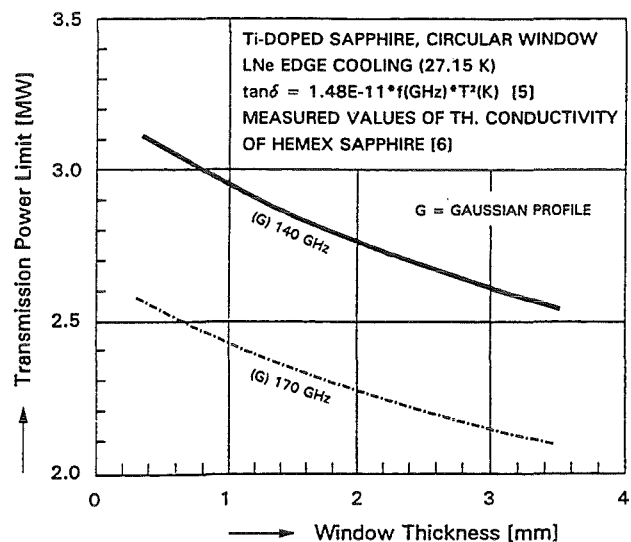
Fig. 2: Transmission Power Limit as a Function of Disk Thickness for Sapphire Windows with LNe Edge Cooling

3. Assessment and design of a non-cryogenic, large-aspect-ratio rectangular, water-cooled single disk torus window system

As an alternative to the distributed window concept [7] under development by the US-ITER Home Team, the EU-ITER Home Team considers a high-aspect-ratio rectangular waveguide window inclined at the Brewster angle. This concept will use water edge cooling of a single disk made out of silicon or diamond. The window assembly consists of a corrugated circular HE11 to corrugated square waveguide transition, a quais-optical corrugated rectangular wave-guide taper to e.g.

Table 1: Power transmission capability of medium aspect-ratio rectangular sapphire windows with LN$_2$ edge cooling

Aperture Size (mm^2)	Aspect Ratio	Elliptical Beam Profile F=flat A=annular	Max. Power Transmission (MW)		Absorbed Power (W)	
			140 GHz	170 GHz	140 GHz	170 GHz
252x32	8:1	F	1.28	1.06	374	376
270x30	9:1	F	1.40	1.17	411	430
156x52	3:1	A	1.27	1.00	315	316
180x45	4:1	A	1.45	1.20	349	352

Table 2: Power transmission capability of large aspect-ratio rectangular silicon and diamond windows (aperture: 680 mm x 12 mm) with water edge cooling

Material	thickn. (mm)	tanδ* [8]	ε$_r$*	k* (W/mK)	P$_{max}$ (MW)	T$_{max}$/T$_{min}$ (K)	Q$_{abs.}$ (W)
140 GHz							
Silicon	1.88	0.11E-4	11.7	148	1.44	395/294	882
Diamond	1.79	0.5E-4	5.7	900	1.78	365/293	1594
170 GHz							
Silicon	1.80	0.09E-4	11.7	148	1.76	394/294	850
Diamond	1.85	0.5E-4	5.7	900	1.76	364/295	1623

* average value at 300 K

200mm x 12 mm with the window, and the rectangular to circular HE11 back transition.

Calculations on the temperature distribution for large-aspect ratio rectangular Brewster windows (680mm x 12 mm) with water edge cooling at 293 K have been performed for 140 GHz and 170 GHz. The results are summarized in Table 2.

The calculations show that Au-doped Silicon (tanδ~1/f) and Diamond (tanδ≈const) are possible candidates even for 170 GHz, CW operation and will be considered in future design considerations.

4.   In-Beam Tests of a Liquid Nitrogen Cooled Sapphire Window at Garching

The series of experiments with a liquid nitrogen cooled sapphire disk operated in the pulsed beam of a Russian high-power gyrotron (140 GHz, 0.5 MW, 1 s) at Garching has been continued. The test facility - described in the last Annual Report - acts as a calorimeter such that the energy absorbed during a shot is obtained from measurements of the temperature increase after the shot.

During the first experiment series in December 1993 140 GHz gyrotrons pulses with power ranging up to 500 kW and 500 ms pulse length could be transmitted. Longer Pulses caused electric arcing or breakdown.

After some improvements a second experiment series followed in January 1995. Owing to a special cold-nitrogen gas flushing system the window calorimeter could be operated with only minor freezing and no rf arcing problems during a whole working day. The maximum pulse length has been 1.3 s at a puls power of nearly 400 kW. Within the experimental uncertainties, the measured loss tangent values of 8±4x10^{-6} in the temperature range between 87 and 95°K are in agreement with cold test measurements for HEMEX sapphire.

Literature:

[1]   H.E. Häfner, P. Norajitra, K. Müller, M. Thumm, "Conceptual Design and Thermodynamics Study of Cryogenically Edge Cooled Windows for ECR Plasma Heating", 18th SOFT, Karlsruhe/Germany, Fus. Techn. 1994, Vol. 1, pp. 505-508.

[2]   H.-E. Häfner, K. Heckert, P. Norajitra, R. Vouriot, A. Hofmann, N. Münch, H.-U. Nickel, M. Thumm, V. Erckmann, "Investigations of Liquid Nitrogen Cooled Windows for High Power Millimeter Wave Transmission", 19th IR&MM Waves, Sendai/Japan, 1994, JSAP Cat. No. AP941228, pp. 281-282.

[3]   (R. Heidinger, "Dielectric Measurements on Sapphire for Electron Cyclotron Wave Systems", Journal of Nuclear Materials 212-215 (1994), pp. 1101-1106.

[4]   Y.S. Touloukian, et al., "Thermophysical Properties of Matter", Vol. 2, IFI/Plenum, New York-Washington, 1970.

[5]   G. Link, R. Heidinger, "Modelling of Intrinsic mm-Wave Absorption in Low Loss Dielectrics With Complex Crystal Structure", Proc. of 18th Intern. Conference on Infrared and Millimeter Waves, Colchester/UK, 6.-10-09.93, SPIE Vol. 2104, pp. 64-65.

[6]   M. Cadeau, H. Rouillon, A. Marcou, "Mesures de Conductivite Thermique du Saphir", CEA-CENG/ DRFMC, Note SBT/CT/93-47, Novembre 1993.

[7]   C.P. Moeller, J.L. Doane and M. DiMartino, "A Vacuum Window for a 1 MW CW 110 GHz Gyrotron", 19th IR&MM Waves, Sendai/Japan, 1994, JSAP Cat. No. AP941228, pp. 279-280.

[8]   V.V. Parshin, R. Heidinger, B.A. Andrev, A.V. Gusev, V.B. Shmagin, "Progress Towards a Silicon-Based Window for High Power Gyrotrons", Proc. of the 7th Joint Russian-German Meeting on ECRH and Gyrotrons, FZK Karlsruhe/Germany, 21.-27.06.95.

Staff:

O. Braz
H.E. Häfner
K. Heckert
A. Hofmann
K. Müller
N. Münch
P. Norajitra
M. Thumm
R. Vouriot

Long Term Materials Programme

Introduction:

The present reporting report essentially covers the first year of the newly established Materials Long Term Programme 1995-1998. Within the coordinated Work Package structure the FZK contributions concentrate on the characterization of low activation ferritic-martensitic steels for First Wall and Blanket components and the first stages of a comprehensive irradiation programme. Main subject of the investigations is the Japanese very low Nb content steel F82Hmod in comparison with different heats of the OPTIFER-type low activation steels developed by FZK.

Subtask 1.2.1 deals with the Japanese steel and gives the results of quality assurance and homogeneity tests, whereas in Subtask 1.2.2 isothermal LCF and thermal fatigue testing is carried out. Fundamental work on the relationship between mechanical and thermal fatigue is reported.

Under Subtask 1.4.1 the results on the characterization of the different OPTIFER-steels are given.

Task 1.5 is devoted to pre- and post-irradiation, fracture toughness of ferritic steels as characterized by impact testing. Within Subtasks 1.5.0 and 1.5.1 investigations are underway to provide a full data base for the effect of temperature and dose on impact toughness and to demonstrate the superiority of the new low activation alloys as compared to the former MANET steels, for which the somewhat too high Cr-content may be responsible for their inferior impact properties.

Subtasks 1.6.1 and 1.6.2 are devoted to the effect of radiation hardening and He accumulation under simulated fusion reactor conditions. A special feature of these experiments is the possibility to apply cyclic mechanical loads during the irradiation.

Some technology related work has been started under Subtask 4.3.1 which deals with the material-related issues of diffusion welding.

Formally covered by a NET-Study Contract, the reporting on our share in the IEA-activity of a conceptual design for an intense neutron source with a fusion-relevant energy spectrum (IFMIF) has been included under the headline of the Materials Long Term Programme. FZK-contributions are in the areas of Neutronics, Test Cell/Test Matrix, and Lithium Target.

H.D. Röhrig

WP 1   Martensitic Steels

1.2.1   Metallurgical and Mechanical Characterization

The associated European Laboratories performed a quality assurance program and homogeneity tests on all delivered F82H mod.-plates. The program included the evaluation of hardness, grain size, content and kind of inclusions and chemical analysis.

- Vickers hardness measurements 200 HV 30 taken from 3 different sections with respect to the rolling direction showed reasonable agreement .This homogeneity is also confirmed by tensile data.

- The average grain size ranging between 50 and 110 µm, differs from lab to lab presumably caused by systematic errors and difficulties in the determination of the prior austenite grain size. To solve these discrepancies a short-program is arranged including the exchange of samples and methods.

- Several types of precipitates, i.e. primary and secondary carbides, and inclusions, mainly oxides of Al, Ti, Ta and Zr were detected and analyzed with respect to their size, shape, distribution and chemical composition (Fig.1). The as-delivered material also developed an absolutely delta-ferrite-free microstructure.
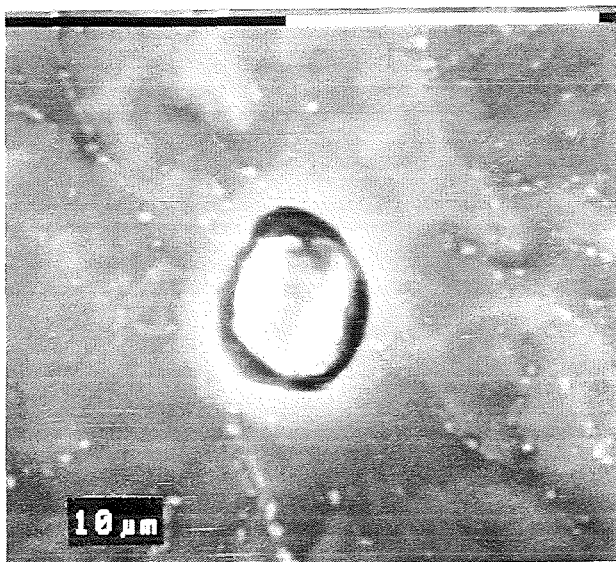

Fig. 1:   Al-Ta inclusion; the dark part of the inclusion contains Al_2O_3 and the bright part Ta-Ti-C

- The comparison of the content of the main alloying elements (Cr, W, Mn, V and C) shows good agreement. The applied analytical methods were XRF (X-ray fluorescence analysis) and OES (Optical Emission Spectroscopy).
  For Nb, an element which determines the long-term radioactivity, larger deviations between the different

laboratories were found ranging from 1 ppm (steel maker) as minimum to 100 ppm (FZK) as maximum values. FZK, CIEMAT/CENIM and PSI therefore agreed to elaborate a common concept how to analyze the "undesirable" impurity elements, which already in very low concentrations can dominate the long-term activation.

It can be concluded, that the material F82H mod. in the as-delivered state shows a very homogeneous microstructure and well balanced mechanical properties over the whole batch investigated by the European laboratories. Further work is needed with respect to the determination of the very small contents of trace elements which can have a detrimental effect on the desired low long-term activation.

Further microstructural investigations have been started by the determination of the content of carbide precipitates. By chemical extraction the carbides have been extracted, filtered and weighed. The carbide concentrations were 0.2 wt.% in the as received condition. After annealing between 650 and 800 °C the carbide contents increased up to about 2 wt.%.

The first investigations of the fractures showed inclusions in the ductile areas, a coalescence of Al_2O_3 and a Ta-rich phase, sometimes with W (Fig.1). These inclusions initiated most of the dimples. Only few inclusions could be found in the cleavage fracture of the lower shelf. The F82H mod has a very strong decrease in the impact transition. No fracture with 50% FATT could be analyzed. In a narrow temperature range sample fracture behavior both in the upper shelf and lower shelf regime could be found. This behavior must be analyzed systematically by microstructural and fractographic investigations.

The martensitic structure was tested with regard to thermal stability. The material was heat treated after the as received condition (1040 °C 38min + 750 °C 2h) and additionally with a further tempering for 0.5h or further quench and temper condition (1040 °C 0.5h and higher annealing temperatures). A partial decarburization of the matrix and hence the formation of ferrite grains at the annealing temperature of 875°C and higher was observed (Fig. 2).

The basic characterization of the Japanese LA-steel F82H mod., heat 9741, allows a first evaluation and comparison with the OPTIFER alloys. The transformation behavior is illustrated in the plotted TTT-diagram (Fig. 3). The A_c and M_s/M_f-values are at the same level as the OPTIFER alloys. The hardening and annealing behavior is comparable, but after an austenitization at 1040°C a relatively large grain size of about 60 - 65 µm exists; in comparison with 15 - 30 µm in the OPTIFER alloys.

In the temperature range from RT up to 700 °C the tensile strength and ductility values correspond to the values of the Ge-containing alloy after the standard heat treatment (1040 °C 0,5 h + 750 °C 2h) (Fig. 4). The Charpy-V-impact properties are more unfavorable in the temperature range of -60 °C and
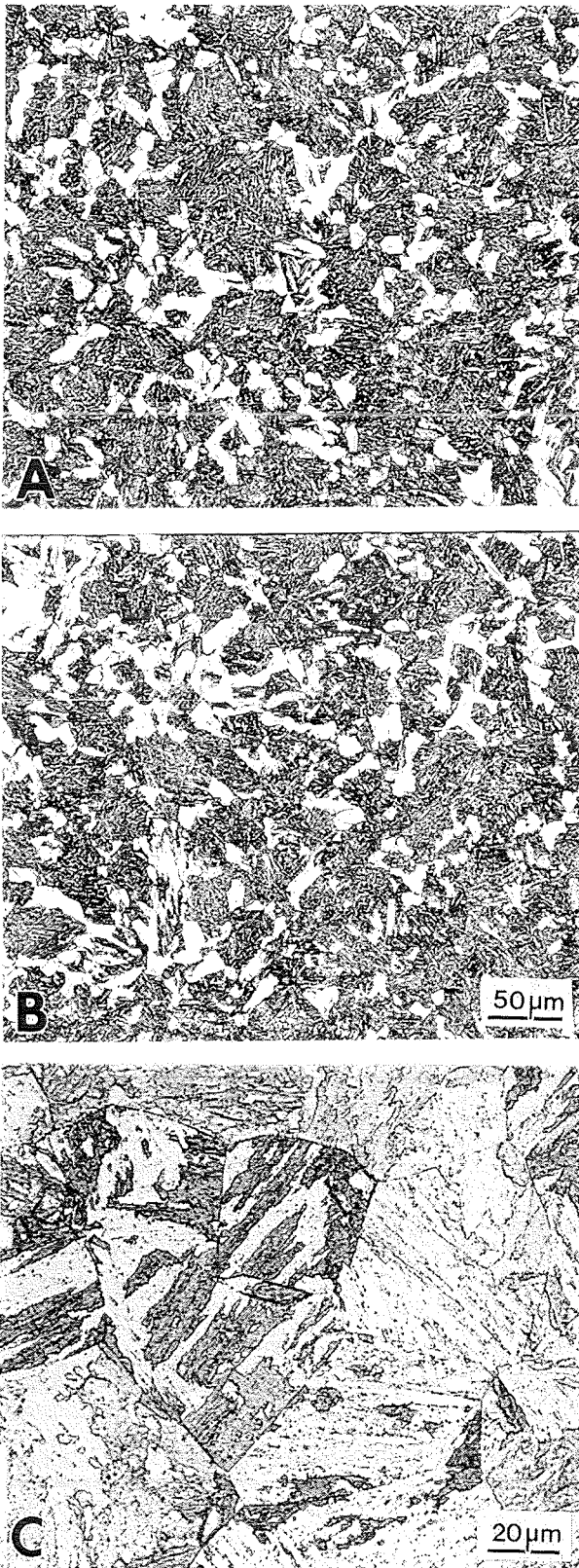
Fig. 2: A) Ferrite formation after as received condition and 875 °C 0.5h
B) Ferrite formation after as received condition and 1040 °C 0,5h + 875 °C 2h
C) Microstructure after 1040 °C 0,5h + 750 °C 2h

+80 °C. The FATT was determined at -20 °C compared with -43 °C of Ge-OPTIFER alloy.

The material has a wide range or potential in its heat treatment to get a fine grain for better mechanical properties. In order to discover the most advantageous tensile and impact properties the thermal treatment of austenitizing temperature and annealing temperature of the steel had been varied systematically. For the different thermal treatments in dependence of the test temperature the impact energy of the Charpy V-notch impact bending tests are shown in Fig. 5. The lowest DBTT of -55 °C could be obtained with a heat treatment of 920 °C/0.5h + 750 °C/1h. The tensile data of the as received conditions are summarized in Fig. 6. The tensile properties are located closely above and below the required value. Fig. 7 shows a combination of the 0.2%-yield strength (at 500 °C) and the DBTT in dependency of the different heat treatments. The best austenitizing temperature for high strength and low DBTT is 920 °C. Different combinations of strength and toughness can be selected using different annealing temperatures.

Staff:

E. Materna-Morris
M. Schirra
L. Schäfer
R. Lindau

Material : F82H-mod.　　　　　Heat-N⁰:9741
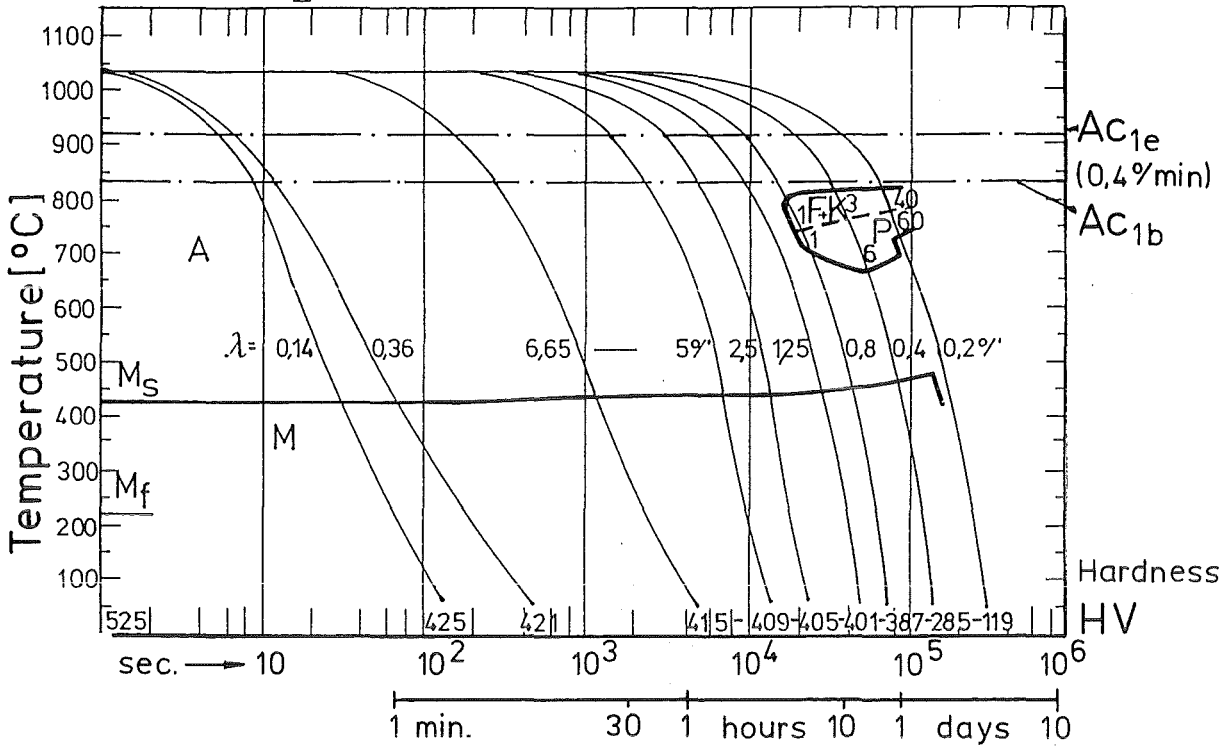
Austenitizing:1040°C 15 min　Grain-size(ASTM):7-8,+6

Fig.:　TTT-diagram for continuous cooling
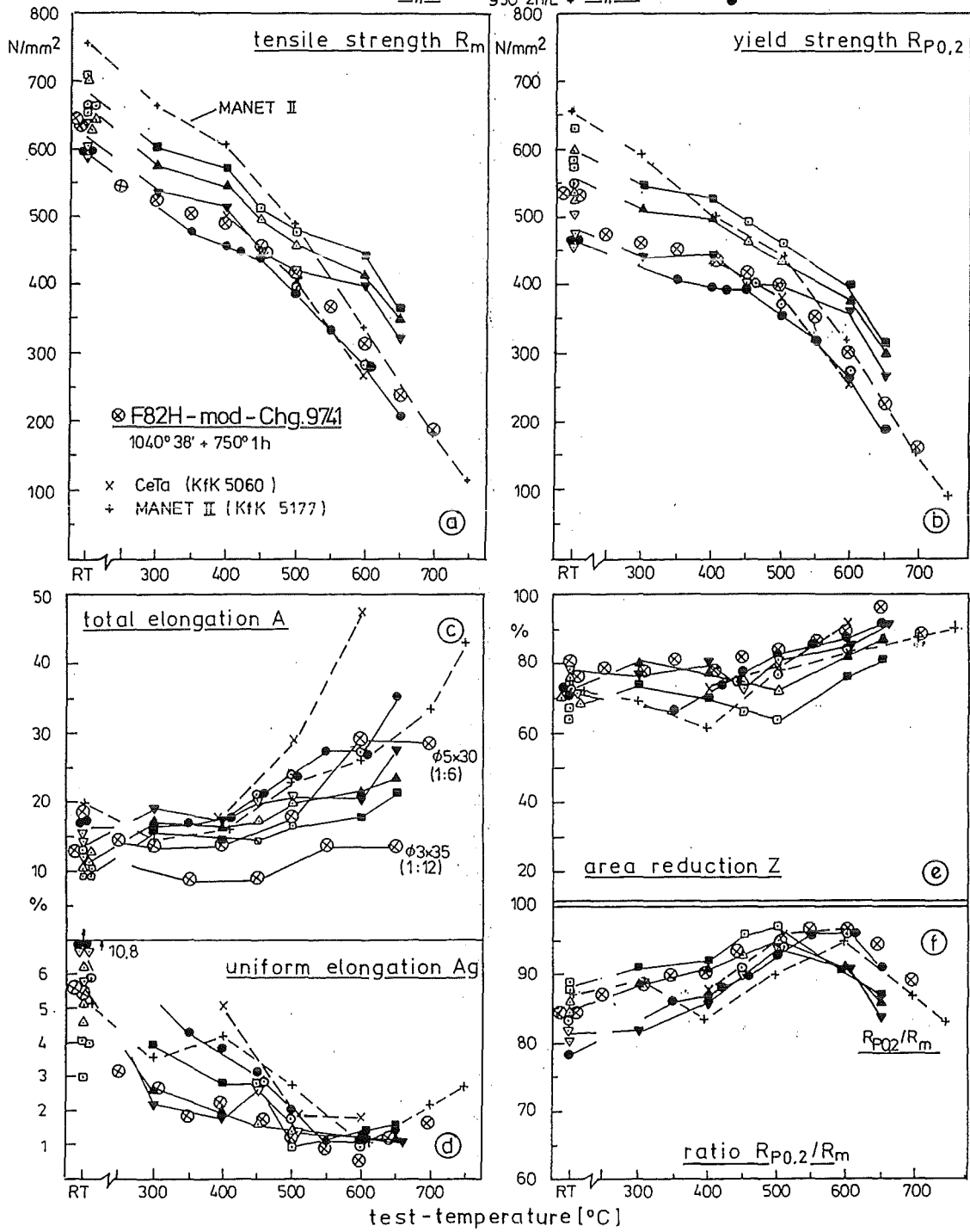
Fig. 3:　TTT-diagram for continuous cooling

Fig. 4: Tensile test result vs. test temperature for F82H mod. and OPTIFER alloys
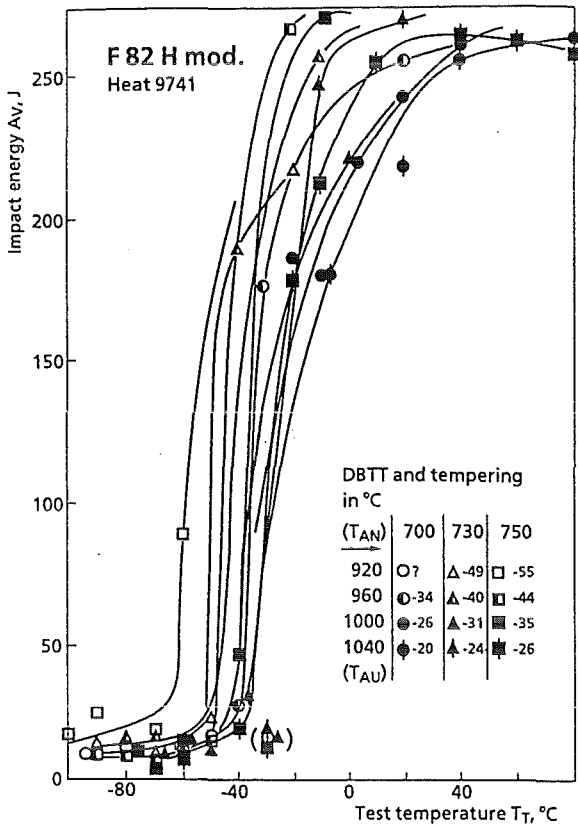
Fig. 5: Impact energy of the steel F82H mod. in different material conditions in dependence of the test temperature
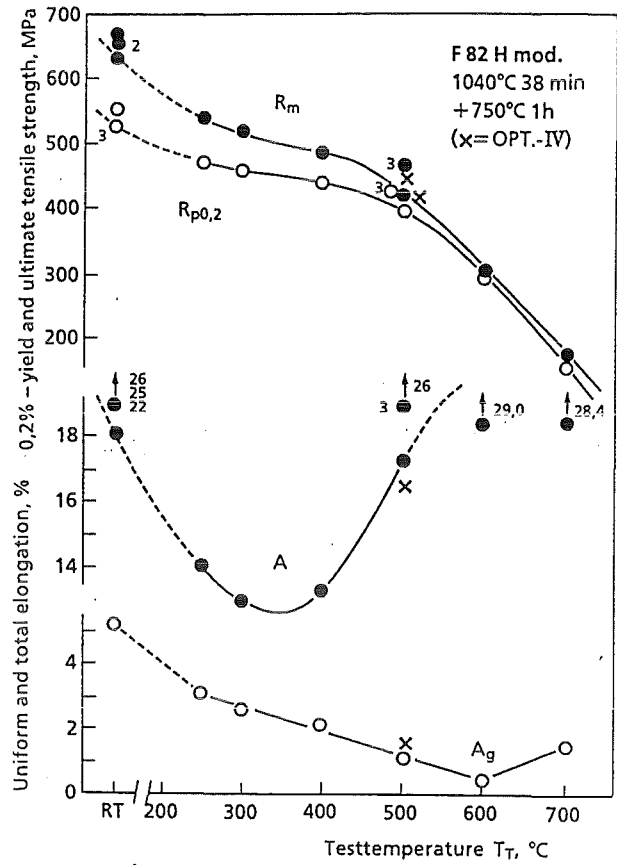
Fig. 6: Tensile properties of the steel F82H mod. in the materials condition 'as received'
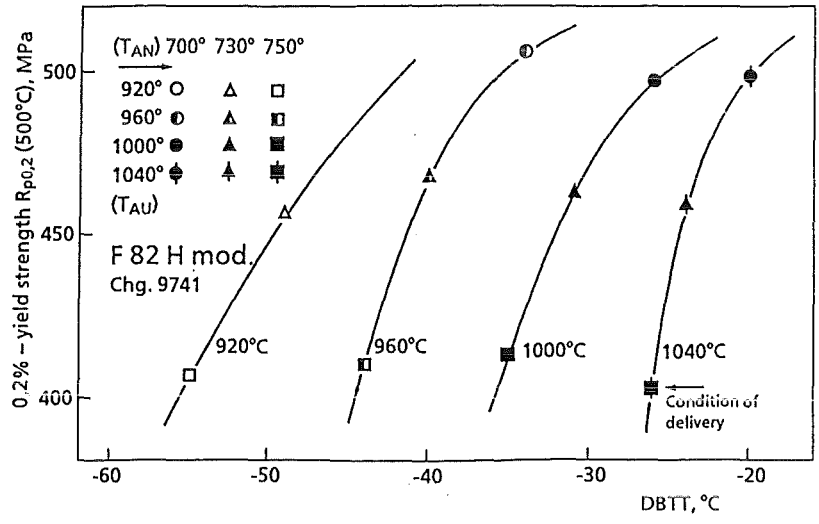
Fig. 7: 0.2%-yield strength and DBTT of the steel F82H mod. in different material conditions

1.2.2 (MANET 3.2)
Fatigue and Creep Properties of Base Material F82H mod

1. Life Prediction for Isothermal and Thermo-Mechanical Fatigue

Structural components of a DEMO-blanket are subjected during service to alternating thermal and mechanical stresses as a consequence of the likely pulsed reactor operation. Of particular concern is the fatigue endurance of martensitic steels like MANET and F82H mod under cyclic strains and stresses produced by these temperature changes. In order to design such structures, operating under combined mechanical and thermal cycling, fatigue life has to be calculated with reasonable accuracy. It is proposed to describe thermal and isothermal mechanical low-cycle fatigue data of MANET I and II steels by a single damage model, including plastic strain, temperature and strain rate as variables. This model presents notable advantages for the designer.

Currently, fatigue life prediction is based on isothermal fatigue data obtained at a chosen (often maximal operational) temperature. It has been shown that in some cases this approach is non-conservative. The generation of test data by thermal-mechanical fatigue experiments, simulating more accurately the service conditions, has thus become necessary. Nevertheless, these experiments are very expensive; they are neither standardized nor applied in design codes. Therefore, thermal fatigue resistance still has to be predicted from isothermal fatigue data.

The analysis of thermal and isothermal fatigue data had been performed in a wide range of temperatures, strains and strain rates, in order to extend a modified Manson-Coffin damage law.

In case of isothermal low-cycle fatigue (LCF) the average strain inbetween the ridges of the hourglass specimen was controlled. This results in an inhomogeneous redistribution of strain along the gauge length of the specimen, which is even amplified by the softening behaviour at various strain amplitudes.

Therefore, a detailed analysis was performed [1] to obtain a relation between the applied average strain range and the local strain range at half-life of the specimen, which is a decisive factor for the life evaluation.

It results in an iterative numerical procedure which adjusts cycle by cycle the parameters of the hysteresis loops to the load measured in the experiments. In the first approximation the total and plastic strain ranges in the central part of the specimen can be found, for each average strain range and each temperature. Figure 1 shows for a typical LCF hysteresis loop a good agreement between measured and calculated loop using this procedure.

For calculating the thermo-mechanical fatigue (TMF) hysteresis loops of hollow hourglass samples this analysis had
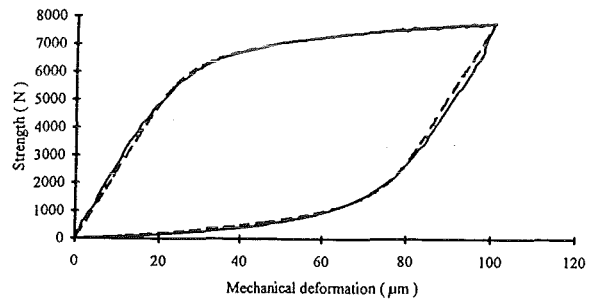

Fig. 1: Comparison between measured (full curve) and calculated (dotted curve) hysteresis loops of a LCF experiment at 550°C with a total strain of 1.33 %

to be modified by introducing a temperature dependance of the parameters. In Figure 2 is shown a typical TMF hysteresis
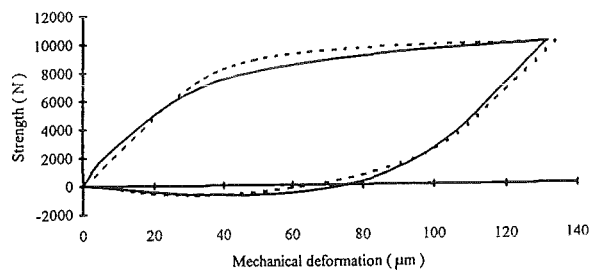

Fig. 2: Comparison between measured (full curve) and calculated (dotted curve) hysteresis loops of a TMF experiment cycling between 200 and 550°C with a total strain of 1.33 %

with a good agreement between the measured and the calculated loop using this procedure.

From literature (Degallaix et al. [2]) it is known, that the complete high temperature LCF behaviour, in a wide temperature range, can be described by considering that the damage process is controlled simultaneously by two kinds of mechanisms, depending upon the plastic strain range, athermal or thermally-activated. In case of LCF loading it was sufficient to use room temperature data, to determine, by a least-squares method, the values of the coefficients. It can be noted that the relatively small value of the apparent activation energy, $Q = 12$ kcal/mol, indicates that the contribution from thermally-activated mechanisms to the damage per cycle remains relatively weak, even at the highest temperatures, and thus, that the temperature dependence of LCF behaviour of the MANET steels is moderate.

Figure 3 shows the very good correlation between the experimental and calculated LCF-values. All points fall within a scatter band with a factor of 1.39.

Based on the Taira equivalence concept [3], the calculation of damage for TMF loading will be done on the stabilized hysteresis loop, using a linear damage rule. The damage will
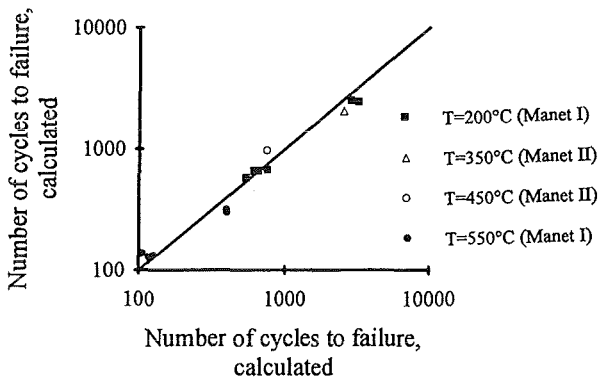
Fig. 3: Data correlation of MANET I and II for LCF loading using the modified Coffin model

be calculated from the elementary contributions of plastic strain, temperature and strain rate during the entire hysteresis loop.

The integration of the elementary increment of damage (assumed to be isothermal, and connected at each time with the increments of plastic strain and temperature) on the TMF cycle will give an estimation of the fatigue life.
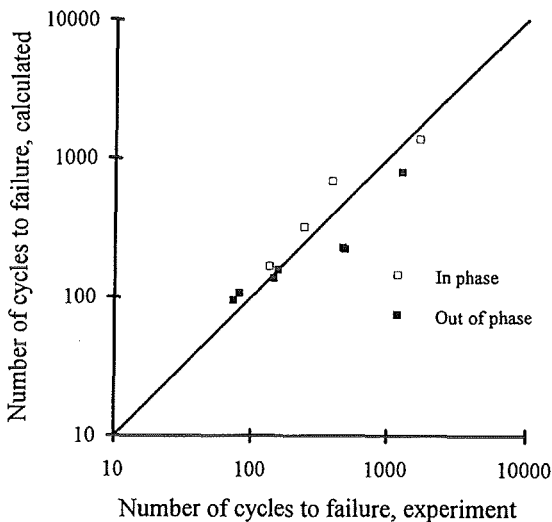
Figure 4 shows the good correlation between the

Fig. 4: Data correlation of MANET I for in phase and out of phase TMF loading between 200 and 550°C using the modified Taira model

experimental and calculated TMF-values.

Both damage models express the detrimental effect of higher temperatures on fatigue life. Moreover, the models present notable advantages for the designer. As they correspond to singles and continuous "fatigue strength surfaces", they enable a reliable interpolation to be made throughout the studied domain of strains and temperatures, and allow for

reasonable extrapolation out of this domain, provided that no different metallurgical phenomena occur [4].

2. Experimental Results

Isothermal and thermo-mechanical fatigue experiments with and without hold-times on MANET II are finished. The number of cycles to failure is slightly lower as compared to results of MANET I [5].

Since 25 mm thick plates of F82H mod are available now, preparation of cylindrical samples was initiated.

Literature:

[1] G. Degallaix, J. Rech, Y. Desplanques, C. Petersen and F. Wolter, Proc. of Int. Symp. Fatigue under Thermal and Mechanical Loading, Petten (N.H.), The Netherlands, May 22-24 1995, in press.

[2] G. Degallaix, MAT-TEC 90, Technologie, comportement et traitement des matériaux,Eds.: C. Bathias et al., IITT-Int. Publ. Paris (France), (1990), p. 37.

[3] S. Taira, ASTM STP 520 (1973), 80.

[4] C. Petersen, R. Schmitt and D. Garnier, Proc. of ICFRM-7, Obninsk, Russia, Sept. 25-29 1995, in press

[5] Nuclear Fusion Report, Annual Report of the Association FZK/EURATOM, Oct. 93-Sept. 94, FZKA 5515, EUR 16100EN, ed. G. Kast, Jan. 1995

Staff:

C. Petersen
M. Pfeifenroth
D. Rodrian
W. Scheibe
R. Schmitt
H. Schneider
W. Schweiger
(F. Wolter)

1.4.1 (LAM 3)
Metallurgical and Mechanical Characterization

The OPTIFER alloys have been developed in the frame of martensitic low-activation steels. The results of the physical and mechanical investigations on the OPTIFER alloys with W and Ta have been reported. A further heat alloyed with Ge is investigated now and has been patented in the meanwhile [1]. The characterizing tests of all alloys are finished and published [2].

The Ge-containing OPTIFER alloy shows in comparison to the Ta containing alloy a thermal retardation of the pearlite transformation. The behavior during hardening and annealing is comparable with the W-containing alloy. The tensile strengths are equivalent to the CETA alloy, but with the technological advantageous hardening temperature of 950 °C. In this way a predominant impact strength could be obtained as could be seen in Fig. 1. A final evaluation about the creep rupture strength and the creep behavior can be carried out after completion of long time tests.

In order to compare the different OPTIFER alloys all heats had been tempered at

$$900\,°C \quad 0.5h + 730\,°C \quad 2h.$$

This thermal treatment leads to a very good impact toughness [3]. The results of the impact tests are collected in Fig. 2. The impact energies measured in Charpy V-notched impact bending tests on ISO-V samples of the different OPTIFER alloys are shown in dependence of the test temperature. The DBTT's are the following:

OPTIFER-Ia, heat 664, DBTT = -91 °C

OPTIFER-Ib, heat 667, DBTT = -95 °C

OPTIFER-II, heat 668, DBTT = -64 °C

OPTIFER-III, heat 666, DBTT = -24 °C

OPTIFER-IV, heat 986489, DBTT = -110 °C

According to the DBTT, the alloy OPTIFER-IV showed the best results. In order to take advantage of the full potential of impact toughness for this steel, the thermal treatment had been varied. Fig. 3 shows the impact energy of the steel OPTIFER-IV in different conditions of heat treatments in dependence of the test temperature. During the systematic combinations of the quenching and annealing temperatures the following DBTT's for ISO-V-specimens (and for KLST-specimens in parenthesis) could be reached:

900 °C 0.5h + 700 °C 2h; DBTT = -102 °C (not measured)
900 °C 0.5h + 730 °C 2h; DBTT = -110 °C (-135 °C)
900 °C 0.5h + 750 °C 2h; DBTT = -118 °C (-136 °C)

950 °C 0.5h + 730 °C 2h; DBTT = -105 °C (not measured)
950 °C 0.5h + 750 °C 2h; DBTT = -111 °C (-137 °C)

1000 °C 0.5h + 730 °C 2h; DBTT = -93 °C (-86 °C)
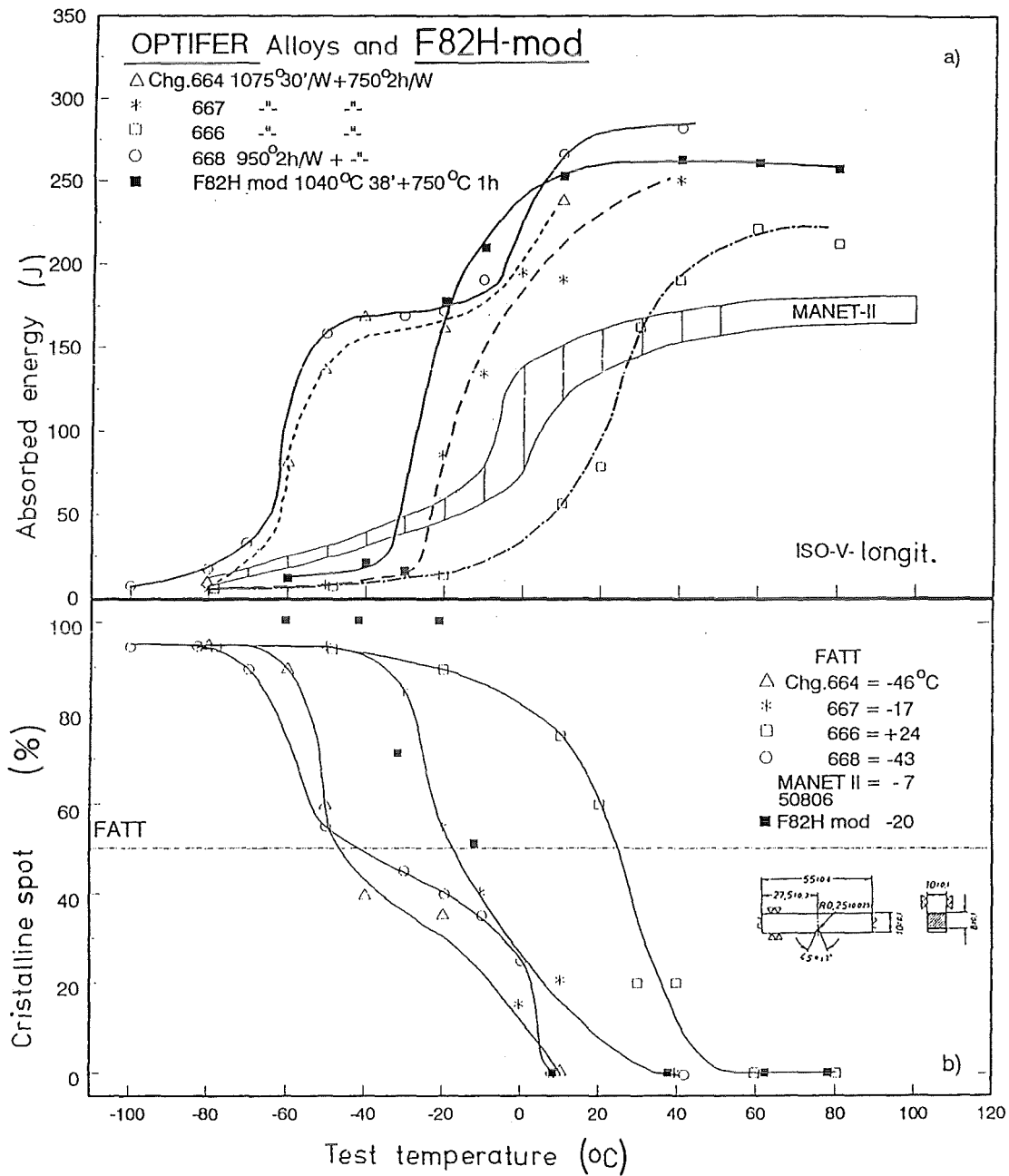1000 °C 0.5h + 750 °C 2h; DBTT = -100 °C (not measured)

The thermal treatment influences the impact toughness and the tensile strength countercurrently. Therefore it is useful to consider both properties together. The Fig.4 represents the 0.2%-yield strength (at 500 °C) versus the DBTT after different heat treatments. The best austenitizing temperature for high strength and low DBTT is 900 °C. One can select different combinations of strength and toughness using different annealing temperatures. The steel OPTIFER-Ia has the highest strength and the steel OPTIFER-IV has the best combination of high strength and toughness. Fig. 4 shows comparatively the dependencies of the different OPTIFER alloys.

The materials have been investigated in standard heat treatment in transmission electron microscopy. The alloys have a similar microstructure, with the exception of OPTIFER-III. This alloy is dominated by a TaC formation. The coarse carbides bind too much of carbon, so that the free carbon of the matrix is relatively low and the typical martensitic lath structure could not develop. A round coarse inhomogeneous grain size distribution occurred.

The carbide content has been determined by chemical extraction. The OPTIFER alloys Ia and II had about 2.2 wt.% of carbides after the standard heat treatment of 1075 °C 0.5h + 750 °C 2h.

Literature:

[1] M.Schirra, K.Ehrlich, L.Schäfer: Germanium enthaltender Stahl und seine Ver-wendung. Patent 44 32 516 vom 18.7.95.

[2] M.Schirra, K.Ehrlich, S.Heger, M.T.Hernandez, J.Lapena: OPTIFER, ein wei-terer Schritt zur Entwicklung niedrigaktivierender martensitischer Stähle. FZKA-Bericht 5624, September 1995.

[3] L.Schäfer, M.Schirra, K.Ehrlich: Mechanical properties at low-activation martensitic 8-10 CrWVTa steels of type OPTIFER. Paper presented at ICFRM-7, 25.-27.9.95, Obninsk, Russia.

Fig. 1: Impact energy and crystalline spot vs. test temperature. (FATT = Fracture Appearence Transition Temperature

Staff:

K. Ehrlich
E. Materna-Morris
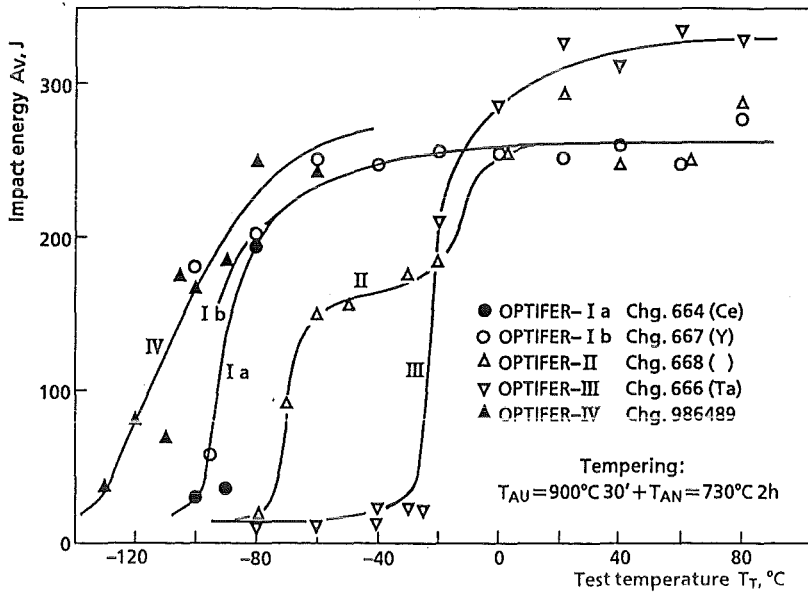D. Preininger
M. Schirra
L. Schäfer

Fig. 2: Impact energy of different OPTIFER alloys in the material condition 900 °C 0.5h + 730 °C 2h in dependence of the test temperature.
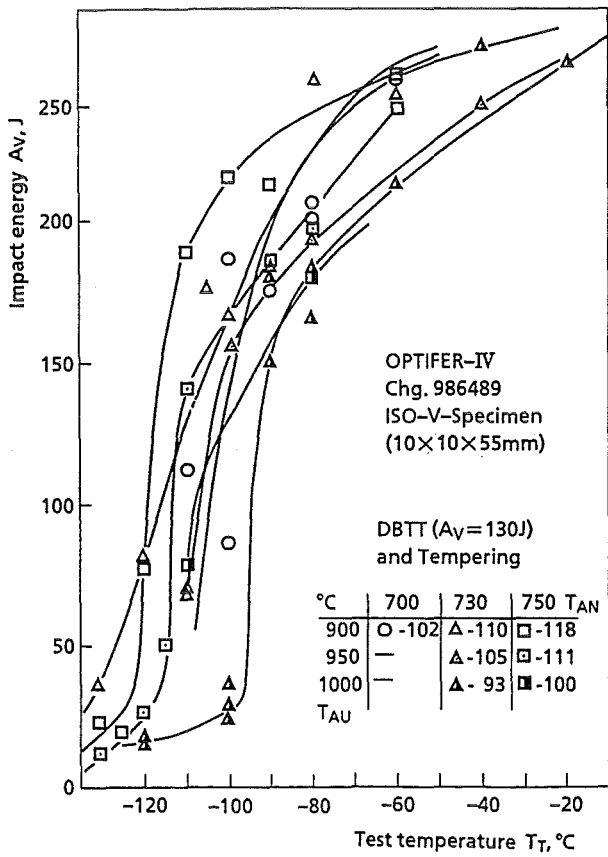

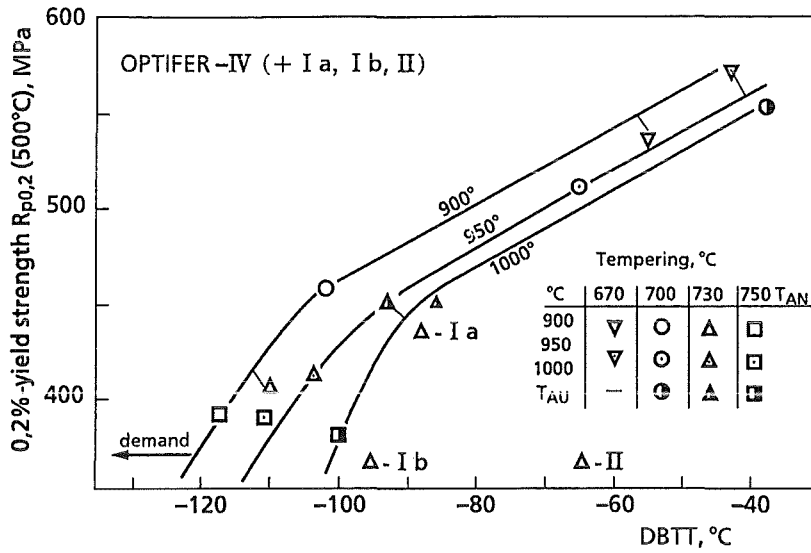Fig. 3: Impact energy of the steel OPTIFER-IV in different material conditions in dependence of the test temperature.

Fig. 4: 0.2%-yield strength and DBTT of the steel OPTIFER-IV after different thermal treatments.

1.5.0 / 1.5.1 (MANET 3.4)
HFR Irradiation MANITU / TESEO

1. Introduction

The problem of radiation-induced deterioration of fracture toughness remains to be a key issue for the application of ferritic/martensitic steels as structural materials for fusion reactors. In the previous investigation (SIENA program) it has been demonstrated that, after irradiation in a materials testing reactor to a dose of 10 dpa or even less, at temperatures around 300°C, the shift in Charpy impact properties of 10-12 % Cr steels , as characterized by an increase of the ductile-to-brittle transition temperature (DBTT) and a decrease of the upper shelf energy (USE), can be unacceptably high. In the context of these results there was, at that time, a vital interest to learn more about the evolution of this degradation with fluence and about the possibility of even more damage (or lack of annealing effects) at lower irradiation temperatures.

With these objectives the MANITU irradiation project was started with staged doses of 0.2, 0.8, and 2.4 dpa and temperatures between 250 and 450 °C as target values. During the planning of the experiment several new aspects came at right time, which enabled us to fill the available space in the rigs in addition to the MANET steels with specimens of different promising low-activation alloys and thus redirect the goals of the experimental program.

Up to now some of the results from the 0.2 dpa and most of the 0.8 dpa irradiation are available and allow us to draw interesting conclusions with respect to the temperature effect on impact properties and the improvement attained by the introduction of new alloys with both a reduced Cr-content and a reduced long-term activation.

2. Experiments

The heat treatments of the alloys have not in all cases been optimized to the utmost and may thus leave some room for further improvement. Table 1 gives the chemical composition of the steels with a ranking order of the alloying elements that facilitates the distinction of characteristic deviations and allows for numerous speculations about the influence of composition on the different impact properties before and after irradiation.

Charpy specimens have been produced from the available materials according to the European standard for subsize specimens. All tests have been carried out with the same, instrumented facility which is installed in the Hot Cells.

To elucidate the influence of irradiation not only the absolute but also the incremental values (ΔDBTT, ΔUSE, $\Delta\sigma$) are used.

The irradiations of the MANITU programme are all carried out in the HFR, Petten. The target value of 0.8 dpa was reached within about -2 % and +15 % depending on the core position of the specimens. The irradiation temperatures of 250, 300, 350, 400, and 450 °C were maintained within about ±5 % by a proper balance between n,γ-heating and compartment cooling with different He-Ne mixtures. A total number of 180 specimens (or at least 5 for each material and temperature) ensured a sufficient number of measurement points in order to connect and group them to curves with the irradiation temperature as abscissa and the materials as parameter.

3. Results

Fig. 1 shows the USE as a function of irradiation temperature. The number of curves can be divided into two groups where the low activation alloys (LAA) generally maintain a high impact toughness in the whole temperature range, whereas the MANET steels behave much poorer but show some recovery above 350 °C. The same picture, although a little more complex, is conveyed from a presentation of the incremental values, ΔUSE, normalized to the USE before irradiation, as shown in Fig. 2. The second message from this figure is that the decrease in fracture toughness of the MANET steels is - in contrast to the LAA - dramatic below 350 °C for doses as low as 0.8 dpa.

If we now look at the DBTT curves (Fig. 3) we find again that the MANET steels behave quite bad at the low irradiation temperatures, whereas the LAA are significantly better and the ORNL steel even outstanding. At the higher irradiation temperature the picture changes in a way that DBTT of all materials attains (or maintains) values below 0 °C. The shift in DBTT as shown in Fig. 4 reveals essentially the same behaviour, but here it comes out somewhat clearer that the ORNL steel shows a deterioration at the high temperatures. At present we would like to refrain from any speculation concerning helium embrittlement or the like.

Dynamic yield stress measured at 100 °C and its incremental values, as shown in Fig. 5 and 6, shows a similar tendency as DBTT. This leads to an interesting correlation between DBTT and σ_{Dy}, and ΔDBTT and $\Delta\sigma_{Dy}$, respectively, showing a common, almost straight line for all materials (Fig. 7 and 8). It is significant that the LAA are suffering less of irradiation hardening and less of irradiation induced embrittlement compared to the MANET steels. A promising result is the behaviour of the ORNL steel. Within an acceptable degree of irradiation hardening it shows almost no increase in low temperature embrittlement.

4. Conclusions

● All materials show irradiation hardening which decreases with higher irradiation temperatures. The dynamic yield stress and the irradiation induced shift of the conventional MANET steels is much higher at low irradiation temperatures compared to the low activation alloys.

● Among all examined materials the ORNL steel shows the very best embrittlement behaviour after neutron

Table 1: Chemical composition of the different alloys in wt.%

	10-11 % Cr-NiMoVNb steels		low activation alloys			
	MANET I	MANET II	OPTIVER Ia	OPTIVER II	F82H std.	ORNL
Cr	10.8	9.94	9.3	9.43	7.73	8.9
W			0.965	0.005	2.06	2.01
Ge				1.1		
N	0.02	0.023	0.015	0.016	0.0027	0.0215
C	0.14	0.1	0.1	0.125	0.092	0.11
Mn	0.76	0.79	0.5	0.5	0.083	0.44
Ta			0.066	ca. 0.02	0.018	0.06
P	0.005	<0.006	0.0047	0.004	0.003	0.015
S	0.004	<0.007	0.005	0.002	0.003	0.008
V	0.2	0.22	0.26	0.28	0.189	0.23
B	0.0085	0.007	0.006	0.006	0.003	<0.001
Si	0.37	0.14	0.06	0.038	0.09	0.21
Ni	0.92	0.66	0.005	0.005	0.032	<0.01
Mo	0.77	0.59	0.005	0.005	0.0053	0.01
Al	0.054	<0.02	0.008	0.008	0.01	0.017
Co	0.01	<0.02			0.0024	0.012
Cu	0.015	<0.01	0.035	0.007	0.0059	0.03
Nb	0.16	0.14	0.009	0.009	0.0057	
Zr	0.059	0.034				<0.001
Ce			<0.001	<0.001		
Ti			0.007	0.007	0.0104	<0.01
Fe	balance	balance	balance	balance	balance	balance

irradiation. Below irradiation temperatures of 400°C the already minor deterioration in DBTT remains practically constant.

• Though the low neutron fluence of this irradiation experiment does not yet allow to draw general conclusions, it can be stated that all examined low activation materials provide clearly better impact properties than the corresponding MANET alloys. Looking at the remarkably favourable irradiation embrittlement behaviour of the ORNL steel a solution of the embrittlement problem within fusion applications seems to be possible with ferritic-martensitic Cr-WVTa alloys.

• Further irradiation experiments have to verify these encouraging results with the low activation alloys at higher and especially more fusion relevant dose levels. Besides, the complexity of temperature dependency will probably be reduced with higher fluences.
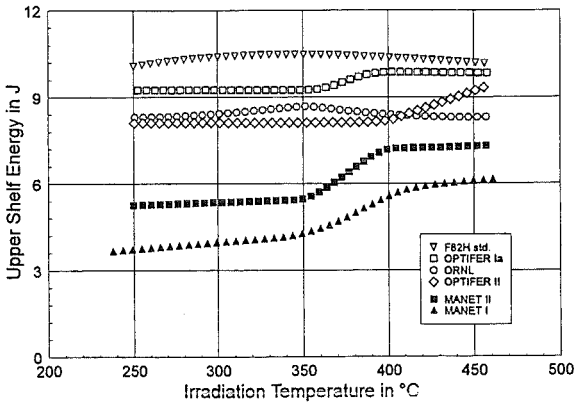
Fig. 1: Upper Shelf Energies vs. irradiation temperature (param.: materials)

Fig. 4: Irradiation induced shifts of Ductile-to-Brittle Transition Temperature vs. irradiation temperature (param.: materials)

Fig. 2: Irradiation induced shifts of Upper Shelf Energy vs. irradiation temperature (param.: materials)

Fig. 5: Dynamic yield stresses measured at 100 °C vs. irradiation temperature (param.: materials)
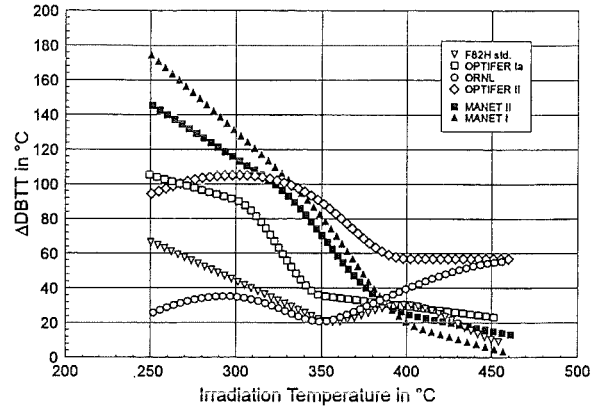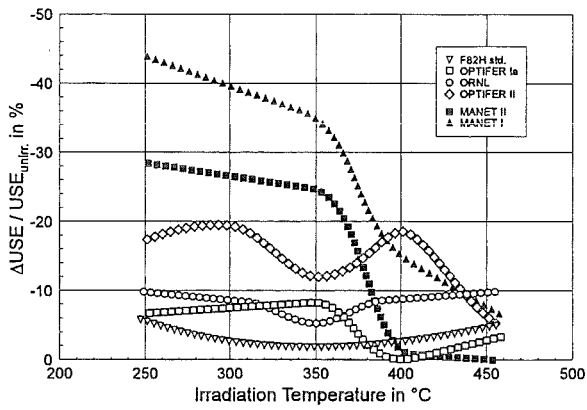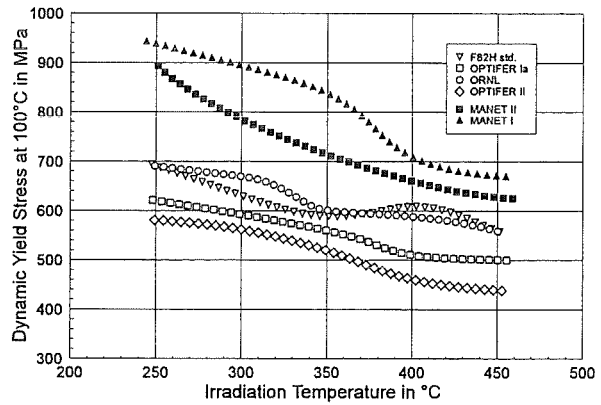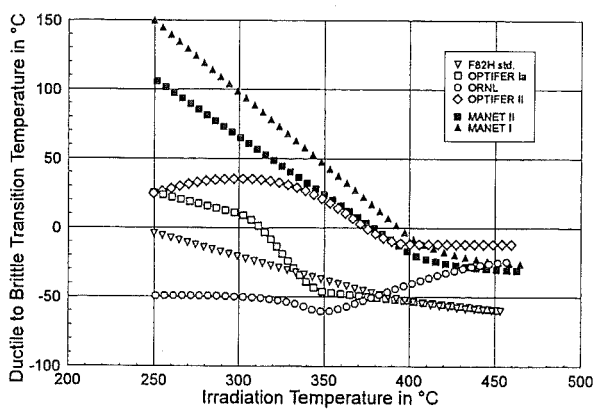

Fig. 3: Ductile-to-Brittle Transition Temperatures vs. irradiation temperature (param.: materials)
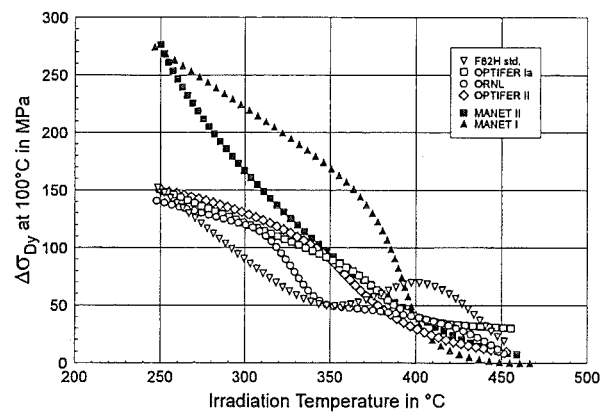

Fig. 6: Irradiation induced shifts of dynamic yield stress vs. irradiation temperature (param.: materials)

Fig. 7: Embrittlement vs. hardening
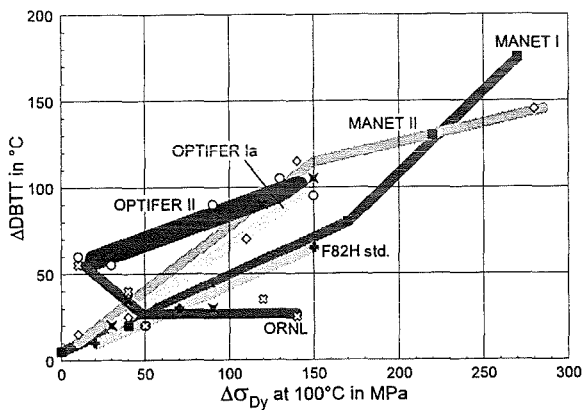
Fig. 8: Shift of embrittlement vs. shift of hardening

Literature:

[1] M. Rieth, B. Dafferner, H.D. Röhrig, C. Wassilew, Fusion Engineering and Design 29 (1995) 365-370.

[2] M. Rieth, B. Dafferner, H. Ries, O. Romer, Bestrahlungsprogramm MANITU: Ergebnisse der Voruntersuchungen und der Kerbschlagbiegeversuche mit den unbestrahlten Werkstoffen, Forschungszentrum Karlsruhe, Wissenschaftlicher Bericht FZKA 5550, April 1995.

[3] M. Rieth, B. Dafferner, H. Ries, O. Romer, Bestrahlungsprogramm MANITU: Ergebnisse der Kerbschlagbiegeversuche mit den bis 0,8 dpa bestrahlten Werkstoffen der ersten Bestrahlungsphase, Forschungszentrum Karlsruhe, Wissenschaftlicher Bericht FZKA 5619, Oktober 1995.

[4] M. Rieth, B. Dafferner, H.D. Röhrig, Charpy Impact Properties of Low Activation Alloys for Fusion Applications after Neutron Irradiation, Seventh International Conference on Fusion Reactor Materials, Obninsk, Russia, 25-29 September, 1995.

[5] M. Rieth, B. Dafferner, Low Temperature Embrittlement Behaviour of different Ferritic-Martensitic Alloy for Fusion Applications, Seventh International Conference on Fusion Reactor Materials, Obninsk, Russia, 25-29 September, 1995.

Staff:

B. Dafferner
A. Drasl
W. Kunisch
H. Ries
M. Rieth
O. Romer

1.6.1 / 1.6.2 (MAT 5)
Effects of Radiation Hardening and He in LAM / In-Beam Fatigue

Task 1.6: Mechanistic Investigations

The Dual Beam Facility of FZK, where a-particles ($\leq$ 104 MeV) and protons ($\leq$ 40 MeV) are focussed onto a target, was developed as a research tool for materials within the European Fusion Technology Programme. This high energy Dual Beam Technique allows the simulation of fusion neutrons by systematic variation of hydrogen, helium, and damage production in thick metal and ceramic specimens as well as the simulation of Tokamak relevant thermal and mechanical loads in proposed plasmafacing materials.

Next Tokamak fusion devices such as the International Thermonuclear Experimental Reactor (ITER) are characterized by the pulsed plasma burn and off-burn periods. These dynamic operating conditions causing oscillating temperatures and temperature gradients are responsible for fatigue and creep fatigue of the structural components. The combination of fatigue and additional neutron irradiation is considered as the most important lifetime-limiting failure mode of first wall materials. After several years of development novel experiments can be performed at the cyclotron facility of FZK, which allows a close simulation of realistic fusion conditions by simultaneous irradiation and fatigue loading.

Simultaneous irradiation and fatigue, can develop a different microstructure resulting in an inherent modified material response. Strain controlled in-beam fatigue of ferritic-martensitic 12 % Cr steel MANET under -particle irradiation has been performed at T = 420 °C [1]. For temperatures above 400 °C the superposition of irradiation induced hardening and radiation-enhanced strength recovery is observed. For fusion reactor operation a lower temperature range between T = 250 °C and 300 °C is discussed, a range where significant irradiation induced mechanical material deterioration is expected. Therefore special emphasis was laid on the analysis of the stress response MANET steel on strain-controlled push-pull fatigue at T = 250 °C during irradiation, without irradiation and after irradiation. A major concern is also the role of the microstructure.

1. Experimental

The different strain controlled isothermal fatigue tests have been conducted with hollow fatigue specimens made of the modified 12 % Cr-steels MANET I and II in the standard heat treatment [1] with the following test conditions:

2. Mechanical Properties

2.1 Stress response and lifetime limit

Low cycle fatigue is commonly regarded as the most appropriate mechanism for the characterization of the specific fatigue life of fusion-relevant materials. Low cycle fatigue is usually described by the Coffin-Manson law, which correlates

Temperature	250 °C
Environment specimen outside	vacuum $\leq 5 \times 10^{-3}$ Pa
Environment specimen inside	purified He-gas
Damage production rate	$(1.0\text{-}1.7) \times 10^{-6}$ dpa/s
Helium production rate	$(6\text{-}10) \times 10^{-4}$ appm He/s
Helium contents:	
Post-irradiation	400 appm
In-beam	18-320 appm
Fatigue mode	continuous push-pull cycling, (R = -1)
Strain range $\Delta\varepsilon$	(0.45-1.0)%
Strain rate $d\varepsilon/dt$	8×10^{-4} s^{-1}

the number of cycles to failure with the plastic strain range. Nevertheless, the dependency of lifetime and stress shows a much better agreement than of lifetime and plastic strain as can be seen from Fig. 1 where the total stress amplitude of
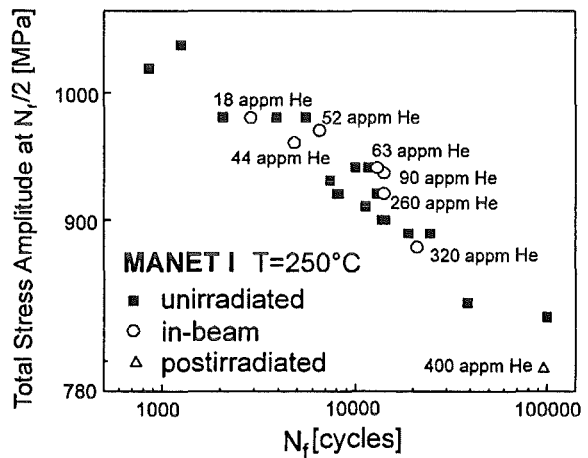
Fig. 1: Lifetime of in-beam, postirradiation and nonirradiation fatigue experiments

MANET I at $N_f/2$ is plotted as a function of N_f.

All the fatigue lifetimes of unirradiated, in-beam and postirradiated specimens are grouped in a scatterband along a line following Basquin's law

$$N_f (\Delta\sigma)^\alpha = \text{const.}$$

which normally applies only for high cycle fatigue.

2.2 In-beam versus postirradiation fatigue

Fig. 2 shows a comparison between in-beam, post-irradiation
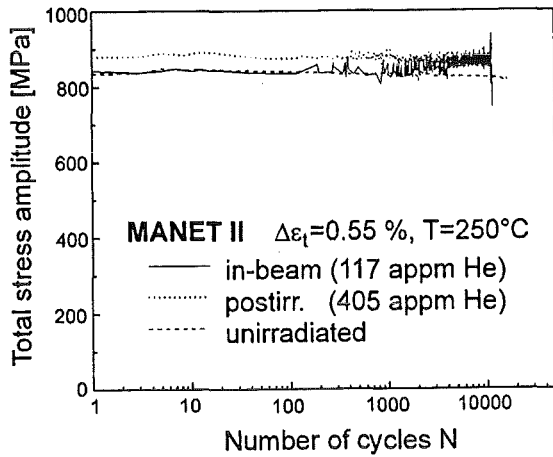
Fig. 2: Stress response of in-beam, post- and nonirradiation fatigue

and non-irradiation fatigue tests for MANET II.

At a total strain range of $\Delta\sigma_t = 0.55$ % the lifetimes for the in-beam and the postirradiation tested specimens are in the same range around $N_f = 11000$ wheras the lifetime of the unirradiated tested specimen is roughly 50 % higher. The shape of the curves can be explained by the microstructural evolution. Fatigue testing leads to a cyclic softening, that, typical for ferritic steels, becomes apparent in a continuous decline of the stress amplitude and - in terms of microstructure - in the formation of subgrains and dislocation cells. The higher stress amplitude of the post-irradiation tested specimen can be attributed to hardening by irradiation induced obstacles like helium bubbles which impede the cyclic motion of dislocations during deformation. Nevertheless, the same slope of both curves points to the same fatigue mechanism in this strain range. This hardening accelerates crack propagation and consequently reduces fatigue life.

The stresses of the unirradiated and in-beam specimen are, naturally, the same at the beginning of the fatigue tests, exhibiting in this phase only a slight softening.

After about one thousand cycles the competing processes, cyclic softening and irradiation induced hardening, become apparent. The hardening begins to dominate the stress response of the in-beam specimen until the stress of the postirradiation specimen is reached and the specimen fails.

2.3 Postirradiation fatigue at higher strain ranges

Fig. 3 gives a comparison between postirradiation (400 appm He) and nonirradiation fatigue of MANET II for $\Delta\sigma_t = 0.7$ %. The post-irradiation tested specimen exhibits the typical irradiation hardening (Fig. 3a). During fatigue both specimens show cyclic softening which is significantly stronger for the postirradiated specimen at this strain range and also stronger than the softening at $\Delta\sigma_t = 0.55$ % which leads to the assumption that the fatigue mechanism has changed. Obviously the higher applied strain range effects an
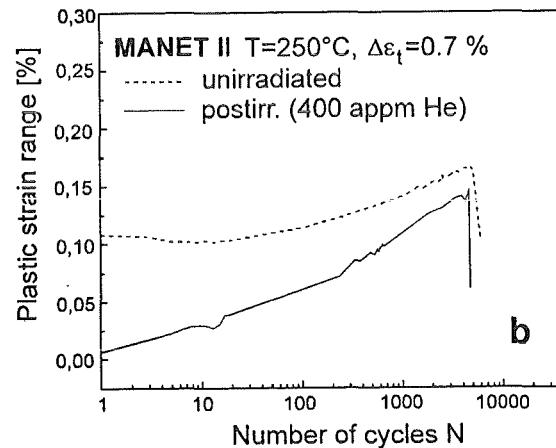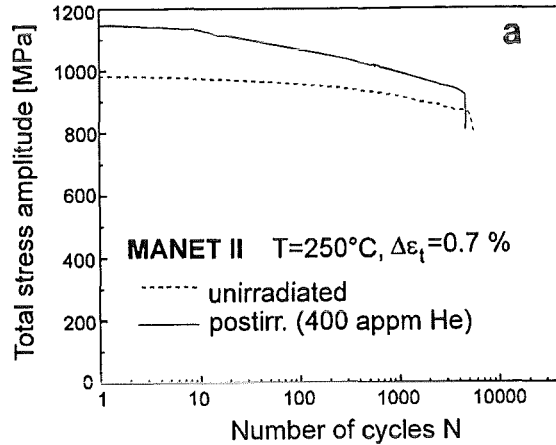
Fig. 3: (a) Stress response and (b) plastic strain range of postirradiation fatigue at $\Delta\sigma_t = 0.7$ %

unlocking of the pinned dislocation lines resulting in a higher number of dislocations cyclically moving on their slip planes. This is expressed macroscopically by a strength recovery and leads also to the typical fatigue subcell microstructure.

The difference in lifetime between unirradiated and postirradiated specimen is lower than for lower strain ranges. The original irradiation induced loss of mobility of dislocations means a loss of plasticity. This is shown in Figure 3b), where the plastic strain range of the irradiated specimen starts significantly lower than the plastic strain range of the unirradiated specimen. The softening is expressed by an increase of the plastic strain ranges. The distance between the plastic strain ranges decreases with increasing number of cycles.

3. Conclusions

(1) The lifetime of in-beam and unirradiated MANET I specimens in strain controlled fatigue experiments at a fusion relevant temperature of 250° C is well described by Basquin`s law using the total stress amplitude at $N_f/2$.

(2) In-beam fatigue slows down softening and irradiation in-duced hardening occurs. The lifetime is shorter than for nonirradiation fatigue.

(3) Postirradiation fatigue shows higher stresses from begin-ning and earlier failure. At higher strain ranges fatigue efor-mation can effect a certain strength recovery.

Literature:

[1]   R.Lindau, A.Möslang, Journal of Nuclear Materials 212-215 (1994) 599.

[2]   J. Bertsch, R.Lindau, A.Möslang, Proc. 7th Intern. Conf. on Fusion Reactor Materials ICFRM-7, Obninsk, Russia, Sept., 25-29, 1995

[3]   R.Lindau, A.Möslang, Journal of Nuclear Materials 179-181 (1991) 753.

[4]   R.Lindau, A.Möslang, Journal of Nuclear Materials 191-194 (1992) 915.

Staff:

S. Baumgärtner
G. Bürkle
D. Preininger
G. Hecker
R. Lindau
A. Möslang

WP 4   Materials Application and Technology

4.3.1   (MANET 2.3)
Weldability Tests (Diffusion Welding)

The quality of diffusion weldings of the steel MANET-II had
been tested and reported in [1]. In order to verify and com-
plete these results, some specimens for tensile-, bending- and
impact bending tests have been fabricated and the tests have
been started.

A new heat of a low activating martensitic steel had been de-
veloped and ordered in order to carry out future diffusion
welding tests with such an advanced material.

Literature:

[1]   G. Haufler, Diffusionsschweißen von Probeplatten aus
       MANET 2 für gekühlte Blanketstrukturen (Abschlußbe-
       richt), KE Stuttgart, 1-TB-241/94 (1994)

Staff:

L. Schäfer

Neutron Source

ERB 5000 CT 950013 NET (NET 94-366)
Conceptual Design of the Lithium Target and of the Experimental Test Assembly of the D-Li Neutron Source (Phase 1)

After a Conceptual Design Activity (CDA) study on an International Fusion Materials Irradiation Facility (IFMIF) has been launched under the auspices of the IEA, working groups and relevant tasks have been defined and agreed in an IEA-workshop that was held September 26-29, 1994 at Karlsruhe [1]. The Mission of IFMIF is to provide an accelerator-based, Deuterium-Lithium (D-Li) source to produce neutrons with a suitable energy spectrum at sufficient intensity and irradiation volume to test samples of candidate materials to full lifetime of anticipated use in fusion energy reactors.

To evaluate technical concepts, critical issues and urgent tasks, three subgroups have been identified at the Karlsruhe workshop, September 1994:

- Accelerator System
- Lithium Target System
- Test Cell System

During summer 1995 another subgroup, the Design Integration Group, has been established.

IFMIF-CDA on Test Cell System

For the Test Cell System 11 tasks were identified which can be grouped into the three major fields neutronics, test matrix/users and test cell engineering. In order to discuss recently achieved results and to coordinate necessary activities for an effective design integration, a technical workshop on the Test Cell System was initiated. This workshop was organized on July 3-6, 1995 by the Institute for Materials Research at the Forschungszentrum Karlsruhe and attended by 20 specialists working in the fields of neutronics, fusion materials R&D, and test cell engineering in the European Union, Japan, and the United States of America.

The presentations and discussions during this workshop have shown, together with the elaborated lists of action items, that on the basis of already existing concepts and computer codes significant progress has been achieved in all three fields, and that from the future IFMIF experimental program for a number of materials a database covering widespread loading conditions up to DEMO-reactor relevant end-of-life damage levels can be expected [2].

1. Neutronics

For conceptually designing the IFMIF test cell with its loadings, detailed neutron transport calculations are required. The most suitable method is the continuous-energy Monte-Carlo method in the form of the code MCNP ("Monte Carlo Neutron and Photon transport") from Los Alamos National Laboratory. However, nuclear data for incident neutron energies up to 50 MeV have to be provided because the nuclear data files developed for deuterium-tritium fusion do not consider energies beyond 20 MeV.

At the CDA level, there are three alternative possible approaches for obtaining the required nuclear data:

1. use data from a standard fusion file with a simple extrapolation beyond 20 MeV, e.g., by keeping each cross section constant between 20 and 50 MeV,

2. calculate cross sections by advanced methods of nuclear reaction theory,

3. perform full-fledged evaluations of experimental cross section data. (This quality of the nuclear data will be indispensable in later stages of the IFMIF design.)

Approach 1 has been used by the US team and has been useful to obtain approximate information at a very early stage. These results (and similar ones from JAERI) were presented and discussed at the IFMIF Test Cell Workshop in July 1995, organized by and held at FZK. They confirm earlier recommendations that a beam spot size of 5 cm x 20 cm is a good compromise between maximum test volume, small flux gradients, and flexibility of the test cell configuration. They also indicate that an increase of beam energy from 30 to 40 MeV would roughly double the high-flux test volume; however, serious reservations with respect to the correspondingly increased high energy tail of the neutron spectrum could not be dissipated. Therefore, uncertainty analyses mainly on gas production and transmutation rates, taking into account neutron energies up to 50 MeV, are urgently needed.

Approach 3 of the above list is being pursued by JAERI. It represents a major effort which will take several years.

At FZK, approach 2 is used. By cooperation with the Institute of Nuclear Power Engineering (INPE), Obninsk, Russia, complete cross section data in the ENDF/B-V1 format (including double-differential cross sections) are obtained, in which the parts beyond 20 MeV are calculated using state-of-the-art theoretical modeling. They will be processed at FZK for use with the MCNP code. At the time of writing, data files have been completed for Fe-56, Na-23 and K-39, the principal nuclides of steels and NaK coolant. After their processing, which is underway, these files will enable better neutronic calculations to be performed for both gas-cooled and NaK-cooled conceptual loaded test cells, in order to ensure that IFMIF will adequately simulate the neutronic environment in fusion reactors.

Staff:

C. Broeders   U. von Möllendorff
I. Broeders   D. Woll
U. Fischer

2. Test Matrix / Users

For the high flux region, equivalent to a > 2 MW/m^2 first wall neutron loading, detailed specimen loading matrices have been elaborated. Assuming a beam-on-target availability of 70% in this high flux test volume of approximately 0.5 liter, damage levels of 15 to 40 dpa/year can be achieved. The present loading matrix is based on 7 miniaturized specimen geometries, it allows within a ten to twenty year program the irradiation up to DEMO-relevant lifetime doses in a wide temperature range, and different heats from all three reference structural materials (ferritic/martensitic steels, vanadium alloys and SiC/SiC composites) will be included. In contrast to former concepts the specimens are encapsulated to avoid a direct interaction with the coolant.

While the high flux region has to provide materials data based on postirradiation examinations, the medium low and very low flux regions are important for selected in-situ tests for a design data base on structural materials and allow instrumented tests on special purpose materials (e.g. Rf windows, diagnostic materials, ceramic breeding materials, superconducting materials). Although such experiments often require sophisticated techniques, significant progress has been achieved during the last few months. Even for in-situ tests with controlled mechanical loadings design concepts are available in the meantime. However, a comprehensive matrix of reference in-situ and instrumented tests including out-of-cell equipment requirements, has still to be established.

Initial listings of the equipment necessary to perform the various postirradiation tests on miniaturized specimens at the IFMIF facility show, that beside standard hot cells for structural materials with an estimated area requirement of nearly 500 m^2 additional space will be necessary for tritium handling hot cells. An advanced hot cell facility designed for post-irradiation examination of various kind of miniaturized specimens ("modular type hot cell") was also proposed.

3. Test Cell Engineering

An advanced design concept based on NaK as coolant is available for the high flux test chamber. It can also be applied to conventional instrumented tests in lower flux test regions. NaK is suitable within the temperature regime of interest for metallic structural materials, and its heat capacity guarantees sufficiently good temperature control during beam-on and beam-off periods. On the other hand, experiences with various helium gas cooled reactor and accelerator devices together with recent calculations have shown, that helium gas as a coolant allows similar package densities in the high flux region, but has significant advantages e.g. with respect to the allowable temperature window, safety considerations and overall test cell flexibility. However, additional investigations for the helium cooling option are urgently needed to guarantee temperature stability for "loss of beam" conditions and to establish an integrated test assembly design. Therefore, a competing assessment of both concepts,

necessary for a design integration, was postponed by a few months.

Finally, design concepts for the entire set of test assemblies were discussed, and preliminary shielding analyses including estimations of the thickness of the test cell walls, were performed. Figure 1 shows an elevation view of the present Test Cell design, which has been significantly changed. All vertical test assemblies are accommodated together with the Li-target in one common test cell without any barrier between the Li-target backwall and the high flux test assembly. The test cell has a vacuum vessel which also serves as a steel liner for the confinement of radioactive material in off-normal events.

Several advantages are combined having a common test cell:

- The produced activity is concentrated in the lowest possible volume.

- The common test cell without barrier improves the Li-target access and allows maximum usage of the high flux test volume.

- The common vacuum environment ($\sim 10^{-1}$ Pa) meets several safety requirements and simplifies interface considerations between test assemblies and target as well as between test cell and accelerator beam lines.

Literature:

[1]   K. Ehrlich and R. Lindau, Proceedings of the IEA Technical Workshop for an Intern. Fusion Materials Irradiation Facility; KfK, 26. - 29. Sept. 1994, FZKA report 5553 (1995).

[2]   A. Möslang and R. Lindau, Proceedings of the IEA-Technical Workshop on the Test Cell system for an Intern. Fusion Materials Irradiation Facility; FZK, 3. - 6. July 1995, FZKA report 5633 (1995)

Staff:

E. Daum
K. Ehrlich
R. Lindau
A. Möslang

4. Lithium Target System

For the Lithium Target System seven tasks were identified. In order to exchange the current results of the study and to coordinate the activities for the design integration, the first technical workshop on the lithium target system was held in

the period of July 18-21, 1995, at the Tokai Research Establishment of the JAERI [3].

In the working groups it has been agreed, that the reference option for the lithium target should consist of a lithium jet with one free surface (towards the deuteron beam) and a back wall (towards the test cells). In this design the evaporation behaviour of lithium at the free surface is of major importance. Therefore our activities have been concentrated on the following problems:

1.   Modelling of the heat deposition in the lithium jet

2.   Thermal hydraulic analysis of lithium jet with incident beam.

1.   The profile of the deposited heat due to the stopping of the deuterons has been calculated for monoenergetic and gaussian-shaped energy distribution of the beam. Accurate models for both electronic and nuclear stopping powers were utilised.
A comparison with other studies showed, that there are significant differences in the literature in the position of the heating peak as well as in the shape of the heating profiles. However these differences influence the thermal hydraulic response of the lithium jet, which is effective on the maximum temperature of the free surface and consequently on the boiling margin and evaporation rate. The calculated heating profile displayed also a significant dependence on the temperature profile in the lithium target.
In the further work, a study of the sensitivity of these

two quantities (boiling margin and evaporation rate) on the heating profile is necessary.

2.   The thermal hydraulic response of the lithium jet with incident beam was simulated with the widely tested finite element code FIDAP (Fluid Dynamics Analysis Package).

The IFMIF reference target was modelled in the following conditions:

●   two-dimensional curved geometry (radius = 250 mm), stationary jet;

●   average velocities between 2 and 20 m/s;

●   heating-up based on the power deposition calculations, beam energy 35 MeV, current 250 mA;

●   strong coupling between the velocity and temperature fields (i.e. in the momentum and energy conservation equations, the temperature dependence of the lithium properties and the buoyancy force were included).

The temperature and velocity fields have been obtained for two initial velocity profiles: uniform (slug profile) and parabolic. The maximum temperature at the free surface, the temperature profiles across the jet at different positions along the jet and the pressure distributions were particularly monitored (Table 1). These informations allow us to calculate the boiling margins in the jet and at the free surface, and the evaporation rate.
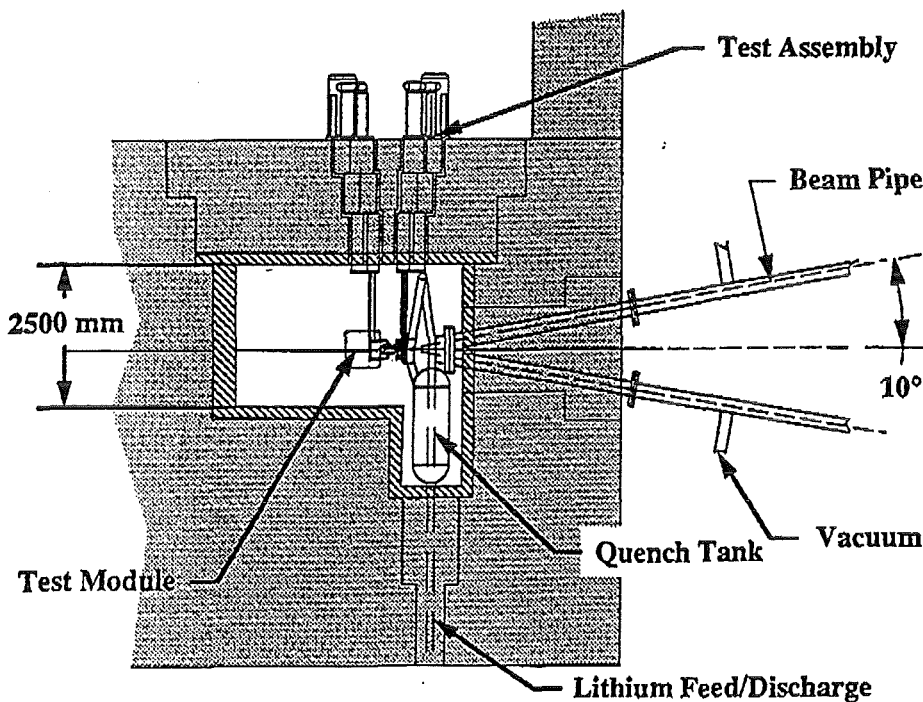

Fig. 1:   Elevation view of the present test cell design of IFMIF

Table 1: Parametrisation of the jet average velocity

Average jet velocity	m/s	10	12.5	15	17.5	20
Average jet temperature	°C	271	261	255	250	246
Jet maximum temperature	°C	585	517	470	437	410
Free surface maximum temperature	°C	294	279	270	263	257
Maximum pressure difference	Pa	4230	6660	9550	13100	17000
Free surface minimum boiling margin $(10^{-4}$ Pa)	°C	5	20	29	36	42

Typical results of temperature distribution in the jet are presented in Fig. 2 together with the contour plot of the calculated heating deposition.

Most of the results for the reference IFMIF target are consistent with those of Japanese and American partners [3].

We found that the temperature distribution is strongly dependent on both the initial velocity profile and the heating profile. The most important dependence was observed for the maximum temperature on the free surface.

The work will be continued with an improved simulation of the heating profile , taking into account the temperature distribution in the jet. The velocity distribution at the nozzle outlet will be accurately simulated. The influence of the problem parameters on the boiling margin and the evaporation rate will be analysed within a sensitivity study.

Literature:

[3]   Proceedings of the IFMIF-CDA Technical Workshop on Lithium Target System, July 18-21, 1995, JAERI 95-019, Tokai, Japan
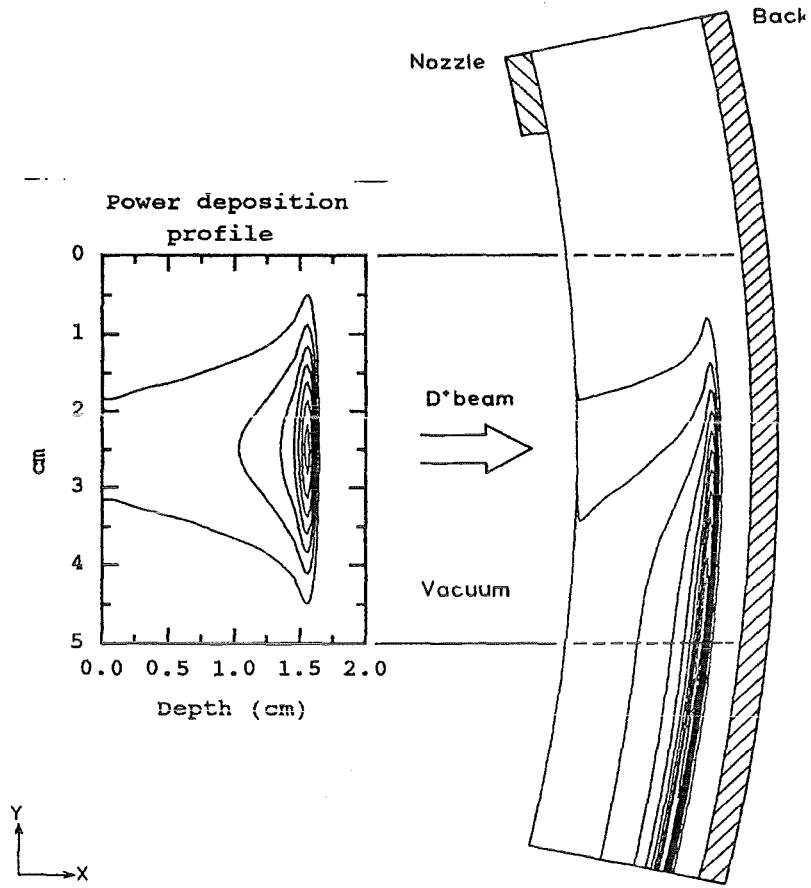
Staff:

W. Cherdron
W. Schütz
I. Tiseanu

Fig. 2: Temperature distribution and the contour plot of the power deposition for the reference IFMIF target (average velocity = 17.5 m/s)

Blanket Development Programme

Introduction:

Within the European Fusion Technology Programme four different blanket concepts have been developed for the future demonstration reactor DEMO:
A water-cooled Pb-17Li liquid metal (WCL) concept, a selfcooled Pb-17Li liquid metal-cooled concept with helium-cooled first wall (the dual coolant concept DCL), a helium-cooled solid breeder-in-tube (BIT) concept, and a helium-cooed solid breeder-out-of tube (BOT) concept.

The blanket development programme was started in 1989 and has mainly been carried out by CEA, ENEA and FZK, with smaller contributions from JRC Ispra and ECN Petten. The work has been coordinated by the Blanket Coordination Group (BCG). It is foreseen to select, in a European Blanket Concept Selection Exercise (BCSE), by the end of 1995 the two most promising concepts for further development within the European long term programme beyond 1995. This includes the design and construction of test blanket modules for testing in ITER.

Up to now the FZK work concentrated on the BOT and DCL concepts.

The Solid Breeder Blanket Tasks (BS)

The solid breeder design work (Subtask BS DE-D) includes also small scale thermomechanical and fabricability tests and safety oriented studies. The FZK solid breeder material programme (Subtask BS BR-D) has concentrated, in agreement with the European partners, on lithium orthosilicate. This subtask includes preparation, characterization, irradiation and postirradiation examination as well as measurement of the physical, chemical and mechanical properties. Of special interest are the in- and out-of-pile tritium release studies, performed at FZK and within the common breeder development programme in several European reactors. The behaviour of irradiated beryllium, especially the influence of large neutron fluences and high temperatures on swelling, embrittlement and tritium trapping as well as the inpile compatibility of beryllium with ceramic and structural material is being investigated in subtask BS BE-D.

The main non nuclear testing facility to prove the feasibility of FZK's solid breeder design is the helium loop HEBLO, in which elements as well as canister sections can be tested (Subtask BSNN-D).

The Liquid Metal Blanket Tasks (BL)

The design activities (Subtask BL DE-D) concentrated on a solution featuring an inboard / outboard selfcooled blanket with a helium cooled first wall, the so-called Dual Coolant Concept.

Of great importance to the development of the selfcooled blanket is the knowhow and the data base of magneto-hydrodynamic (MHD) behaviour of liquid metal flow aquired in theoretical and experimental studies of subtask BL MHD-D. The test facility MEKKA and the cooperation with Argonne National Laboratory play a central role in the MHD development.

In addition to design and MHD activities FZK studies the physico-chemical behaviour (Subtask BL PC-D), especially corrosion of structural materials in the lithium lead eutectic (Pb-17Li) and the behaviour of impurities (Polonium) including methods of clean-up. The Pb-17Li loops TRITEX and PICOLO are the main testbeds for the experimental studies.

A critical issue for selfcooled liquid metal blankets is the development and qualification of electrically insulating coatings to reduce the MHD pressure drops in the blanket. This work including the assessment of irradiation effects is being performed in subtask BL EI-D.

Safety and reliability studies are being performed in subtask BL SA-D.

A. Fiege

BS DE-D   Design Work

1.   Demo Blanket Design Work

The design work on the BOT solid breeder blanket for application in a DEMO reactor is part of the European Blanket Development Programme in which four blanket concepts are developed with the aim to select in 1995 the two most promising concepts for further development [1].

The thermomechanical analysis has been completed for the last reference blanket concept with cooling plates [2, 3] shown as isometric view in Fig. 1. The aim of the analysis has
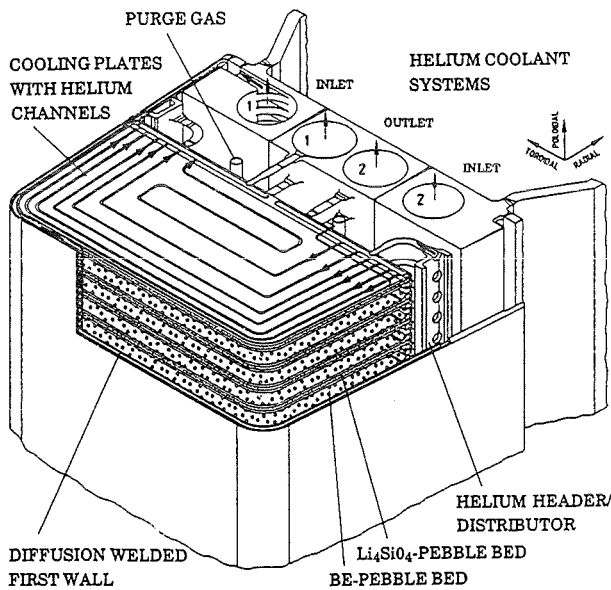

Fig. 1:   Layout of an outboard blanket segment in an isometric representation (detail around the torus equatorial plane).

been to demonstrate that the blanket temperatures and stresses are within permissible limits. More details of the calculations are given in [4]. A short summary of the main results and design data is presented in Table 1. The temperature and stress calculations were carried out for both cases of average and maximum surface heat loads of the First Wall of 0.4 and 0.5 MW/m², respectively, by using the FE-program ABAQUS [5]. The results of stresses were evaluated with respect to the ASME-Code [6]. In the evaluations of stresses the stress safety factor for the welding seam according to DIN 18800 has been set at 1.0 as recommended in [7] in case of static loading and 100 % examination of the welding seams (First Class Quality Control). The results show that all temperatures and stresses are well below the design basis   Figures 2 and 3 show the FE models used in the temperature and stress calculations.

Further improvements on design details have been made, among others concerning the welding techniques applied to connect the cooling plates and the blanket box. Figure 4 shows e.g. an alternative solution of build-up welding for connecting the cooling plate with the First Wall. This allows

Table 1:   Summary of main results and design data

A) Thermohydraulics	Out-board segment	In-board segment
First Wall heat flux [MW/m²]		
- maximum	0.5	0.5
- average	0.4	0.4
Max. power density [MW/m³]		
- MANET	25	22
- ceramic	37	33
- beryllium	15	12
Helium cooling:		
- total power to be extracted (nuclear-power+surface heat flux) [MW]	36	23
	8	8
- pressure [MPa]	250/450	250/450
- temperature inlet/outlet [°C]	35.6	22
- mass flow rate [kg/s]	75	50
- max. velocity in cooling channels [m/s]	0.3	0.26
- pressure drop in segment [MPa]	0.4	0.36
- total pressure drop in the whole helium loop [MPa]	520	510
- max. temperature [°C]	910	890
. First Wall	640	600
. ceramic	550	545
. beryllium	500	495
. ceramic/steel interface	350	350
. beryllium/steel interface	2.40	1.33
- min. ceramic temperature [°C]**		
- pumping-power* [MW] (total for one reactor: 158 MW)		

*) Blower efficiency of 80 % is assumed.
**) 300-350 °C at the rear edge (0.2% of tot. cer. volume).

B) Mechanical stresses in outboard segment, calculated for maximum surface heat load	
Boundary conditions:	
- internal pressure [MPa]	8
- FW surface heat load [MW/m²], average/ maximum	0.4/0.5
Max. FW temperature [°C], at external plasma side of FW	520
von Mises stresses [MPa]:	
- primary membrane (helium header)	189
limit set by ASME	227
- primary membrane+bending (helium header)	258
limit set by ASME	341
- primary+secondary (external plasma side of FW)	332
	452
limit set by ASME	
max. permissible internal pressure of the segment box during operation (extrapolated) [MPa]	9.6

to better control the welding seams but requires, on the other hand, a larger radial distance of the points connecting
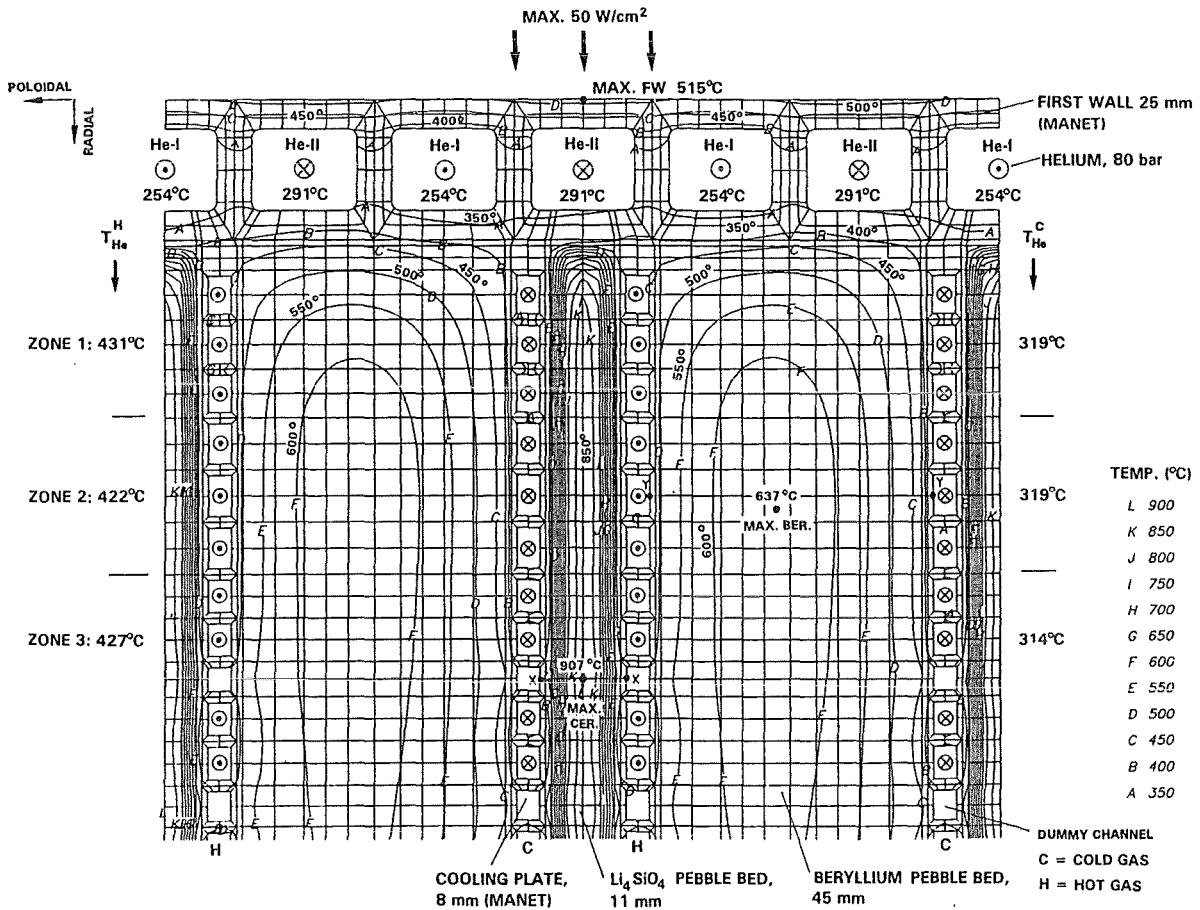
Fig. 2: Radial-poloidal Section of the FW and Blanket in the Front Part of the Outboard Blanket at the Torus Equatorial Plane.
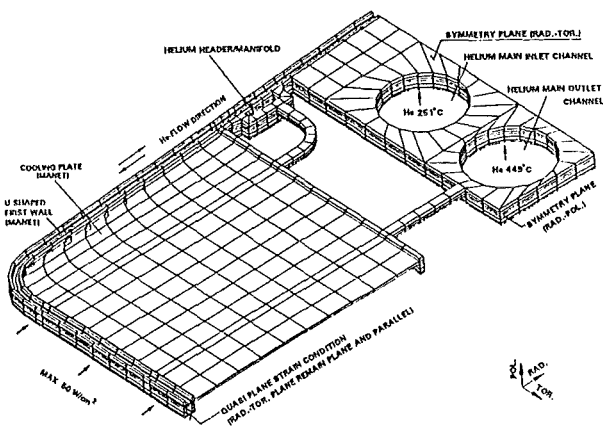
Fig. 3: Isometric View of a Poloidal Portion of the Outboard Blanket used for the FEM Calculations.

Fig. 4: Arrangement of Cooling Plates with an Alternative Solution of Welding (Buzild-up Welding).

the plates to the First Wall. This causes an increase in helium temperature in the First Wall, due to the additional heat transfer from the pebble beds to the First Wall cooling channels.

Moreover, in the last overall structural design of the blanket an improvement has been made consisting in a slight extension of the poloidal height of the blanket segment in order to achieve a greater tritium breeding ratio. The recent

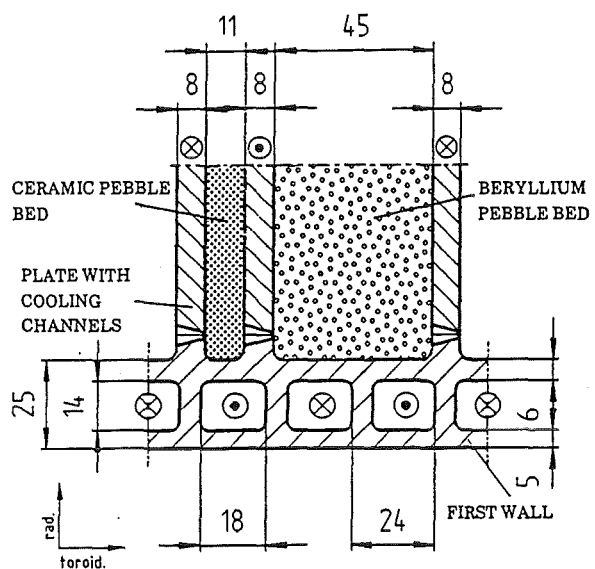neutronics calculations have shown that the maximum power densities in ceramic, beryllium and steel decrease by about 5 %, 4 % and 3 %, respectively. These two modifications lead to an increase of the maximum FW temperature to 530 °C, which is still quite acceptable, and to a decrease of the maximum temperature in the ceramic to 890 °C, while the maximum temperature in the beryllium maintains the same value of Table 1.

To improve the weldability and to minimize the distortion of the structure the design of the joint between FW and cooling plates has been changed. The new design is shown in Fig. 5.
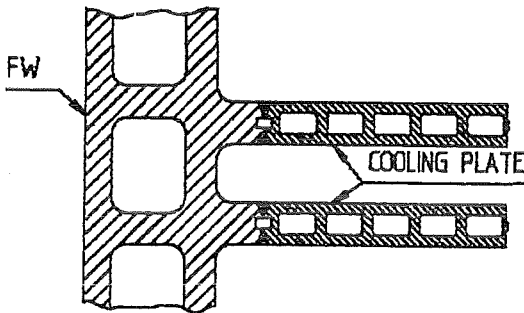

Fig. 5:   Weld connection between First Wall and cooling plates (new design).

After all cooling plates are fixed in the U-shaped FW mechanically or by point welding to stabilize the FW segment each plate will be welded to the FW from both sides. In the old design it was planned to weld all plates from one side. The new design decreases the volume of the weld and the heat load in the material and causes a reduction of shrinkage and distortion of the structure. No preheating is necessary because the maximum thickness of the weld is smaller than 6 mm. A thermal analysis has been carried out because the distance between FW and cooling channel in the plates increases to a maximum value of 14 mm (dependent on the used welding method). The maximum steel temperature in the cooling plates amounts for this case to 521 °C which is still acceptable.

Another alternative solution for arrangement in the rear blanket part of the helium main supply channels of the cooling systems (Fig. 6), including assembly flow, has been investigated.

Literature:

[1]   S. Malang, L. Anzidei, M. Dalle Donne, L. Giancarli, E. Proust, European Blanket Development for a DEMO Reactor, 11th TMTFE, New Orleans, Louisiana, USA, June 19-23, 1994.

[2]   M. Dalle Donne, U. Fischer, P. Norajitra, G. Reimann, H. Reiser, European DEMO BOT Solid Breeder Blanket: The Concept Based on the Use of Cooling Plates and Beds of Beryllium and Li4SiO4 Pebbles, 18th SOFT,
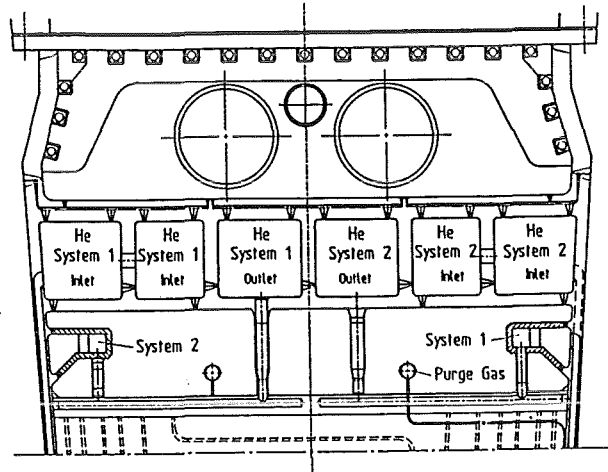
Fig. 6:   Horizontal cross section of the rear part of the outboard blanket with an alternative solution for arrangement of helium main supply channels.

Karlsruhe/Germany, Fusion Technology 1994, Vol. 2, pp. 1157-1160.

[3]   M. Dalle Donne (comp.), European BOT Solid Breeder Blanket, KfK 5429, November 1994

[4]   P. Norajitra, Thermohydraulics Design and Thermo-mechanics Analysis of Two European Breeder Blanket Concepts for DEMO, FZKA 5580, 1995.

[5]   Hibbit, Karlsson Sorensen, ABAQUS User's Manual Version 4.9, Providence, R.I., USA.

[6]   ASME Code, edition 1986.

[7]   Tochtermann/Bodenstein, Konstruktionselemente des Maschinenbaus, Part 1, 75, Springer, 1969.

Staff:

M. Dalle Donne
U. Fischer
H. Gerhard
T. Heider
K. Müller
P. Norajitra
G. Reimann
R. Ruprecht
I. Schmuck
K. Schleisiek

2.   Thermohydraulic Code Development

The cooling systems of the blanket segments are characterized by numerous parallel and serial cooling

channels with countercurrent flow and conductive heat transfer perpendicular to the flow direction. For the reliable determination of the coolant temperature, which is a prerequisite for the thermomechanical analysis of the blanket structure an efficient thermohydraulic computer code is required which would allow to avoid the iterations presently required. A review of commercially available codes showed that none of them would fulfill adequately the requirements. It was therefore decided to develop such a tool on the basis of the code MAGS which in its original version is a code for safety analyses of superconducting magnets. Work was started early in 1995. A large part of the necessary modifications have been realized and successfully tested. First applications are related to a First Wall section with 8 cooling channels connected to two independant cooling circuits. The next development steps will be the inclusion of the breeding zone near to the First Wall in the calculation and the testing of the transient capabilities of the code.

Staff:

I. Acalovschi
R. Meyder

First Wall Plate 1

First Wall Plate 2

Cooling Plate

Fig. 7: Diffusion bonded plates with cooling channels.

3. Technological Investigations

The diffusion bonding test performed under the EC MANET Steel Program with a view to manufacturing plates with integrated cooling channels demonstrated good weldability of the MANET material featuring high strength and vacuum tight bonds between the plate components. However, it also appeared that the joining parameters, especially the contact pressures, have to be carefully adapted to the cooling channel structures [8].

In a second test series, likewise performed in cooperation with the Institut für Kerntechnik und Energiewandlung, Stuttgart, these problems are being studied on three plate components with DEMO typical cooling channel structure, First Wall and cooling plate (Fig. 7).

First post-test examinations yielded good bonding results for all plates. No inadmissible deformation of the webs occurred on FW plate 2 whose web height to width ratio is unfavorable; this has been achieved among others by the shape given to the webs and their conical support.

Using the bonding parameters determined in these tests, larger plate components having similar FW cooling channel structures will be bonded to undergo subsequently bending tests.

Literature:

[8]   G. Haufler: Diffusionsschweißen von Probeplatten aus MANET 2 für gekühlte Blanketstrukturen, Forschungs-
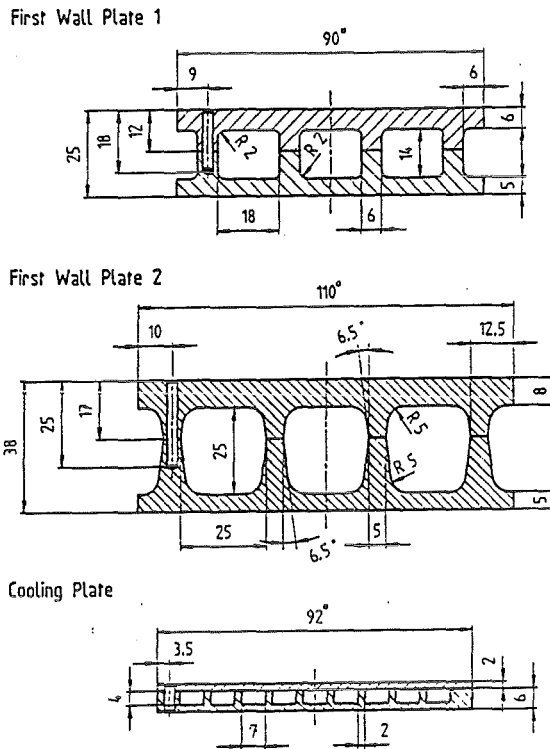
institut für Kerntechnik und Energiewandlung, Stuttgart, 1-TB-241/94 (1994).

Staff:

G. Reimann
R. Ruprecht

4. Blanket Segment Design and Manufacturing

To improve the weldability and to minimize the distortion of the structure the design of the joint between FW and cooling plates has been changed. One old and one new design are shown in Fig. 8. After all cooling plates are fixed in the U-shaped FW mechanically or by point welding to stabilize the FW segment each plate will be welded to the FW from both sides. In the old design it was planned to weld all plates from one side. The new design decreases the volume of the weld and the heat load in the material and causes a reduction of shrinkage and distortion of the structure. No preheating is necessary because the maximum thickness of the weld is smaller than 6 mm.

A thermal analysis has been carried out because the distance between FW and cooling channel in the plates increases to a maximum value of 14 mm (dependent on the used welding
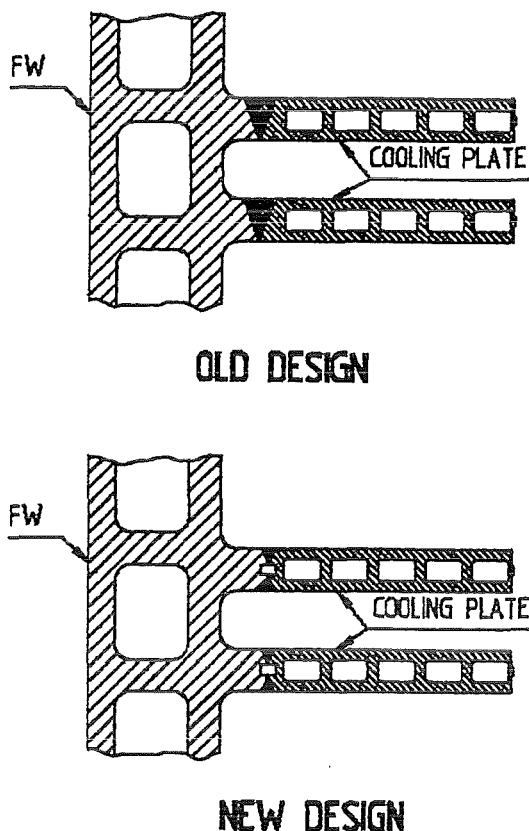
OLD DESIGN

NEW DESIGN

Fig. 8: Weld connection between First Wall and cooling plates

method). The maximum steel temperature in the cooling plates amounts for this case to 521 °C which is still acceptable.

Primary stress calculations have been carried out for two situations. For normal conditions (80 bar in the cooling channel) and for a leak in the cooling system (80 bar in the whole segment box) the maximum primary stress amounts to 93 MPa and 150 MPa, respectively. These values are also below the tolerable limit.

The development work on blanket segment manufacturing technologies is described under tasks 4.3.1 und BLDE-D1.

Staff:

H. Gerhardt
T. Heider
I. Schmuck
K. Schleisiek

5. Safety and Reliability Investigations

The safety and reliability related work included a contribution to the Blanket Concept Selection Exercise (BCSE) involving the four European blanket concepts, investigations

of specific thermal transients of the BOT blanket under off-normal conditions, and availability analyses of blanket systems.

5.1 Contribution to the Blanket Concept Selection Exercise

The safety implications of the four European blanket concepts have been assessed by Working Group 6a in the frame of the BCSE [9] (compare Chapter BL SA-D). Medium to large differences were found between the four concepts with regard to the 23 safety issues evaluated. The overall safety rating yielded small advantages of the solid breeder blankets over the liquid breeder blankets, and among the solid breeder variants the breeder inside tube (BIT) concept was rated slightly better than BOT. The main reasons for the latter were (a) the larger vulnerability of the multiplier to accidental chemical reactions in BOT (small beryllium pebbles with large surfaces at high temperatures) and (b) uncertainties in temperature control in the whole blanket due to flow maldistribution in numerous parallel and narrow coolant channels in BOT. On the other hand the BIT design was judged to be inherently more endangered by heavy disruptions. In 17 out of 23 issues both solid breeder concepts were rated equally.

From the identification and evaluation of the safety concerns a number of issues evolved requiring further in-depth studies on solid breeder blankets as follows:

- Vulnerability of blanket structure to extreme disruptions
- Tritium implantation in first wall
- Tritium release from beryllium
- Tritium control in helium coolant and purge gas
- Tritium losses in steam generators
- LOCA temperature and pressure transients
- LOFA, LOHS (loss of heat sink) transients
- Activation products mobilization and source term generation
- Chemical reactions and hydrogen production of Be
- Control of impurities in beryllium
- Sputter products transport in and removal from beryllium
- Natural convection in helium cooling system
- Flow maldistribution in parallel and narrow coolant channels
- Development of low activation material
- Recycling of beryllium and breeder material

5.2 Thermal Transients under Off-normal Conditions

Thermal transients were analised for the helium cooled first wall of the outboard blanket using the finite element code FIDAP for a specified loss of coolant accident (LOCA) in one of the two FW cooling systems and for a loss of flow accident (LOFA) in both cooling systems [10]. The model comprised half a channel of each of the two cooling systems, one cooling plate, and the pertaining zones of the breeder and multiplier pebble beds (Figure 9). The analysis was performed in two steps, at first with a rather coarse 3D mesh to compute the transient helium temperatures and then adopting a finer 2D mesh to compute the temperature distribution in the
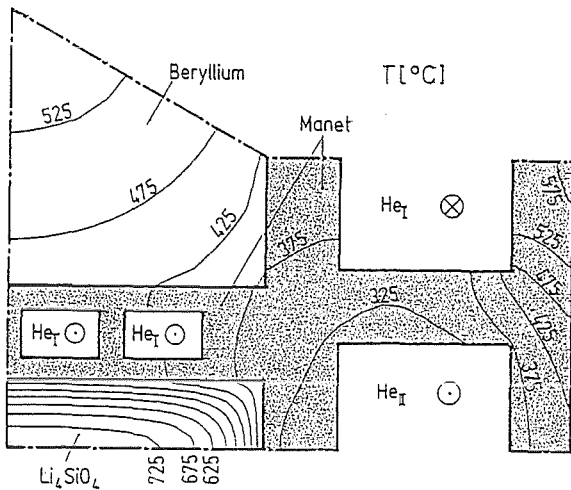
Fig. 9: Example of temperature contours in a section of the outboard FW and adjacent pepple beds at 10 s into the LOCA in FW channel He_I

structure and pebble beds. In both accident scenarios the maximum temperature was reached at the toroidal side of the segment in the equatorial midplane. The peak values obtained in the first wall were 590 °C for the LOCA and 565 °C for the LOFA, that is 70 K and 45 K, respectively, above the nominal operating peak temperature. They occur at 10 and 14 seconds after the begin of the accident and last for a few seconds only. Hence they are not considered as critical in terms of the structural integrity.

First blowdown characteristics (pressure transients, release times, momentum forces) were assessed for double-ended pipe breaks of different sizes in the main helium cooling system [10]. The conditions chosen were typical for an outboard cooling subsystem, i.e., helium inventory of 1152 m³ at 8 MPa, 350 °C, pipe diameters of 1.2 m (main pipe), 0.35 m and 0.2 m (feeders to segments). Analytical computations assuming reversible adiabatic expansion of the pressurised helium yielded draining times of 3, 40, and 100 s for the three pipe diameters mentioned. To study the effect of wall friction and heat transfer from the pipe walls to the helium during outflow, a simple RELAP model was established, leading to increased draining times of 4, 80, and 260 s, respectively. In the case of a double-ended break of a cooling channel in the first wall the release time was estimated to 3.5 hours. The momentum forces of the gas stream immediately at the beginning of discharge were obtained with the RELAP model to 4220, 170, and 66 kN for the three pipe diameters mentioned.

The requirements for active cooling of the blanket segments during handling were briefly investigated. A 2D radial-poloidal analysis of the equilibrium temperature distribution in a segment without active cooling has been performed with FIDAP, presuming as heat source the afterheat produced one day after shutdown. Heat exchange to the surrounding air (30 °C, 0.1 MPa absolute) by means of free convection and radiation was modelled. The resulting radial temperature

distribution in case of surface cooling at the front wall only, and adiabatic boundaries at the side and back walls (simulating the in-situ situation) revealed a structural temperature of 300 °C at the front side and a maximum of 420 °C at the back side. The effect of radiation turned out to be significant. As these temperatures are within design limits active cooling during handling is, a priori, not necessary from the structural integrity point of view. There may evolve more stringent restrictions from other aspects.

5.3 Reliability/Availability Analyses of Blanket Systems

The availability of the blanket system including the external cooling circuits has been assessed for the four European blanket concepts in the frame of the BCSE [10]. The results are summarised in Chapter BL SA-D.

Literature:

[9] K. Kleefeldt, G. Marbach, T. Porfiri: EU DEMO Blanket Concept Safety Assessment, FZKA report, to be published.

[10] M. Dalle Donne et al.: Development of the European DEMO BOT Solid Breeder Blanket, FZKA report, to be published.

Staff:

F. Dammel
K. Gabel
K. Kleefeldt
K. Schleisiek
H.Schnauder

6. Mesh Refining Procedure for Integral Electromagnetic Analysis of Fusion Reactor Components

6.1 Introduction

Integral formulations for eddy current problems have been successfully introduced in the electromagnetic analysis of fusion tokamak devices. The advantage of such formulations, in comparison with differential or mixed formulations, is a large gain in computational efficiency for structures where the ratio of conducting material to vacuum is low. In this case the discretization effort is greatly reduced due to the elimination of the vacuum problem from the formulation. The disadvantage of this method is the management (calculation, storage and inversion) of dense matrixes, which are obtained from numerical approximation.

In addition, field calculations are effected by an inherent problem. As all the conducting part can change significantly the response of the structure due to the shielding of magnetic and electric fields, all the conductors must be in principle

taken into account in the model. This results in this particular case, in an enormous amount of freedom degrees.

These factors force to use a relatively coarse mesh, giving only a good representation of the broad response of the system. Local effects which on the contrary require an extremely fine model of the investigated details, are completely neglected in the calculation.

An attempt to overcome these problems has been published [11]. In that report a procedure of mesh refinement is presented, limited, however, to components electrically insulated from the main system, whose influence in the analysis of the main system can be neglected.

This paper presents a generalized mesh refining procedure for an integral element method, in which a subdomain (electrically connected or insulated to the remainig system) is refined. This subdomain represents the detail of interest, in which a local distribution of current and magnetic force is required. The influence of the remaining electromagnetic system is taken into account as external conditions, which have been previously calculated on the basis of a coarse mesh over the whole system. It follows, therefore, that all the computational resources can be concentrated on the numerical solution of the subdomain.

The presented calculations have been performed with a three-dimensional computational program based on an integral formulation of the eddy current using edge elements [12].

6.2 Numerical Method

The conducting body is divided in two integration domains (see Fig. 10). Ω_2 represents the detail of interest, Ω_1 the
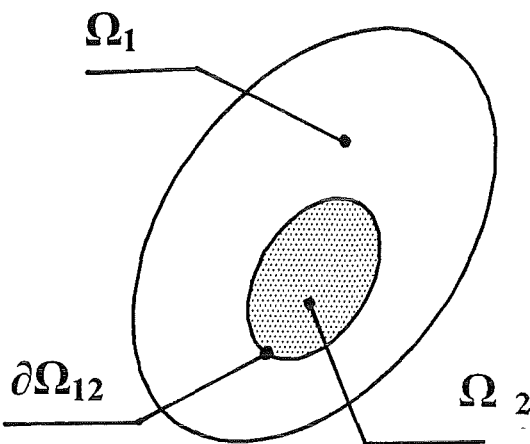

Fig. 10: Integration domains

remaining structure. The quasi-static approximation of the Maxwell equations for non-ferromagnetic materials is applied on the integration domain Ω_2.

$$\tilde{\eta}(\vec{r}) \cdot \vec{j}(\vec{r},t) + \frac{\mu_0}{4\pi} \int_{\Omega_2} \frac{\frac{\partial \vec{j}(\vec{r}',t)}{\partial t}}{|\vec{r}-\vec{r}'|} dV'$$

$$= -\frac{\partial \vec{A}(\vec{r},t)}{\partial t} - \vec{\nabla}\Phi(\vec{r},t) \qquad (1)$$

$$-\frac{\mu_0}{4\pi} \int_{\Omega_1} \frac{\frac{\partial \vec{j}(\vec{r}',t)}{\partial t}}{|\vec{r}-\vec{r}'|} dV'$$

with the following conditions

$$\vec{\nabla} \cdot \vec{j} = 0$$

$$\left(\vec{j} \cdot \vec{n}\right)_1 = \left(\vec{j} \cdot \vec{n}\right)_2$$

The integral which represents the contribution of the eddy currents to the vector potential has been divided in two parts. As the variable j is supposed to be known in Ω_1, the contribution of the integral on this domain appears here in the right side of the equation.

The application of the Galerkin procedure to (1) brings us to the following linear differential system.

$$[L]\{\tfrac{\partial I}{\partial t}\} + [R]\{I\} = \{V(t)\}$$

$$-[L_E]\{\tfrac{\partial I_1}{\partial t}\} - [L_B]\{\tfrac{\partial I_{12}}{\partial t}\} - [R_B]\{I_{12}\} \qquad (2)$$

In this equation [L] and [R] are the inductance and the resistance matrices for the domain Ω_2, {V(t)} the variation of the external flux on the same domain.

The remaining terms take into account the influence of the domain Ω_1 ; [L_E] is the mutual induction between the two domains, [L_B] and [R_B] are used to calculate the voltage drop (inductive and resistive respectively) caused by the current flowing through the boundary $\partial\Omega_{12}$. The current {I_1}, associated at the Ω_1 domain, and {I_{12}}, associated at the boundary $\partial\Omega_{12}$, have been calculated in a previous calculation.

6.3 Application and Discussion

As an example of the application of this procedure, we have produced the results of calculation for the Demo blanket, which are hereby presented. Further information about Demo assessment can be found in [13].

Fig.11 shows the mesh used for the electromagnetic analysis of the Demo reactor during plasma disruptions. All the most relevant parts of the electromagnetic system are taken into account in the developed model: the vacuum vessel, 48 outboard blankets, 32 inboard blankets (each composed of an upper and a lower component) and the PF-coils. The resulting
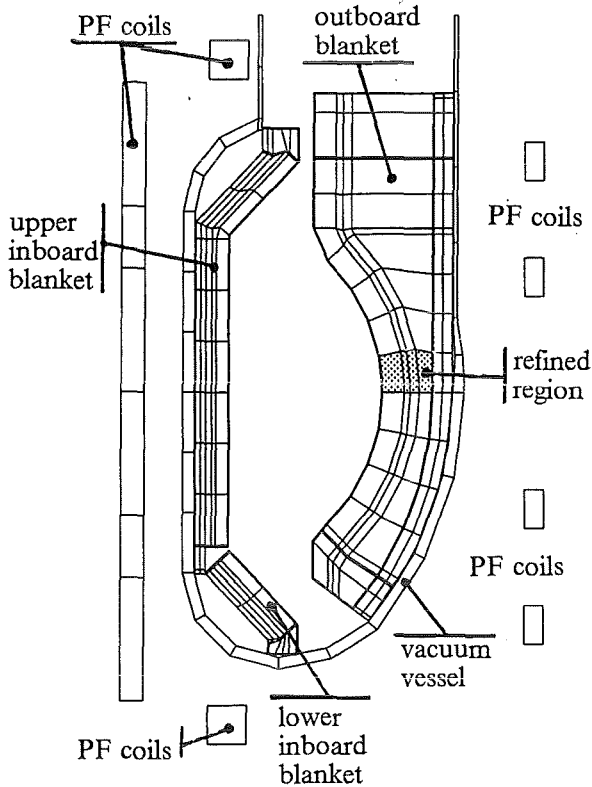
Fig. 11: Electromagnetic model of Demo

coarse mesh can only show the electromagnetic response of the system in terms of average quantities (i.e. eddy currents, see Fig.12).
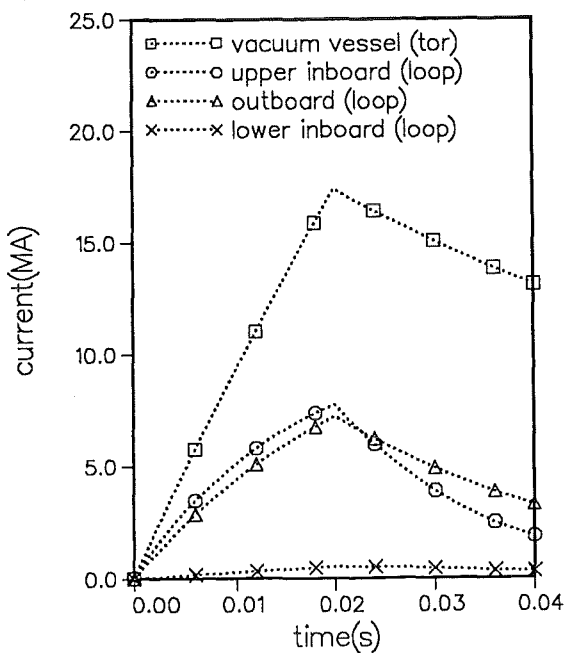

Fig. 12: Eddy current vs. time.

The refining mesh procedure is applied to a subdomain located in the equatorial region of the outboard blanket. The subdomain (that consists of 14 elements in the coarse model) has been refined using 828 elements; it means a local refining factor of about 60.

Table 2: Model size for Demo outboard calculation

Model	Coarse	Refined
Node No.	1706	1410
Element No.	864	828
Freed.Deg.No.	1152	1137
Rotation No.	48 (x7.5°)	1

In Table 2 the most important parameters of the schematization are summarized. Compared are the dimensions of the coarse and refined mesh. The important details of the design (e.g. the cooling channels in the first and side walls or the coolant manifolds in the back plate) can be taken into account in the calculation, as shown in Fig. 13.
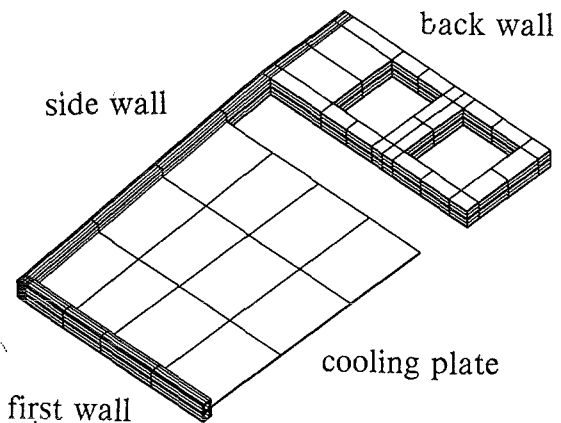
Fig. 13: Refined mesh of the outboard equatorial section.

Fig. 14 shows the calculated force density for the refined model. The new force density distribution is different from that calculated with the coarse model. This is caused both by the reduction of the current flow section (e.g. first and side wall) and by the change of current direction (e.g. around manifolds in the back wall). Furthermore, we obtain current and force distribution for elements such as the cooling plates, which are not modelled at all in the previous calculation.

This analysis allows for a more accurate calculation of the magnetic force distribution, which can be used for the stress analysis of the components.

6.4 Conclusions

We have presented and tested satisfactorily a refining mesh procedure for integral electromagnetic analysis of fusion reactor components. Starting from a coarse mesh calculation

of the whole electromagnetic system, an analysis of one or more refined subdomains can be performed using the results of the previous calculation as external and boundary conditions. Hence, single components can be analyzed in detail with a reasonable amount of freedom degree. The developed code has been applied to evaluate the electromagnetic behaviour of the outboard blanket box of the Demo reactor.

Further applications of the code should involve analyses for divertors, antennas or cooling pipes·

Literature:

[11]   L. Bottura and S. Chiocchio, " A "Zoom" Procedure for Integral Electromagnetic Analysis", EMF '94 Workshop, Capri (Italy), August 1994, EUR 16112 EN, pp.93-106.

[12]   R. Albanese and G. Rubinacci, "Integral Formulation for 3D Eddy Current Computation Using Edge Elements", IEE Proc., 135A, 457-462(1988).

[13]   L.V. Boccaccini and P. Ruatto, "Mechanical behaviour of the European B.O.T. blanket during electromagnetic off-normal transient conditions", presented at the 18th SOFT, Karlsruhe (1994), to be published.

Staff:

L. V. Boccaccini
M. Dalle Donne
P. Ruatto
B. Tellini

7.   Computation of Generation and Impact of Electromagnetic Fields on Ferromagnetic Structures Surrounding the Plasma in a DEMO Fusion Reactor

7.1   Introduction

The Karlsruhe Research Centre (FZK) is developing within the European Technology Programme (EFTP) a BOT (Breeder Out of Tube) Solid Breeder Blanket for the nuclear fusion demonstration reactor (DEMO) [14]. The steel MANET (MArtensitic for NET) has been chosen as structural material because it can withstand the high neutron fluence in DEMO (70 dpa) without appreciably swelling.

MANET is a ferromagnetic material with nonlinear magnetic behaviour. As it is used in the region surrounding the plasma, the magnetic field distribution outside and inside the blanket structure can be significantly modified. When a plasma disruption occurs - i.e. the plasma current decays from 20MA to zero in 20ms - large eddy currents are induced in the structure. These currents interact with the external magnetic field resulting in electromagnetic forces whose magnitude can be greater then in the case without ferromagnetic structural material.

The computer code AENEAS has been developed at FZK to allow electromagnetic calculations in presence of magnetic materials. The paper presents basic formulation of the code and results of calculation performed for the DEMO BOT outboard blanket segment.

7.2   Basic Formulation

The code AENEAS is based on an extension of an already existing code for nonmagnetic materials [15]. That is to say, the transient eddy current problem for a conducting body Ω with a ferromagnetic subdomain Ω_M is described taking into account the contribution of magnetization density M to the magnetic vector potential A by the integral formulation

where η is the electrical resistivity tensor, J the current density, A_e the magnetic vector potential of external fields, Φ the scalar electric potential and the apices distinguish the source points from the field ones. Solenoidality conditions for J are also considered. As the new unknown M is introduced, a second coupled equation is required to solve the problem. To this purpose a single-valued nonlinear relation between M and magnetic field strength H is considered in Ω_M
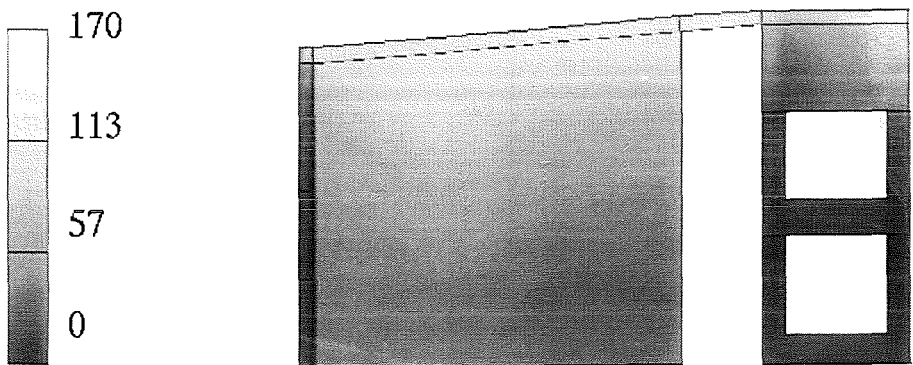

Fig. 14:   Force density distribution (in MN/m^3)

$$\eta(\vec{r})\vec{J}(\vec{r},t)+\frac{\mu_0}{4\pi}\int_\Omega \frac{1}{|\vec{r}-\vec{r}'|}\frac{\partial \vec{J}(\vec{r}',t)}{\partial t}\,d\tau' =$$

$$-\frac{\partial \vec{A}(\vec{r},t)}{\partial t}-\vec{\nabla}\Phi(\vec{r},t)$$

$$-\frac{\mu_0}{4\pi}\int_{\Omega_M}\frac{\partial \vec{M}(\vec{r}',t)}{\partial t}\times\vec{\nabla}'\left(\frac{1}{|\vec{r}-\vec{r}'|}\right)\,d\tau' \qquad (1)$$

$$\vec{M}(\vec{r},t)=\chi\Big(\big|\vec{H}(\vec{r},t)\big|\Big)\vec{H}(\vec{r},t) \qquad (2)$$

where

$$\vec{H}(\vec{r},t)=\frac{1}{4\pi}\int_\Omega \vec{J}(\vec{r}',t)\times\vec{\nabla}'\left(\frac{1}{|\vec{r}-\vec{r}'|}\right)\,d\tau'$$

$$+\frac{1}{\mu_0}\vec{\nabla}\times\vec{A}_e(\vec{r},t)$$

$$+\frac{1}{4\pi}\vec{\nabla}\times\int_{\Omega_M}\vec{M}(\vec{r}',t)\times\vec{\nabla}'\left(\frac{1}{|\vec{r}-\vec{r}'|}\right)\,d\tau' \qquad (3)$$

$$-\vec{M}(\vec{r},t)$$

and the scalar magnetic susceptibility χ is a function of the module of H.

The coupled problem given by (1) and (2) is solved numerically applying the Crank-Nicolson-Galerkin method. J is approximated by using edge elements, while for M are used zero-order elements: it means, M is taken uniform in the interior of an element and zero outside. Time evolution for J and M are obtained solving iteratively at each time step the finite element approximation of (1) and (2). A optimum relaxation parameter β for M is calculated at each iteration step considering the maximum value of χ among the elements by

$$\beta =\frac{1}{1+\chi_{max}} \qquad (4)$$

When distribution of J and M are known, the corresponding contributions to force and torque acting on Ω can be computed by means of

$$\vec{F}_1 = \int_\Omega \vec{J}(\vec{r},t)\times\vec{B}_0(\vec{r},t)\,d\tau \qquad (5)$$

$$\vec{C}_1 = \int \vec{r}\times\Big(\vec{J}(\vec{r},t)\times\vec{B}_0(\vec{r},t)\Big)d\tau \qquad (6)$$

$$\vec{F}_2 = \int_\Omega \Big(\vec{\nabla}\times\vec{M}(\vec{r},t)\Big)\times\vec{B}_0(\vec{r},t)\,d\tau$$

$$+\int_{\partial\Omega}\Big(\vec{M}(\vec{r},t)\times\vec{n}\Big)\times\vec{B}_0(\vec{r},t)\,dS \qquad (7)$$

$$\vec{C}_2 = \int_\Omega \vec{r}\times\Big[\Big(\vec{\nabla}\times\vec{M}(\vec{r},t)\Big)\times\vec{B}_0(\vec{r},t)\Big]d\tau$$

$$+\int_{\partial\Omega}\vec{r}\times\Big[\Big(\vec{M}(\vec{r},t)\times\vec{n}\Big)\times\vec{B}_0(\vec{r},t)\Big]dS \qquad (8)$$

where B_0 is the total magnetic field less that given by J and the magnetic material is replaced by volume and surface Amperian currents $J_M=\nabla\times M$ and $K_M=M\times n$ [16]. Due to the assumption made for M, only currents KM are present. The Equivalent Magnetizing Current (EMC) method is used to compute surface integrals in (7) and (8) [17].

7.3 Results and Discussion

The code AENEAS has been used to compute electromagnetic forces acting on the DEMO BOT blanket outboard segment during a plasma disruption. The finite element model consists of a complete outboard blanket box and Vacuum Vessel segment. It includes 1084 8-node elements (972 of which belong to the ferromagnetic structure) with 1239 active edges (Fig. 15). Full description of model and calculation assumptions are given in [18].

The magnetization curve of MANET [19] has been modelled using Akima's method [20] (Fig. 16). MANET is fully saturated for low applied fields and the direction of M is determined almost only by the toroidal magnetic field (6 Tesla). The influence of the saturated magnetic material on the poloidal magnetic field is slight, and when a plasma disruption occurs the varying plasma magnetic field "sees" the same situation as the structure would be nonmagnetic. That means, the pattern of J is approximately the same with or without magnetic structural material and the increase of forces and torques (5) and (6) is caused only by the thickening due to M of the toroidal component of B_0. This increase is about 20% in the part of the structure where the highest stresses are expected. Total force and torque (7) and (8) have been also calculated and values at plasma quench end are compared in Fig. 17 with those for (5) and (6).

Static stress analysis has been performed for Lorentz force density distribution f=JxB where total field B is considered. The highest von Mises stress value (162 Mpa) in the structure is obtained on the side wall of the box. It is lower then the yield stress value for MANET (560 Mpa at 350°C). Comparison with ASME norms for nuclear components [21] shows that the outboard structure can withstand the mechanical stress

7.4 Conclusions and Future Work

AENEAS, a code for electromagnetic computations in presence of magnetic material, has been used to compute electromagnetic forces acting on a DEMO Blanket Segment during a plasma disruption. Results show that the DEMO BOT outboard blanket box can withstand the mechanical stress caused by a plasma disruption remaining below the elastic limit. Total force due to interaction between magnetization of the structure and applied field has been also calculated. Further effort has to be put in this case to investigate local force distribution so that a complete stress analysis can be performed.

Literature:

[14]   M. Dalle Donne et al., European DEMO BOT Solid Breeder Blanket, KfK 5429, Kernforschungszentrum Karlsruhe, 1994.

[15]   M.R. Albanese and G. Rubinacci, IEE Proceedings 135A (1988) 457-462.

[16]   M.W. F. Brown, Magnetoelastic Interactions, Springer, Berlin, 1966.

[17]   M.T. Kabashima et al., IEEE Trans. on Magnetics 24 (1988) 451-454.

[8]   L. V. Boccaccini, P. Ruatto, in: Herschbach (Ed.), FUSION TECHNOLOGY 1994, Elsevier 1995, Amsterdam, pp. 1153-1156.
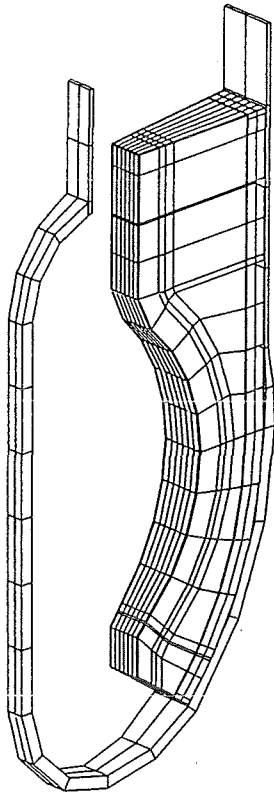
Fig. 15:   Finite element model of DEMO BOT Blanket Segment.

caused by a plasma disruption remaining below the elastic limit.
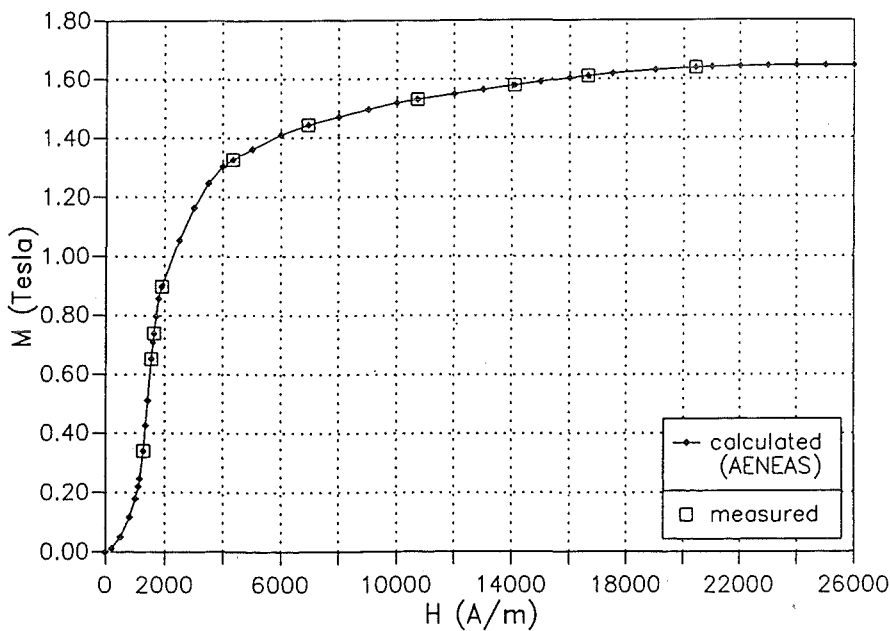

Fig. 16:   Magnetization curve of MANET.

Sect A x=8.315 y=0.0 z=9.950

$F_{1x} = 1.51$	$C_{1x} = 57.25$	$F_{2x} = -5.22$	$C_{2x} = 19.21$
$F_{1y} = -0.83$	$C_{1y} = -11.09$	$F_{2y} = 2.77$	$C_{2y} = 38.66$
$F_{1z} = 0.18$	$C_{1z} = -0.07$	$F_{2z} = 9.91$	$C_{2z} = 0.14$

Sect B x=8.315 y=0.0 z=7.500

$F_{1x} = 1.27$	$C_{1x} = 59.20$	$F_{2x} = -5.03$	$C_{2x} = 13.84$
$F_{1y} = -0.85$	$C_{1y} = -7.63$	$F_{2y} = -3.64$	$C_{2y} = 26.15$
$F_{1z} = 0.21$	$C_{1z} = -0.08$	$F_{2z} = -14.69$	$C_{2z} = -0.23$

Sect C x=9.202 y=0.0 z=0.0

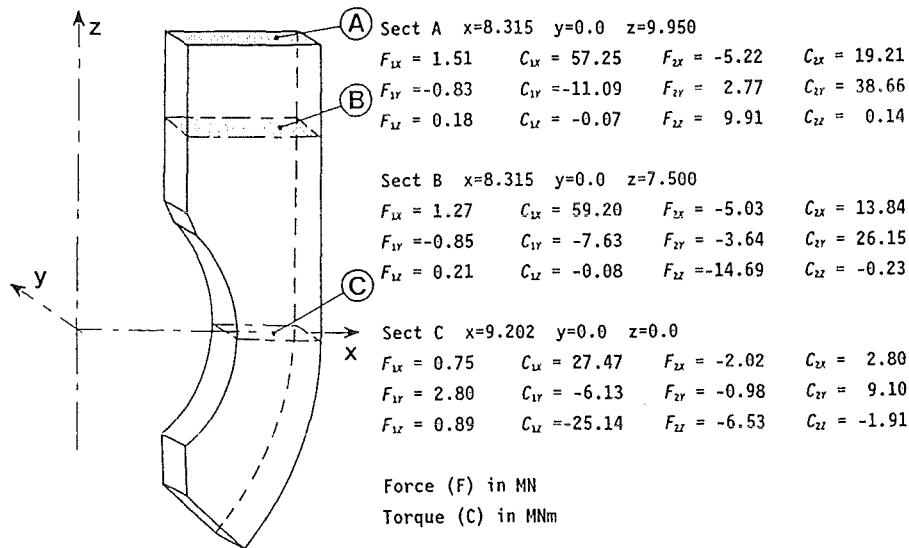|			
$F_{1x} = 0.75$	$C_{1x} = 27.47$	$F_{2x} = -2.02$	$C_{2x} = 2.80$
$F_{1y} = 2.80$	$C_{1y} = -6.13$	$F_{2y} = -0.98$	$C_{2y} = 9.10$
$F_{1z} = 0.89$	$C_{1z} = -25.14$	$F_{2z} = -6.53$	$C_{2z} = -1.91$

Force (F) in MN
Torque (C) in MNm

Fig. 17: Resultant forces and torques at plasma quench end for different horizontal sections. These quantities are calculated on the geometrical center of each section and refer to the lower half in which the structure is cutted by the section.

[19] K. A. Hempel and W. Salz, private communication, RWTH Aachen, January 1995.

[20] K.H. Akima, Journal of ACM 17 (1970) 589-602.

[21] ASME-Code, Section III, Division 1, NB-3200, "Design Conditions".

Staff:

L.V. Boccaccini
M. Dalle Donne
P. Ruatto
B. Tellini

BS BE-D   Beryllium

BS BE-D 1   Beryllium Properties

Impurities Effect on the Swelling of Neutron Irradiated Beryllium

Abstract

An important factor controlling the swelling behaviour of fast neutron irradiated beryllium is the impurity content which can strongly affect both the surface tension and the creep strength of this material.

Being the volume swelling of the old beryllium (early sixties) systematically higher than that of the more modern one (end of the seventies), a sensitivity analysis with the aid of the computer code ANFIBE (ANalysis of Fusion Irradiated BEryllium) to investigate the effect of these material properties on the swelling behaviour of neutron irradiated beryllium has been performed.

Two sets of experimental data have been selected: the first one named Western refers to quite recently produced Western beryllium, whilst the second one, named Russian refers to relatively old (early sixties) Russian beryllium containing a higher impurity rate than the Western one.

The results obtained with the ANFIBE Code were assessed by comparison with experimental data and the used material properties were compared with the data available in the literature. Good agreement between calculated and measured values has been found.

1.   Introduction

In order to generate confidence in the results provided by the code ANFIBE [1] and to assess its prediction capabilities, it was necessary to compare the calculated results with a large number of reliable experimental data [2-11].

The large variety of experimental conditions referring to both in-pile and out-of-pile tests has constituted a reliable benchmark, providing good examples of gas behaviour in beryllium under different steady state and transient conditions and for different metallographic features of the samples.

The proposed analysis is aimed at defining the confidence level of the predictions for the ranges of parameters and the operating conditions to which the code can be applied and to assess the influence of the key variables affecting the overall kinetics and dynamics of gas in beryllium during fast neutron irradiation.

The measured or calculated helium generation rate instead of the neutron flux was taken as the characterizing parameter for the considered swelling experiments. The use of helium content instead of fast fluence is due to the fact that radiation-induced dimensional changes in beryllium

subjected to fast neutron irradiation are dominated by helium-bubble swelling.

2.   Material Properties

The modelling of the experimental results requires a realistic assessment of a number of parameters determining the helium behaviour in beryllium along with physical and mechanical properties of beryllium. The method which has been followed in carrying the swelling analysis deals with experiments where the conditions (i.e. irradiation temperatures, helium generation rates, impurity contents, etc.) were reasonably well known, as well as with the use of a set of experimental physical properties for the material of interest.

Two sets of data have been selected: the first one named Western refers to Western beryllium produced quite recently, whilst the second one, named Russian refers to relatively old (early sixties) Russian beryllium containing a larger amount of impurities.

Unfortunately, some of the experimental data and material properties crucial to helium modelling in irradiated beryllium are currently very scattered or unavailable. Particular attention has been done in minimizing the number of parameters that can be varied to match the model to the experimental results. The two most important material properties affecting the swelling of beryllium under irradiation are the surface tension and the thermal creep and they are both affected by the amount of impurities in the material.

2.1   Surface tension

In theoretical models of gas-driven swelling in metals, the surface tension of solid material as a function of the temperature is an important variable because it is one of the most important parameters governing the swelling behaviour. This material property is, however, very sensitive to the manufacturing processes and impurity contents, so its experimental value is scattered over a quite large range. It is known that impurities in the metal matrix can strongly affect the surface tension by reducing its value for the pure material. For this reason particular care has been done in selecting the surface tension equations both for Western and Russian beryllium [12-16].

The experimental data on surface tension of beryllium available from the literature are generally for high temperatures near the melting point. However, if one considers temperatures where the atomic diffusion is significant ($T > 0.5T_m$), the surface tension has the same numerical value as surface free energy [15] and its dependence on temperature may be given by [16-17]:

$$\gamma\,(T)\,[N\,/\,m] = \gamma\,(T_m) - K \times (T - T_m) \qquad (1)$$

γ (T_m) being the surface tension at the melting point and K a constant varying between 0 and 3×10^{-3} [17]. In the present analysis the average value $K = 1.5 \times 10^{-3}$ was assumed for the modern Western beryllium and γ(T_m) was chosen equal to 1.96 N/m as given in Ref. [18]. For the Russian beryllium the value γ(973 K) = 0.85 N/m was chosen as reference, close to the value reported in the literature for beryllium produced in the early sixties (like the Russian beryllium) [13]. This value is about three times smaller than that for the Western and more modern beryllium. Therefore, for Russian beryllium a surface tension with a temperature dependence similar to that for Western one but having a magnitude about three times smaller has been chosen for the present analysis. The surface tension for Western and Russian beryllium as a function of temperature is shown in Fig. 1.
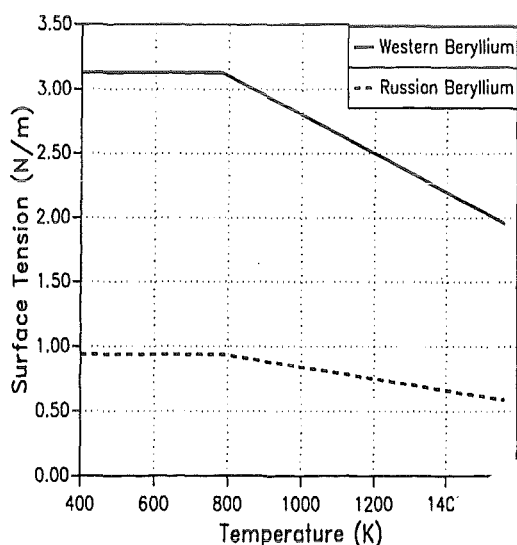

Fig. 1: Surface tension for Western and Russian beryllium as a function of temperature

2.2 Thermal and irradiation creep

Referring to the thermal creep law one must make a distinction between Western and Russian experimental data too. In the former case, in fact, a thermal creep law has been found in the literature and thus used for the analysis [19-20]. In the latter case (and in general for all kind of old beryllium), however, only a very scattered set of data has been found in the literature, which did not directly refer to the considered set of Russian samples irradiated at high temperature [21].

The creep strength of beryllium is controlled by grain size, oxide distribution, initial dislocation density and concentration of certain impurity elements [21]. The most important single factor controlling the creep strength of beryllium is indubitably the impurity content. The principal impurities in beryllium are beryllium oxide, carbon, iron, aluminium, silicon and magnesium. The beryllium oxide impurities have an indirect influence on creep strength through their effects on the recrystallization temperature and grain boundary mobility, whilst iron and carbon appear to have only a minor influence on creep strength. On the

contrary, above temperatures of 650-700 °C the beryllium creep strength is considerably reduced by the presence of aluminium, magnesium and silicon, and this reduction becomes more marked as the temperature increases [21-22].

Due to their practical insolubility in beryllium, these three elements (which are normally located on the grain boundaries where they form noncontinuous lenticular globules) can form low-melting phases. Indeed the melting points of aluminium and magnesium are 660 °C and 650 °C respectively, while Al-Si and Al-Mg eutectics melt at temperatures as low as 577 °C and 450 °C respectively [21-22]. Once these liquid phases are formed on the beryllium grain boundaries, due to the impossibility of a shear stress to be transmitted by a liquid, they will act as a cavity, so determining a stress concentration at their tips. As a consequence, an accelerated grain boundary shear and cracking will occur around each liquid globule, so causing a pronounced grain boundary sliding and an accelerated creep rate.

The difference in creep strength between the weakest and strongest beryllium grades which have been found in the literature was about 20 times and the difference in creep rate was about 8 orders of magnitude [21]. A parametric analysis was thus necessary in order to identify the set of parameters (pre-exponential factor, stress exponent and activation energy for thermal creep) which is able to better match the model to the experimental results. The chosen thermal creep laws are shown in Figs. 2 and 3 for Western and Russian
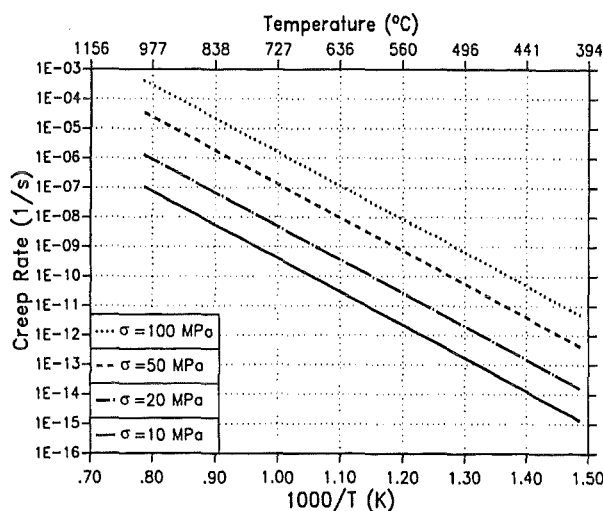

Fig: 2: Thermal creep rate for Western beryllium as a function of temperature

beryllium respectively. The stress exponent for creep law is in both cases equal to 3.6, that is higher than one: this means that creep mechanisms in beryllium entail dislocation climb and cannot be interpreted as a simple diffusional creep phenomenon. The activation energy for creep Q_c has been assumed equal to 216.2 kJ/mol for both Western and Russian beryllium for temperature up to 650 °C. However, for $T \geq 650$ °C, corresponding to the melting temperature range of Al
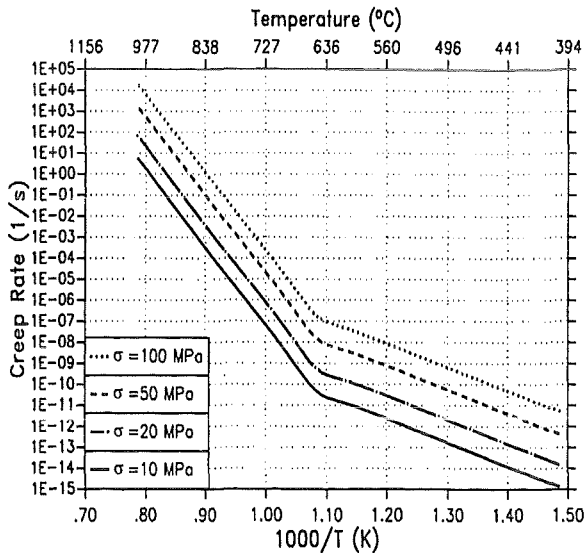
Fig. 3: Thermal creep rate for Russian beryllium as a function of temperature

and Mg, Q_c has been assumed equal to 710.9 kJ/mol for the Russian beryllium, which is within the range of values given in Ref. [21] for beryllium grades containing impurities.

Referring to the irradiation creep, the mechanism governing this phenomenon in beryllium is at present not well known, thus it is not possible to make a prediction of the enhancement of creep under irradiation in a wide range of temperatures. Only one experiment of irradiation creep in beryllium has been reported in the literature [23] and the corresponding steady state creep rate law has been used for the present calculations. Although this correlation refers to a single experimental test it can be in any case taken as a reference for the evaluation of the irradiation creep rate at all temperatures where self-diffusion is insignificant. In any case, probably the effect of the enhancement of irradiation creep plays only a minor role in governing swelling behaviour of beryllium for temperatures higher than 250 °C due to the prevalence of the thermal creep.

3. Experimental Data

Beryllium Western and Russian irradiation experiments carried out in different fission reactors [2-11] at temperatures ranging from 50 to 970 °C and at neutron fluences up to $5.0 \cdot 10^{26}$ m^{-2} ($E_n > 0.8$-1 MeV), with helium contents up to 26100 appm were used for the calibration of ANFIBE code.

The major part of the swelling data are, however, for beryllium irradiated both at low temperatures up to very high fluences and at low fluences up to high temperatures [2-5][7-8][10]. The only available Western swelling data referring to relatively high irradiation temperature (T=427-487 °C) and, at the same time high fast neutron fluence (up to 10^{26} m^{-2}) come from Beeston's experiments [6]. The other set of well characterized high temperature Western irradiated beryllium refers to specimens irradiated in the SILOE reactor in

Grenoble (BEGONIA Experiment) at temperatures up to 700 °C but a relatively low fast neutron fluence (up to $2.5 \cdot 10^{25}$ m^{-2}) [9].

A set of experiments has been found in the literature with reference to Russian beryllium samples irradiated at temperatures up to 970 °C and at fast neutron fluences up to 10^{26} m^{-2} ($E_n > 0.8$-1 MeV) [11].

4. Comparison with ANFIBE Calculations

A comparison between calculated and experimental swelling data for in-pile Western irradiated beryllium is shown in Fig. 4 each point of which, classified according to the irradiation
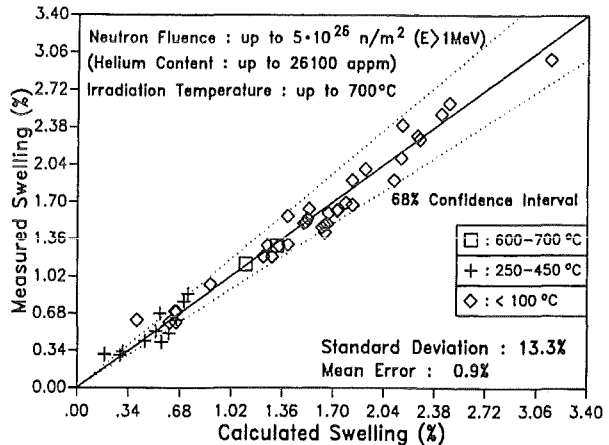

Fig. 4: Comparison of calculated and experimental swelling data for in-pile irradiated Western beryllium [2-9]

temperature, represents the swelling behaviour of a single neutron irradiated beryllium specimen. The agreement between calculated swelling and experimental data is excellent.

A comparison between calculated and experimental beryllium swelling data for the available Western experiments referring to relatively high irradiation temperature and, at the same time, relatively high fast neutron fluence [6] [9] is shown in Fig. 5.

Also in this case ANFIBE correctly predicts the experimental results; the discrepancies are due both to the uncertainty in the experimental conditions (i.e. fast flux, helium generation rate, volumetric heat generation, etc.) and in the relevant beryllium properties (i.e. creep law) which are affected by impurity content and manufacturing processes in a stronger way than in the case of low irradiation temperature.

As it has been previously pointed out, another set of experiments refers to Russian beryllium samples irradiated both at high temperature and at high fast neutron fluence [10-11]. However, being these data obtained for a very old beryllium (early sixties) the physical properties of which differ very much from those of the more modern beryllium, an
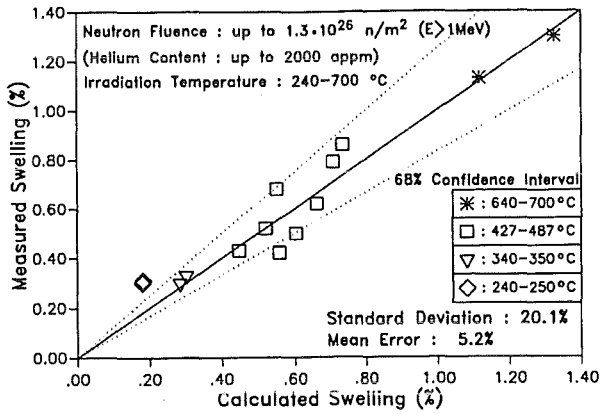
Fig 5: Comparison of calculated and experimental swelling data for high temperature in-pile irradiated Western beryllium [6] [9]

additional calibration analysis was required in order to good characterize these experiments.

For a helium reference creation rate of 4000 appm He per 10^{26} m^{-2} fast neutron fluence cited in the literature [10-11], the measured swelling of Russian beryllium is always higher than that of the more modern Western one containing the same He quantity and subjected to similar irradiation conditions. This fact is clearly illustrated in Fig. 6, which shows
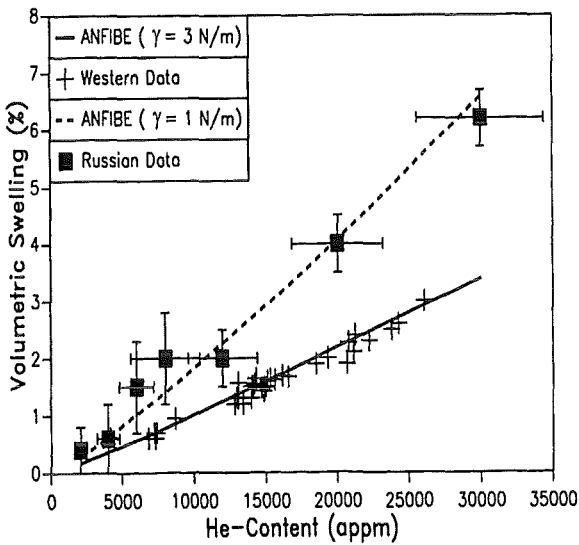

Fig. 6: Swelling of Western and Russian beryllium irradiated at temperatures below 100 °C as a function of helium content [2-11]

the volumetric swelling of beryllium irradiated at temperatures below 100 °C as a function of helium content in comparison with the prediction of the ANFIBE code.

A likely reason for this behaviour is that, due to its quite poor quality (i.e. high impurity content) the Russian beryllium has a surface tension which is lower than that of the Western, more modern one.

Fig. 6 shows that the Russian experimental data agree quite well with the ANFIBE predictions based on the surface tension values shown in Fig. 2. At these low temperatures the thermal creep doesn't play any role.

Swelling increases at low temperatures almost linearly with the gas content, as expected from theoretical considerations. At low irradiation temperatures, in fact, when the mobility of the vacancies and interstitials is very low and the gas atoms are practically immobile in the lattice, helium cannot migrate to the grain boundaries where it could coalesce to form big intergranular bubbles, which causes the departure from linearity in swelling behaviour.

On the contrary, the situation is quite different for the samples irradiated at high temperatures (up to 970 °C) and at fast neutron fluences up to 10^{26} m^{-2} [11] for which, due to both the rapid coalescence of the gas bubbles and the reduction of the mechanical strength of the material, one should expect a non-linear increase of the swelling with the gas content and the influence on creep strength due to the impurity content (i.e. Al, Mg) in beryllium must also be taken into account.

Fig. 7 shows the volumetric swelling as a function of the irradiation temperature for the Russian beryllium [11] at different fast neutron fluences as compared with the predictions of ANFIBE. In this case a creep law taking into account the possible presence of liquid phases at the grain boundaries has been used as shown in Fig. 3. The agreement between the experimental data and the ANFIBE predictions is also here quite good.
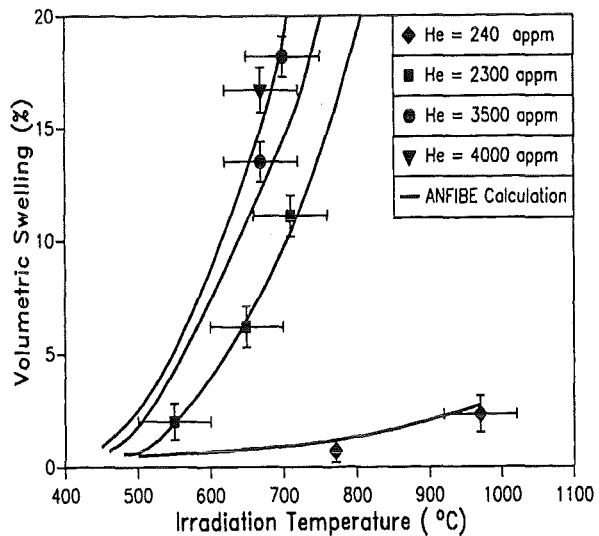

Fig. 7: Comparison of calculated and experimental swelling for Russian beryllium irradiated at high temperatures and high fluences [10-11]

5. Conclusions

An important factor controlling the swelling behaviour of beryllium under neutron irradiation is the impurity content which can strongly affect the material properties.

Beryllium irradiation experiments carried out in different fission reactors at temperatures ranging from 50 to 970 °C and at neutron fluences up to $5.0 \cdot 10^{26}$ m^{-2} ($E_n > 0.8$-1 MeV), with helium contents up to 26100 appm were compared with the predictions of the computer code ANFIBE.

Two sets of data have been selected: the first one named Western refers to Western beryllium produced quite recently (end of the seventies), whilst the second one, named Russian refers to relatively old (early sixties) Russian beryllium containing a higher impurity rate than the Western one. The comparison between calculated and experimental swelling data shows that:

1. The swelling of Russian beryllium irradiated at low temperature (T<100 °C) is systematically higher than that of the Western and more modern one. This behaviour has to be attributed to the fact that the old Russian beryllium has a relatively high amounts of impurities in comparison with Western beryllium. This fact causes a decrease of the surface tension thus determining a reduction of the mechanical strength of the material which opposes the deformation of the metal under the thrust of the helium-bubble overpressure.

2. The swelling of Russian beryllium irradiated at high temperature and, at the same time, at high neutron fluence is much higher than that of the Western beryllium. This is likely due to the fact that some impurities (i.e. Al, Mg, Si) can form, due to their practical insolubility in beryllium, low-melting phases which are in the liquid form at temperature higher than 650-700 °C. Once these liquid phases are formed on the beryllium grain boundaries they act as a cavity so causing a pronounced grain boundary sliding and an accelerated creep rate. The enhancement of the thermal creep rate and, at the same time, the decrease of the surface tension due to the presence of impurities, will determine a strong increase of the swelling for high irradiation temperature.

Literature:

[1] F. Scaffidi-Argentina, "Modellierung des Schwellens und der Tritium-Freisetzung von bestrahltem Beryllium", FZKA Report 5632 (to be published).

[2] D.L. Baldwin and M.C. Billone, "Diffusion/Desorption of Tritium from Irradiated Beryllium", Journal of Nuclear Materials 212-215 (1994) 948-953.

[3] M.C. Billone et al., "Tritium and Helium Behaviour in Irradiated Beryllium", Fusion Technology 19 (1991) 1707-1714.

[4] L. Sannen et al., "Helium Content and Swelling of Low Temperature Irradiated/Post-Irradiated Annealed Beryllium", CEN/SCK Report FT/Mol/93-07.

[5] J.M. Beeston, "Properties of Irradiated Beryllium: Statistical Evaluation", EG&G Idaho Report, TREE-1063 (1976).

[6] J.M. Beeston et al., "Comparison of Compression Properties and Swelling of Beryllium Irradiated at Various Temperatures", Journal of Nuclear Materials 122-123 (1984) 802-809.

[7] E. Koonen, "Study on Irradiation Effects and Swelling of Irradiated Beryllium", CEN/SCK Report, Reactor Safety Analysis BR2 Department (1989).

[8] J.M. Beeston et al., "Gas Retention in Irradiated Beryllium", EG&G Idaho Report, EGG-FSP-9125 (1990).

[9] V. Levy, "Rapport Final du Contrat SBB-BS1", CEA Report, Centre d'Etudes de Saclay, N.T. SRMA 92-1955 .A 3591-532 (1992).

[10] G.A. Sernyaev, "Beryllium Swelling and Spontaneous Cracking under Low Temperature Irradiation", SF Nikiet Internal Report.

[11] G.A. Sernyaev, "Beryllium Swelling in High-Temperature Neutron Irradiation. Main Structure Factors Role", SF Nikiet Internal Report.

[12] G. Caglioti et al., "Surface Energy for Brittle Fracture in Metals from Phonon Frequencies", Journal of Applied Physics, Vol. 42 No. 11 (1971) 4271-4276.

[13] J. Barnes and G.B. Reddings, "The Behaviour of Helium Atoms Injected into Beryllium", Journal of Nuclear Energy 10 (1959) 32-35.

[14] V.K. Kumirov, "The measurement of the Surface Tension of Some Pure Metals in the Solid State", Materials Science and Engineering 60 (1983) L23-L24.

[15] R. Swalin, "Thermodynamics of Solids", John Wiley and Sons, Inc., NY, 1962, p.181.

[16] D.A. Porter and K.E. Easterling, "Phase Transformations in Metals and Alloy", Van Nostrand Reinhold (UK) Co. Ltd., 1981, p.113.

[17] D.E. Dombrowski, Brush-Wellman, Private Communication (1992).

[18]   Ullmann's Encyclopedia of Industrial Chemistry, Vol. A4, Weinheim, 1985, p.12.

[19]   M.C. Billone and W.T. Grayhack, "Summary of Mechanical Properties Data and Correlations for Li2O, Li4SiO4, LiAlO2 and Be", ANL/FPP/TM-218 Report, Argonne National Laboratory, 1988.

[20]   M.C. Billone, Private Communication (1992).

[21]   D. Webster and D.D. Crooks, "Factors Influencing the Creep Strength of Hot Pressed Beryllium", Metallurgical Transaction 6A (1975) 2049-2054.

[22]   D. Webster and D.D. Crooks, "Creep Mechanisms in Beryllium", Metallurgical Transaction 7A (1976) 1307-1315.

[23]   R.V. Hesketh, "Proc. of the International Conference on Solid State Physics and Research with Accelerators", BNL-500883(C-52) (Physics-TID-4500), Brookhaven National Lab., September 1967, p. 389.

Staff:

M. Dalle Donne
J. Lebkücher
F. Scaffidi-Argentina
A. Weisenburger
H. Werle

BS BE-D 2   Tritium Release from Neutron Irradiated
Beryllium: Kinetics, Long-Time Annealing and
Effect of Crack Formation

Abstract

Since beryllium is considered as one of the best neutron
multiplier materials in the blanket of the next generation
fusion reactors, several studies have been started to evaluate
its behaviour under irradiation during both operating and
accidental conditions.

Based on safety considerations, tritium produced in beryllium
during neutron irradiation represents one important issue,
therefore it is necessary to investigate tritium transport
processes by using a comprehensive mathematical model and
comparing its predictions with well characterized
experimental tests.

Because of the difficulties in extrapolating the short-time
tritium release tests to a longer time scale, also long-time
annealing experiments with beryllium samples from the
SIBELIUS irradiation have been carried out at the
Forschungszentrum Karlsruhe. Samples were annealed up to
12 months at temperatures up to 650 °C. The inventory after
annealing was determined by heating the samples up to 1050
°C with a He+0.1 vol% H_2 purge gas.

Furthermore, in order to investigate the likely effects of
cracks formation eventually causing a faster tritium release
from beryllium, the behaviour of samples irradiated at low
temperature (40-50 °C) but up to very high fast neutron
fluences (0.8-3.9·10^{22} cm^{-2}, $E_n \geq 1$ MeV) in the BR2 reactor has
been investigated. Tritium was released by heating the
beryllium samples up to 1050 °C and purging them with
He+0.1 vol% H_2. Tritium release from high-irradiated
beryllium samples showed a much faster kinetics than from
the low-irradiated ones, probably because of crack formation
caused by thermal stresses in the brittle material and/or by
helium bubbles migration.

The obtained experimental data have been compared with
predictions of the code ANFIBE with the goal to better
understand the physical mechanisms governing tritium
behaviour in beryllium and to assess the prediction
capabilities of the code. Good agreement between calculated
and experimental data has been found.

1.   Introduction

Solid breeder blankets of fusion reactors require beryllium as
neutron multiplier to achieve adequate tritium breeding. In
the fast neutron field of the blanket, helium and tritium is
produced in beryllium. Therefore, besides compatibility with
other blanket materials, helium-induced swelling and tritium
retention are of concern.

Although the tritium production rate in beryllium is two to
three order of magnitude smaller than that in the breeder
ceramic, because of the slow release at typical blanket
temperatures [1], the inventory in beryllium might become
large during the DEMO blanket lifetime (≈ 3 years) and is
therefore a safety concern.

The produced tritium can diffuse through the lattice and/or
be captured by structural traps such as intragranular helium
bubbles, closed porosity, grain boundaries, etc. If tritium is
trapped in a helium-filled bubble, it follows the fate of the
bubble and will be released only if the bubble is vented into
an open porosity network, through which the gas can escape
with effectively no activation energy. On the other hand,
because beryllium of commercial purity always contains some
oxide inclusions (which tend to collect at grain boundaries
where they form globular phases), beryllium oxide can react
with tritium to form beryllium hydroxide which is
energetically stable with respect to single tritium atoms.
Tritium chemically bound in form of beryllium hydroxide at
oxide inclusions requires a sufficiently high thermal energy to
be released. In fact, under the action of heating, beryllium
hydroxide may dissociate and tritium in atomic form can be
re-injected into the lattice. Tritium in excess of what the
lattice can dissolve either diffuses through the lattice and
escape from the specimen or is captured by gas bubbles,
depending on the present global bubble density and size.
Due to the two different tritium trapping mechanisms in
beryllium, the release kinetics will be thus different
depending on gas bubble density and size, and on irradiation
or annealing temperature.

Therefore, release kinetics of neutron-generated tritium of
two types of beryllium samples (SIBELIUS and MOL) has been
studied. For beryllium samples which were in contact with
breeder ceramic during irradiation, a second type of tritium
inventory, due to implantation from the ceramic, was
observed. Because it is difficult to extrapolate the short-time
kinetics data to time scales comparable to the blanket
lifetime, also long-time annealing experiments (up to 12
months at temperatures up to 650 °C) have been performed.
With the MOL samples, which were irradiated up to very high
fast neutron fluences of 3.9·10^{22} cm^{-2} (DEMO blanket
$\leq 2.5 \cdot 10^{22}$ cm^{-2}), also effects of crack formation on tritium
release were observed.

To describe the irradiation behaviour of beryllium the
computer code ANFIBE has been developed [2]. The
experimental results have been compared with the ANFIBE
predictions with the goal to better understand the
mechanisms governing tritium transport and to assess the
prediction capabilities of the code.

2.   Experiments

2.1   Samples and irradiation conditions

The beryllium pellets (8 mm Ø x 2 mm) for the SIBELIUS
irradiation [3] were made by the Brush-Wellman
(specification B-26, arc cast, BeO ≤ 300 ppm). The structure is
characterized by grains as large as 2 mm and some
intergranular cracks; a cold worked layer resulting from
machining is observed on the surface; the density determined

from the masses and dimensions varied between 1.79 and 1.82 g/cm³ and was in the average 1.805 g/cm³ (98% theoretical density) [4]. The SIBELIUS irradiation was performed 1990 in the SILOE reactor at CEN Grenoble to a fast ($E_n \geq 1$ MeV) neutron fluence of $6 \cdot 10^{20}$ cm⁻². The irradiation temperature was 550 °C, except for capsule 1, where it was 270 °C. Whole, fresh pellets, but also smaller samples made from pellets that were previously used for metallographic investigations were studied. The previously used pellets were cleaned and axially cut to quarters of pellets.

The second type of beryllium samples (type MOL) were provided by CEN Mol [5,6]. The samples were made from cylindrical bars (15 mm Ø x 100 mm) fabricated by Kawecki Berylco Industries by vacuum hot pressing of impact attritioned powder of 100 mesh at least (grade S-200 E). The average grain size amounts to 10-13 µm. The specific BeO content is < 2%, the bulk density corresponds to 99.5% of the theoretical density. The bars have been irradiated at 40-50 °C in the BR2 reactor to a fast ($E_n \geq 1$ MeV) neutron fluence of 0.8, 2.8, $3.9 \cdot 10^{22}$ cm⁻². After irradiation the bars were ultrasonically treated to remove the outer oxide layer. Then they were rinsed with water and dried. Appropriate samples were cut from the bars. A cutting method which did not severely heat the samples was used to prevent release of contained gases. During the cutting it was experienced that the irradiated material was rather brittle [5].

2.2   Facilities and procedures

The main characteristics of the tritium release facilities are: the sample chamber is connected by a short, heated line (≈ 300 °C) to a Zn-reductor (≈ 390 °C). The reductor transforms any tritium water to tritium gas. This avoids problems with tritium water absorption and allows quantitative tritium measurements. The tritium activity of the purge gas is measured with an ionization chamber and/or a proportional counter. The released tritium inventory is determined by integrating the measured release rate over the time.

Two tritium release facilities have been used: a first series of experiments have been performed in the hot cell facility, where the maximum sample temperature was restricted to 900 °C. It turned out that this temperature is not sufficient to release all tritium. Therefore, in a second series of experiments most of the samples were heated to 1050 °C. By heating some samples to even higher temperatures, it has been checked that essentially all tritium is released at 1050 °C within several hours.

For the tritium release investigations, the samples were purged with high-purity He+0.1 vol% H2. Two heating procedures were applied: either linear ramps with 5 °C/min or a stepwise temperature increase.

For the long-time annealing studies, the quarters of pellets from the SIBELIUS irradiation have been used. The samples were inserted at definite positions in a tube furnace to

achieve the desired annealing temperatures of 380, 450, 550 and 650 °C and were purged with 5 l/h high purity He. After removal from the annealing furnace, the residual tritium inventory was determined by purging and heating the samples up to 1050 °C in the tritium release facilities.

2.3   Results and discussion

Release kinetics

It is expected that if beryllium is in direct contact with breeder ceramic during irradiation, a fraction of the 2.74 MeV tritons (range in ceramic $\approx 40\mu$m) produced in the ceramic is implanted into the surface layer of beryllium, leading to an additional inventory which was estimated to be several times larger than the neutron-produced one. This has been confirmed by the measured tritium release of SIBELIUS pellets which were in contact with ceramic during irradiation (Fig. 1).
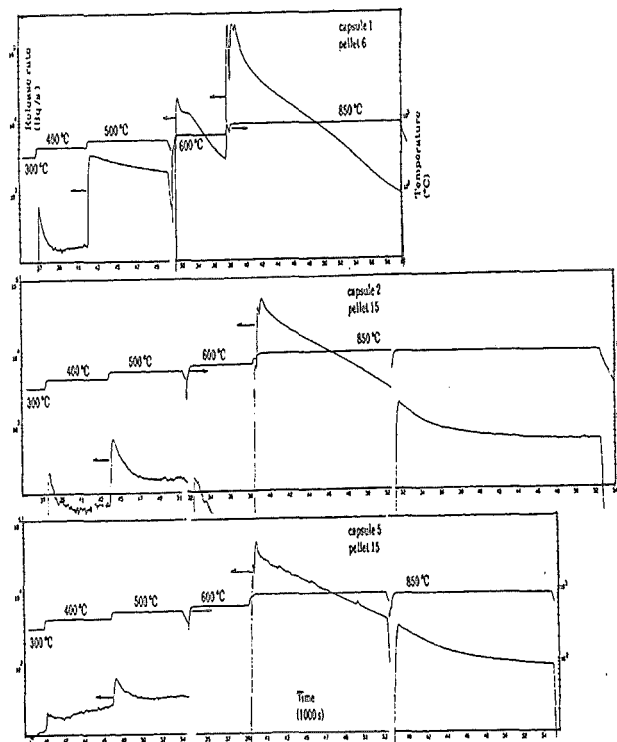

Fig. 1:   SIBELIUS beryllium samples, whole pellets: release of implanted (top) and neutron-generated tritium (center, bottom)

Pellet 6 of capsule 1 was irradiated at 270 °C and contained a high implanted inventory (total specific inventory 4100 MBq/g), which is released already at 500 °C (Fig. 1 top). For the other two pellets (pellet 15 of capsule 2 and pellet 15 of capsule 5), which were irradiated at 550 °C, the implanted tritium was evidently released already during irradiation (total specific inventory 1500-1600 MBq/g) and the neutron-generated tritium is released only above 600 °C.

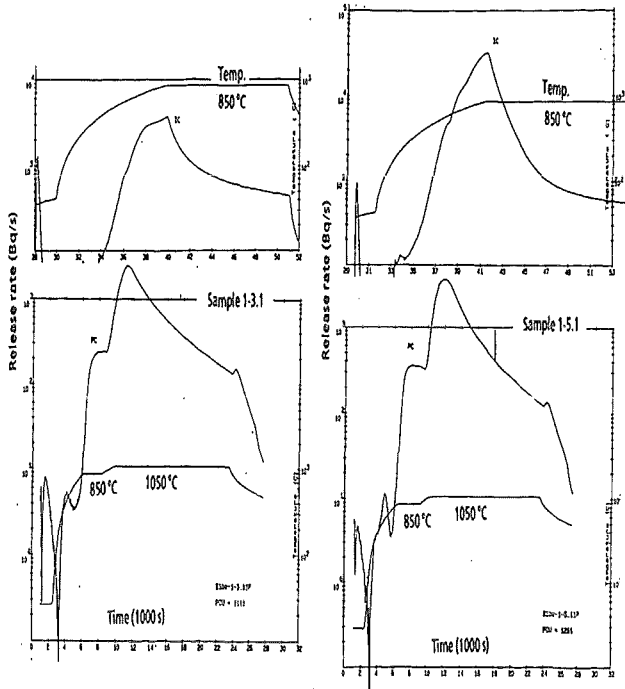In Fig. 2 tritium release of not-annealed quarters of SIBELIUS

Fig. 2: SIBELIUS beryllium samples, not-annealed quarters of pellets: release of neutron-generated tritium

pellets irradiated at 270 °C is shown. Sample 1-3.1 (1 capsule no. - 3 pellet no. 1 quarter no.) was not, sample 1-5.1 was in contact with ceramic during irradiation, but contained only a small implanted inventory, because the bulk is released during cleaning and cutting of the pellets. The release starts to increase with temperature above about 600 °C. At 850 °C it initially decreases fast, but achieves a nearly constant value after several hours, indicating a remarkable residual inventory, which is confirmed by the 1050 °C runs during which the residual inventories of 15-40% are released.

In Fig. 3 tritium release from the MOL samples 110A-9c, irradiated with the lowest fast fluence (0.8·10²² cm⁻²) is shown. Similar as for the SIBELIUS samples, the release starts to increase above about 600 °C, but decreases very slowly at 850 °C. Correspondingly, only a small fraction (11%) of the tritium is released at 850 °C, the bulk (83%) is released at 880 °C and the residual 6% at 1050 °C. The behaviour at 880 °C is very surprising: at constant temperature, normally the release rate decreases monotonically with the time, whereas here, after several hours, it starts to increase to a maximum and finally decreases again. After the maximum, strong oscillations of the release rate are observed. A similar behaviour has been previously observed by Baldwin and Billone [7] for beryllium irradiated at 75 °C. During heating at constant temperature, after a time lag of 2 to 4 hours a burst release of tritium was seen. Details are given in Tab. 1.

Their explanation, that this burst release is due to the migration of helium bubbles which leads to the formation of interconnected grain-edge tunnels to the sample surface, looks very reasonably.
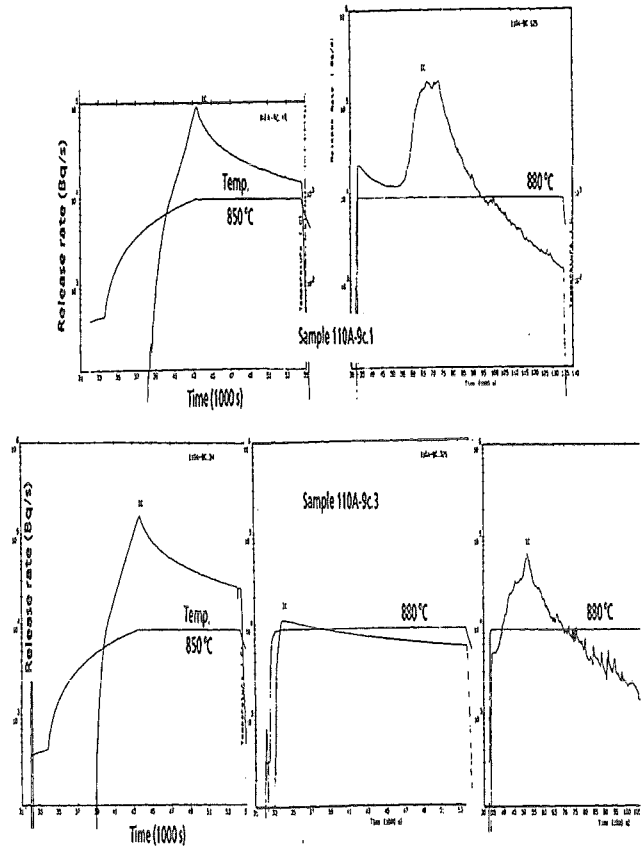

Fig. 3: MOL beryllium samples 110A-9c (fast fluence 0.8·10²² cm⁻²): release of neutron-generated tritium

Table 1: Burst release temperature for various beryllium samples observed by Baldwin and Billone [7]

Sample density (% of the theoretical)	81%	99%	100%
Fast fluence, E_n ≥ 1 MeV [cm⁻²]	2.6·10²¹	2.6·10²¹	5.0·10²²
Temperature of burst release [°C]	600	900	600

Tritium release of the highly irradiated MOL samples 110A-9a (fast fluence 2.8·10²² cm⁻²) and 137A-22b (fast fluence 3.9·10²² cm⁻²) is much faster than that of weakly irradiated samples 110A-9c and of the SIBELIUS samples, as is clearly shown in Fig. 4. Release drops fast at 850 °C and correspondingly essentially all tritium (94-96%) is released at this temperature. Also in contrast to samples 110A-9c, no burst release was observed. An explanation which is consistent with the fast release is that in this highly irradiated samples the formation of the interconnected grain-edge
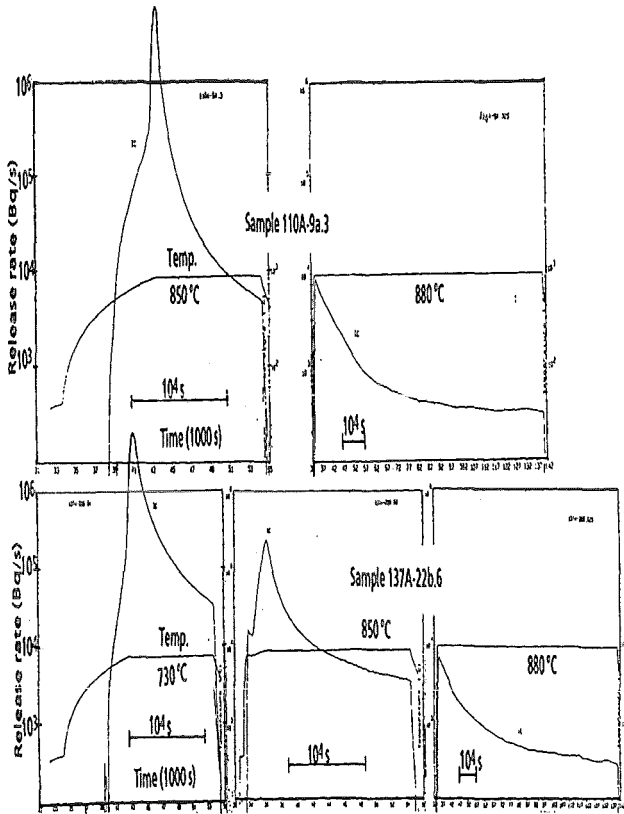
Fig. 4:   MOL beryllium samples 110A-9a (fast fluence
            2.8·10²² cm⁻²) and 137A-22b (fast fluence 3.9·10²²
            cm⁻²): release of neutron-generated tritium

tunnels occurs already during irradiation. The different
kinetics is also demonstrated in Tab. 2, where the fractional

Table 2:   Fractional tritium release for SIBELIUS and MOL
           beryllium samples

Temp [°C]	SIBELIUS samples not-annealed, quarters of pellets			MOL samples		
	1-3.1	1-5.1	2-11.2	110A-9c	110A-9a	137A-22b
850	0.59	0.85	0.58	0.11	0.94	0.96
880				0.94	0.96	0.97
1050	1.0	1.0	1.0	1.0	1.0	1.0

release at different temperatures is given.

Long-time annealing (SIBELIUS samples, quarters of pellets)

The residual specific inventory after annealing is shown as
function of annealing time with the annealing temperature
as parameter in Fig. 5. Tritium release is very slow below 400
°C and moderately fast between 450 and 550 °C. At 650 °C,
the inventory decreases pretty fast to several percent during
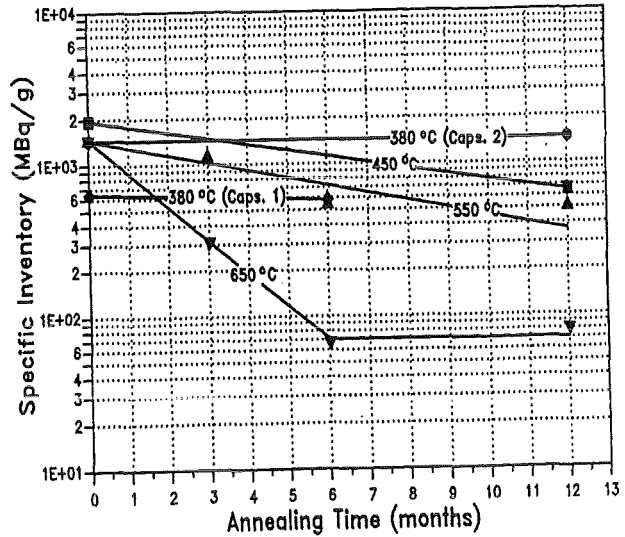

Fig. 5:   Residual specific inventory vs. annealing time for
            neutron-generated tritium in beryllium, parameter
            annealing temperature (SIBELIUS samples,
            quarters of pellets)

the first six months, but afterwards it remains essentially
constant.

The data of Fig. 5 have been roughly fitted by straight lines -
although at 650 °C the decrease is not exponential - and
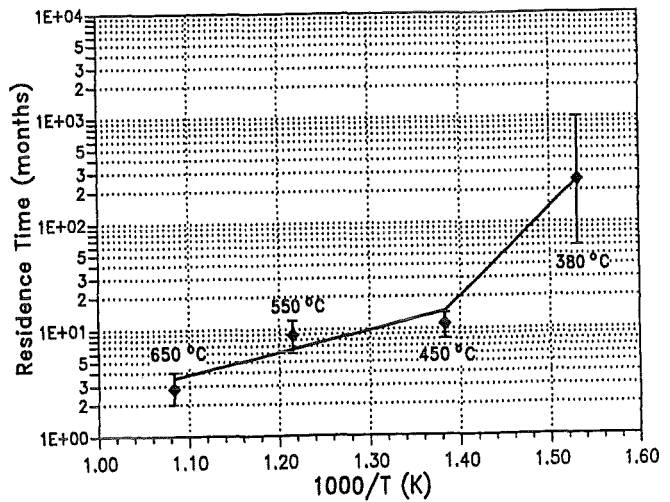

Fig. 6:   Residence time vs. annealing temperature for
            neutron-generated tritium in beryllium (SIBELIUS
            samples, quarters of pellets)

tritium residence times have been determined (Fig. 6), which
correspond to the time at which the inventory has decreased
to 37% (1/e) of the initial value.

Although due to both experimental data scattering and not-
exponential decrease, the uncertainty of the residence times
in Fig. 6 is quite large, to our knowledge no other data on
long-time tritium release from beryllium are available for
fusion blanket predictions. From Fig. 6 it can be seen that at

temperatures below about 400 °C, essentially all produced tritium is retained in beryllium.

3. Comparisons with ANFIBE Predictions

In order to better understand the physical mechanisms governing tritium release behaviour in beryllium, as well as to generate confidence in the results provided by the code ANFIBE and to assess its prediction capabilities, it was necessary to compare the calculated results with a large number of reliable experimental data as described in [2].

Samples 2-13 and 5-11/13 of the SIBELIUS series, both irradiated at 550 °C, and successively annealed at 550 and 650 °C respectively up to 12 months has been taken as reference for long-time annealing calculations with the ANFIBE code. Although both samples were, during irradiation, in contact with ceramics and ANFIBE cannot yet take into account the effects of implanted tritium, they were in any case chosen due to the fact that, in a similar way as for samples 2-15 and 5-15, in both cases essentially all implanted tritium, but only a small fraction of the neutron-generated tritium was released during the irradiation at high temperature.

A comparison in terms of fractional tritium release as a function of the annealing time between experimental data and predictions of ANFIBE is shown in Figs. 7 and 8. The
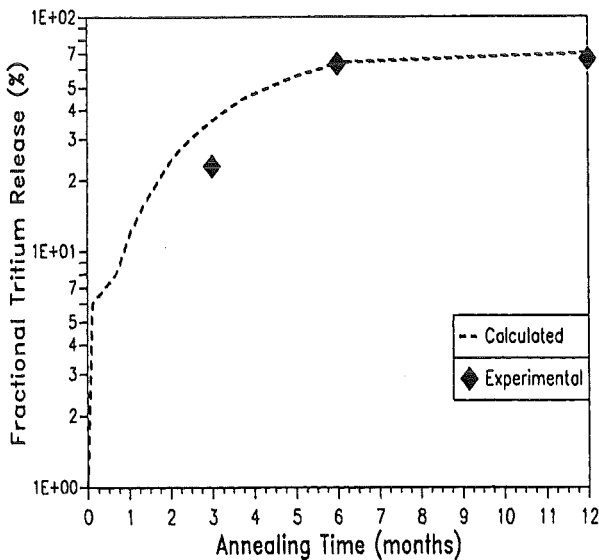

Fig. 7: Comparison of calculated and measured (SIBELIUS sample 2-13) fractional tritium release during annealing at 550 °C as a function of time

agreement between calculated and experimental data is satisfactory. The predicted residence time of neutron-generated tritium is about 6 months for sample 2-13 (annealing temperature 550 °C) and 2 months for sample 5-11/13 (annealing temperature 650 °C) respectively. These values are in reasonable agreement with the experimental results shown in Fig. 6.
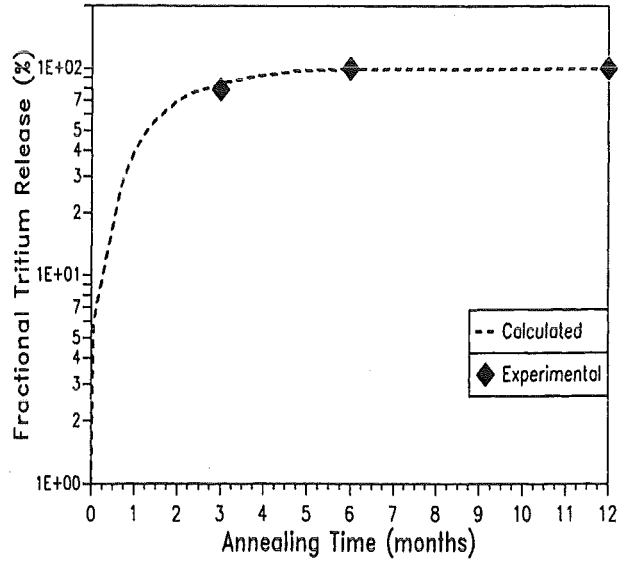

Fig: 8: Comparison of calculated and measured (SIBELIUS sample 5-11/13) fractional tritium release during annealing at 650 °C as a function of time

In order to investigate the possible crack formation eventually causing an increased tritium release from beryllium, the behaviour of two samples both irradiated at low temperature but at very different fast neutron fluence in the BR2 reactor and successively out-of-pile annealed at high temperature has been investigated.

In the first case the behaviour of the sample 110A-9c.3 of the MOL series (fast fluence $0.8 \cdot 10^{22}$ cm^{-2}) was investigated. As previously pointed out, the in-pile irradiation was followed by a temperature ramp with a slope of about 5 °C/min from room temperature up to 850 °C. As shown in Fig. 9, the tritium release rate has a rapid increase during the temperature ramp and then it tends to slowly decrease as the annealing temperature remains constant. The comparison between calculated and experimental data shows in this case a good agreement.

On the contrary, for the sample 110A-9a.3, which was irradiated with a fast neutron fluence of $2.8 \cdot 10^{22}$ cm^{-2} and successively out-of-pile annealed up to 850 °C in the same way as the previous one, a sharp peak is observed in the experimental tritium release rate curve during the temperature ramp probably because of microcracks formation. Due to the higher neutron fluence, in fact, the beryllium specimens has become more brittle than in the previous case and consequently it easily cracked under thermal stresses. A comparison between the calculated and the experimental tritium release is shown in Fig. 10. Since ANFIBE doesn't account yet for the effect of the microcracks, the code prediction cannot be, in this case, in good agreement with the experimental data as for sample 110A-9c.3.
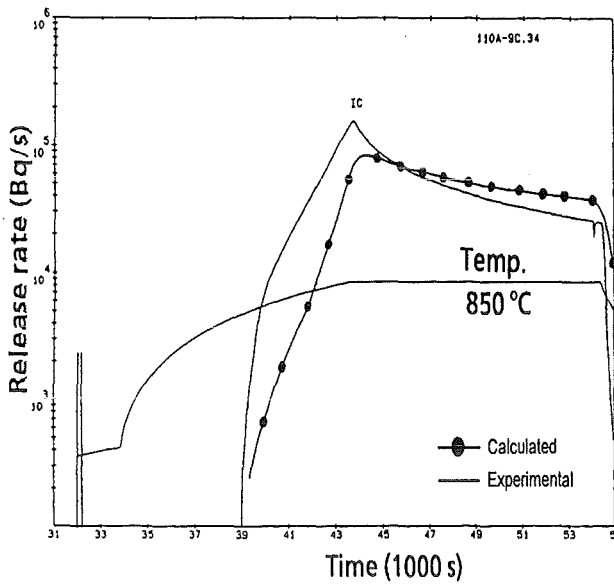
Fig. 9: Comparison of calculated and measured tritium release rate as a function of time for moderately irradiated beryllium (fast fluence $0.8 \cdot 10^{22}$ cm^{-2}, MOL sample 110A-9c.3)
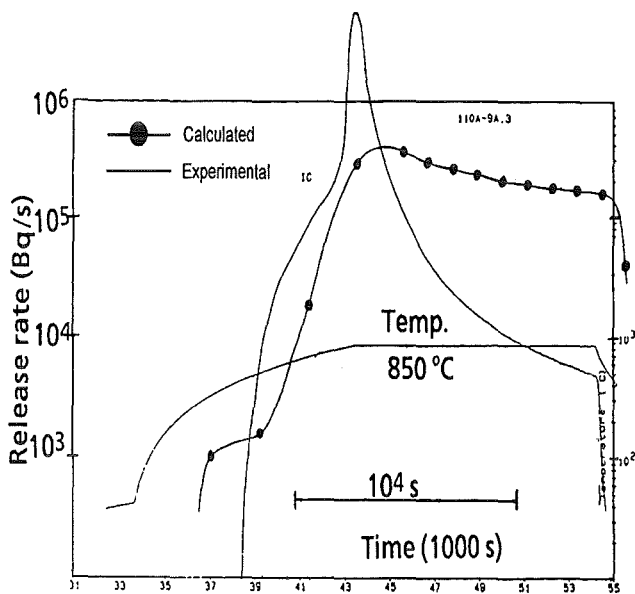

Fig. 10: Comparison of calculated and measured tritium release rate as a function of time for highly irradiated beryllium (fast fluence $2.8 \cdot 10^{22}$ cm^{-2}, MOL sample 110A-9a.3)

4. Conclusions

In the present work both stepped and ramp annealing experiments were done to investigate tritium release behaviour from irradiated beryllium. Tritium release kinetics from two types of beryllium samples (SIBELIUS and MOL) has been studied. Comparison of the experimental data with the prediction of code ANFIBE was also performed with the goal

to better understand the mechanisms governing tritium transport and to assess the prediction capabilities of the code.

According to previous studies, it was found that the release of neutron-generated tritium in beryllium is very slow if compared with ceramics. Furthermore, the present work indicates that for beryllium which is in direct contact with breeder ceramic during irradiation, a fraction of the 2.74 MeV tritons (range in ceramic $\approx 40 \mu$m) produced in the ceramic is implanted into the surface layer of beryllium, thus leading to an additional inventory which was estimated to be several times larger than the neutron-produced one. Analysis of samples from the SIBELIUS series indicates that pellets irradiated at relatively low temperature (270 °C) retain, during irradiation, most of the implanted and essentially all the neutron-generated tritium. On the contrary, pellets irradiated at 550 °C, seem to release all the implanted tritium already during irradiation, while the neutron-generated tritium is released only after annealing at temperatures above 600 °C.

Long-time annealing of beryllium samples from the SIBELIUS series indicates that tritium release is very slow below 400 °C and moderately fast between 450 and 550 °C, while at 650 °C the inventory decreases fast during the first 6 months and then remains essentially constant as confirmed by ANFIBE calculations too.

Beryllium samples from the MOL series irradiated with the lowest fast fluence ($0.8 \cdot 10^{22}$ cm^{-2}) show, in a similar way as for the SIBELIUS samples, a release which starts to increase above about 600 °C, but decreases very slowly at 850 °C. Correspondingly, only a small fraction (11%) of the tritium is released at 850 °C, the bulk (83%) is released at 880 °C and the residual 6% at 1050 °C. On the other hand, a surprising behaviour was observed at 880 °C: during heating at constant temperature, after a time lag of several hours a burst release was observed, probably due to migration of helium bubbles leading to the formation of interconnected grain-edge tunnels to the sample surface. With other samples irradiated up to very high fast neutron fluences of $3.9 \cdot 10^{22}$ cm^{-2}, a much faster tritium release than in the case of weakly irradiated samples was observed. Comparison of experimental data with ANFIBE predictions indicates that this effect is due to microcracks formation during the out-of-pile heating phase. This is confirmed by the fact that highly irradiated beryllium from the MOL series showed a rather brittle behaviour during the cutting phase of the samples.

Although, at this stage, not all the mechanisms governing the release of tritium in irradiated beryllium have been fully understood, comparison of the code predictions with experiments indicate that, for the cases considered so far, the most important phenomena were accounted for by ANFIBE. However, to further improve the availability of the code predictions, in-pile experiments at high temperatures and, at the same time, high fast neutron fluences are clearly required.

Literature:

[1]   W. Dienst, D, Schuld, H. Werle, "Tritium Release of Li4SiO4, LiO2 and Beryllium and Chemical Compatibility of Beryllium with Li4SiO4, LiO2 and Steel (SIBELIUS Irradiation)", KfK Report 5109, 1992.

[2]   F. Scaffidi-Argentina, "Modellierung des Schwellens und der Tritium-Freisetzung von bestrahltem Beryllium", FZKA Report 5632 (to be published).

[3]   N. Roux et al., "The SIBELIUS Experiment: Study of the Irradiation Behaviour of Beryllium/Ceramics and Beryllium/Steel Compacts.", J. Nucl. Mater. 179-181 (1991) 827-830.

[4]   N. Roux et al., "Compatibility Behaviour of Beryllium with LiAlO2 and LiZrO2 Ceramics with 316L and 1.4914 Steels in SIBELIUS", J. Nucl. Mater 191-193 (1992) 168-172.

[5]   L. Sannen, "Characterization of Irradiated Beryllium", CEN Mol Report FT/Mol/92-01, July 1992.

[6]   L. Sannen, Ch. de Raedt, "The Effects of Neutron Irradiation on Beryllium", Proceedings of the SOFT-17 Conference, Rome, 1992.

[7]   D.L. Baldwin, M.C. Billone, "Diffusion/Desorption of Tritium from Irradiated Beryllium", J. Nucl. Mater. 212-215 (1994) 948-953.

Staff:

M. Dalle Donne
J. Lebkücher
F. Scaffidi-Argentina
A. Weisenburger
H. Werle

BS BR-D   Breeder Material

BSBR-D 1/D 2   Preparation and Characterization of Ceramic Breeder Materials

Thermal Properties of Li_4SiO_4 and Phase Studies in the Li_4SiO_4-Li_2SiO_3 Range of the Li_2O-SiO_2 System

The enthalpy, the heat capacity and the second order transitions of Li_4SiO_4 were measured by differential thermal analysis and high temperature calorimetry between room temperature and 1030°C. The material used were single-phase 1.0 mm diameter spheres which had been manufactured by Schott Glaswerke through air spraying of Li_4SiO_4 melts. The product was crushed, pelletized to appropriate dimensions and heated in dry air at 900°C for ten minutes in order to remove absorbed water and to attain complete crystallization of the phase.

X-ray diffraction of Li_4SiO_4 by the Guinier method at room temperature revealed a monoclinic phase with the space group $P2_1/m$ (No. 11) and the lattice parameters a = (529.6 ± 0.2)pm, b= (611.0 ±0.3)pm, c = (514.5 ±0.2) pm, β = (90.27±0.05)°. 14 diffraction lines were evaluated. X-ray density ρx = 2.39 Mg/m³. Z = 2.

Two second order transitions of Li_4SiO_4 were observed by anisothermal calorimetry due to possible excitations of molecular rotations or vibrations or to destruction of electrical ordering. In this case, the heat capacity increases in a limited temperature range and passes a finite maximum value at the critical temperature T_c. No volume change of Li_4SiO_4 is connected with this type of transition. The critical temperatures are 665°C and 723°C. The integrals of the excess heat capacities $C_{p,xs}$ above the basic C_p vs. T curve of Li_4SiO_4 are $\int C_{p,xs}\, dT = 900$ J/mol and $\int C_{p,xs}\, dT = 630$ J/mol in the temperature ranges of the transitions, 921 - 956 K and 979 - 1008 K, resp. The maximum C_p above the basic curve is estimated to be 3·R/2 for both transitions. A possible isotope effect on the transition temperatures of Li_4SiO_4 and on the eutectic temperature of Li_4SiO_4 in equilibrium with the phase higher in SiO_2 concentration was investigated on materials containing Li-nat (7,5 % 6Li) and enriched Li (50 %6Li). No isotope effect was observed. The enthalpy and the heat capacity of Li_4SiO_4 determined by isothermal drop calorimetry between room temperature and 1300 K are given in analytical form by $H°_T - H°_{298} = -17156 + 73.694 · T + 0.10321 · T^2 - 4163115 · T^{-1}$ J/mol and $C_p = 73.694 + 0.20642 · T + 4163115 · T^{-2}$ J/K·mol. Numerical data are compiled in Table 1.

The Li_4SiO_4-Li_2SiO_3 range of the phase diagram of the pseudobinary Li_2O-SiO_2 system was reinvestigated because an additional intermediate metastable or stable high temperature phase was supposed. Experiments were performed on specimens from melted Li_2O-SiO_2 ingots of Schott Glaswerke in the concentration range 33 - 50 at. % SiO_2 by differential thermal analysis and by anisothermal high temperature calorimetry up to 1300°C and by room temperature X-ray diffraction. The samples were

Table 1:   Enthalpy $H°_T$ - $H°_{298}$ and heat capacity Cp of Li_4SiO_4

T in K	$H°_T$ - $H°_{298}$ in J/mol	C_p in J/K·mol
298	0	182.1
400	18427	182.3
500	37168	193.6
600	57278	209.1
700	79056	226.7
800	102651	245.3
900	128145	264.6
1000	155587	*
1100	185010	304.2
1200	216433	324.3
1300	249873	344.5

* range of second order transition

encapsulated in platinum foils in order to reduce evaporation and mass loss due to increasing Li_2O vapour pressure. A stable high temperature phase exists with the composition $Li_6Si_2O_7$ which forms peritectically at 1030°C and decomposes eutectoidally at 1020°C. A eutectic was observed between Li_4SiO_4 and Li6Li_2O_7 at 1025°C and 38.3 at. % SiO_2, see Fig. 1. $Li_6Si_2O_7$ can be maintained at room temperature by rapid cooling and crystallizes in a tetragonal structure with a = 770.6 pm and c = 486.1 pm, space group $P42_1m$ (No. 113). The phase decomposes into Li_4SiO_4 and Li_2SiO_3 by annealing below 1020°C and by slow cooling, resp. Additional experiments by Schott Glaswerke revealed further a phase transition of $Li_6Si_2O_7$ in the stable or metastable temperature range.

Li_4SiO_4 slightly enriched with 2 mass % SiO_2 is foreseen as ceramic breeder material. The air-sprayed pebbles pass a Li_4SiO_4-$Li_6Si_2O_7$ two-phase field during rapid cooling of the manufacturing process. $Li_6Si_2O_7$ is retained at room temperature. Therefore, after the fabrication process, a high-temperature heat treatment is recommended below 1020°C.
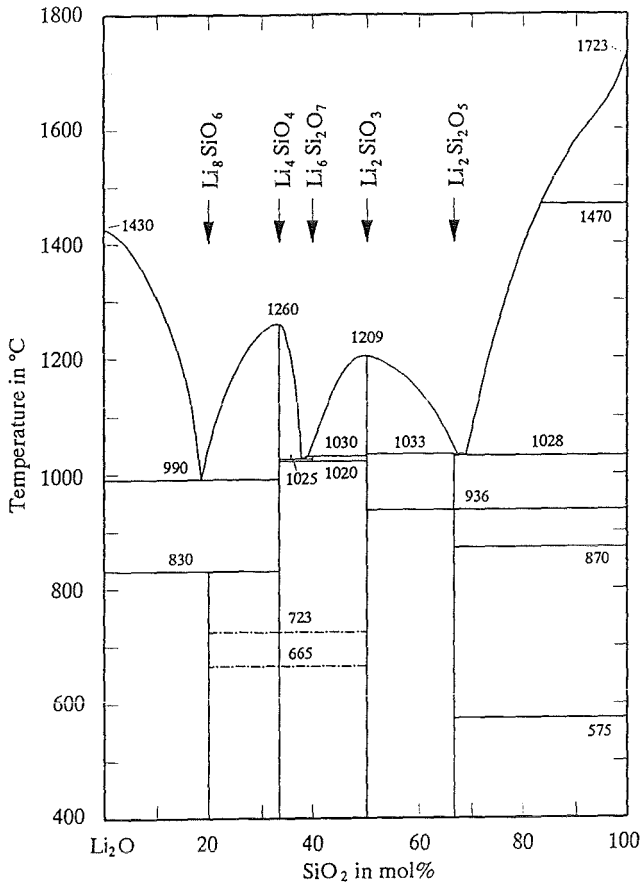
Fig. 1:   Phase diagram of the pseudobinary Li₂O-SiO₂ system

Staff:

H. Kleykamp
W. Laumer
S. Claus (Diplomandin)

BS BR-D 3   Irradiation Testing and Post Irradiation Examination

The BOT Solid Breeder Blanket Concept deals with lithium orthosilicate and beryllium pebbles. In a first draft the blanket breeder material and the neutron multiplier beryllium were arranged in a mixed bed cooled by high pressure helium flowing in tubes.

In a second draft the two pebble specimen were separated by cooled Manet plates (Fig. 1).
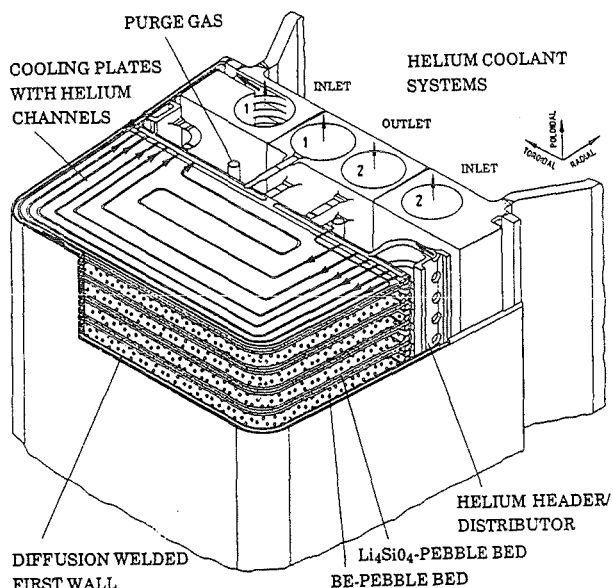

Fig. 1:   Blanket cannister

This new concept has 2 advantages compared with the mixed bed:

● compatibility problems between breeder and n-multiplier Be are avoided, and

● the manufacturing of the cooling system by diffusion welding of the Manet plates is easier and avoids the leakage problems of many welded tubes.

In this contribution we present results of post irradiation examination of the iradiation experiments CORELLI 2; EXOTIC 6, ALICE 3 and the so called Beryllium Experiment.

The mechanical and thermal stability under irradiation of both Li_4SiO_4 and Be as well as good T release properties have to be proven by these examinations.

CORELLI 2 (burn up < 1at%)

CORELLI 2 performed in the SILOE reactor Grenoble was a vented experiment of capsules with a mixture of Li-orthosilicate and Be pebbles.The aim was to study swelling and compatibility in contact with beryllium. Furtheron the seperation of irradiated pebbles of Be and Li-orthosilicate was succesfully effected..

EXOTIC 6 (burn up < 3 at%)

EXOTIC 6 was a vented experiment performed in the HFR Petten. For FZK Li-orthosilicate and Li-zirconate pebbles were irradiated. Decapsulation was already done at Petten. At FZK Hot Cells/Fusion Ceramic Lab. the mechanical stability and T-release were examined. The results of measurements of compressive force are shown in Tab. 1. The testing machine is depicted in Fig.2.

ALICE 3 (burn up: 3 at%)

In this irradiation experiment pebbles of Li-orthosilicate and -irconate were irradiated in He filled capsules in the frame of a Common European Task in the OSIRIS reactor Saclay/France.

The investigation of the influence of additives as SiO_2 and Al_2O_3 on the structural stability and T-release of Li-orthosilicates was the main purpose of the FZK activity in this experiment. The influence of these additives on the compressive strength was examined besides T-release. (Tab. 1). As can be seen the compressive force of Li-orthosilcate pebbles is not affected by Li burnup up to 3 at%.

Beryllium Experiment (burn up: 3,7 at%)

The objective of this experiment was the investigation of the T-inventory, swelling and embrittlement of Be spheres. A total of 8 closed capsules was irradiated in the HFR/Petten, two of them contained a mixed bed of Be-and Li-orthosilicate pebbles, whereas the remaining 6 were filled by 2 fractions of Be spheres. Measurement of compressive force beeing in preparation, we report here on results of He pycnometry and metallography (Fig. 3+4) together with microhardness measurements (Fig. 5).

Fig. 3 depicts the macroscopic surfaces of the 2 fractions of Be-spheres, Fig. 4 shows their metallographic cross sections. As can be seen the big pebbles derived from the Brush Wellmann Redox Process have an irregular surface and inner pore structure, whereas the small pebbles (Rotating Electrode Process) possess a smooth surface with only few closed pores. Microhardness measurements shown in Fig.5 show a change of Vickers hardness distribution, due to irradiation (Center & outer region of the cross section). Image analysis of the large Be spheres gives a hint, that swelling occurs first in the closed pores. He- and Hg- porosimetry measurements could not prove a significant density change. Measurements by immersion porosimetry are planned for the future.

Conclusion

The results of Post Irradiation Examination (PIE) gave no hint of detrimental failures of neither the Li-orthosilicate nor the Beryllium spheres up to 3 at% Li burnup.

Tab. 1: Compressive strength of Li - orthosilicate pebbles after n-irradiation

	COMPLIMENT	ALICE 3	ALICE 3	EXOTIC 6
Capsule No.	173, 174, 175, 176	A + B	C1	1
Burnup [%]	0.3 | 1.0	3.0	3.0	3.0
Material	Li_4SiO_4	$Li_4SiO_4 + 2.2\% SiO_2$	$Li_4SiO_4 + 2.2\% SiO_2 + 1\% Al_2O_3$	Li_4SiO_4
Manufacturer	Schott	Schott	Schott	Schott
Compressive Force [N]	7.2, 6.1, 4.7, 5.2	5.7	7.3	12.7
Standard Diviation [N]	2.6, 1.9, 2.0, 2.0	2.9	3.7	3.0
Deformation [µm]	37, 39, 38, 38	36	34	36
Standard Deviation [µm]	11, 17, 15, 14	17	10	11
No. of Measurements	23, 21, 24, 22	24	27	22
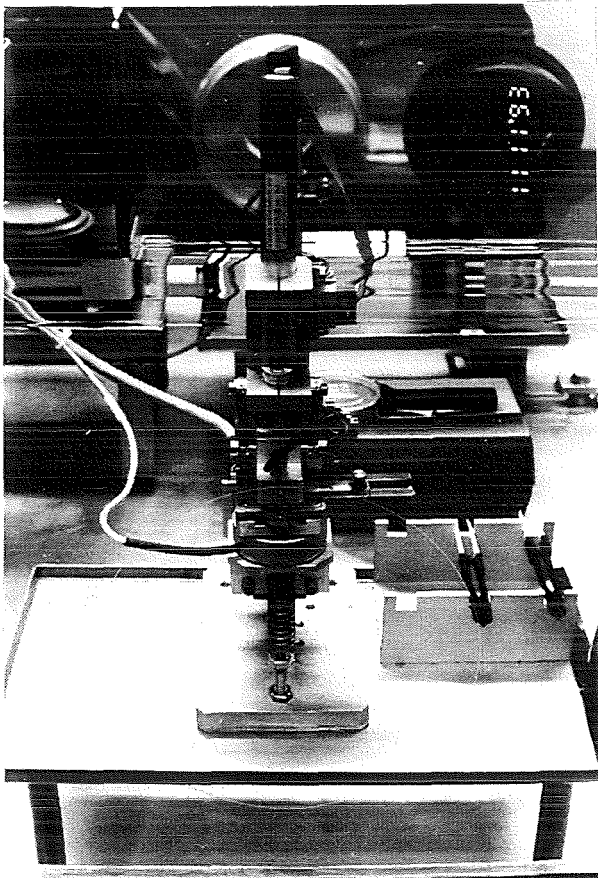
Fig. 2: Installation for measuring the compressive strength of Li compounds

Big Pebble (2 mm dia.)

Small Pebbles (0.1 - 0.2 mm dia.)

HVT HEISSE ZELLEN 50:1
BE/PE-5-1.2/18 0.25 MM
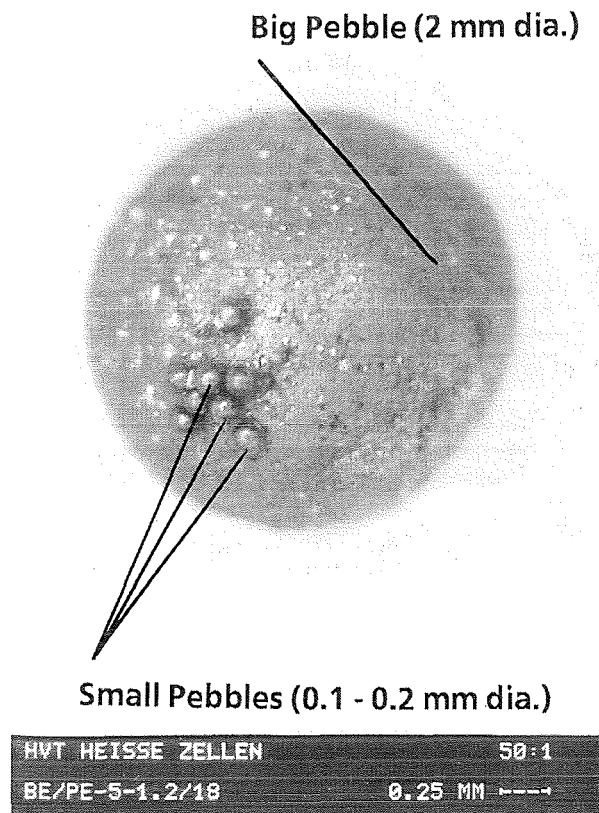
Fig. 3: Macroscopic surface of different irradiated Be pebbles (Be experiment)
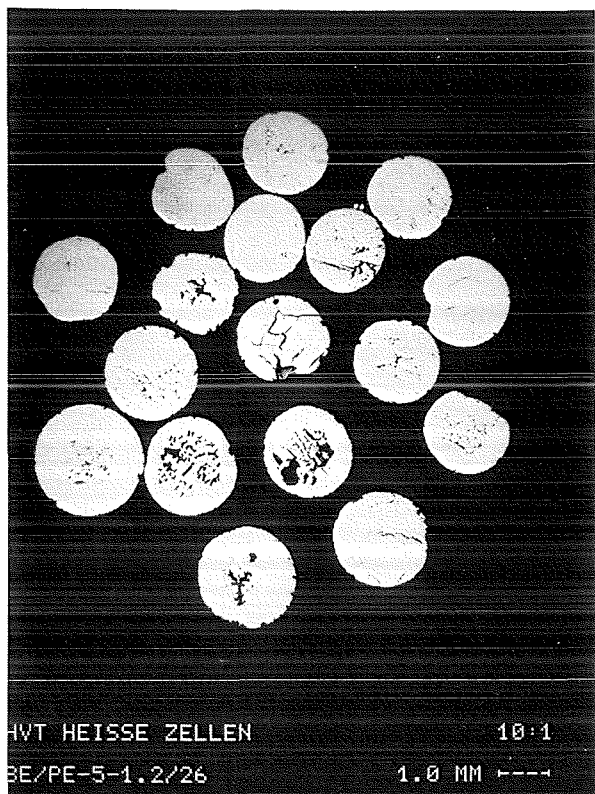
Fig. 4: Metallographic cross sections of Be pebbles (Be experiment)

Literature:

[1] K.R. Kummerer et al.: Fusion Technology (1990) p. 827-831

[2] P. Weimar, H. Steiner: 2nd Intern. Workshop on Ceramic Breeder Blanket Interaction, Paris, Sept. 22 - 24 (1993)

[3] P. Weimar, H. Steiner, H. Zimmermann, L. Dörr: 18th SOFT Karlsruhe, Aug. (1994)

[4] L.Dörr, D. Schild, H. Werle: 18th SOFT Karlsruhe, Aug. (1994)

[5] M. Dalle Donne et al.: 18th SOFT Karlsruhe, Aug. (1994)

[6] H. Zimmermann, KfK 4525 (1989)

[7] W. Dienst et al.: ICFRM, Stresa (1993)

Staff:

E. Kaiser
D. Knebel
B. Neufang
R. Pejsa
O. Romer
H. Steiner
P. Weimar
S. Weih
F. Weiser
H. Ziegler

Fig. 5: Change of microhardness distribution in Be pebbles due to n-irradiation.

BS BR-D 4   Tritium Release

In solid breeder blankets the tritium inventory in the breeder and multiplier is an important safety aspect. Tritium release for the materials foreseen for the BOT blanket concept (lithium orthosilicate, lithium metazirconate and beryllium pebbles) is therefore studied inpile and out-of-pile.
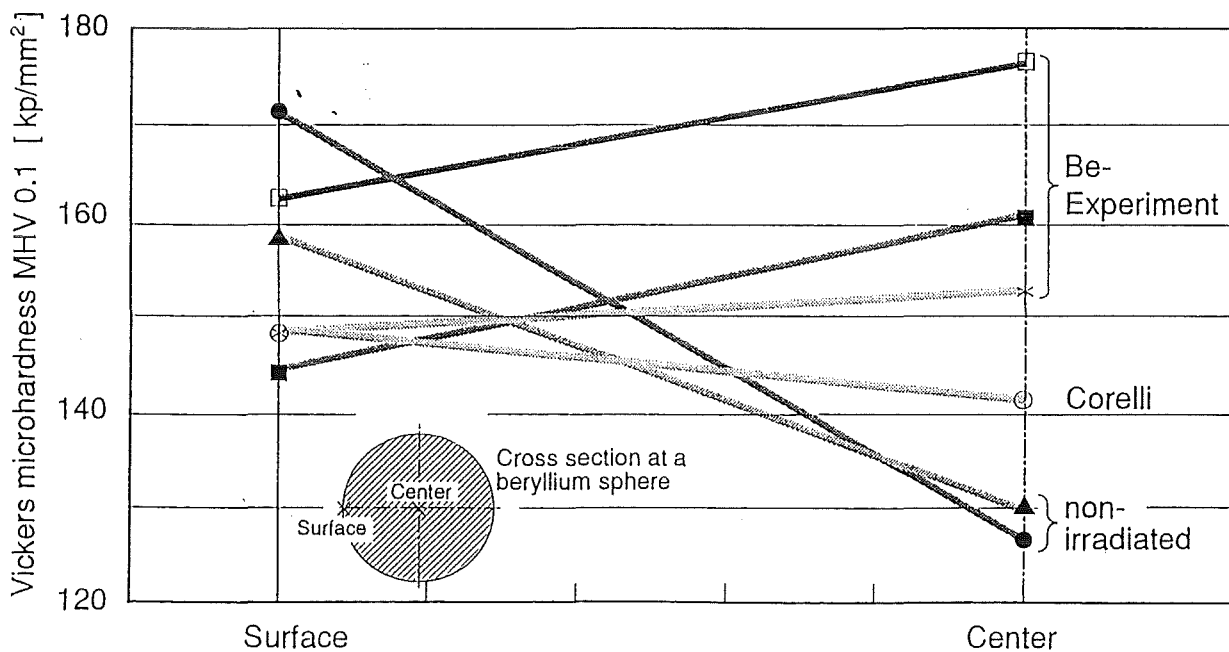
Purged inpile tests

The joint European, high-burnup inpile test EXOTIC-7 has been completed February 1995. Beds of lithium orthosilicate pebbles and mixed beds of orthosilicate and beryllium pebbles were provided by FZK. The ceramic pebbles were prepared from lithium enrichted to 50 % in Li6 and achieved a lithium burnup of 6 to 18 % (DEMO ≤ 10 %). The most important results were: tritium release behaviour was not significantly effected by burnup and the pebbles remained essentially intact [1]. PIE of the samples is in progress.

Out-of-pile tests

PIE of the lithium orthosilicate and metazirconate pebbles from the joint European, medium-burnup (3 %) test EXOTIC-6 showed a similar tritium release behaviour as for weakly irradiated pebbles [2]. This confirms the inpile observation from EXOTIC-6 [3] and EXOTIC-7 [1], that tritium release is not significantly effected by burnup.

Because for beryllium no inpile tritium release data are available, long-time annealing experiments (up to 12 months at temperatures up to 650 °C) have been performed to provide data for first estimations of tritium inventories under blanket-representative conditions. Beryllium samples irradiated to a fast neutron fluence of $6 \cdot 10^{20}/cm^2$ (SIBELIUS experiment) were annealed by purging with He at different temperatures for different times. From the initial and the residual tritium inventories after annealing, tritium residence times as a function of temperature have been estimated for beryllium (Fig. 1). The data show that below about 400 °C essentially all neutron-produced tritium is retained during the DEMO blanket lifetime of about 3 years [4, 5].

With beryllium samples irradiated in the BR2 Mol to very high fast neutron fluences of up to $3.9 \cdot 10^{22}/cm^2$ (DEMO blanket ≤ $2.5 \cdot 10^{22}/cm^2$), the influence of neutron irradiation on tritium release was studied. It was observed that above a neutron fluence of about $1 \cdot 10^{22}/cm^2$, tritium release from beryllium becomes faster, probably due to the migration of helium bubbles, which leads to the formation of interconnected grain-edge tunnels to the sample surface [5, 6].

In the closed capsule irradiation "Beryllium", beds of large (2 mm) and small (0.2 mm) beryllium pebbles and mixed beds of large and small beryllium and small (0.2 mm) orthosilicate pebbles were irradiated in the HFR Petten to a fast neutron fluence of about $1 \cdot 10^{21}/cm^2$. The goal was to get first informations concerning swelling, embrittlement and tritium release of the beryllium pebbles. The main results of the PIE
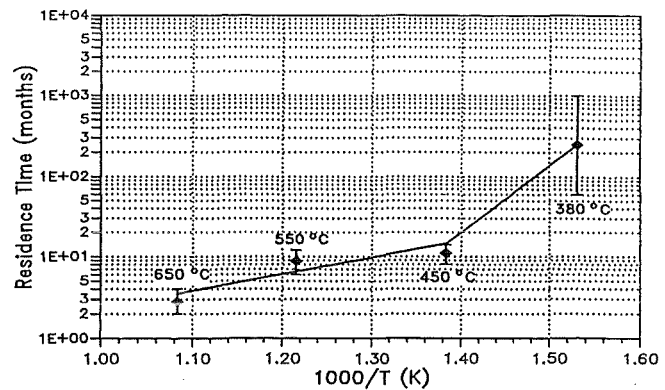

Fig. 1:   Residence time as function of temperature for release of neutron-generated tritium from beryllium.

trtium release studies were: 1) release of neutron-generated tritium from the small beryllium pebbles with low BeO content (0.08 wt%) is remarkably faster than from the large pebbles with high BeO content (0.3 wt%) and 2) a huge amount of tritium is implanted into beryllium which is in contact with lithium ceramic during irradiation; from the small beryllium pebbles the implanted tritium is released pretty fast, whereas from the large spheres, release of implanted tritium is comparable slow than that of neutron-generated [2].

Literature:

[1]   J.G. van der Laan et al., "Irradiation Behaviour of Ceramic Breeder Materials at High Lithium Burnup", ICFRM-7, Obninsk, September 1995.

[2]   P. Weimar, H. Werle, "Irradiation Behaviour of Lithium Orthosilicate and Beryllium Pebbles", 4th Int. Workshop on Ceramic Breeder Blanket Interactions, Kyoto, October 1995.

[3]   H. Kwast et al., "The Behaviour of Ceramic Breeder Materials with respect to Tritium Release and Pellet/Pebble Mechanical Integrity", J. Nucl. Mater. 212-215 (1994) 1010.

[4]   H. Werle et al., "Long-Time Tritium Release from Neutron-Irradiated Beryllium", FZK, Internal Report, August 1995.

[5]   F. Scaffidi-Argentina, H. Werle, "Tritium Release from Neutron Irradiated Beryllium: Kinetics, Long-Time Annealing and Effect of Crack Formation", 2nd IEA Int. Workshop on Beryllium Technology for Fusion, Jackson Lake Lodge, September 1995.

[6]   H. Werle, "Release of Neutron-Generated Tritium from
        Beryllium", FZK, Internal Report, October 1994.

Staff:

E. Damm
T. Eberle
H. Jakisch
F. Scaffidi-Argentina
A. Weisenburger
H. Werle
H. Ziegler

BS NN-D Non Nuclear Tests

BS NN-D 1   Helium Blanket Test Loop (HEBLO)

In October 1994 the second HEBLO experiment was started. Its purpose is to perform temperature transient tests on a mixed beryllium/ceramic pebble bed which, in addition, is subjected to mechanical loading. Its configuration corresponds to the previous blanket concept with cooling coils.

The bulk bed (90 mm in diameter and 250 mm in   height) is passed by three hairpin shaped coolant pipes with helium gas flow from the temperature transient test facility of the HEBLO loop (Fig. 1). The maximum temperature amplitude is

are installed within the pebble bed at one level on the surface of the coolant pipes and with different spaces between them.

During the experiment the development of temperatures within the pebble bed and the pressure drop in the purge gas stream are measured so that changes in the pebble bed can be recognized from the thermohydraulics conditions.

Operation of the experiment has advanced well and is scheduled for termination in October 1995. The number of temperature cycles by late September was 1740 cycles performed above 200/350 °C, 1190 of them above 260/425 °C. Pressure loading of the bulk bed through the pneumatically driven piston was chosen to be between 1 and 5 MPa, as shown in Fig. 1.
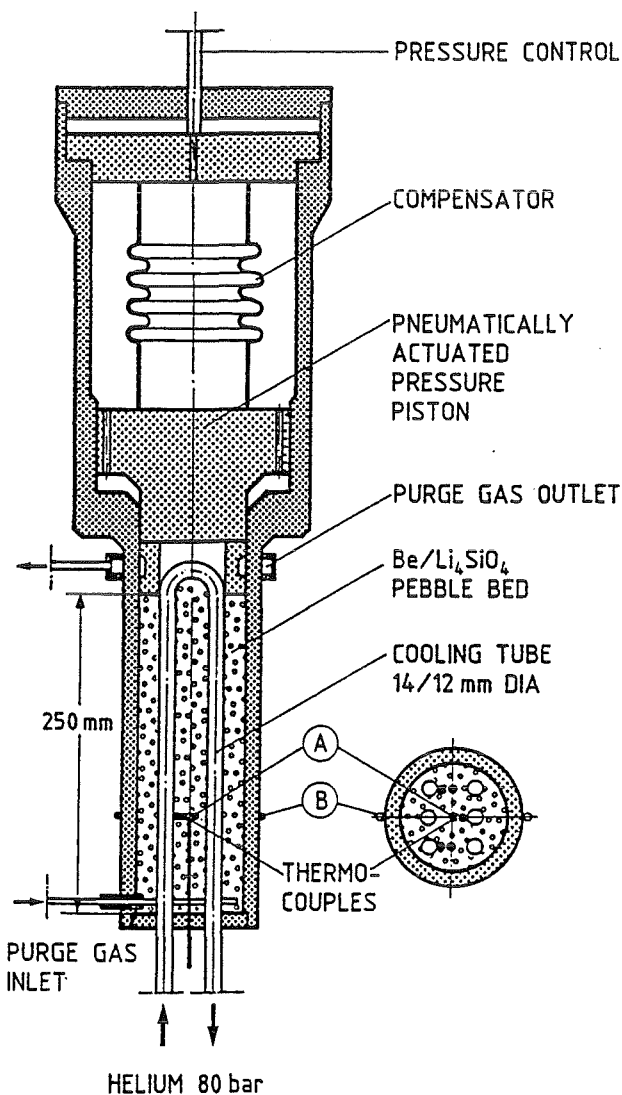
In Fig. 2 the measured pressure loss in a helium purge gas

Fig. 1:   Test Section with Mixed Pebble Bed Be/Li$_4$SiO$_4$ and Cooling Coils
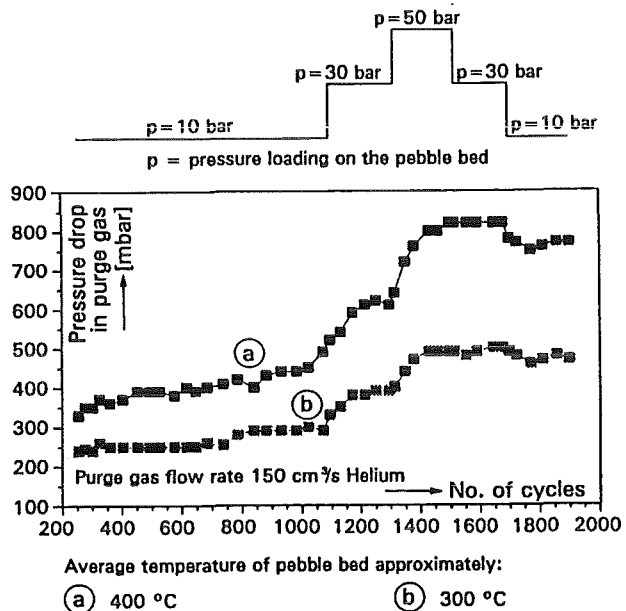
Fig. 2:   Pressure Drop in Purge Gas under Various Pressure Loadings on the Pebble Bed Over the Test Cycles Measured at two Average Pebble Bed Temperatures of About 300 °C and 400 °C

170 K (260/ 430 °C), the temperature ramp is approx. 30 K/s, and the duration of the cycle is 2 x 300 s. Mechanical loading of the bulk bed is effected by a pneumatically driven piston up to a maximum pressure of 5 MPa. Several thermocouples

stream for a helium flow of 150 cm³/s is plotted for the total duration of the experiment and a mean bulk bed temperature of approx. 300/400 °C (plots a and b). An increase in mechanical loading of the bulk bed causes a slight increase in pressure drop which, upon stepwise reduction of loading, is not reversed at once. Only upon a further decrease to the initial value of 1 MPa slightly diminishing pressure reduction was observed. This is probably attributable to self-blocking of the pebble bed or also to the frictional resistance of the pneumatically driven piston system.

Pressure loading of the pebble bed improves also thermal conductivity and heat transfer. This is shown in Fig. 3 where the transient temperature developments at the helium gas inlet (curve 1), in the center of the pebble bed (family of curves 2) and at the external wall of the test bed (family of

Fig. 3: Transient Temperature Profiles During a Test Cycle Measured at the Helium Gas Inlet and in the Various Zones of the Test Section

curves 3) have been represented. It is visible that under higher pressure loading of the pebble bed the temperature in the test rig rises more steeply.

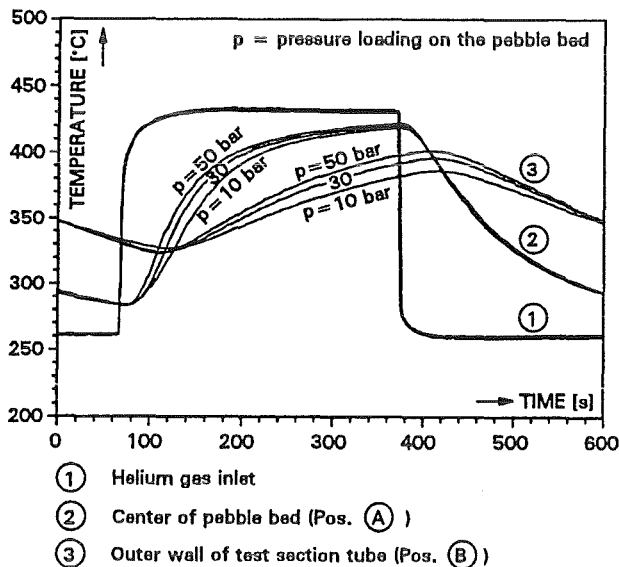It is planned to make a post-test examination of the pebble bed after termination of the experiment. It is to provide, e. g., information about the amount of wear due to friction and of broken pebbles and about possible interactions of the individual materials. For this, the test bed will be cut apart at an industrial firm which possesses facilities for handling beryllium. At various points samples of pebbles will be collected which will then be subjected to post-test examinations at the Karlsruhe Research Center (FZK).

It is planned to build a third HEBLO test rig after termination of this experiment which, according to the last blanket reference concept with cooling plates, will be provided with separate beryllium and ceramic pebble beds. Figure 4 shows a blanket segment selected for the HEBLO experiment. The existing HEBLO loop will be modified and extended and its thermohydraulics thus adapted to the new test conditions. First thermohydraulics design work was performed. The present efforts concentrate on the design and manufacture of heating plates for simulation of the heat sources in the interior. Following modification of the facility the new test bed will probably start operation in late 1996.

Staff:

M. Dalle Donne
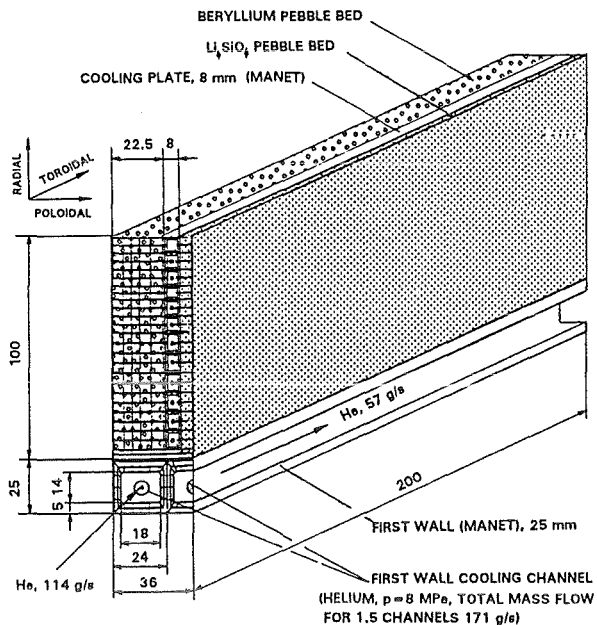H. Lehning
P. Norajitra
D. Piel
G. Reimann
R. Ruprecht

Fig. 4: Portion of DEMO Outboard Blanket with Cooling Plates and Separated Be and Li_4SiO_4 Pebble Beds to be Tested in the Next HEBLO Test Section

BS NN-D 3   Blanket Coolant Purification System

The helium coolant system of a solid breeder blanket will contain tritium originating from tritium permeation through the first wall and through the canister walls and tubes of the blanket purge gas system. In the following, a concept of a coolant purification system (CPS) is described which has beeen developed for the purification of a 0.1% fraction of the helium coolant stream. The main tasks of the CPS are:

- to extract hydrogen isotopes as well as solid, liquid or gaseous impurities from the main coolant system and thus to maintain the radioactivity and impurity concentrations below specified levels;

- to provide an oxygen potential which is sufficiently high for maintaining the integrity of the tritium permeation barriers (oxide layers) in the main coolant system; this is done by adding a certain amount of water and hydrogen to the CPS;

- to remove condensed water that may be entrained in the cooling gas following a steam generator-tube failure.

Some characteristic data of a CPS for the BOT concept are given in the following Table:

Gas flow rate	2.4 kg He/sec = $4.9 \cdot 10^4$ Nm^3/h
Pressure	8 MPa
Total amount of gas	20 000 kg He
Gas inlet temperature	723 K
Gas outlet temperature	523 K
Radioactive impurities	HT, HTO, activated corrosion products
Non-radioactive impurities	H_2O, N_2, corrosion products
Tritium removal efficiency	> 95 %

The $\underline{Q_2\ content}$ (Q = H, D, T) in the coolant can be calculated as follows:

permeation from First Wall : 0.8 mole T + 1.1 mole D per day [1]

permeation from Purge Gas System: 0.27 mole T + 98 mole H per day [1]

The amount of H is in accordance with the amount of T and results when the swamping ratio in the purge gas system (He:H_2 = 1000), the purge gas mass flow rate (0.6 kg He/sec),

and the higher permeation of H in comparsion to T (factor 1.732) are taken into account.

Thus, the total permeation rate into the coolant is 100 mole Q/day = 2.1 mole Q_2/h.

As 0.1 % of the coolant is continuously purified with an efficiency of 95 %, the Q_2 concentration in the coolant will increase to an equilibrium concentration c_e which is reached when the Q_2 removal rate is equal to the Q_2 permeation rate.

The calculated value of c_e is 10^{-6} (or 1 ppm). The equilibrium amount of Q_2 in the coolant is then 5 mole Q_2, and this amount includes about 1 % HT, i.e.

$$0.05\ mole\ HT = 0.2\ g\ HT.$$

In a similar way, one can calculate corresponding numbers for the $\underline{water\ content}$ of the coolant which results from unavoidable small leaks of the steam generator. If an integral leakage of 4 kg water/day is assumed, one gets an equilibrium concentration of 4.5 ppm. The equilibrium amount of water in the coolant is 22.55 mole $\approx$ 406 g.

It is expected, that most of the molecular tritium (0.2 mole HT) will undergo isotopic exchange with the H_2O content of the gas, so that the risk of tritium permeation to the water side of the steam generator is strongly reduced (at least by a factor of ten).

System Description (Fig. 1)

The gas stream entering the CPS upstream of the steam generator through a regulation valve is transferred to an oxidizer unit containing a precious metal catalyst (Pd or Pt on alumina). An over-stoichiometric amount of oxygen is added to obtain a quantitative conversion of HT to HTO and of H_2 to H_2O. The high temperature of the gas (720 K) improves the kinetics of the oxidation process.

The gas then passes the first heat exchanger to be cooled to 423 K and a filter system for removal of particulate material. The system consists of two sections, a centrifugal dust separator (for larger particles) and an arrangement of felted and sintered stainless steel fibers (for smaller particles).

The gas is now cooled down to room temperature in the second heat exchanger and sent to a water separator which removes condensed water that may be present in the case of a steam generator-tube failure.

Normally, the water separator will not be needed because the Q_2O concentration will be in the range of 5 ppm as mentioned above. To freeze out the water content, the gas is first cooled to 250 K in a precooler and then to 150 K in the main cooler. The amount of water to be frozen out under the conditions described above is 4.9 kg/day. The size of the cooler (it is designed like a coiled tubular heat exchanger) is
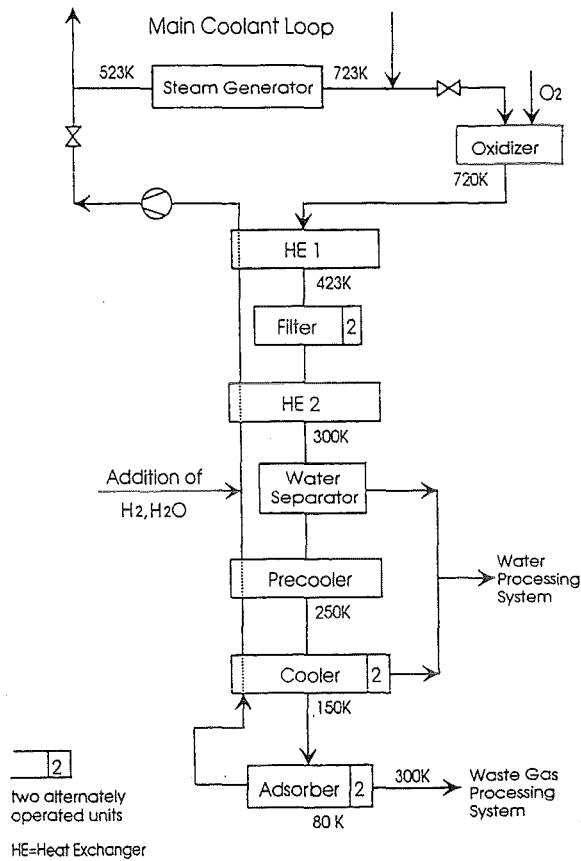
Fig. 1:   Coolant Purification System

determined mainly by the gas flow rate, the gas pressure, and the regeneration cycle time.

Finally, the gas is sent to a 5A molecular sieve bed cooled with LN_2 to adsorb the remaining gaseous impurities, i.e. O_2, N_2, and hydrogen isotopes, which eventually have not been oxidized. The inlet and the outlet side of the bed are equipped with mechanical filters to prevent a carry-over of particulate material during normal operation (downward flow) and regeneration (upward flow). The size of the MS beds can be chosen to be smaller than that of the cooler. The actual size, however, will result from an optimization process between cooling power and operation / regeneration cycle time.

The pure helium is carried back in a recuperative way through the cooler and the precooler. After having passed the two heat exchangers HE2 and HE1 the gas has been warmed up again to a temperature > 520 K, so that it can be returned into the main coolant loop downstream of the steam generator.

If the water content of the coolant is smaller than assumed above it may be necessary to add a certain amount of hydrogen and water to provide a sufficiently high oxidation potential for maintaining the integrity of the oxide layers in the main coolant system which act as tritium permeation barriers.

Regeneration

Some components must be regenerated before their retention capacity has been reached. The particulate filters will be transferred to the waste disposal system after exchange.

The cooler loaded with ice will go off line while the gas flow is directed to the second cooler. The first cooler is depressurized and warmed up to room temperature to liquefy the water which is then drained into a water container and sent to the water processing system (where the hydrogen isotopes are extracted by utilizing the water gas shift reaction).

A similar procedure is carried out with the adsorber bed. While the second unit goes into operation, the first one is warmed up to room temperature. The desorbing impurities are sent to the waste gas processing system.

Remarks on Safety, Reliability, and Availability

The principle of the coolant purification system is based on the design of cooling systems for a NET/ITER blanket test module [2] and for a gas cooled fast breeder reactor [3]. A high degree of reliability / availability is reached in these systems since only well-proven purification technology is used, and the number of components with rotating or moving parts is minimized.

Off-normal conditions of either the main cooling system or the CPS will be handled as follows:

a)   Steam generator tube failures (identified by the moisture monitoring system of the main cooling system) will lead to an increased humidity in the slip stream whichmay deteriorate the oxidation capability of the oxidizer unit [4]. In the improbable case of a water content > 5 weight % it will be necessarry to bypass the oxidizer.

b)   Loss of pressure in the CPS (as a consequence of a leakage or a line break) will actuate automatically closing block valves which are located at the inlet and the outlet of the CPS. In addition, it will be necessary to provide a secondary containment for the CPS to avoid any uncontrolled release of radioactivity to the outside.

c)   Loss of purification capability which could occur by loss of cooling water or loss of low-temperature refrigeration can be tolerated for a short period of time, i.e. as long as the activity level in the cooling system does not exceed the specified limits. During this time, the CPS will be totally or partially bypassed until redundant cooling systems become available; otherwise, the reactor will be shut down or reduced in power.

An additional task for the CPS emerges, if the main coolant system has to be depressurized; in this case, the coolant is sent to the helium storage system, from where the processing can be started as described above if an additional heater is provided to warm up the gas to 720K.

Literature:

[1]   M. Dalle Donne, private communication, June 1995

[2]   M. Dalle Donne et al., DEMO-Relevant Test Blankets for NET/ ITER, KfK 4929, Oktober 1991

[3]   General Atomic Project 2102, 750-MW (e) Gas Cooled Fast Breeder Reactor Demonstration Plant, GA-A 13459 (1976)

[4]   M. Nishikawa et al., Catalytic Oxidation of Tritium in Wet Gas, J. Nucl. Sci. Technol. 22, No.11 (1985) 922

Staff:

H. Albrecht
E. Hutter

BL DE-D   Design Work

The subjects of this task are the design of liquid metal blankets for the application in a DEMO reactor, the development and the design of blanket test modules in NET/ITER, and, for both cases, the conceptual design of suitable external loops for heat and tritium extraction.

This work is part of the Europan Blanket Development Programme in which four blanket concepts are developed with the aim to select in 1995 the two most promising concepts for further development [1].

Thermomechanical Analysis

Design work on the "Dual Coolant Blanket" concept [2,3,4] in which the First Wall (FW) is cooled by helium and the breeding zone by the circulating liquid metal breeder ("self-cooling") has been continued. A perspective view of an outboard blanket segment is shown in Fig. 1.
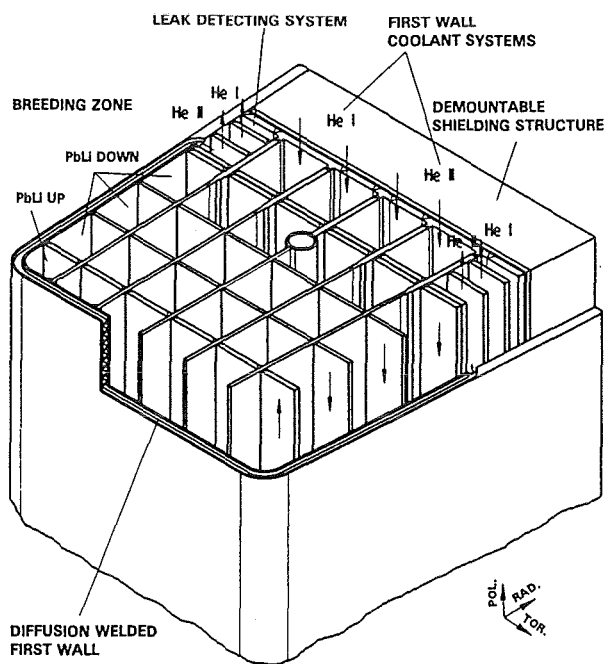

Fig. 1:   Perspective view of an outboard blanket segment

The thermomechanical analysis of the reference Dual Coolant Blanket has been completed [6]. The aim of the analysis is to demonstrate that the blanket temperatures and stresses are within permissible limits. After layout of the blanket for an average surface heat load of 0.4 MW/m² supplementary 3D stress calculations with the FE-Program ABAQUS [5] were carried out for the most severe case with a maximum surface heat load at the First Wall of 0.5 MW/m². It is supposed that the maximum surface heat load can be expected to occur on the equatorial plane of the blanket. The results show that for the maximum surface heat load of 0.5 MW/m² a shield temperature of at least 300 °C, which is slightly higher than the value of 285 °Cassumed for the case of average surface heat load , is required in order not to exceed the ASME limits

for the sum of primary and secondary stresses. This higher shield temperature would also lower the stresses in the case of average heat load.

In Figs. 2 and 3 the respective distributions of the temperature and the total von Mises stress have been represented for the case of maximum surface heat load. The maximum stress in the First Wall, measured at the point of maximum temperature, 527 °C, is 450 MPa and is well below the admissible 3·Sm value of 465 MPa.

In order to improve the weldability and to reduce the primary stresses, the design of the webs between the He channels of the FW and the joints between the FW and the partitioning walls of the breeder zone have been slightly modified. Fig. 4 shows the new design together with the mesh and the boundary conditions used in the 3 D analysis with the ABAQUS code. In the poloidal direction, the strain calculated in the previous 2 D analysis of the blanket segment [7] was applied as prescribed boundary condition. The maximum temperature occurs at the plasma facing surface near to the webs and amounts to 505 and 544 °C for surface heat loads of 0.4 and 0.5 MW/m², respectively. The reason for the slight increase against the original design is the larger thickness of the base of the webs.

The maximum primary stress under normal operating conditions amounts to 81 MPa and occurs at the joints between the FW and the partitioning wall. This value is below the ASME limit for MANET at the local temperature of 325 °C, which amounts - in case of bending and including the 20.000 h creep strength - to 325 MPa. Under failure conditions (pressure of 8 MPa also in the breeder zone as a consequence of a leak of the helium system) the maximum primary stress increases to 218 MPa. This is likewise below the ASME limit. The primary stress at the plasma facing wall amounts to 98 MPa compared to an allowed value of 188 MPa at temperature of 544 °C at this location.

The total v. Mises stress is not significantly affected by the design modification.

The First-Wall which is submitted to the high heat-flux from the plasma and the pressure of the coolant is one of the structures most likely to experience thermal ratcheting. Even without a detailed knowledge about the geometry in the pre-design phase it should be possible to predict a ratcheting behaviour. This demands a very simplified analysis: The plasma facing wall of the cooling channel is considered as a beam, with the one-dimensional calculations being conservative in regard to a two- or three-dimensional one. This allows a "Bree"-diagram to be constructed regarding only the local loadings in the FW. In addition only elastic perfectly-plastic material is considered. A hardening-effect will reduce the possibility of ratcheting.

The diagram (Fig. 5) shows the temperature induced thermal bending moment MT versus the mechanical loading Mp (here Mp=1/12 pl² for the lateral line load representing the coolant pressure on a double cantilever beam). Considering

only the coolant pressure and the temperature gradient in the First Wall the present Blanket-Designs are in the safe regimen of elastic material response.

Fabrication Technologies

The FW in this concept consists of two plates with integrated cooling channels which are bonded by diffusion welding. After this welding the FW panel is bent into U-shaped sections which are connected to a banana-shaped segment box by E-beam welding.

These fabrication technologies are applicable to the other EU-DEMO blanket concepts, too, and have been investigated in more details (see [4]).

Bending Tests:

To obtain the U-shape of the blanket box the diffusion bonded FW plates with integrated cooling channels have to be bended with angles of about 96 ° for the inboard and 86 ° for the outboard blanket segments. To investigate this fabrication step, a study was carried out to exhibit the methods and parameters of the bending process (temperature, filling material, bending machine), and to elaborate an experimental program.

As a result of the preliminary bending study [8] it can be stated that no major problems are expected in the bending process. Nevertheless, bending tests with representative FW plates have been started in May 1995.

After the production of the bending tools the first tests with 3 solid plates have been carried out at the end of September to investigate the general material behaviour. In October 3 further plates with integrated cooling channels will be bended.

To ascertain specific bending parameters like the location of the neutral plane, the maximum and local deformation, and the geometry variations during bending, these tests will be accompanied by FEM calculations.

EB welding and quality control:

An important detail of the Dual Coolant Blanket Concept is the joint between the U-shaped poloidal sections of the FW. According to the safety and reliability criteria which admit no single weld between plasma and helium or Pb-17Li, electron beam double welds are envisaged for this purpose. The gap between the two welds additionally serves for leak detection.

An investigation was performed in collaboration with an industrial manufacturer [9] to demonstrate the feasibility of the EB double weld and to ensure assessment of proper
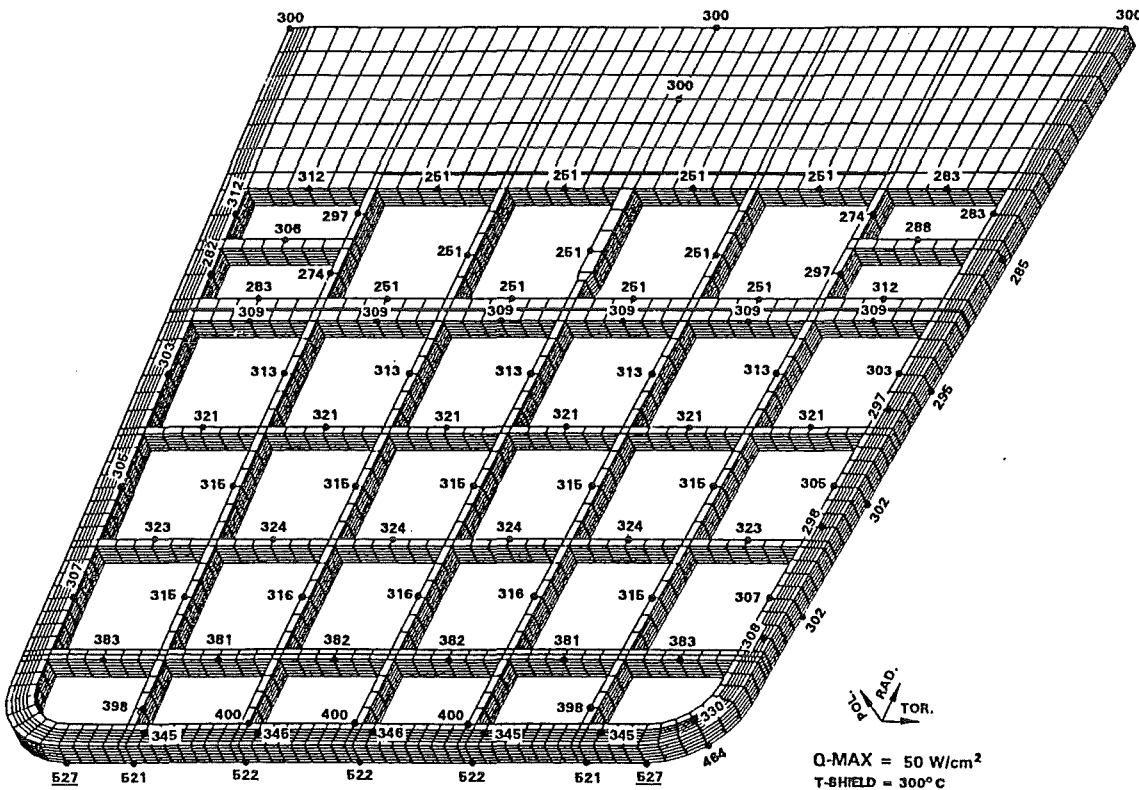

Fig. 2:   Temperature Distribution in the Centre of the Blanket for a maximum Surface Heat Load of 50 W/cm² and Unchanged Helium Flow
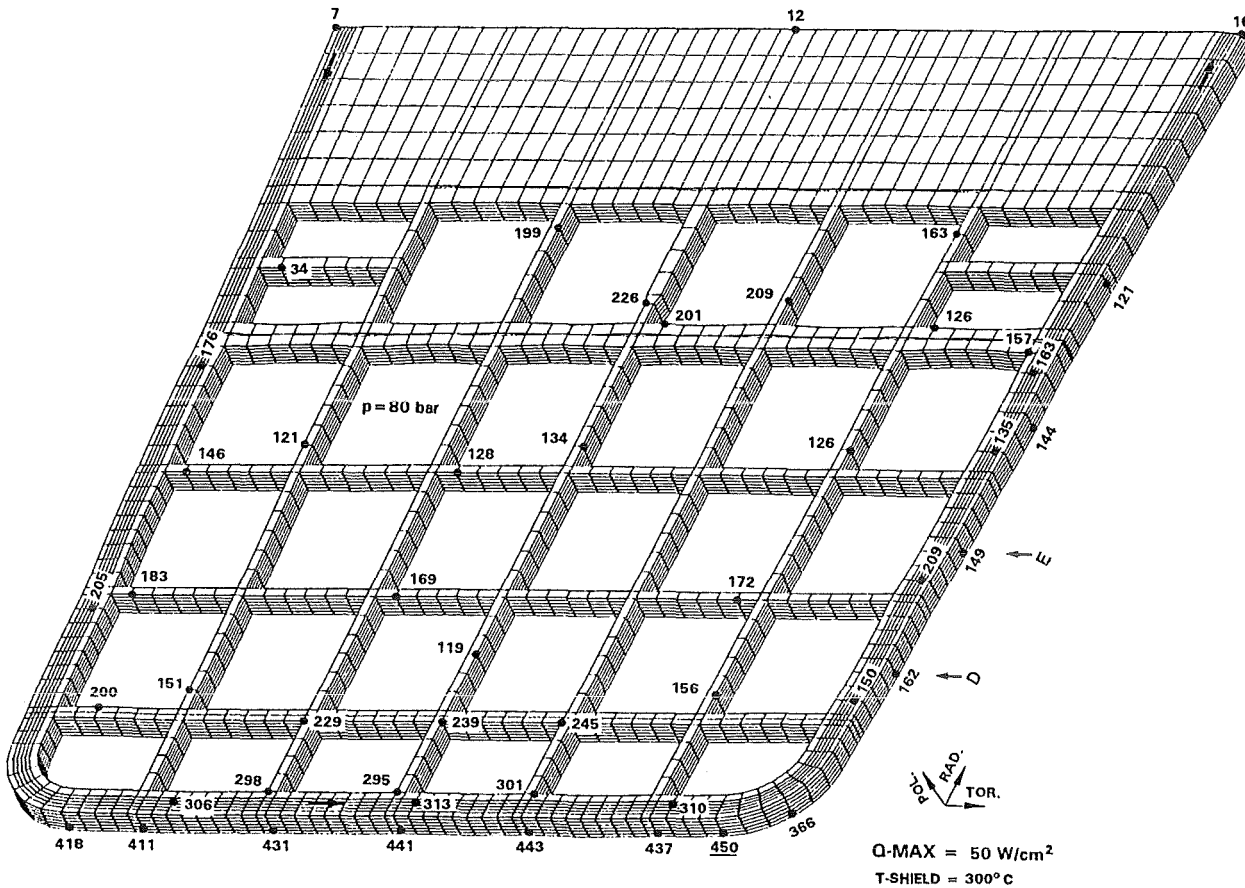
Fig. 3: Von Mises Primary Plus Secondary Stresses in the Blanket Centre for a Maximum Surface Heat Load of 50 W/cm² and an Average Shield Temperature of 300 °C

quality of the weld by NDE techniques. A sketch of the weld is given in Fig. 6, where a specimen design is shown which allows for visual control of the leak detection gap after welding. As a result of the investigations, it can be stated that [4]

- the feasibility of the EB welding has been demonstrated
- the use of single pass EB welding is possible as the leak detection gap remains open after welding
- NDE results show that, generally, NDE of the EB weldings is possible even in case of the presence of cooling channels
- additional investigations on the sensitivity of NDE are recommended (which are currently being performed).

A single gross error (displacement of the EB weld in one of the specimens), which was detected by NDE, was attributed to a deviation of the EB due to insufficient demagnetization. Careful demagnetization and control before welding can prevent this effect. Besides this error, the welds exhibited a proper quality.

It is envisaged to apply advanced techniques using numerical methods for propagation of ultrasonic (US) waves to predict the sizing and location capability of specific US testing arrangements.

Future work is also aimed at establishing methods for reliability analysis which is based not on empirical failure rates of characteristic welds but on failure probabilities based on the scatter in the size and detection uncertainties of faults in welds as well as the fracture resistance of the material. A first approach in this direction - at this stage using literature data – has been already presented in Ref. [10]. It was possible to establish qualitative criteria for suitable inspection strategies and it is felt that this approach can be very useful in leading to input quantities for a probabilistic system safety analysis.

Diffusion welding: see Subtask Manet 2.3

External circuits

A complication of the Dual Coolant blanket concept results from the need for two completely different heat- and tritium extraction systems from Pb-17Li and helium, respectively.

A system has been developed where both coolants deliver the heat to a common steam cycle as shown in Figure 7. Helium is mainly used for preheating whereas most of the evaporation is performed in the Pb-17Li heat exchangers. This split results from the given coolant temperatures (He: 250/350 °C, Pb-17Li: 275/425 °C) in order to achieve a large enough

radial
poloidal
toroidal
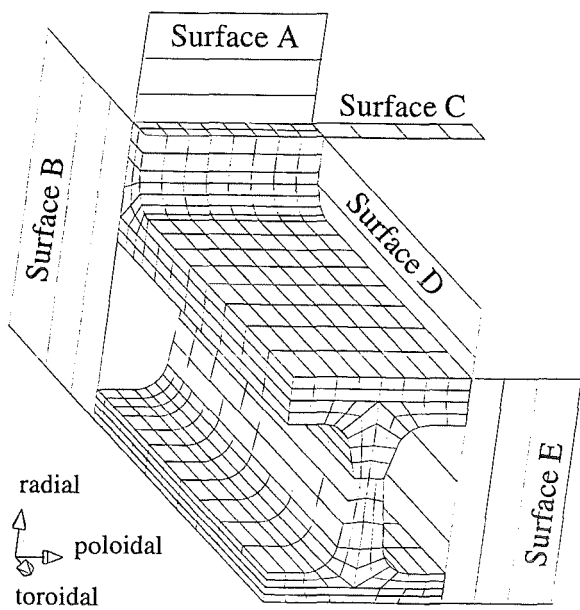
Boundary Conditions:

Surface A: toroidal displacement=0
Surface B: forced poloidal displacement;
stay parallel to surface D
Surface C: radial displacement=0
Surface D: poloidal displacement=0
Surface E: free toroidal displacement;
stay parallel to surface A

Fig. 4: 3D Model of First Wall with Boundary Conditions

temperature difference at the pinch point in the steam generators ($\Delta T_{pinch,He} = 27$ K, $\Delta T_{pinch,Pb-17Li} = 17$ K).

One of the main goals was to design the heat extraction systems with a high redundancy in order to obtain a sufficiently high availability of the blanket system.

Separated cooling systems are proposed for the inboard and outboard blanket segments since the pressure drop is different in the two regions. Additionally, the helium cooling is subdivided into two completely separated systems in order to provide high redundancy for afterheat removal. For safety reasons the Pb-17Li cooling system of the outboard region is subdivided, too, into two independent systems in order to reduce the mass of activated liquid metal in one system. There are at least 2 parallel loops in each of the seven independent cooling systems for redundancy and maintenance reasons. This subdivions of the primary loop system is listed in Table 1.

The result of this redundany in all primary systems is a decisive increase of the availability. However, it requires a considerable increase in costs by both the rather large number of loops and the overcapacity installed in the cooling system. The total installed cooling capacity of the helium system is 76
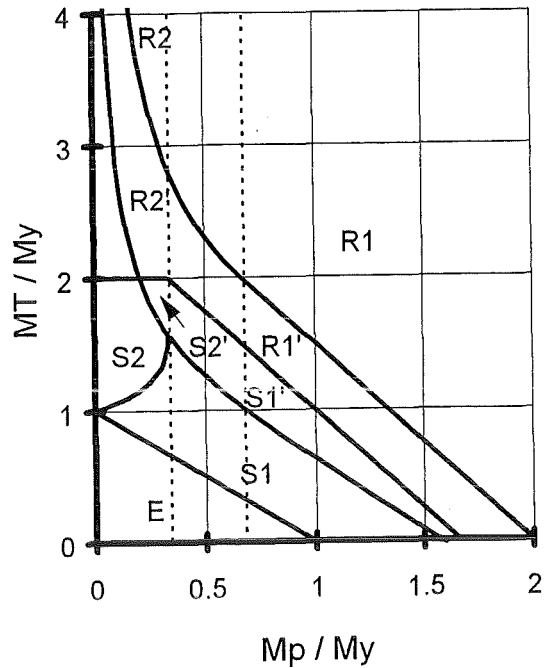
Fig. 5: Ratcheting-diagram for thermal ratcheting of bending type and elastic perfectly-plastic material.
Regions:
R: Ratcheting
S: Shakedown (plastic response in one cycle only)
E: elastic response
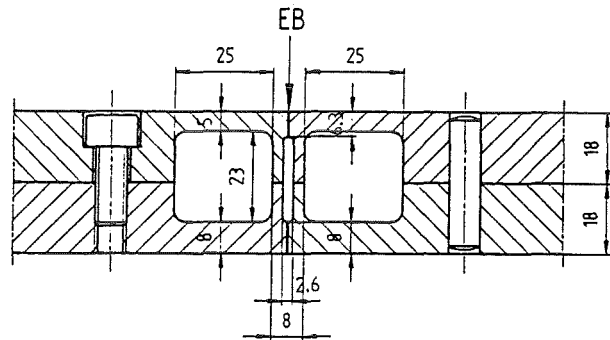
Fig. 6: EB welding specimen (parts dismountable for visual inspection of leak detection gap)

% higher than the power to be extracted. For the Pb-17Li loops the overcapacity amounts to 46 %.

The required powers of the helium blower and the liquid metal pump have been evaluated. Assuming a blower and pump efficiency of 0.8, the power for the helium blower and the liquid metal pump for the whole reactor totals to 31.3 MW and 2.3 MW, respectively. More details of the calculations are given in [6].
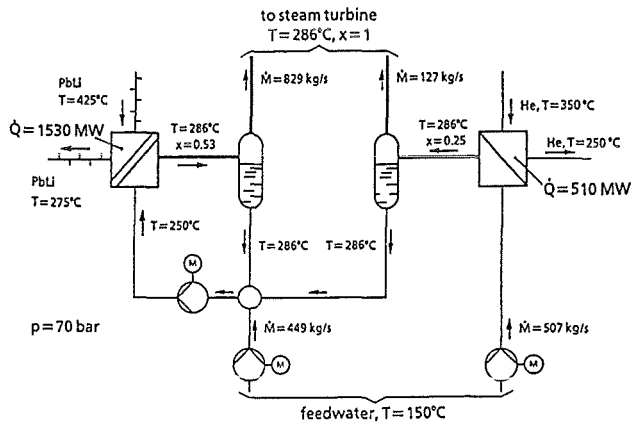
Fig. 7: Steam generating system

Table 1: Subdivision of the primary loop systems

	inboard blankets	outboard blankets
Helium:		
. number of independent systems	2	2
- number of parallel loops in each system	2	3
- design value for each parallel loop	90 MW	90 MW
Pb-17Li:		
- number of independent systems	1	2
- number of parallel loops	4	3
- design value for each parallel loop	140 MW	280 MW

Literature:

[1] S. Malang, L. Anzidei, M. Dalle Donne, L. Giancarli, E. Proust, European Blanket Development for a DEMO Reactor, 11th TMTFE, New Orleans, Louisiana, USA, June 19-23, 1994

[2] G. Kast (comp.), Nuclear Fusion Project, Annual Report of the Association KfK/Euratom, Oct. 93 - Sept.94, FZKA 5515, January 1995

[3] S. Malang, K. Schleisiek (ed.), Dual Coolant Blanket Concept, KfK 5424 (Nov. 1994)

[4] S. Malang, M. Tillack (comp.), Development of Self-Cooled Liquid Metal Breeder Blankets, FZKA 5581, 1995

[5] Hibbit, Karlsson Sorensen, ABAQUS User's Manual Version 4.9, Providence, R.I., USA

[6] P. Norajitra, Thermohydraulics Design and Thermomechanics Analysis of Two European Breeder Blanket Concepts for DEMO, FZKA 5580, 1995

[7] H. Gerhardt, Global Stress of the DEMO Liquid Metal Blanket, FZK Internal Report, May 1995

[8] G. Haufler, M. Kopf, D. Kolev: Studie zum Biegen von Platten mit Kühlkanälen. KE Stuttgart Bericht 1-TB-242/94 (1994)

[9] H. Breitling, EB-Schweißen und US-Prüfung von Doppelschweißnähten für heliumgekühlte Erste Wand, Arbeitsbericht KWU NT1 BGL/95/002.

[10] S. Zhang, H. Riesch-Oppermann, Probabilistic Assessment of Non-Destructively Determined Flaws in Welds, Fusion Engineering and Design (1995), in press.

Staff:

S. Böhmer
U. Fischer
H. Gerhardt
T. Heider
S. Malang
K. Müller
P. Norajitra
G. Reimann
J. Reimann
R. Ruprecht
H. Riesch-Oppermann
K. Schleisiek

BL PC-D   Physico Chemistry, Purification of Pb-17Li

1.   Compatibility of metals and alloys with Pb-17Li

The evaluation of more than 300 tests of 31 metals and alloys in static Pb-17Li is completed. All results are compiled in report FZKA 5596 [1]. As an example solubility functions are shown in Fig. 1. Other results were steady state dissolution
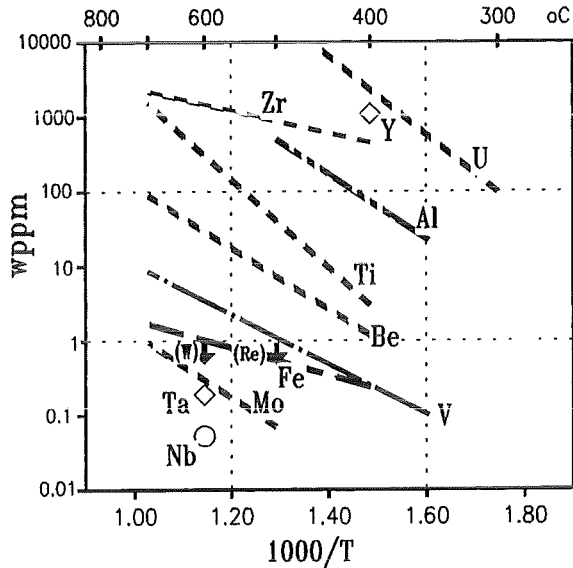

Fig. 1:   Solubilities of metals in Pb-17Li

rates, reaction zones, grain boundary attack, new intermetallic compounds with Ti, Zr, Y and U, and diffusion coefficients.

2.   Behavior of lithium in TRITEX-facility

The ferritic loop TRITEX [2] was operated in experimental phase VI at 450 °C, with the cold traps in main flow at 260 °C. When the flow rate decreased to low values, the loop was stopped after 2000 hours operation time.

An investigation of the cold trap system showed, that there was a blocking just behind the isothermal cold trap 2. At this position an 1 cm long plug of solid LiPb, melting point 482 °C, was found.

The initial Li concentration [3] was about 17 at.%. During operation, the concentration dropped to the eutectic composition of 15.8 at.%. The "excess" lithium was deposited as LiPb. Besides the mentioned plug, the compound was deposited at cold spots with a solid phase. These were a freeze valve and the diffusion type cold trap 3. This is in agreement with observations with capsules as described before [4].

Operating Pb-17Li loops with cold spots, therefore, needs a carfull control of the Li-concentration. However, Li adjustment causes no problems [5].

3.   Solubility of Bi in molten Pb-17Li

Because of the importance of bismuth as precursor for Po-210, solubilities of Bi in mixtures of Pb and Li were determined. Li_3Bi will be in equilibrium with Pb-Li mixtures [6] and this compound was used in the experiments. Li_3Bi has a melting point of 1145 °C. It was fabricated by melting the elements in an Mo crucible in a welded Nb capsule.

Fig. 2 shows solubility functions at different Li-concentra-
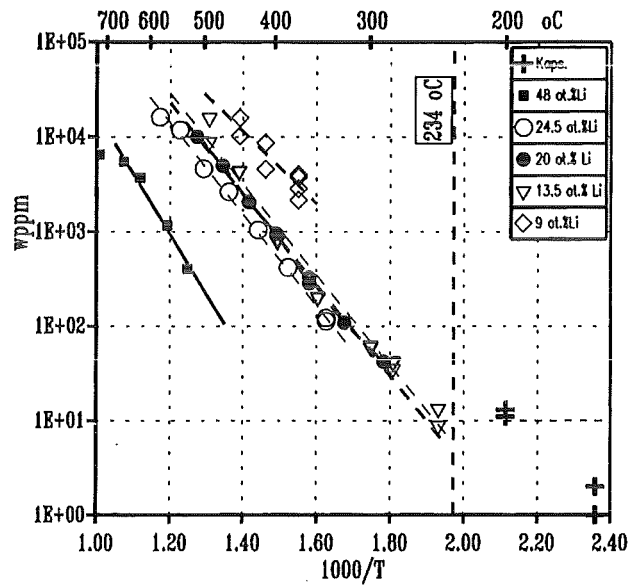
Fig. 2:   Solubilities of Bi in Pb-Li mixtures

tions. The solubilities are too high for blanket operation even at cold trap temperatures [7]. The removal of Bi to values below the required 10 wppm, however, is possible. In phase 6 of TRITEX, the Bi concentration dropped from 30 to below 10 wppm. Bi was enriched in the mentioned diffusion type "cold traps" with a solid phase. An enrichment up to 1 wt.% (!) was found.

Literature:

[1]   H. Feuerstein et.al., FZKA 5596 (1995)

[2]   H. Feuerstein et.al., p.85, KFK 4774 (1990)

[3]   H. Feuerstein et.al., p.119, KFK 5288 (1993)

[4]   H. Feuerstein et.al., p.357, Proc. Intern. Conf. on Liquid Metal Systems, Karlsruhe, Germany, march 16-18, 1993

[5]   H. Feuerstein et.al., p.1257, Fusion Technology 1994

[6]   P. Hubberstey et.al., J.Nucl. Mater. 212-215 (1994) 1021

[7]   H. Feuerstein et.al., to be published

Staff:

J. Beyer
S.Bucke
H. Feuerstein
L. Hörner
S. Horn

BL EI-D   Electrical Insulation in Self-cooled Liquid Metal Breeder Blankets

1.   Direct Electrical Insulation

1.1   Deposition of Directly Insulating Layers on Structure Material

An electrically insulating layer is necessary in a self-cooled liquid metal breeder blanket to maintain an acceptable low magnetohydrodynamic (MHD) pressure drop [1]. Alumina seems to be a suitable material which is stable in Pb-17Li at 450 °C [2], and the resistivity is much higher than the required value even at high temperature.

Alumina coating on MANET steel was applied using a hot-dip aluminizing method [3] with following oxidation procedure. Unfortunately, the formed oxide layer is not dense. For improvement the oxidation behavior and the properties of the intermetallic layers, different elements were added to the Al melt. The addition of 1wt% Y had no influence on the thickness and composition of the intermetallic layers. The oxidation was faster by the Y doped specimens compared to steel dipped in pure Al. Dense oxide layers could not be produced.

The other element added was Si [4]. This is already an established industrial process. Iron metal plate was hot-dip aluminized at Thyssen. The preheated sheet was coated for this purpose by exposing for some seconds in an Al melt with 10wt% Si. MANET was immersed into a melt with the same composition but under different conditions. The cold specimens were dipped into the melt at 700 °C for up to 10 min.

The formation of the required oxide scale on top of the aluminide layer was performed by using two different methods: high temperature oxidation in air and anodic oxidation at room temperature. The specimens, prepared in an industrial process, have thinner intermetallic layers and the overlayer is free of iron. The oxidation of these specimens leads to uniform and dense oxide layers, not so by the MANET specimens, prepared in our lab. In the future, we will have a facility, in which the specimens can be preheated before dipping. The thinner intermetallic layers and the absence of iron in the surface should be beneficial for the oxidation.

All hot-dip aluminized specimens, oxidized and unoxidized, were exposed to static Pb-17Li up to 1200 h at 450 °C. After the corrosion experiment, only the high-temperature oxidized specimens showed no attack by Pb-17Li. Compared to the others, the thickness of the overlayer has not changed.

1.2   Facility for Hot-Dip Aluminizing

In order to optimize hot-dip aluminizing a device has been developed as an extension to an existing glovebox where specimens of up to about 200 mm length can be preheated with temperature control in a reducing atmosphere (Ar + 5% H2) and subsequently dipped into the separately heated Al

bath (Fig. 1). The device has been assembled and put into service.
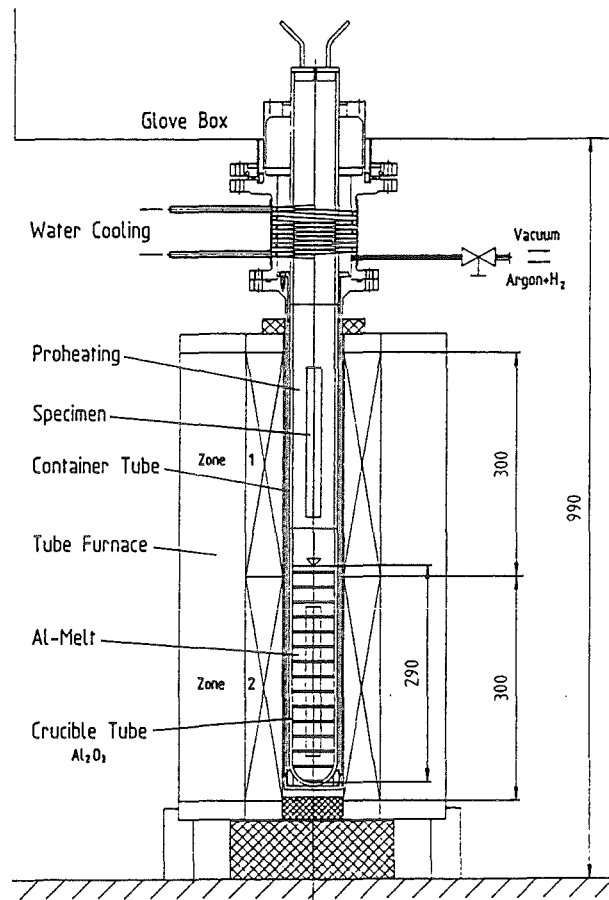
Fig. 1:   Facility for hot-dip aluminizing

Literature:

[1]   A. Terlain, H. Glasbrenner, H.U. Borgstedt, G. Benamati: "Blanket Selection Exercise WG 8: Coatings", CEA-Report SCECF 366, July 1995.

[2]   H.U. Borgstedt, H. Glasbrenner: "Development of a direct insulation layer for a self-cooled liquid metal fusion reactor blanket", Fus. Engin. Des. 27 (1995) 659-662

[3]   H. Glasbrenner, H.U. Borgstedt, Z. Peric: "Compatibility of insulating materials in Pb-17Li alloy", in: Material behaviour and physical chemistry in liquid metal systems II, Karlsruhe, March 16-18 (1993) 95-104.

[4]   H. Glasbrenner, Z. Peric, H.U. Borgstedt: "Alloying of aluminum and its influence on the properties of aluminide coatings: oxidation behavior and the chemical stability in Pb-17Li", Intern. Conf. Fus. Reactor. Mat. 7, Obninsk, 25.-29.09.1995.

Staff:

H.U. Borgstedt (bis 31.3.)
H. Glasbrenner
J. Heger
J. Konys (ab 01.07.)
H. Lehning
G. Reimann
Z. Voß
R. Vouriot

2. Tritium Permeation Barrier

In the water-cooled blanket concept, coatings are necessary as tritium permeation barriers to limit tritium losses from the breeder into the coolant water. Alumina is a suitable coating material to be used as tritium permeation barrier. Various methods for the formation of alumina layers on MANET surface to reduce the permeation have been already investigated, i.e. plasma spray or powder pack aluminization. Deuterium permeation tests on hot-dip aluminized and oxidized MANET, prepared in FZK, have been done in close collaboration with JRC Ispra.

MANET steel, hot-dip aluminized at 800 °C up to 10 min was oxidized in air at 950 °C for either 10 h (sample I) or 30 h (sample II) to build an Al_2O_3 scale on top of the intermetallic layer. In Fig. 2, the reduction of the permeation rate of deuterium

Fig. 2: Arrhenius plot of the permeation rate of deuterium through bare and hot-dipped aluminized MANET steel.

through bare and hot-dipped aluminized MANET is shown as Arrhenhius plot. Reduction of two orders of magnitude for sample I and more than three orders of magnitude for sample II were achieved.

These first results are very promising. The improvement of hot-dipping and oxidation process in order to produce coatings with better mechanical properties and a dense oxide scale, should lead to a further reduction of the permeation rate.

Literature:

[5]   H. Glasbrenner, A. Perujo, E. Serra: "Hydrogen permeation behaviour of hot-dip aluminized MANET steel", Titium Techn. in Fission, Fusion and isotopic Applications, Belgirate, 28.05.-03.06.1995.

Staff:

H.U. Borgstedt (bis 31.03.)
H. Glasbrenner
J. Konys (ab 01.07.)
Z. Voß

3. Irradiation Behaviour of Insulating Coatings

3.1 Neutron Irradiations

To investigate the so-called Radiation Induced Electrical Degradation (RIED) effect as a function of the n-dose, performance of a n-irradiation test using polycrystalline Al_2O_3 at HFR-Petten was proposed.

At first, it was planned to irradiate the specimens in a vacuum. Problems were caused, however, by gas leakage into the specimen volume from the ends of the porous, mineral-insulated triaxial cables. In addition, no irradiation- and high-temperature resistant material was known for sealing the cable ends. Hence, the specimen volume is filled with gas even after evacuation and this gas is ionized by gamma irradiation. The freely movable ions and electrons can form a branch current to the different electrodes and, thus, reduce the accuracy of the measurements intended. Elsewhere, similar experiments were performed in a helium atmosphere under normal pressure conditions. It was therefore decided to irradiate one evacuated capsule and one capsule filled with He in the gamma field of the fuel element store at HFR-Petten. The geometry was to be similar to that of the actual irradiation capsules, however without Al_2O_3 specimens and without thermocouples.

The main result from the gamma tests is that at comparable pairs and polarities, ionization currents of the same orders of magnitude are measured for both chambers. As far as this aspect is concerned, both capsule types are equally suitable
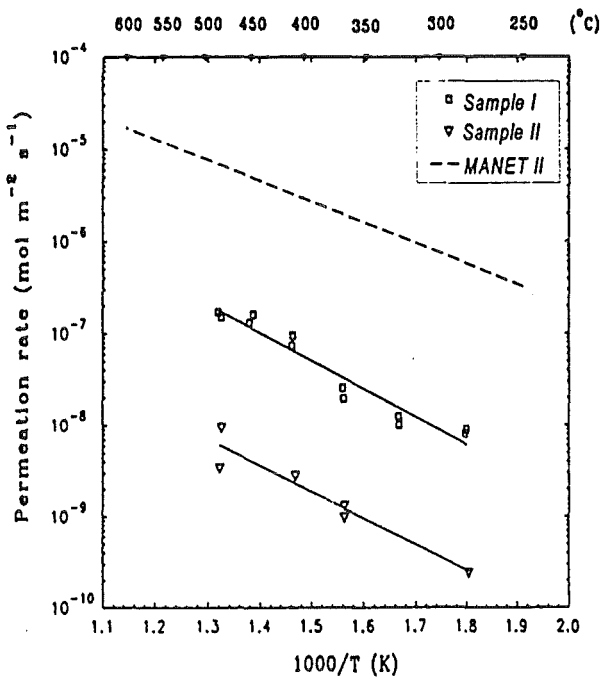
for the irradition experiments and other criteria are then relevant for selection.

Taking into consideration the gamma dose rates of 8.3 Gy/s at the fuel element irradiation position and 1.3×10^4 Gy/s at the C5 neutron irradiation position under reactor full power, ionization currents of the voltage electrode of 1.4×10^{-3} A and 1.1×10^{-3} A can be calculated from the measured currents at a voltage of 50 V and positive and negative polarity, respectively. According to [6], a current smaller by a factor of 0.05 is measured at the current electrode with negative polarity and the other conditions being the same. Consequently, a current of about 6×10^{-5} A will have to be expected at the current electrode in the experiment.

It is assumed that the ionization current at the current electrode remains constant and that a total current variation of 10% can be proved reliably. This corresponds to a current variation of 6×10^{-6} A and a variation of specimen resistance of 8×10^6 Ω at a voltage of 50 V. Taking into account the specimen dimensions, a conductivity variation of 1.2×10^{-6} $(\Omega m)^{-1}$ is obtained. Hence, the range of interest between 1×10^{-8} $(\Omega m)^{-1}$ and 1×10^{-2} $(\Omega m)^{-1}$ for the RIED effect can be covered experimentally to a considerable extent.

Given the gamma heating of up to 13 W/g during reactor irradiation, melting of a part of the capillary pipe needed for the helium capsule due to overheating cannot be excluded. Therefore, the vacuum version will be used for the experiments.

As a consequence of the additional gamma experiments and of delay in the manufactoring of the test capsules, the start of the neutron irradiation is postponed to early in 1996.

Literature:

[6]   E. Farnum, T. Shikama et al.;
       "Radiation-Induced Electrical Degradation Experiments In The Japan Materials Test Reactor"; to be published in the Journal of Nuclear Materials

Staff:

J. Aberle
K. Schleisiek
G. Schmitz

BL MH-D Magneto-Hydro-Dynamics (MHD) in Self-cooled Liquid Metal Breeder Blankets

The work performed concentrated on i) investigation of MHD turbulence mechanisms in order to improve heat transfer ii) the detailed documentation of the MHD work performed in the years 1992-95 [1] and iii) the evaluation of MHD issues for the Dual Coolant (DC) and the Water Cooled Blanket (WCB) in the frame of the Blanket Concept Selection Exercise (BCSE).

Flow structure downstream of a 90° bend perpendicular to the magnetic field

The aim of this work was to show whether 90° bends in the plane perpendicular to the magnetic field act as turbulence promoters for the flow in subsequent ducts. Investigations with sharp-edged and rounded 90° bends with conducting and nonconducting walls were performed. Figure 1 shows the
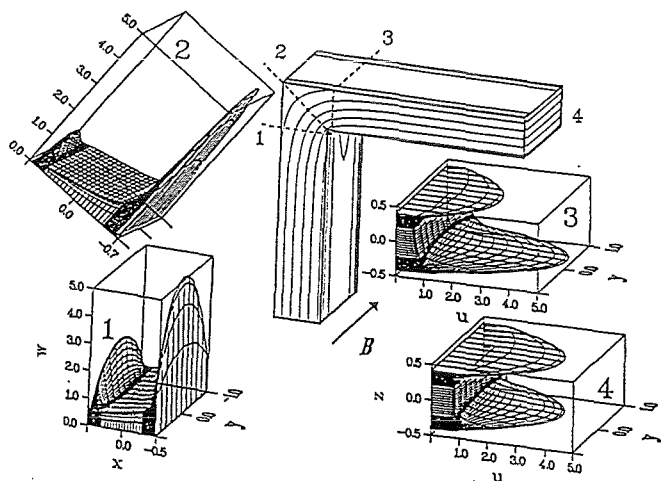

Fig. 1: Calculated velocity distribution in conducting bend (C=1, Ha=500, N→∞)

calculated mean velocity distribution for a bend with conducting walls: an increase of the velocity jet near the inner corner is observed. Mercury experiments were performed; distributions of the mean velocity and velocity fluctuation were measured using different types of traversable multi-potential-probes.

Figure 2 shows a characteristic results for bends with nonconducting walls; downstream of the inner corner a zone of reduced velocity u occurs associated with considerable levels of fluctuating velocity components u`and w. In general the results show that a two-dimensional vortex structure already occurs at moderate ratios of the Reynolds to Hartmann number. These vortices are supposed to be generated by velocity gradients both due to the flow deflection in the bend and due to inertia effects downstream of the inner corner.
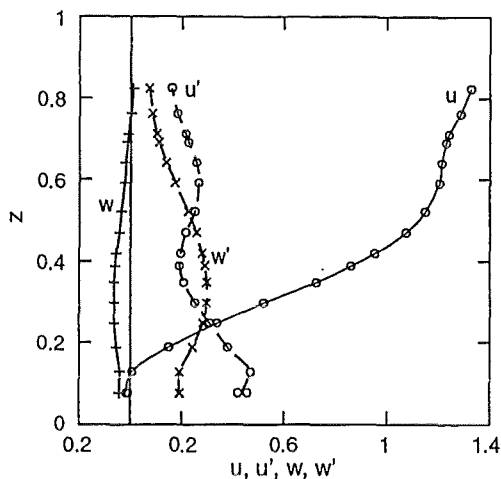

Fig 2: Velocity and velocity fluctuations for a nonconducting bend (Ha=530, N=8,x=2.5)

MHD heat transfer and pressure drop in an electrically insulated channel

The final evaluation of the experiment which was conducted in the MEKKA facility shows that the pressure drop has been about 3 to 6 times higher than predicted for laminar flow in a perfectly insulated channel. After inserting the turbulence promotors (TP) the pressure drop shows a level at high interaction parameters N, which was about 30 % higher than in the case without TP`s but exhibits a strong increase with decreasing N. Due to the nonperfect insulation the velocity profile showed an M-shaping but by far not as pronounced as predicted taking the 3 times higher pressure drop as a reference for the calculations. After starting a vortex structure above Re=4500 the MHD heat transfer expressed by an effective heat conductivity k_{turb} increased constantly from k_{turb}/k_f=1 to 2.8 for the smooth duct and to about 7, respectively, for the duct with 2 TPs at Hartmann numbers Ha≈5000 and Pe≈2200.

A cost-benefit analysis demonstrated that this kind of TP`s is effective for MHD flow at high interaction parameters but at low interaction parameters this means that at high Peclet number the pressure drop increases drastically due to inertia effects reducing the benefit-cost ratio [2].

MHD heat transfer and pressure drop in a rectangular channel with thin conducting walls without and with turbulence promotion

In this experiment one side wall (wall parallel to the magnetic field) of a rectangular test section is heated over a length of 500 mm with a radiation heater (Fig. 3). The test section, of cross section 80 mm by 40 mm is made of stainless steel, the Hartmann walls (walls perpendicular to the magnetic field) are 1 mm thick, the side walls 6 mm thick.
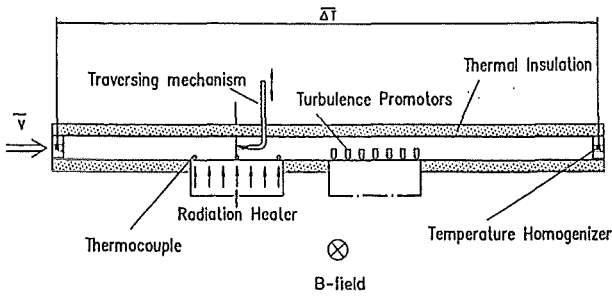
Fig. 3: The heat transfer experiment WTM1 in a channel with rectangular cross section and thin conducting walls, a = 0.04 m, CH = 0.0121, heated length 0.5 m

With the radiation heater a homogeneous heat flux of up to 20 W cm² can be reached. The heater can be moved along the axis of the test section thus enabling the investigation of heat transfer at two positions without removing the test section from the liquid-metal loop. At the first position heat transfer in a simple rectangular channel, in the second position, heat transfer in a channel fitted with electrical turbulence promotors are investigated. The turbulence promotors are copper strips embedded in the Hartmann walls.

The first experimental results show that the pressure drop in the test section without turbulence promotors (TPs) agree well with the theoretical predicted values and that the electrical TP`s increase the pressure drop only by 20-30%. No dependance of the pressure drop from the Interaction parameter was found with nor without electrical TP`s.

The measured velocity profile in the section without TP` showed the predicted M-shaping and for velocities above 0.4 m/s rather high turbulence intensities near the heated wall (Fig. 4).

Stability criterion for the onset of 2-dimensional MHD-turbulence caused by shear layers

The onset of 2-dimensional MHD-turbulence on shear layers with steep velocity gradients has been investigated theoreteically and experimentally. For MHD flows exhibiting vortex type flow pattern a model has been developed which accounts for vorticity production caused by nonhomogeneous electrical conductivity of the channel walls as well as for vorticity dissipation due to Joule and viscous effects. By choosing a special distribution of the wall conductivity it is possible to create initial velocity profiles which loose their stability and show time dependent vortex type flow pattern once the parameters exceed critical limits [4].

The corresponding experiments to validate the model has been conducted in an improved version of the GALINKA-loop [5] installed in the dipole-magnet of the MEKKA facility. The special distribution of the conductivity of the Hartmann walls has been realized by glueing a copper strip on the electrically insulating walls. The experimental results of the stability
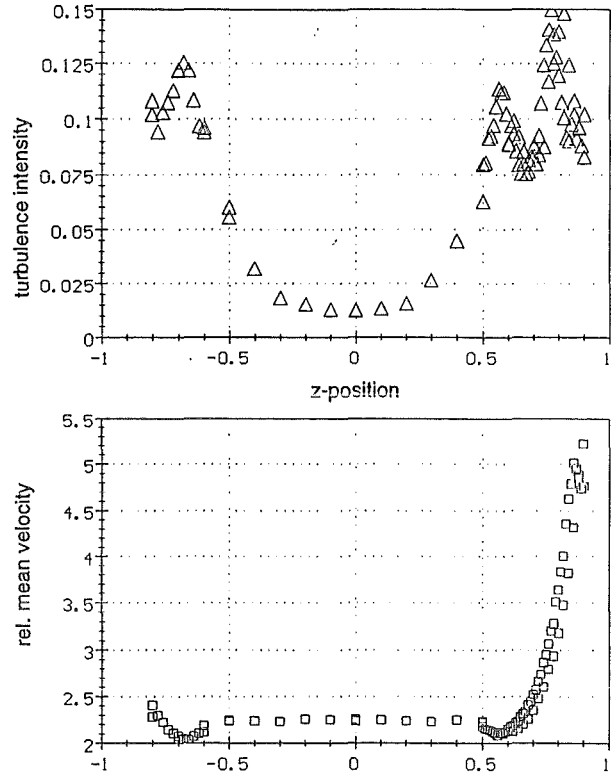
Fig. 4: Velocity and turbulence intensity distribution in the midplane of the heat transfer test section, B = 2.03T, v̄ = 0.96m/s, Ha = 4840, Re = 56200, N = 560

limits as well of the spectral power density agree very well with the theoretical results (Fig. 5).
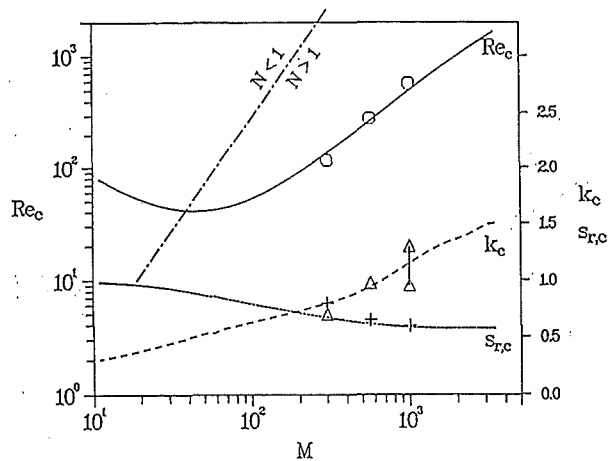
Fig. 5: Measured and predicted limit for the onset of 2-dim. MHD vortex flow in the GALINKA II, Re_c the critical Reynolds, k_c the critical wave number, $S_{r,c}$ the critical rate of the advection to the mean flow in the duct,.

Main results of Working Group MHD for the BCSE [4]

Two design versions of the DCB and WCB were considered: The reference designs use an electrically insulating direct coating either on the total surface of the structural material (DCB) or on a part of the surface (WCB). In the back-up designs the liquid metals is in contact with metal walls (MANET structure in case of the WCB and Flow Channel Inserts (FCI) for the DCB).

The following issues have been identified and analysed in detail: pressure drop, heat transport, tritium transport, corrosion product generation and transport. As a separate issue, the degradation of insulation is included which comprises the effects on pressure drop and transfer processes.

For the DCB, the critical issue is the degradation of insulation (for FCI`s this issue might be less severe). Pressure drop (for intact insulation) is of medium importance and requires future R&D work. The other issues are of minor importance.

For the WCB, all issues are evaluated to be of minor importance which, however, still necessitates R&D work in order to optimize the design. One topic to be mentioned is free convection flow within the blanket box.

Staff:

L. Barleon
L. Bühler
F. Debray
E. Höschele
R. Kirchner
H. Kreuzinger
L. Leboucher
K.J. Mack
J. Reimann
R. Stieglitz
R. Vollmer

Literature:

[1]   S. Malang, M. Tillack (Comp. (1985): Development of Self-Cooled Liquid Metal Breeder Blankets, FZKA 5581

[2]   J. Reimann, I. Bucenieks, L. Bühler, S. Dementjev, A. Flerov, I. Platnieks (1995): Flow structure downstream of a 90° bend perpendicular to the magnetic field, MAHYD 95, August 24-26, Jurmala, Latvia.

[3]   L. Barleon, L. Bühler, U. Burr, R. Stieglitz (1995): Integral MHD-Heat Transfer Behaviour in Ducts with Electrically Insulated Coated Walls, MAHYD 95, August 24-26, Jurmala.

[4]   L. Bühler (1994): Instabilities in 2D MHD flows. 2nd international conference on energy transfer in magnetohydrodynamic flows. Sept. 26-30, Aussois, France.

[5]   Nuclear Fusion Project Annual Report of the Association KfK/EURATOM, (1993), KfK 5288.

[6]   J. Reimann, G. Benamati, R. Moreau (1995): Report of Working Group MHD for the Blanket Concept Selection Exercise (BCSE), FZKA 5652.

BL SA-D   Safety and Reliability/Availability Analyses

Most of the safety related work performed under this heading was devoted to the Blanket Concept Selection Exercise (BCSE) which aims at selecting two of the four European blanket concepts for further development. The results arrived at in Working Group Safety are summarised below. The conclusions drawn from the general safety assessment pertaining to the Dual Coolant Blanket, the FZK variant of the self-cooled liquid metal breeder, are presented thereafter. The subsequent sections describe the more specific work in the field of thermal transients under off-normal conditions, blanket behaviour during electromagnetic transients, and reliability/availability analyses, the latter being also part of BCSE.

Contribution to the blanket concept selection exercise

The safety implications of the four European blanket concepts developed since 1989 have been assessed by Working Group 6a (one of a total of 14 Working Groups with members from CEA, ENEA, and FZK) in a comparative way. 23 safety issues have been identified and the four concepts were evaluated against each issue, applying a methodology adopted by all working groups. Part of the issues could only be assessed qualitatively based on engineering judgement. The individual issues ratings were then summed up to yield the overall safety rating.

Medium to large differences were found between the four concepts with regard to individual safety issues which almost counterbalance in the overall safety rating, yielding in a normalised form the values of 0.64 for the 'breeder inside tube', 0.62 for the 'breeder outside tube', and 0.61 for both the 'dual coolant' and the 'water cooled' liquid metal breeder concept. Therefore, in view of the remaining uncertainties the small differences do not allow to apply a clear ranking with respect to safety. This is particularly true when comparing the two liquid metal breeder blankets. In the contest of the solid breeder blankets against the liquid metal breeder blankets a small advantage in favour of the solid variants has been found, mainly due to the larger amount and mobility of radioactive material in the liquid breeder blankets. These, however, depend on engineering safeguards and assumed accident scenarios which are also provisional at present. Nevertheless, the findings documented in [1] will be used as part of the final rating involving the results from all working groups.

Conclusions of the safety assessment of the Dual Coolant blanket concept

No insurmountable safety problems have been identified for the dual coolant blanket in the course of the BCSE process. The safety assessment has become part of the status report [2]. Yet, a number of concerns need further investigations or optimisation as outlined under the following five subheadings.

Blanket material and toxic material inventory: The total blanket volume (all inboard and outboard segments, full toroidal coverage) amounts to 1020 m^3 with fractions of 40/41/16/3 percent for steel/Pb-17Li/helium/void, respectively. The total Pb-17Li inventory amounts to 15 x 106 kg and the total helium inventory amounts to 6300 kg. The large Pb-17Li inventory poses some safety concerns in case of a major LOCA with subsequent potential activation products release to the environment. Improvements can be obtained by (a) reducing the inventory by optimising the liquid metal circuitry (availability versus redundancy, increased flow velocity in piping), (b) appropriate plant layout (isolation valves, steam generator position), (c) improved mobilisation modelling (especially Hg evaporation from a Pb-17Li spill). The tritium inventories in fluids are small (57 g in Pb-17Li, <6.3 g in helium, and about 0.4 g in NaK) and do not raise severe safety concerns to the public in accidental situations. On the other hand, the routine release via steam generators relies on permeation barriers, the reliability and durability of which have still to be proved. The tritium permeation through Pb-17Li pipe walls as well as the tritium control in the first wall helium coolant require further R&D effort with impact on plant layout. Activation products inventory in the structural material MANET decays slowly, reaching hands-on levels only after very long times (105 years) which is a problem common to all blanket concepts.

Energy sources for mobilisation: The main energy sources result from decay heat and work potential of the first wall helium coolant. Except for the first few seconds (see paragraph fault tolerance below) the afterheat is dominated by the decay in structural material rather than in the Pb-17Li. In the medium to long term (hours to days) the afterheat is moderate compared to the thermal inertia of the system and can be rejected by one of the three separate cooling systems connected to each segment. For instance, the afterheat would cause adiabatic temperature rises in isolated parts of the blanket immediately after shutdown of about 0.15 K/s in the first wall, 15 K/day in the shield region and in the Pb-17Li, and 50 K/h in the mixed material of the outboard blanket. It is expected but needs to be proved that heat rejection can also be maintained in the case of natural convection circulation. Regarding the work potential, the helium inventory from one outboard cooling subsystem would pressurise the vacuum vessel in the case of a LOCA to 0.45 MPa. This is moderate compared to purely helium cooled concepts, but may require some extra expansion volume depending on the design pressure of the vacuum vessel. The blowdown times are short (few seconds) and the momentum forces of a double-ended major pipe break are high (2000 kN). A third energy source are the potential chemical reactions of liquid metal. The reaction kinetics of Pb-17Li with water, air, nitrogen, and concrete are limited as numerous experiments indicate. A major safety concern is seen in the NaK/water reaction in the steam generators with potential failure propagation. This problem requires medium scale experiments.

Fault tolerance: Stresses induced by disruptions do not seem to create severe safety concerns at the present state of knowledge (see below). However, large uncertainties still

exist in the modelling assumptions with regard to physics phenomena, mechanical boundary conditions, design features, effect of poloidal field coils, and material strength. Further R&D is needed which is not specific to a particular blanket concept. Short term temperature transients for the LOCA cases investigated are moderate, but the scenarios are to be extended to LOCAs occurring simultaneously in more than one cooling subsystem and to LOFA cases. The latter imply also transition periods to achieve natural circulation heat transfer. In those cases a more realistic afterheat assessment in Pb-17Li is needed which accounts for the short term decay and for dilution of activation products due to circulation in external circuits. Further attention should also be given to a LOCA in the NaK circuit.

Tritium and activation products release: The early and chronic dose for overly conservative tritium release scenarios from Pb-17Li, helium, and NaK are close to, or beyond, dose limits presently discussed. An activation products release scenario from a major Pb-17Li spill into the vacuum vessel yields a moderate early dose of 10 mSv. Hg-203 is by far the dominating nuclide contributing with 98.9 % followed by Po-210 and tritium. The release scenarios have to be refined aiming at reducing overly conservative assumptions. In general, this complex is not considered critical for design basis accidents. In particular, the release of Po-210 is no longer regarded as a feasibility issue, since both the generation and the mobilisation of this isotope have been overestimated by orders of magnitude in former investigations. Beyond design basis accidents need further analyses.

Waste generation: The amount of high level waste is dominated by the structural material MANET, the choice of which was a common working hypothesis in the blanket concept selection exercise. The total amount of MANET from one complete set of blanket segments (without demountable and permanent shield) to be disposed of amounts to 1400 tons (180 m^3) with decay heats one year after shutdown ranging from 1.6×10^4 W/m^3 for the first wall material down to 1.1×10^3 W/m^3 for the breeding zone. In the removable shield the corresponding value is 2.6×10^2 W/m^3.

Thermal transients under off-normal conditions

The work was limited to a few blowdown calculations for the first wall helium cooling system with RELAP, since the ATHENA code needed for liquid metal flow analyses has not yet been made available to FZK. In the context of thermal blanket behaviour under off-normal conditions the requirements for active cooling of the blanket segment during handling have been assessed. Calculations of the equilibrium blanket temperatures have been carried out for various conditions, i.e., with and without Pb-17Li, with two or four sides of the segment passively cooled, with helium or air as surrounding medium, and with or without active cooling of the first wall. As heat source the radial afterheat profile (poloidally averaged) generated one day after shutdown was assumed. As heat sink the surrounding air or helium at free convection, and radiation were modelled.

The maximum temperature differences between the structure and the environment in equilibrium with surface cooling only at the front and back wall (representing the beginning of the segment withdrawal) were computed to 265 K and 215 K when using air or helium as filling and surrounding medium, respectively. An additional calculation using the maximum afterheat occurring in the blanket mid-plane and surface cooling only by free convection of air yielded a maximum temperature difference of 325 K. It is even lower if the segment is filled with Pb-17Li, namely 265 K. These results show, that handling the blanket segments without active cooling will not lead to excessive temperatures as long as free convection cooling at the front and rear side is assured. It may be even necessary to heat the blanket to prevent the liquid metal from freezing and to equalise the temperature profile. This can be achieved by circulating helium of, e.g., 250 °C through the first wall cooling channels. Then the peak temperatures would stabilise at 265 °C with stagnant Pb-17Li and 305 °C without Pb-17Li.

Blanket behaviour during electromagnetic transients

The improved 3d finite element code CARIDDI is able to deal with a freely evolving plasma current and toroidal electrical conductivities. A model of the DEMO reactor comprising the outboard blankets, the plasma, the vacuum vessel and the poloidal field coils was developed. Applying this model several CARIDDI computations were conducted. They revealed that the electrical design of the first wall is very important not only to active control of the plasma and the evolution of instabilities but also to the quantity and quality of the blankets' mechanical loading during a plasma disruption.

Fig. 1 shows some results of the linear dynamic ABAQUS computations which use the nodal electromagnetic forces determined by CARIDDI as input. Since the main interest is focussed on the blanket and the first wall the results in the other structural parts and in the plasma are not presented here.

The layer of elements facing the plasma represents the first wall. Its resistivity is varied from an insulated case to the resistivity of copper, which is a physically proper range. The figure shows that there is an optimum resistivity of the first wall where the transmitted momentum to the blanket becomes a minimum. This value depends on the initial current distribution in the plasma and on the blanket design.

The blanket support proved to have strong influence on the resulting stresses. The blanket in Fig. 1 is only weakly fixed at the upper part of the back plate. So maximum von Mises stresses in the range of 1000 MPa occur which are too high. By fixing one further nodal point at the bottom of the blanket the deflection and the maximum stresses are reduced decisively to an acceptable amount. The fact that the maximum stresses are located in the first wall is connected to the interaction of the huge toroidal currents and the poloidal fields of the PF coils.
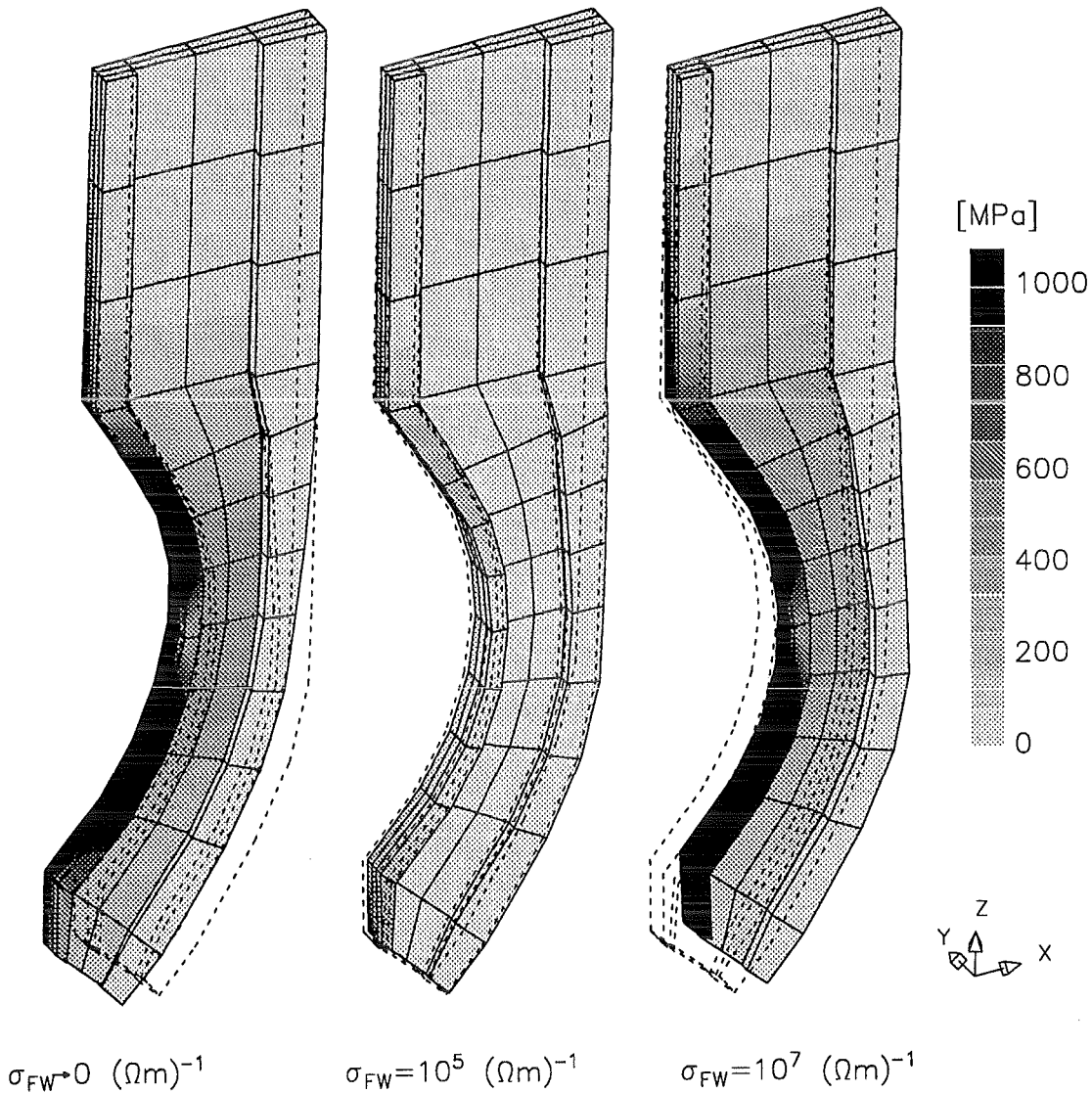
Fig. 1: Stresses and displacements in the outboard blanket segment during electromagnetic transients for various resistivities of the first wall

Further radial forces which are not included here will be induced in the vessel and eventually in the blankets by the variation of the magnetic property of the plasma during the disruption. Further work on this topic has to be done.

Reliability/availability analyses of blanket systems

The availability of the blanket system including the external cooling circuits has been assessed for the four European blanket concepts in the frame of the BCSE. In order to do this in a consistent way the boundary conditions for the analyses had to be harmonised among the partners (CEA, ENEA, FZK) involving a common data base, definition of basic events, mean time to repair (MTTR), and the domain of the blanket system to be considered.

The results of the assessment are summarised Table 1 giving the availability in five domains of the blanket system for a MTTR=3 months, namely (a) first wall (FW) alone, (b) blanket proper excluding the FW, (c) complete blanket, i.e.,

combination of a and b, (d) external cooling system, and (e) blanket system including the cooling circuits, combination of c and d. Note that the FW availability of 90.6 % has been evaluated for the DC concept and was then assumed to be equal for all concepts since several FW design options are still under discussion.

Regarding the blanket proper (domain c) it can be stated that the availabilities are very similar for all concepts, ranging form 84.4 to 87.7 %. Large differences become evident in the cooling systems, where the high redundancy foreseen for the BOT and DC concept pays off, reaching an availability of 99.4 and 98.5 %, respectively. In contrast, the BIT and WC concepts employing no remarkable redundancy exert much lower availabilities for the cooling system (domain d). Consequently, this is reflected in the overall availability of the blanket system. Here we obtain 86 % for BOT and DC, 76 % for WC and 52 % for BIT. It is to be emphasised that the trade-off between redundancy and availability is a strategic

Table 1: Comparison of the availability of the European blanket concepts for various blanket domains (%)				
Domain	Solid breeder blankets		Liquid breeder blankets	
	Breeder outside tube (BOT)	Breeder inside tube (BIT)	Dual coolant (DC)	Water cooled (WC)
a) First wall	90.6	90.6	90.6	90.6
b) Blanket excl. FW	95.3	93.3	96.8	95.4
c) Blanket incl. FW	86.3	84.4	87.7	86.3
d) External circuits	99.4	61.3	98.5	87.8
e) Blanket system	85.8	51.7	86.4	75.8

problem rather than a technical one and is common to all concepts.

We conclude that the availability of the blanket system is dominated by that of the blanket proper if sufficient redundancy is employed in the cooling systems. The analysis needs refinement toward improving the data base, elaborating the design, and including further ancillary systems.

Literature:

[1]   K. Kleefeldt, G. Marbach, T. Porfiri: EU DEMO blanket concept safety assessment, FZK internal report, to be published.

[2]   S. Malang, M. S. Tillack: Development of self-cooled liquid metal breeder blankets, FZKA 5581, September 1995.

Staff:

F. Dammel
K. Gabel
T. Jordan
K. Kleefeldt
K. Schleisiek
I. Schmuck
H.Schnauder

BL UR-D 1 Irradiation Behaviour of Insulating Coatings

Among the properties of importance of insulating ceramic materials under irradiation the electrical behaviour plays a central role in various control and diagnostic components as well as for the selection and design of blanket and vacuum current breaks. AlN is presently regarded as a suitable insulator with a multiple advantage: It is supposed to serve as coating of structural Vanadium alloys in order not to limit the upper operational temperature to 450-500°C through oxidation and interstitial pick-up, and it should prevent magnetohydrodynamic (MHD) pressure drops in liquid metal blankets by maintaining acceptable electrical resistivity values.

Well described in the literature is the radiation induced conductivity (RIC), which is due to the excitation of electrons from the valence to the conduction band by x- and γ-rays or by charged particles. RIC often has been shown to be in a wide range proportional to the density of these energetic ionizing particles. It immediately disappears when the particle current is turned off. Even under intense neutron irradiation where the ionizing dose rates usually are much smaller compared to charged particle irradiations, RIC is orders of magnitude above the thermal induced conductivity at elevated temperatures. Meanwhile, a significant irreversible loss of the electrical insulating capability, called radiation induced electrical degradation (RIED) has been found in several ceramics e.g. in some Al_2O_3 grades, when an electric field is applied during charged particle and neutron irradiation. However, these observations were questioned, because by some other authors it was shown, that an apparent increased irradiation-induced conductance must not necessarily be attributed to bulk properties but can also be explained by an enhanced deposition of carbon at the ceramic surface during irradiation, leading to short-circuit currents [1,2].

The prime objective of the present work was: Firstly, to investigate whether polycrystalline AlN can suffer a permanent loss of the electrical resistivity quickly, when an electric field is applied during irradiation, and, secondly, to provide well defined data on the in-situ and postirradiation electrical conductivities σ and $σ_0$ under fusion relevant loading conditions (damage and ionizing rates, temperature, electrical field, heat load). The significance of these results and their relation to current blanket designs will be discussed.

1.   Experimental

The specimen preparation and the experimental set-up is described more detailed in the preceding annual report.

All irradiations were performed using the high energy Dual Beam Facility of FZK, where α-particles (≤104 MeV) and protons (≤30 MeV) can be focussed onto a common target. In the past this facility has already shown to be a valuable instrument in investigating irradiation effects on thick specimens. For the present investigations, however, only the α-particle beam was used. Among others, practically homogeneous energy depositions, displacement damage rates and ionizing dose rates have been achieved which could be verified by computer calculations with the Monte Carlo transport code TRIM-cascade and the Boltzman transport code BOLT.

2.   Results and Discussion

Standard methods have been used to measure the DC resistance or conductivity of the ceramic specimens. A more detailed description is given in ref. [2]. It is important to note, that all conductivity measurements are done in vacuum and not in gaseous environment in order not to falsify the results by leakage currents from possible charge carriers of the environment.

2.1   Displacement damage dependency

Fig. 1 shows the electrical conductivities s and s0 versus the displacement damage for specimens irradiated at 300, 380 and 500 °C. The out-of-beam conductivity $σ_0$, measured always three minutes after turning off the α-particle beam, decreased at all temperatures investigated during the early stage of irradiation. Before 10^{-3} dpa had been reached, $σ_0$ dropped from the temperature dependent value of the unirradiated specimen to low values of typically $(2-4) \times 10^{-11} (Ωm)^{-1}$ at 300 and 380 °C. Irradiation at 500°C also produced a large decrease in $σ_0$. It can be seen that immediately after irradiation the conductivity begins to decrease and has reduced by four orders of magnitude by 0.02 dpa. Although during further irradiation a moderate reincrease was observed, $σ_0$ remained at all temperatures below the initial value of the unirradiated specimen. From the shape of the $σ_0$ measurements it can be speculated, that an incubation dose of about 0.08 dpa exists for low irradiation temperatures. The special experimental set-up made it possible to rule out that the observed increase during the 300 °C irradiation is caused by surface contamination and therefore should be attributed to bulk property changes.

The in-beam conductivity σ, measured continuously during irradiation, also decreased by at least one order of magnitude and saturated after about 0.02 dpa at all temperatures. After this saturation level of typically $(1.5-6) \times 10^{-8} (Ωm)^{-1}$ had been reached, σ-variations can be directly attributed to beam current fluctuations. Because during all AlN irradiations $σ_0$ remained orders of magnitude below σ, the in-beam conductivity σ is governed by the radiation induced conductivity (RIC), which immediately ceases when the particle beam is turned off.

An additional AlN specimen was irradiated to 0.03 dpa at 450 °C, where an exceptional high radiation induced electrical degradation (RIED) was observed in Vitox-alumina [2] at identical irradiation conditions. This AlN sample also showed a rapid decrease of $σ_0$ to values of $2 \times 10^{-11} (Ωm)^{-1}$, very similar to the 380 °C irradiation in Fig. 1.

2.2 Temperature and ionizing dose dependency

The electrical conductivity σ_0, measured before irradiation, shows the same reciprocal temperature dependency in all specimens (Fig. 2), indicating a well established fabrication process. Irradiation at 380 °C improves the conductivity by more than three orders of magnitude without significant changing the activation energy. This irradiation modified conductivity remains well preserved during isochronal annealing up to 550 °C. Irradiation at 300 °C to 0.09 dpa, however, did modify the activation energy from 0.84 eV (unirradiated samples) to 0.23 eV, which suggests a change in the conduction mechanism. Fig. 3 describes after irradiation at 380 °C the temperature dependent RIC of AlN during exposure to ionizing radiation. The electrical conductivity at a given ionizing rate (closed symbols) is practically independent of the temperature at low temperatures and follows closely the behaviour of the base conductivity (open symbols) at high temperatures. Thus, depending on temperature, the total conductivity σ is either governed by RIC or by the thermal conductivity.

Electrical conductivity measurements during 104 MeV α-particle irradiation can be made over a range of dose rate covering several orders of magnitude as shown in the log/log plot of Fig. 4 where the specimen temperature was maintained at 380 °C. From figs. 3 and 4 it can be seen that even at blanket relevant temperatures and a representative first wall dose rate of about 3000 Gy/s the electrical conductivity σ_0 is still many orders of magnitude below the critical value of $\sim 10^{-3}(\Omega m)^{-1}$ which determines the onset of
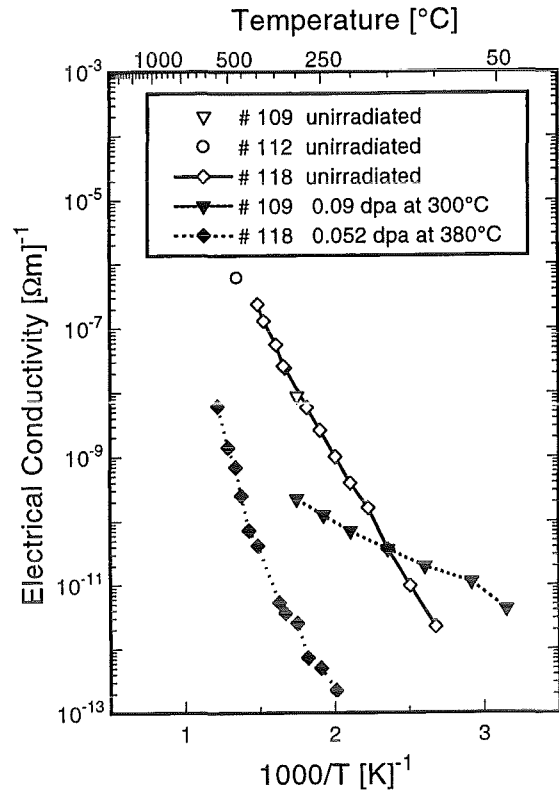

Fig. 2: Temperature dependence of σ_0 before irradiation, as well as after irradiation at 300 and 380 °C

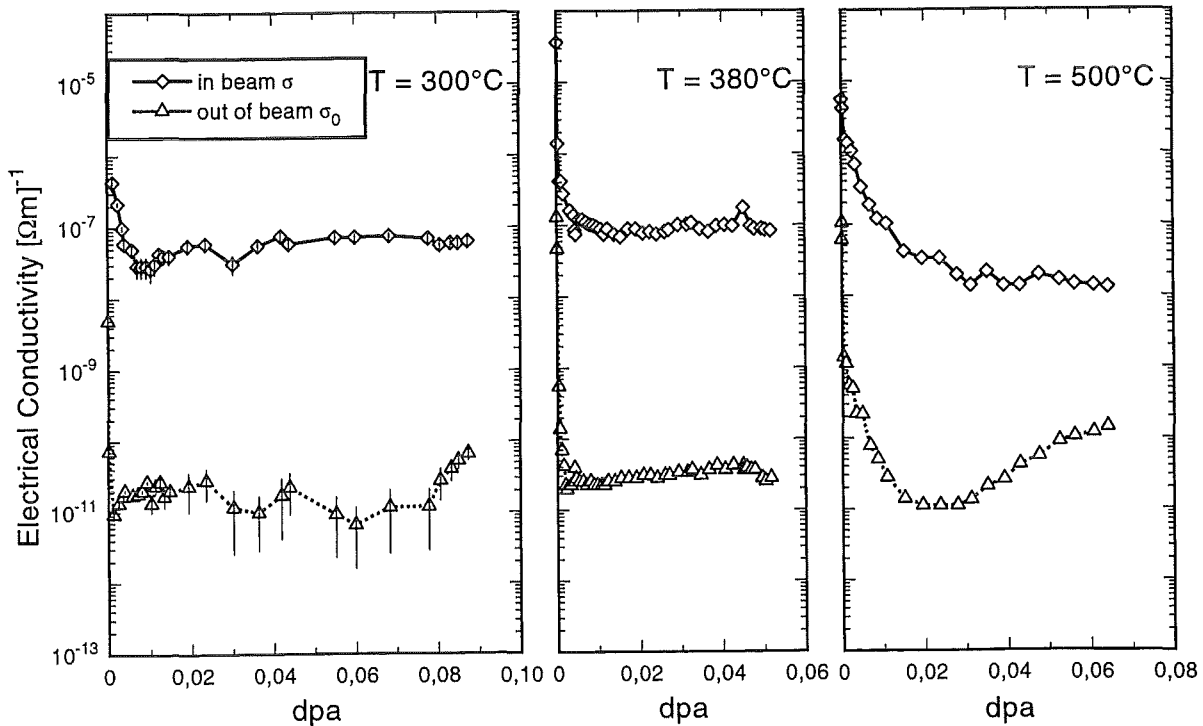MHD pressure drop in present self-cooled blanket designs.

Fig. 1: Electrical volume conductivity between 300 and 500 °C during (σ) and after (σ_0) 104 MeV α-particle irradiation in high vacuum with an applied DC electric field of 100 kV/m
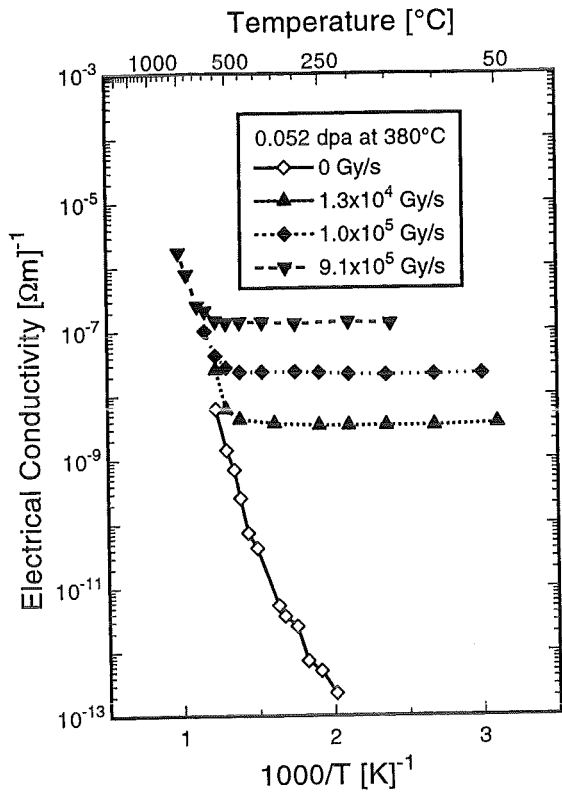
Temperature [°C]

Fig. 3: Electrical conductivity after irradiation to 0.052 dpa at 380 °C, with and without ionizing irradiation
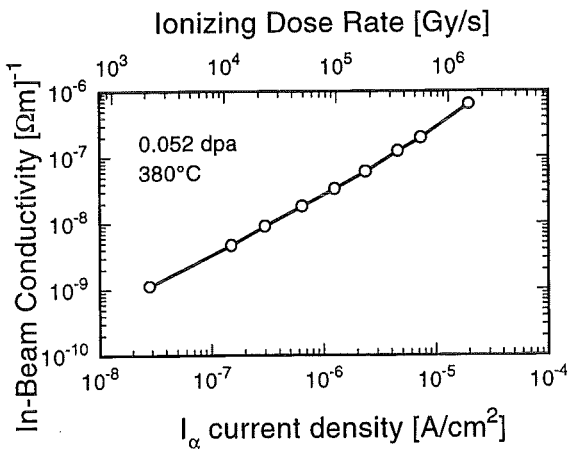
Ionizing Dose Rate [Gy/s]

Fig. 4: Electrical conductivity of AlN versus reciprocal temperature, with and without ionizing irradiation

Finally, these investigations also have shown that relevant dose rate versus conductivity measurements need sufficiently long damage exposure, that means, they should not be carried out before σ_0 of the impurity dependent unirradiated specimen has dropped to the base conductivity.

3. Conclusions

The general consensus of the present data, that, at least in the dpa range below 0.1 dpa, irradiation between 300 and 500 °C certainly does not degrade the electrical conductivity in the investigated AlN samples is a promising result for coating developments, but has to be confirmed to much higher dpa-values. Although σ_0 remained for all temperatures investigated below the initial value of the unirradiated specimen, further irradiation experiments may be necessary to clarify the nature of the increase of σ_0 at 0.08 dpa during the 300 °C irradiation.

Literature:

[1]   R. Lindau and A. Möslang, Proc. 7th Intern. Conf. on Fusion Reactor Materials ICFRM-7, Obninsk, Russia, September, 25-29, 1995.

[2]   A. Möslang, E. Daum, and R. Lindau, Proc. 18th Symposium on Fusion Technology; Karlsruhe, Germany, August 22-26, 1994 , Edrs: K. Herschbach, W. Maurer, J.E. Vetter (North Holland, 1995), p.1313.

Staff:

S. Baumgärtner
G. Bürkle
G. Hecker
R. Lindau
A. Möslang

Appendix I: Allocation of Tasks

Task No.		Title	FZK Departments

Plasma Facing Components and Plasma Engineering

Task No.		Title	FZK Departments
G 17 TT 25 EU	(T 226 b)	Plasma Disruption Simulation	INR
G 52 TT 246 EU	(T 26/T 246)	Ceramics for Heating and Current Drive and Diagnostic Systems	IMF I
G 17 TT 25 EU	(T 227)	Tritium Permeation and Inventory	INR
G 16 TT 16 EC	(T 9)	Fabrication and Testing of Water Cooled, Small size FW Mock-ups	IMF II, IATF

Superconducting Magnets

Task No.	Title	FZK Departments
MCOI 1/2	ITER TF-Model Coil Development	ITP
N 11 TT 19 94-02-95 FE 02 (MTOS 1)	Preparation of ITER TF-Model Coil Test Facility	ITP, HPE, HVT
MBAC	High Field Operation of NbTi at 1.8 K	ITP

Vacuum and Fuel Cycle

Task No.		Title	FZK Departments
G 18 TT 22 EU	(T 228)	Cryopump Development	HIT, ITP
N 32 TT 08 EU	(T 299)	Development of Plasma Exhaust Processing Technology	HVT/TLK, IRCH
TEP 3		Tritium Storage	HVT/TLK, IRCH

Vessel In-Vessel

Task No.		Title	FZK Departments
G 16 TD 17 EU	(D 202)	Shielding Blanket Development and Design	INR
G 16 TD 21 EU	(D 203)	Breeding Blanket Development and Design	INR
G 16 TT 82 EU	(T 218)	Shielding Neutronic Experiments, Heat Deposition and after Heat Measurements, Tritium Neutronic Experiments	INR, TU Dresden
NDB 1		Neutronics Data Base Development	INR
NDB 2-2		Neutronics Data Base - Shield Penetration Experiments	TU Dresden

Remote Handling / Maintenance

Task No.	Title	FZK Departments
RHT 1	Articulated Boom Transporter	HIT, HVT, IRS, IAI, AG-Mol
T 43	Remote Pipe Welding and Cutting	HIT

Safety and Environment

Task No.		Title	FZK Departments
SEA 3		Analysis of Reference Accident Sequences	IRS
CTA-EU-D 36	(SEP 2)	Environmental Impact of Tritium and Activation Products	INR, HS

Studies for ITER / NET

ERB 5000 CT 940027 NET	(NET 94-343) Quench Analysis for Magnet Safety Assessment	ITP
ERB 5000 CT 950044 NET	(NET 95-379) Nb_3Al Measurement for the Japanese Home Team	ITP
ERB 5000 CT 940059 NET	(NET 94-358) Assessment of the Use of High Temperature Superconductor in the ITER Current Leads	ITP
ERB 5000 CT 950064 NET	(NET 95-384) ITER Magnets and TFCM Stress Analysis	IRS

Development of ECRH Power Sources

| Gyrotron Development (includes ITER Task G 52 TT 03 FE) | ITP |
| High Power Windows (includes ITER Task G 52 TT 0 FE) | IMF III, ITP |

Long Term Programme for Materials Development

WP 1 Martensitic Steels

1.2.1		Metallurgical and Mechanical Characterization	IMF I
1.2.2	(MANET 3.2)	Fatigue and Creep Properties of Base Material F82H mod	IMF II
1.4.1	(LAM 3)	Metallurgical and Mechanical Characterization	IMF I
1.5.0 / 1.5.1	(MANET 3.4)	HFR Irradiation MANITU / TESEO	IMF II, HVT-HZ
1.6.1 / 1.6.2	(MAT 5)	Effects of Radiation Hardening and He in LAM / In-Beam Fatigue	IMF I

WP 4 Materials Application and Technology

| 4.3.1 | (MANET 2.3) Weldability Tests (Diffusion Welding) | IMF II |

Neutron Source

| ERB 5000 CT 950013 NET | (NET 94-366) Conceptual Design of the Lithium Target and of the Experimental Test Assembly of the D-Li Neutron Source (Phase 1) | INR, IMF I, IRS |

Blanket Development Programme

DEMO relevant BOT Solid Breeder Blanket

BS DE-D	Design Work	INR, IRS, IMF III
BS BE-D	Beryllium	INR
BS BR-D	Breeder Material	IMF I, IMF III, HVT-HZ, INR
BS NN-D	Non Nuclear Tests	INR, IMF III, IRCH, HIT

DEMO Relevant Self-cooled Liquid Metal Breeder Blanket

BL DE-D	Design Work	IRS, INR, IATF, IMF II, IMF III
BL PC-D	Physico Chemistry, Purification of Pb-17Li	HIT
BL EI-D	Electrical Insulation in Self-cooled Liquid Metal Breeder Blankets	IMF III, IRS
BL MH-D	Magneto-Hydro-Dynamics (MHD) in Self-cooled Liquid Metal Breeder Blankets	IATF
BL SA-D	Safety and Reliability/Availability Analyses	IRS
BL UR-D 1	Irradiation Behaviour of Insulating Coatings	IMF I

Appendix II: Table of ITER / NET Contracts

Theme	Contract No.	
Quench Analysis for Magnet Safety Assessment	ERB 5000 CT 940027 NET	(NET 94-343)
Nb$_3$Al Measurement for the Japanese Home Team	ERB 5000 CT 950044 NET	(NET 95-379)
Assessment of the Use of High Temperature Superconductor in the ITER Current Leads	ERB 5000 CT 940059 NET	(NET 94-358)
ITER Magnets and TFCM Stress Analysis	ERB 5000 CT 950064	(NET 95-384)
Conceptual Design of the Lithium Target and of the Experimental Test Assembly of the D-Li Neutron Source (Phase 1)	ERB 5000 CT 950013	(NET 94-366)

Appendix III: FZK Departments Contributing to the Fusion Project

FZK Department	FZK Institut/Abteilung	Director	Ext.
Institute for Materials Research	Institut für Material- und Festkörperforschung (IMF)	I. Prof. Dr.K.-H. Zum Gahr II. Prof. Dr. D. Munz III. Dr. J. Haußelt	3897 4815 2518
Institute for Neutron Physics and Reactor Engineering	Institut für Neutronenphysik und Reaktortechnik (INR)	Prof. Dr. G. Keßler	2440
Institute for Applied Thermo- and Fluiddynamic	Institut für Angewandte Thermo- und Fluiddynamik (IATF)	Prof. Dr. U. Müller	3450
Institute for Radiochemistry	Institut für Radiochemie (IRCH)	Prof. Dr. H.J. Ache	3200
Institute for Reactor Safety	Institut für Reaktor- sicherheit (IRS)	Prof. Dr. D. Cacuci	2550
Central Engineering Department	Hauptabteilung Ingenieur- technik (HIT)	Dr. H. Rininsland	3000
Institute for Technical Physics	Institut für Technische Physik (ITP)	Prof. Dr. P. Komarek	3500
Central Experimental Engineering Department - Hot Cells - Tritium Laboratory Karlsruhe	Hauptabteilung Versuchstechnik (HVT) - Heiße Zellen (HVT-HZ) - Tritiumlabor Karlsruhe (TLK)	Dr. Schubert DI. Enderlein Dr. R.D. Penzhorn	3114 3650 3239
Remote Handling Laboratory	Handhabungstechnik- Labor (HT)	Dr. Scholl	2942
Central Safety Department	Hauptabteilung Sicherheit (HS)	DP. W. Koelzer	2660
Institute for Applied Informatics	Institut für Angewandte Informatik (IAI)	Prof. Dr. H. Trauboth	5700
Central Department for Real-time Data Processing and Electronics	Hauptabteilung Prozeßdatenverarbeitung und Elektronik	Prof. Dr. H. Gemmeke	5635

Contributing:

Institute of Nuclear and Particle Physics, Technical University Dresden	Institut für Kern- und Teilchenphysik der Technischen Universität Dresden	Prof. Dr. K. Seidel	035101/8982

Appendix IV: Fusion Project Management Staff

Head of the Research Unit	Dr. J. E. Vetter	ext. 5460
Secretariate:	Fr. I. Sickinger	ext. 5461
	Fr. I. Pleli	ext. 5466
	Fr. V. Lallemand	ext. 5466
Project Budgets, Administration, Documentation	BW G. Kast	ext. 5462
Studies, ITER / NET Contacts	Dr. J.E. Vetter	ext. 5460
Superconducting Magnets, Gyrotron Development	DI H. Knuth	ext. 5468
Tritium Technology Structural Materials	Dr. H.D. Röhrig	ext. 5463
Blanket Technology, Remote Handling	DI A. Fiege	ext. 5465

Address: Forschungszentrum Karlsruhe GmbH
Nuclear Fusion Project Management

Post Office Box 3640, D-76021 Karlsruhe / Germany

Telephone No: 07247-82- Extensions ....

Telefax No: 07247 - 82 - 5467

Telex No: 17 724 716

e-mail: de:d400:fzk:kfk:pro:pkf-leitung: or

pkf-projektleitung@pro.kfk.fzk.d400.de